Focussed MeV-Ion Micro- and Nano-Beams in the Life Sciences

Selected Applications

Von der Fakultät für Physik und Geowissenschaften

der Universität Leipzig

genehmigte

Habilitationsschrift

zur Erlangung des akademischen Grades

Doctor rerum naturalium habilitatus

Dr. rer. nat. habil.

vorgelegt von

Dr. rer. nat. Tilo Reinert

geboren am 04.06.1969 in Chemnitz

Tag der Verleihung: 15.12.2008

Gutachter:

Prof. Dr. Josef Käs

Prof. Dr. Philippe Moretto

Prof. Dr. Günter Schmahl

Bibliographische Beschreibung

Die vorliegende Arbeit etabliert für Anwendungen in den Lebenswissenschaften den Einsatz hochfokussierter MeV-Ionenstrahlen für nuklear-mikroskopische Methoden der quantitativen Spurenelementanalyse, der 2D- und 3D-Dichtemikroskopie sowie für die gezielte Bestrahlung einzelner lebender Zellen für radiobiologische Experimente. Zur Anwendung kamen die Methoden ortsaufgelöste Protonen induzierte Röntgenfluoreszenzanalyse (particle induced X-ray emission - PIXE), Spektrometrie rückgestreuter Ionen (Rutherford backscattering spectrometry - RBS) und Rastertransmissionsionenmikroskopie (scanning transmission ion microscopy - STIM). Durch eine gezielte Weiterentwicklung des bestehenden Ionenstrahlmikroskops, der Hochenergie Ionennanosonde LIPSION, konnte die Ortsauflösung für Spurenelementanalyse auf unter 300 nm verbessert werden, beziehungsweise die Sensitivität für Metallionen in biologischen Proben auf unter 200 ng/g (3 μmol/l) bei einer Ortsauflösung von 1 μm verbessert werden.

Die Habilitationsschrift umfasst eine kurze allgemeine Einleitung einschließlich der Motivation für den Einsatz fokussierter MeV-Ionenstrahlen sowie einen Überblick über die Anwendungsgebiete und aktuellen Forschungsschwerpunkte. Danach werden kurz die Grundlagen der Technik und Methoden vorgestellt, gefolgt von einer Abschätzung der Auflösungsgrenzen für Elementanalysen und Einzelionentechniken. Danach werden ausgewählte Anwendungen aus verschiedenen Forschungsgebieten vorgestellt. Das erstes Beispiel ist aus der Umweltforschung. Es wird dargestellt, wie mittels ortsaufgelöster Elementspektroskopie eine Abschätzung der Feinstaubbelastung nach Beiträgen einzelner Verursacherquellen erfolgen kann. Dann folgt als Beispiel eine ortsaufgelöste Analyse der Verteilung von Nanopartikeln aus Sonnencremes in Hautquerschnitten zur Risikoabschätzung der Anwendungen von Nanotechnologie in kosmetischen Produkten. Desweiteren werden Studien der Spurenelementverteilung, speziell der von gebundenen Metallionen, in Hirnschnitten auf zellulärer und subzellulärer Ebene erläutert. Das anschließende Beispiel erläutert die Anwendung niedriger Energiedosen in der Radiobiologie anhand des Beschusses einzelner lebender Zellen mit abgezählten einzelnen Ionen. Als letztes Beispiel wird die Anwendung hochfokussierter Ionenstrahlen für die Mikrotomographie gezeigt. Abschließend folgt eine zusammenfassende Bewertung der vorgestellten Anwendungen mit einem Ausblick auf weitere Anwendungen und methodische Entwicklungen. Der Arbeit sind die jeweils ersten Seiten der relevanten Veröffentlichungen mit Beteiligung des Autors als Anhang beigefügt.

Description

Reinert, Tilo:
Focussed MeV-Ion Micro- and Nano-Beams in the Life Sciences
Universität Leipzig, habilitation thesis, language: English
270 pages, 91 references, 26 figures
Summary:

This work presents the development of a sub-micron nuclear microprobe for applications in the life sciences. It includes quantitative trace element analysis with sub-micron spatial resolution, 2D- and 3D-microscopy of density distributions and the targeted irradiation of living cells with counted single ions. The analytical methods base on particle induced X-ray emission spectrometry (PIXE), Rutherford backscattering spectrometry (RBS), scanning transmission ion microscopy (STIM) and STIM-tomography. The specific development of the existing nuclear microprobe LIPSION led to an improved performance of the capabilities for trace element analysis. For sub-micron analysis the spatial resolution could be improved to 300 nm at a sensitivity of about 1 µg/g for metal ions in biological matrices; for a resolution of 1 µm the sensitivity was improved to 200 ng/g (3 µmol/l).

This habilitation thesis comprises a short general introduction including the motivation to utilize focussed high energy ion beams, an overview on the applications and actual research fields. The introduction is followed by the basic principles of the equipments and analytical methods. An estimation of the limits of resolution for element analytical and single ion techniques is given for the Leipzig system. Thereafter, selected studies from different research areas are presented. The first presented application is a study from environmental air pollution research. It is demonstrated that the microscopic elemental analysis of single aerosol particles can be used to assess the contributions from different sources. A further example is the analysis of the distribution of nanoparticles in skin cross-sections for a risk assessment of the applications of nano-sized physical UV-filters in cosmetic products. The risk assessment is followed by the micro-analysis of trace elements, especially of bound metal ions, in brain sections on the cellular and sub-cellular level. After this the application of focussed MeV ion beams in low dose radiobiological research is presented. Finally, the analysis of 3D-density distributions by proton micro-tomography is demonstrated. A summary concludes on the applications and gives an outlook to further applications and methodological developments. The appendix comprises the relevant publications of the author.

In Erinnerung an meine Mutter

Table of Contents

Chapter 1

Introduction

The idea of focussing high energy ions has a long history. Dated back to the beginning of accelerator based nuclear research, the application to materials analysis arose in the early 70ies. A reason was the requirement for improved positional information from analytical techniques using nuclear projectiles. The first development of a microprobe with a focussed ion beam, a so called "nuclear microprobe" (according to electron microprobes) was started at Harwell, UK, [Coo72]. Since then many nuclear microprobes have been build. Today we find more than fifty around the world and several more will follow in the near future.

The main advantage of using nuclear projectiles instead of electrons – for analytical techniques light projectiles i.e. H^+- or He^+-ions are most useful – derives from the fact that ions are much heavier then electrons. Thus, they have a deeper information depth due to lower large angle scattering; they have a lower bremsstrahlung background in X-ray spectrometry and therefore lower detection limits; the backscattering spectrometry is depth sensitive in the micron range; and nuclear reactions can also be utilized for analysis. All these processes are well understood and substantial data bases secure the analytical results.

The excellent quantitative accuracy and the versatility of a nuclear microprobe establishes its applications in a broad range of scientific fields, e.g. high-tech materials, semiconductor-technology, planetary science, geology, and environmental research [Jam97, Tak97, Vis97, Rya04, Mal96], but also in the humanities: art and archaeology, history and forensics [Swa97], physiology, botany, medicine, and many others [Mor97, Prz97].

A nuclear microprobe is not only a non-destructive analytical tool. It is also capable of changing physical properties of materials. The electronic structure, crystal quality and optical properties can be modified to produce 3D-structures, optical wave guides, multi-colour fluorescent materials and even ferromagnetic effects in carbon [Kan03, Men07, Bet07, Teo07, Spe05]. These results are a bright prospect for new technological applications – to benefit from unexpected properties of well established materials.

Modifying solids is only one aspect. A focussed beam of MeV nuclear projectiles can also be used as a precise applicator of ionising radiation to living cells. The precision is not only in the position, e.g. targeting the nucleus or the cytoplasm of a cell, but also in the degree of damage which depends on the ionisation processes, i.e.

the linear energy transfer (LET). This is because the LET depends on the type and energy of the projectile. Both can be selected by the accelerator settings. A further measure is the number of particles applied to the cells, which can be determined by detecting and counting each individual ion of the beam. The so called targeted single ion bombardment is an extraordinary approach to study the principles of low dose effects of ionising radiation to living organisms [Pri03, Zho04, Pri06, Fol07].

The great versatility of nuclear microprobes is demonstrated by the vast number of studies that have been performed during the last 35 years. Hereby, the applications in biological and biomedical fields were always a major part. The pie chart below gives an overview of the distribution of the studies presented at the last nuclear microprobe conference (10th ICNMTA), July 2006, published in [Osi07].
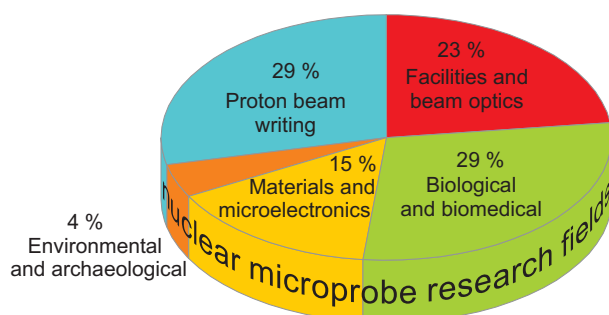
Fig. 1.1: Pie chart of the research fields presented at the last international conference on nuclear microprobe technology and applications, July 2006.

All the microbeam techniques will be even more powerful and bring new insides into many research fields when the spatial resolution will be improved. However, since the beginning at about 1.5 μm more than 30 years ago there was no breakthrough in spatial resolution. Only a few laboratories are able to focus the beam to below 0.3 μm. However, for elemental analysis there was almost no progress in spatial resolution. Studies are performed at resolutions of 1 μm or worse. The long intention to evolve the existing systems or to develop revolutionary systems which improve the spatial resolution by an order of magnitude is still an actual effort.

This habilitation thesis presents the progress and the applications of the Leipzig High-Energy Ion Nanoprobe LIPSION in the field of life sciences. It is divided into a short overview of the microprobe principles and the analytical techniques followed by the improvements to proceed from micro- to nanoprobe, the chapters with the resumes of the applications in environmental research, nanosafety research, brain research and low dose radiobiology, and a chapter on proton-microtomography.

Chapter 2

The High Energy Ion Microprobe

2.1   General overview

The name "high energy ion microprobe" or "nuclear microprobe" refers firstly to the use of focussed ions as probing particles, instead of electrons, and secondly to ion energies above 1 MeV to draw a distinction to the FIB's, the focussed (heavy) ion beams of energies below 100 keV. Even though there are microprobe systems that focus heavier ions (e.g. deuterium, carbon, nitrogen, oxygen,...) with energies well above 10 MeV per nucleon [Fis85, Dol03, Mei95, Doy97] common high energy ion microprobes usually utilize hydrogen and helium ions (H^+ and He^+) up to about 3 MeV.

Another aspect of nuclear microprobes is the beam current. The analytical methods with elemental sensitivity, e.g. PIXE, have cross sections involved in their basic interaction processes that determine the yield of measurable signals. With a standard experimental set-up, beam currents in the range of 50 pA to 1 nA or even more are desired to reach trace element sensitivity. For that the microprobes have to be operated in the "high current mode", a working mode that requires relatively large beam spot sizes (≥ 1 µm). In contrast, the "low current mode" (ca. 1 fA – corresponds to 6000 ions per second) has to be used when each individual ion can be measured (e.g. energy loss in transmission – STIM or the creation of free charge carriers – IBICC). In the low current mode the beam spot sizes can reach sub 100 nm dimensions.

The Leipzig system was developed for very high spatial resolution work even in the high current mode. The components, laboratory building with a high stability room temperature control system and deep-seated concrete baseplates, the ion-accelerator Singletron^{TM} with a high ion source brightness [Mou97], the probe forming lens system of high demagnification configured in a split Russian quadruplet [Dym95] were chosen according to the actual knowledge at that time [But96]. The first focussed ion beam was tested in August 1998. In order to underline the extensive concept for a substantial improvement in microprobe performance, the system's new description was "Nanoprobe" with the name "LIPSION". Figure 2.1 shows a view into the LIPSION laboratory from the 90°-magnet.
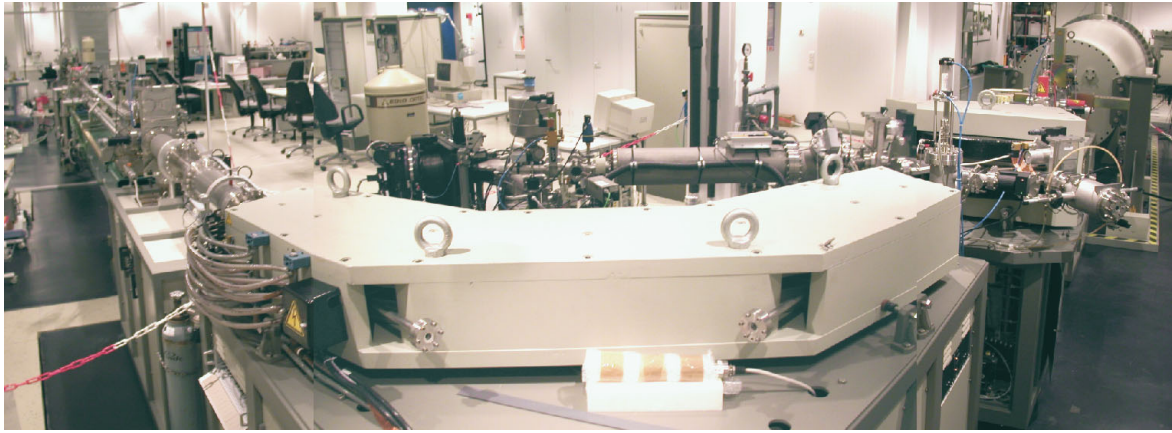
Fig. 2.1: View into the LIPSION laboratory from behind the 90°-magnet; from right: 3.5 MV Singletron[TM] accelerator; to the left: probe forming system.

The Laboratory

The establishment of the Leipzig Ion Nanoprobe laboratory was part of the reconstruction of a whole building. It gave the opportunity to design a new laboratory from scratch. Therefore, the bedplates of accelerator and nanoprobe could be founded in greater depths (approximately 10 m) separately from the surroundings to minimize mechanical vibrations (see the black coloured floor plates in figure 2.1). In order to avoid thermal drifts of the system the room temperature is controlled by a powerful air conditioning system which operates with an accuracy of ±0.5 K. An active compensation system compensates the varying stray magnetic fields from a nearby tram-line which otherwise would derange the beam trajectory and consequently alter the beam spot position in the micrometer range [SPE03].

The Accelerator

A high beam brightness[1] and a high stability of the beam energy are important for high resolution nanoprobe applications. The 3.5 MV Singletron[TM] accelerator provides H$^+$- or He$^+$- ion beams with a relatively high beam brightness of more than $20 \frac{\text{pA}}{\text{mrad}^2 \, \mu\text{m}^2 \, \text{MeV}}$. This seems not to be the limit of the radiofrequency ion source because an approximately four times higher brightness has been reported from the same type of Singletron[TM] in Singapore [WAT03].

The Singletron is in principle a COCKCROFT-WALTON-generator that utilizes the GREINACHER cascade, a voltage multiplier circuit of diodes and capacitors. This principle of high voltage generation achieves a very low voltage ripple, which is in our accelerator $\sim 25 \, \text{V}_{\text{pp}}$. In combination with a very stable 90° analysing magnet which serves as momentum and charge state selector and ion beam monochromator the beam enters the probe forming system with an energy stability of $\Delta E/E = \sim 10^{-5}$.

---

[1]high beam brightness = high beam current density into small divergence

The probe forming system

The whole probe forming system is mounted on a single steel girder, similar to an optical bench, to ensure as much rigidity as possible. The main part of the system is a split Russian quadruplet of magnetic quadrupole lenses. In other words it consists of two pairs of magnetic quadrupoles that are separated from each other. The arrangement provides a large orthomorphic demagnification of about 100 in both directions, i.e. the beam through a circular 100 μm object diaphragm is focussed to a spot of 1 μm.
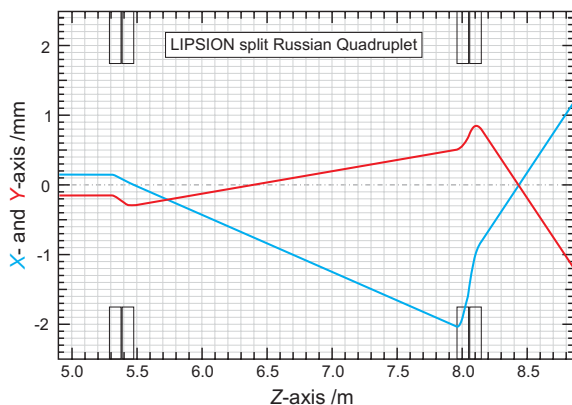
Fig. 2.2: Ion optics raytraycing of the LIPSION system. The initial settings were 100 μm diameter for the object and 300 μm diameter for the aperture collimator.

The large demagnification is an advantage because larger object diaphragms produce less edge scattering effects and therefore less deterioration of the ion beam phase space, the initial spatial and momentum distribution. A further advantage is that the propagation of any vibrational or thermal instabilities of the object position affects the final beam spot position by the factor of 1/100 only.

Everything would be perfect and simple if there would not be the other side of the coin: Having a large demagnification is almost unavoidably connected with large intrinsic spherical aberrations of the ion optical system. They introduce image distortions. Beam trajectories of increasing distances to the optical axis cause a growing beam halo. The degrading influences of these third order contributions on the final beam spot size can be kept reasonably low by limiting the beam divergence, practically spoken using smaller aperture diaphragms. The gain in beam intensity due to the larger object diaphragms has to be paid by smaller aperture diaphragms than usually used in systems with less spherical aberrations. Nevertheless, the performance of the Leipzig split Russian quadruplet compares well with the best systems worldwide.

The probe forming lens system has a large object distance. Consequently, there is also a large image distance, the working distance between the last quadrupole and the focus point. This is a major aspect, because the beam scanner (two pairs of electromagnetic coils) has to be behind the last quadrupole. The reason is, once more, the large spherical aberrations; they do not allow to scan the beam already before the quadrupoles. The long working distance gives also more space for detectors that needs to be installed in the backward direction, such as the detectors for X-rays, backscattered particles and secondary electrons. Last but not least a front view microscope facilitates the positioning of the sample into the beam axis. All these equipments fit between the last quadrupole and the focus point where the sample awaits irradiation or analytical investigations.

RBS
Rutherford Backscattering Spectrometry

light ions
as primary
particles

backscattered
primary
particles

Measurement:
Number and energy
of backscatterd particles

Information:
Number, mass and depth
of collision partners
(with spatial resolution)

PIXE
Particle Induced X-ray Emission

light ions
as primary
particles

characteristic
X-rays

Measurement:
Intensity and energy
of characteristic X-rays
(with spatial resolution)

Information:
element specific
concentration

IL
Ionoluminescence
Measurement:
Light spectrum
Information:
Element speciation

NRA
Nuclear Reaction Analysis
Measurement:
induced nuclear radiation
Information:
Nuclear specification, con-
centration and (with reso-
nant excitation) depth

Ions
as primary
particles

backscatterd
primar ions
(RBS)

characteristic
X-rays
(PIXE)

Light
emission
(IL)

Gamma-
radiation
(PIGE)   h$^+$

e$^-$

e$^-$

Secondary
electrons
(SE)

Ion beam induced
charged collection
(IBICC)

Energy
loss
(STIM)

SEI
Secondary Electron Imaging
Measurement:
Intensity of secondary
electrons from near surface
areas
(spatially resolved)

Information:
Topography

IBICC
Ion Beam Induced Charge Collection

light ions
as primary
particles

Measurement:
Induced charge in the
electrodes in dependency
on applied voltage or
position when scanned

Information:
electronic properties
(e.g. charge carrier mobility,
  trapping, electric field strength)

A   U

STIM
Scanning Transmission Ion Microscopy

Mass distribution

light ions
as primary
particles

Measurement:
Energy loss of transmitted
primary particles
(spatially resolved),
tomography with sample
rotation

Information:
Mass distribution

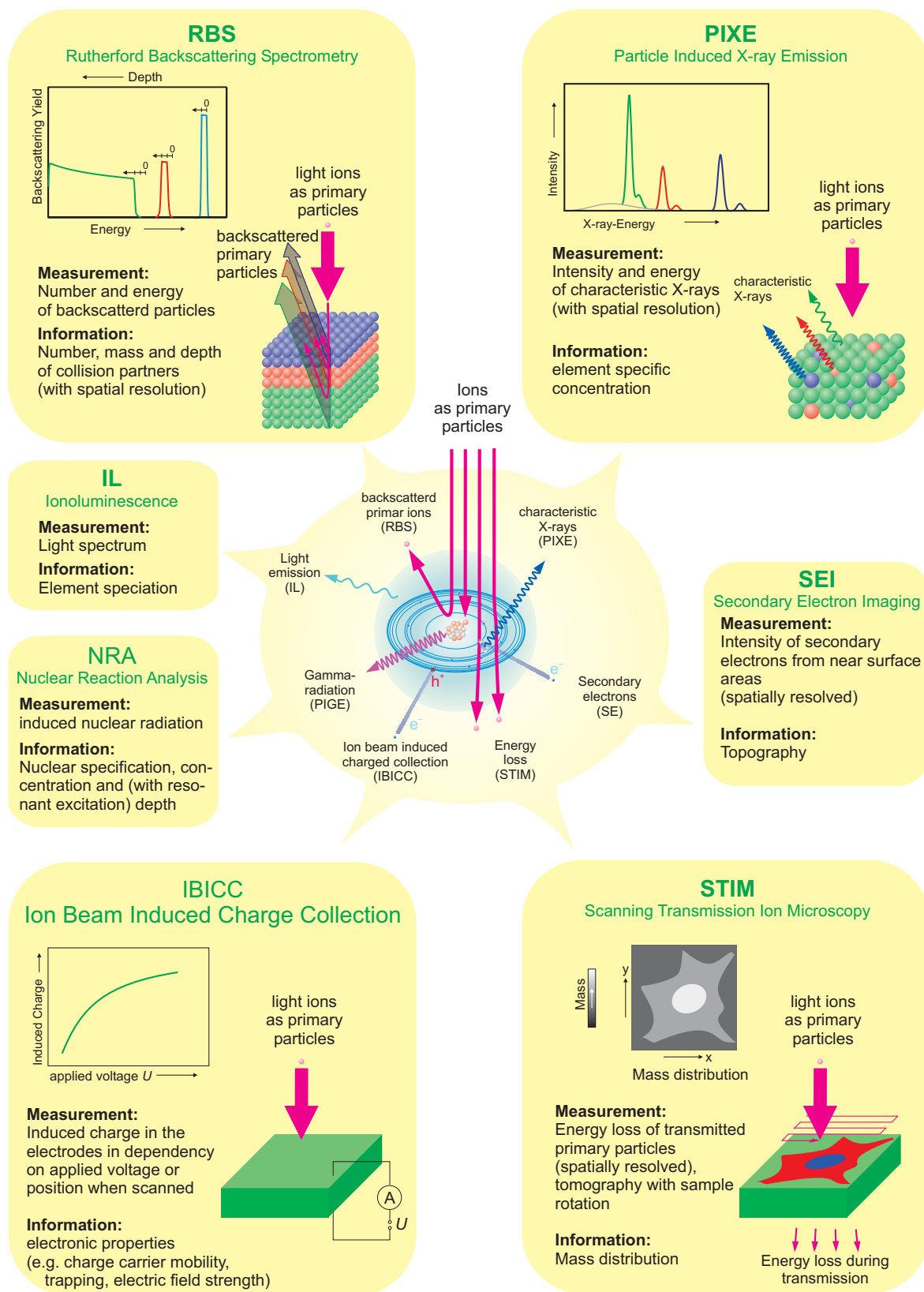Energy loss during
transmission

Fig. 2.3: Schematic representation of ion beam analytical methods.

Analytical Methods

The ion beam interacts with the sample material, its molecules, atoms and nuclei. These manifold interaction processes yield information on a variety of the sample properties. The processes have been subject of nuclear and atomic physics research for many years. Hence, they are today the basis for secured and precise methods of ion beam analysis. The spatial resolution of the methods is achieved by scanning the ion beam over the sample and recording the interaction signals with the positional information. This information allows to create quantitative maps of particular characteristics of the sample such as distributions of elemental concentrations or the mass distribution.

There are several textbooks with detailed descriptions of the analytical methods. A widespread overview of general ion beam analytical methods can be found in the "Handbook of Modern Ion Beam Materials Analysis" [Tes95], whereas the books "Backscattering Spectrometry" and "Particle-Induced X-Ray Emission Spectrometry (PIXE)" concern in particular the two most important analytical methods [Chu78, Joh95]. "Materials Analysis using a Nuclear Microprobe" gives a comprehensive overview with relation to nuclear microprobes [Bre96] and a particular emphasis on applications in the life sciences can be found in "Nuclear microprobes in the life sciences" [Lla98]. Nevertheless, a pictorial representation (figure 2.3) and a few words on the analytical methods shall be given here.

PIXE[2], the spectrometry of particle induced X-ray emission is a quantitative element sensitive analytical method which is based on the capability of MeV-particles to ionize the sample atoms mainly in the K- and L-shell. The subsequent emission of characteristic X-rays yields information on the concentration of a particular element in the sample via the intensity of its characteristic X-ray lines (peaks in the spectrum). The analytical limits of the detection arise from the detection efficiency for the X-rays which depend on the X-ray energy, on the solid angle subtended by the detector(s), and on the peak to background ratio for the X-ray lines in the spectrum. Usually, elements with X-ray lines above 1 keV ($Z > 11$) are detectable with minimum detection limits in the µg/g range. For elements in the range $Z = 21 \ldots 30$ the detection limits can even be below 1 µg/g, e.g. for physiologically important metals like Fe, Cu, Zn in an organic matrix.

RBS, the Rutherford backscattering spectrometry utilizes the elastic scattering of the incident particles on the sample nuclei backwards through an angle close to 180°. The ratio of the energy of the projectile immediately after the scattering process to the incident energy, the so called kinematic factor, yields the information on the mass of the encountered nucleus. Thus, RBS is an element analytical method. The kinematics of the scattering process defines the window for analytical applications. RBS with helium ions achieves a better mass resolution than the proton scattering process. Furthermore, in the case of proton back scattering on light nuclei[3], the scattering cross sections deviates from the classical Rutherford cross sections due to the additional involvement of nuclear forces. For these cases the Ion Beam Nuclear Data Library provides a comprehensive experimental data base for the non-Rutherford cross sections [Gur07].

---

[2]PIXE with spatial resolution is often specified as µPIXE

[3]Especially important when analyzing e.g. biological material with high contents of carbon, nitrogen and oxygen.

Besides the element analytical capability, RBS also probes the depth of the nucleus on which the particle is scattered. The scattering event can occur already at the surface of the sample or in any depth within the particle range. As a consequence, with increasing depth the particle is slowing down, having less energy in the scattering process followed by a further energy loss backwards on the way out of the sample. The final energy of the particle then has a lower energy compared to the scattering process on the same nucleus on the surface. This energy shift is a measure for the depth. RBS is therefore also used to analyse depth distributions of elements, the thickness of a thin layer or the structure of thin multilayers.

STIM stands for scanning transmission ion microscopy, a microscopic technique that creates images of the density distribution. This is mostly used to image the morphology of thin sections[4] of dehydrated biological samples. Scanning over the sample, the residual energy of each transmitted ion (about 10 ions per scanning position) is measured; the median or average difference to the incident energy then gives the energy loss and thus the electron density which is a measure for the mass distribution within the sample.

The main principle for this technique is the electronic stopping power, which is the successive energy loss of the incident particles due to scattering on the electrons of the sample material. The dependency of the energy loss (per unit distance) upon the electron density is approximated by the Bethe-Bloch-formula [BET30, BLO33]. Although this approximation is adequate for most STIM measurements, usually the stopping powers are taken from a software package, based on a vast experimental data base, mainly because the software easily creates stopping power tables for any compound and projectile combination over a selected energy range, also nuclear stopping and bonding corrections for light compounds are included [ZIE].

IBIL – ion beam induced luminescence is a phenomenon that is based on the interaction processes of MeV particles which excite the sample atoms in the optical system, i.e. the outer electron shells. Hence, ion beam induced luminescence yields information on all properties of a material that are related to the outer electron shells, e.g. the type of the luminescence centers, its chemical and structural neighbourhood, phase transitions, specific impurities, or chemical speciation [TOW07].

However, the processes are complex and often interfere with other processes. Activation and co-activation, quenching, thermal effects, or beam damage influence the luminescence. Nevertheless, the method is widely used to study e.g. impurities, defects, crystallinity, or radiation hardness of geological, doped and natural semiconductor, and scintillating materials, or even art objects, especially painting pigments [BRO02, ROS04, QUA07].

IBICC, the ion beam induced charge collection, utilizes the creation of electron-hole pairs after ion impact in a semiconducting or semi-insulating material or device to investigate the electronic properties. The measured signal is the induced charge in the electrodes when the charge carriers in the material move due to an external or intrinsic static electric field. The induced charge depends on the amount of trapping and recombination at point and extended defects, the doping density, minority carrier diffusion length, electric field strength, mobility and collection geometry. A time re-

---

[4]Sections of a few micrometer thickness

solved measurement of the charge induction (TRIBICC) allows to study also the charge carrier dynamics. A recent review on ion beam induced charge collection is given by Breese et al. [BRE07].

SEI, the secondary electron imaging is very similar to the SEI at a scanning electron microscope. A nuclear microprobe induces the emission of secondary electrons from the sample surface, too. The difference is of cause in the primary particles, the ions. The imaging procedure then is the same. The secondary electrons from the sample are detected. The intensity depends on the surface structure and orientation with a higher emission rate at edges and corners. Usually, the electron intensity is recorded without any energy information, because the method is used as a simple qualitative imaging technique for the sample topology.

NRA, nuclear reaction analysis is a method that uses secondary gamma[5] or particle radiation from nuclear reactions. The energy range of nuclear microprobes allows only a restricted number of reactions with light nuclei (e.g. ^{7}Li(p,α)α, ^{11}B(p,α)2α, ^{19}F(p,p'γ)^{19}F). This however, is a complementary approach to analyse concentrations of low Z elements on the µg/g-level which is conventionally not accessible with other methods.

2.2 From Micro- to Nanoprobes

In the 1970s, the first nuclear microprobes did already focus proton beams to spot dimensions of about 2 µm in diameter at a beam current of about 100 pA [COO72, NOB77]. In the early 1980s the Oxford microprobe halved the beam spot to 1 µm [WAT81]. Again ten years later, in the 1990s, beam spots around 0.5 µm have been reported. This development gave the idea to compare the beam spot sizes with Moore's law of the progress in integrated circuit technology (figure 2.4, adopted from [JAM01]).

According to this extrapolation a further significant increase in microprobe performance, may be not yet breaking the 100 nm barrier but beam spot sizes below 200 nm in the high current mode, would have been expected for the new millennium, because beam optics and accelerator technology seemed to be sufficiently advanced. The trend, however, turned out to be much slower than the economically driven technological progress. The beam spot sizes of nuclear microprobes were stuck at around 0.5 µm and these numbers are reports on best values measured, but not the performance at routine work. The best beam spot sizes obviously could not be resumed in standard microprobe analyses, i.e. PIXE or RBS studies. The literature only reveals nuclear microprobe studies with spatial resolutions of 1 µm or more. There are several reasons for that. The most important one is probably the stability of the system.

A beam spot measurement, mostly done on structures like copper or nickel grids, requires in the high current mode only a few minutes of acquisition time. However, studies on trace element distributions with sub-micron lateral resolution will need acquisition times for a scan in the order of an hour. During this time the spatial resolution is easily deteriorated by mechanical or thermal instabilities in the microprobe system, by varying stray magnetic fields, or by instabilities in the lens currents. Furthermore,

---

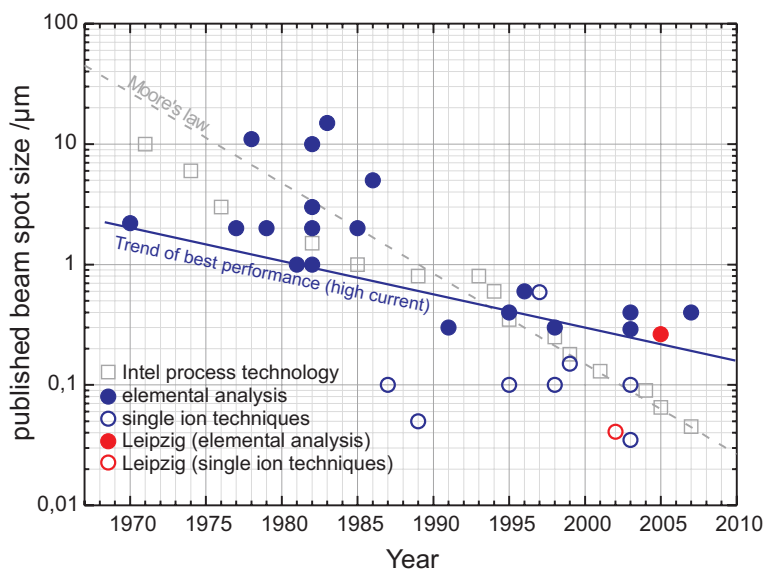[5]PIGE – particle induced γ-ray emission

Fig. 2.4: The development of the beam spot sizes of nuclear microprobes (halves every eleven years) in relation to the advancement of Intel process technology guided by Moore's law (halves every four years).

in the case of biological samples the beam can also cause sample shrinkage or distortions which then limits the attainable spatial resolution. Other sources of resolution deterioration show effects even on the short time scale. Mechanical distortions from persons walking in the lab or vibrations from roughing and turbo pumps. Even the beam scanning system can introduce positioning instabilities of the beam. The scan signal which drives the currents through the scanning coils, could be interfered by disturbing signals from power supplies or from computer parts (e.g. video card). Another contribution to the positioning uncertainty may come from eddy currents in the beam tube induced by the magnetic field of the scan coils. All these effects could be small, not disturbing standard microprobe operation with micron resolution. However, they can be the limiting factor at resolutions below 500 nm.

The Leipzig system avoids mechanical distortions and vibrations with the separated baseplates and by switching off mechanical pumps for high resolution work; ion getter pumps then maintain the vacuum below 10^{-6} mbar. Air conditioning stabilises the temperature to ± 0.5 °C. The influence of stray magnetic fields is reduced by extensively shielding large parts of the beam tube and additionally by the active compensation system. In order to avoid the scanner induced eddy currents the aluminum beam tube was replaced by a glass tube, internally covered with stripes of a conductive coating to avoid upcharging.

In the year 2005 the Leipzig system was subject to simple but efficient revisions concerning the probe forming lens system. An careful alignment of the aperture diaphragms onto the beam optical axis together with an improved focussing procedure allowed the use of larger apertures. Although the Leipzig probe forming system has very large spherical aberration coefficients (about a factor of two compared to other high performance systems), there was only a slight increase of the beam spot size due to the larger aperture diaphragms but a factor of five in beam current. With this

enhanced performance the probe forming system was able to focus a 120 pA proton beam of 2.25 MeV down to 0.5 μm. Accepting a very low beam current of 10 pA a beam focus of less than 300 nm was achieved (figure 2.5, [Rei06]).
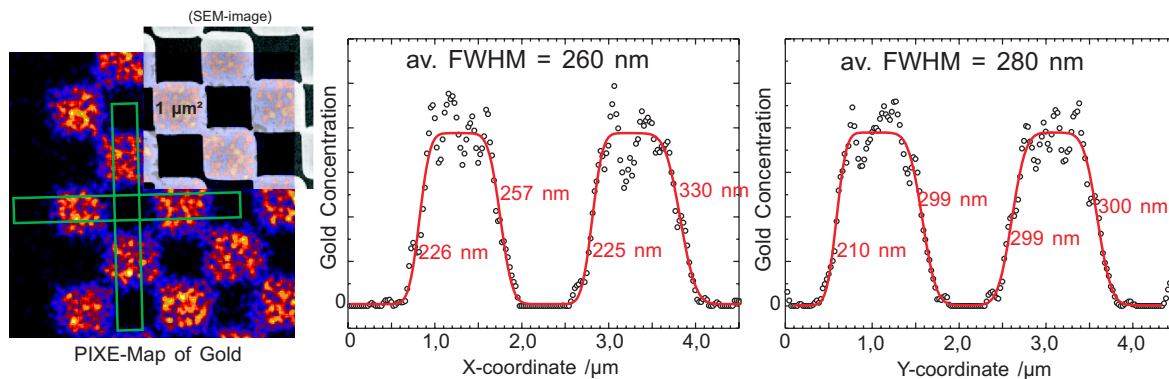

Fig. 2.5: Resolution measurement for elemental analysis (PIXE) on the Chessy test-structure with a 10 pA 2.25 MeV proton beam. The gold map of the 1 μm² squares revealed a resolution of 260 nm × 280 nm (averaged full width at half maximum of the lateral gold profile at four square edges). The overlay on the PIXE gold-map shows a secondary electron micrograph of Chessy.

10 pA of beam current might seem to be not applicable for trace element analysis. On the first glance this is true, because the acquisition time for a μPIXE scan linearly increases with decreasing beam current when the total accumulated charge has to be the same. For a spatially resolved PIXE analysis, however, the accumulated charge per resolution is the dominant number. Hence, a simple calculation shows that a beam of 10 pA can still be appropriate for trace element analysis. If we do not consider the beam current but the accumulated charge per resolution (or map pixel) then we can estimate the scan parameters for 10 pA deduced from a 100 pA beam: A scan of 50 μm × 50 μm with a 0.5 μm beam (100 pA) should have 250 × 250 pixels (2.5 pixels per 0.5 μm beam diameter). One hour acquisition time gives a total charge of 0.36 μC or 5.8 pC per pixel which corresponds to minimum detection limits (for the whole map area) of a few μg/g for transition metals in biological samples. Accumulating 5.8 pC per pixel with a 10 pA beam over 1 h allows a mapping of nearly 80 × 80 pixels, which results in a scan area of 9.5 μm × 9.5 μm (2.5 pixels per 0.3 μm beam diameter). This map would have the same sensitivity for mapping as the 50 μm × 50 μm map but with higher spatial resolution.

Improving the detection efficiency by using multiple X-ray detectors would also help to accept lower beam currents and thus enabling higher spatial resolution. Unfortunately the space around the sample is very limited. Several detectors, for X-rays, backscattered particles, and for secondary electrons, and optical microscope objectives have to be packed in the half space in front of the sample. The conventional and most useful arrangement of X-ray detectors is at 135° with respect to the beam direction.

The Leipzig laboratory operates a retractable 100 mm² high purity germanium IGLET-X (EG&G Ortec) X-ray detector. In order to double the efficiency a second IGLET-X detector has been purchased. Its position is also at 135° quasi at the mirrored position of the other detector. Unfortunately, the new detector has a very bad performance. The spectra show extraordinary tailing at the low energy side of the peaks, a

remarkable non-linearity and an unusual behaviour of the FWHM values with decreasing photon energy. Although the new detector fulfils the specification for FWHM at Mn-K$_\alpha$ of 145 eV, it is not suitable for quantitative PIXE analysis. The manufacturer is asked to revise the detector.

Besides the extension on the detector side, in 2007 the original target chamber and the externally driven sample stage have been replaced by a newly developed target chamber which now includes a new four axis sample stage with additional three axis goniometer. These major modification activities prompted us to readjust the alignment of the two quadrupole duplets. First tests of the performance after the major revisions have shown a further improvement. However, they also confirmed a pulsed displacement of the beam in the order of 0.1% of the scanning amplitude correlated in both directions. Careful examinations suggest that the disturbing signal originate already from the I/O board (Texas Instrument Lab PC+ for ISA) of the scan control computer or from the two channel scan amplifier. A new scan amplifier is already ordered. It consists of two independent one channel transconductance power amplifiers. This replacement is favoured to eliminate the disruptive pulsed beam offsets.

All activities together, the realignment of the quadrupoles, exhausting the focussing system by maximum setting of the aperture, new sample stage and beam scan amplifier, and increasing the X-ray detection efficiency using two detectors the long pursued aim to reach the 100 nm level for (trace) element analysis is realizable at the Leipzig nanoprobe LIPSION with a beam current of about 10 pA. In the low current mode beam spot sizes smaller than 20 nm are also foreseeable. The verification of these prognoses is expected for the near future.

Chapter 3

Environmental Research

Ion beam analysis including PIXE as a tool for elemental analysis is widely used to asses the pollution status of environmental samples, especially for toxic elements. The analysis includes soil, air born particles, plants, and even organs of animals. The information from the assessment supports the identification of the pollution sources and the search for strategies to reduce and even prevent further pollution. A major part of the studies is performed with a broad beam. However, analysing not only the bulk material of the samples but also the substructure by using the µPIXE technique may also give more detailed information. The two following examples of elemental analysis with spatial resolution show the applications to single aerosol particle analysis and to a bioaccumulation study.

3.1 Pollution monitoring by single aerosol particle analysis

Figure 3.1 shows a view over Shanghai. The rapidly growing city suffers from air pollution due to extensive construction and increasing traffic volume. The smog haze over the city, demonstrating the pollution with airborne particles, is the sum of contributions from several sources. Airborne particles, in general defined as total suspended particulate matter (TSP), have different size and shapes. According to their aerodynamic diameters they are divided into different categories: PM_{10}, $PM_{2.5}$, and $PM_{0.1}$. PM stands for particulate matter and the subscript denotes the upper limit of the aerodynamic diameter in micrometer.

The health risk of the particles depends on one hand on the diameter. The smaller the diameter the deeper the particles can enter the respiratory system. Coarse particles greater than 10 µm are filtered by the nasopharynx. PM_{10} enter already the main bronchi and $PM_{2.5}$ enter the terminal bronchioles and alveoli deep in the respiratory system. The particles trapped in the alveoli are no more accessible for the clearance mechanisms via ciliary transport. The remaining alternative to clear the alveoli is to activate macrophages that engulf and, if possible, digest the trapped particles. Finally, the particles themselves or their dissolved substances are incorporated. In this stage the other side of the particle health risk becomes apparent. When the particles remain in the alveoli without being digested, they can cause a chronic inflammatory reaction

Fig. 3.1: View from the Orien-
tal Pearl Tower over the City
of Shanghai (September 2002).
The smog haze between and
above the buildings arises from
the urban and industrial sources
of air pollution.

in the lung. Or, when digested, toxic elements and substances enter the body in a long-term scale and severe health effects cannot be excluded. The increasing interest over the last years revealed not only an earlier trigger of allergies, there might be even a link to cardiovascular diseases via the redox active components of the particles with a putative origin in fossil fuel combustion [DEL05]. The report emphasizes also the need for a detailed epidemiologic research concerning the casual components and sources of the particulate matter.

A standard method of analysing particulate matter is to collect the particles on filters, followed by an analysis of the bulk material. The method is standardised and able to perform large numbers of analyses which substantiate the statistical significance of the results. However, bulk analysis has its limitations in the possibility to identify or to separate the contributions according to their sources or particle sizes.

The group of Prof. Zhu Jieqing, Shanghai Institute of Applied Physics, has developed a new method for a direct assessment of air pollution on the basis of the analysis of single aerosol particles by nuclear microprobe techniques. The main idea behind the new method is that every airborne particle possesses a characteristic spectrum of elemental composition which is in fact a kind of fingerprint of the particle origin. The fingerprint, i.e. the elemental spectrum of a particle is easily obtained by PIXE measurements using the nuclear microprobe. According to their PIXE spectra the particles can be categorized and assigned to the pollution sources when the fingerprint, i.e. the PIXE spectrum of the pollution source is known. In order to establish a set of source categories, initial PIXE measurements on particles collected at different sources have to be performed.

The huge number of collected airborne particles in combination with single particle analysis might seem to be contradictory. However, the practicability results from the fact that from a single PIXE map of several particles the spectrum of each particle can separately be extracted and that the individual spectra do not even need the usual process of peak and background fitting for a quantitative or semi-quantitative elemental analysis. The spectra serve merely as input patterns for a pattern recognition algorithm on the basis of an artificial neuronal network. The neuronal network in this case is an adaptive non-linear data processing algorithm that is trained by reference patterns in order to adapt the parameters for a correct classification of the particle spectra. The characteristic of a spectrum arises from the appearance and the intensity ratios of

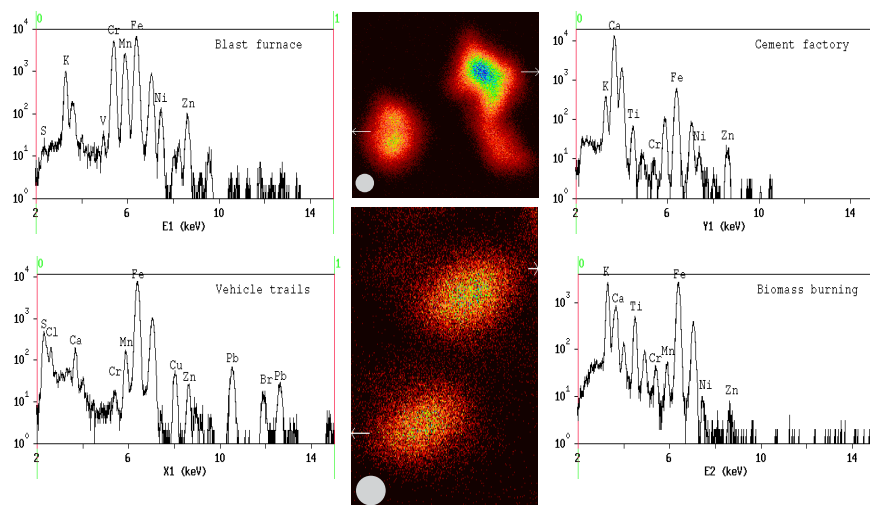particular X-ray lines that are representative for the emitting source.

Fig. 3.2: Four different single particles and their individual PIXE spectra extracted from the raw data map (grey circles correspond to a diameter of 1 μm). The spectrum pattern can be considered as each particle's fingerprint. The strategy of the fingerprint recognition is used to classify each particle according to its source.

Figure 3.2 shows an example of four individual particles of different sources from a feasibility study in Shanghai. The study was initiated by the Chinese Academy of Sciences. The fingerprint database for classification was established by analysing 74 particles of twelve pollution sources thought to be the main emitters of air pollution. The environmental monitoring was done by a cascade impact sampler in the city center of Shanghai. The collected particles, 70% were $PM_{2.5}$, were prepared for the PIXE microprobe analysis. The PIXE spectra of 309 $PM_{2.5}$ measured in the Leipzig LIPSION laboratory were successfully categorized according to their sources.
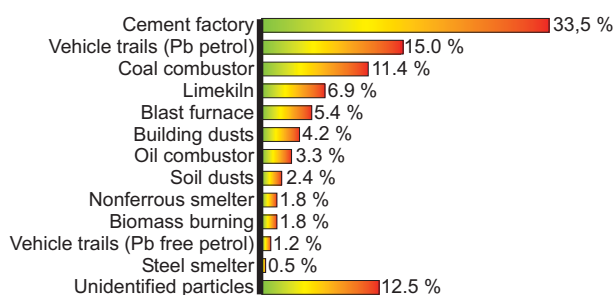

Fig. 3.3: Graphical representation of the contribution of different pollution sources to $PM_{2.5}$ particles in the city center of Shanghai. The sources could be identified by PIXE analysis of single particles with the nuclear microprobe.

Figure 3.3 shows the result of the study. The major contribution, one third, results from the cement industry which is not very surprising due to the enormous consumption of construction material in the rapidly growing city. The second largest contribution comes from vehicle trails and coal combustion whereby the majority of the vehicles obviously run leaded petrol. About 12% of the particles remained unidentified. In these cases the particles might come from different sources than in the data base considered. An extension of the data base would reduce this uncertainty.

3.2   Bioaccumulation of heavy metals

The second example of nuclear microprobe application to environmental research is a study on the intentionally modified bioaccumulation rate in a protist plant, a simple alga. The study was motivated by the possibility to develop new technologies for the decontamination of polluted water or for the exploitation of water bound metals [AHL07]. It is known that many organisms have developed individual protection mechanisms against high concentrations of metals in their surroundings. Most intracellular mechanisms work on the basis of metalloproteins that sequester the contaminants, followed by the transport to the cell membrane where the contaminants are released. Although the underlying molecular processes of these regulations are often not yet fully understood, an inhibition is easily achieved by immobilisation. The algae then accumulate the metals in high concentrations when their detoxification system is blocked. Thus, immobilised biomass represents an effective resource for waste water treatment, economic metal recovery or exploitation.

The gain in efficiency by immobilisation was studied on the algae *euglena gracilis*. The algae were exposed to a high level of the rare earth element neodymium in their cultivating medium. Two groups of algae were cultivated, one group was immobilised with glutaraldehyde, the other group represented the control. Nuclear microprobe analysis was chosen to analyse the bioaccumulation of neodymium. Algae from both groups were prepared on thin nylon films. Simultaneously, RBS and PIXE analyses were done in order to outline the algae shapes and to measure the neodymium content. Figure 3.4 gives an short overview of the analysis and the result on the modified bioaccumulation rate. The control group is shown on the left side. The RBS-map shows the shapes of three algae cells and the Nd-map the corresponding neodymium distribution. There are clear intracellular neodymium hot spots that demonstrate the active detoxification mechanism. The right side shows the result for immobilised algae. Neodymium is distributed over the whole cell. Neodymium is trapped in the algae. The PIXE spectra below clearly show the increase in neodymium concentration.
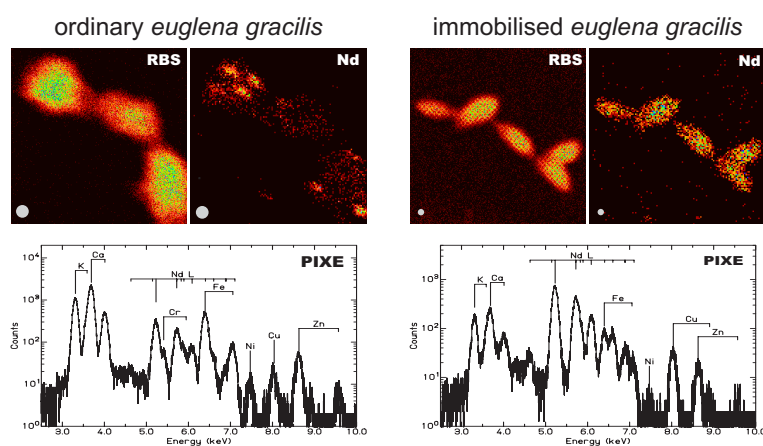

Fig. 3.4: Nuclear microprobe analysis of the bioaccumulation of neodymium by the algae *euglena gracilis* (grey circles correspond to 1 μm diameter. The immobilisation increases the bioaccumulation of metals by inhibiting the algae's detoxification mechanism. This is of technological relevance for waste water treatment.

Chapter 4

Safety of Physical UV Filter – TiO$_2$-Nanoparticles

Physical UV-filters, also called mineral filters, are widely used in sunscreens and daily cosmetic products. A predominant physical UV-filter is nanoscaled titanium-dioxide, TiO$_2$. The material is an efficient absorber in the UV-region and chemically inert, ideal properties to create sunscreens with high sun protection factors. Since the TiO$_2$ can be produced in form of nanoparticles, smaller than 100 nm, they do not show the whitening effect anymore and became very popular. However, with smaller sizes the particles develop new properties that potentially represent new health risks. There is on the one hand the photocatalytic activity, an effect that has to be avoided as much as possible in cosmetic products. This can be done by coating the particles with amorphous alumina or silica. On the other hand nanoparticles in sunscreens might already be small enough to find ways through the skin. The scenario is plausible, the use of sunscreen with nanoparticles as physical UV-filters brings the particles in direct contact with the skin. This clearly represents a high exposure to nanoparticles with the risk of percutaneous uptake.

The chemical and cosmetic industry knew about the possible health risk and initiated many internal studies on the percutaneous penetration. The methods applied were mostly electron microscopy, tape stripping and penetration measurements with Franz diffusion cells. These methods alone, however, can only yield limited information on the penetration behaviour of nanoparticles. High resolution electron microscopy images clearly show individual nanoparticles between the corneocyte layers, giving a useful ultrastructural but no real quantitative view on the penetration (figure 4.1).

Tape stripping is not a very successful approach to quantify the depth distribution of nanoparticles throughout the upper skin layers. Tape by tape in a successive ablation the cell layers of the skin are transferred to the tapes and analysed for their nanoparticle concentrations. The transfer rate and the contributions from accumulations in wrinkles and follicles introduce unknown uncertainties in the analysis. Penetration studies with the tape stripping method are furthermore limited. The probing depth corresponds to the thickness of the *stratum corneum*, the horny layer. Penetration beyond the horny layer into vital tissue is out of range for the tape stripping method.

Franz-cells were developed and used for penetration studies of drugs and nutrient molecules. Although this method is standardised and measures the diffusion through-
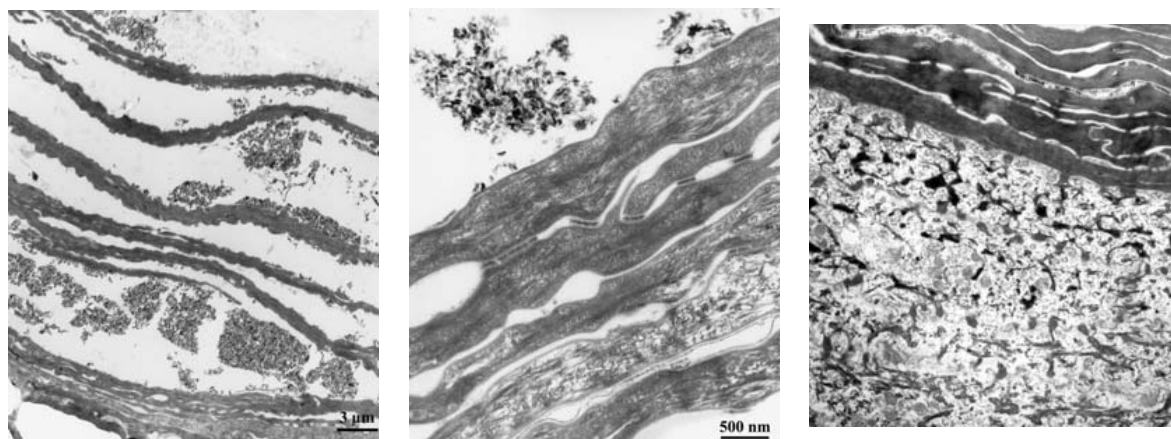
Fig. 4.1: High resolution electron microscopy images of ultrathin cross sections of human skin showing the presence of TiO₂ particles in the topmost corneocyte layers only. The particulate matter in the *stratum corneum compactum* (right) was identified to be of organic origin. (courtesy of J.E. Surlève-Bazeille)

out the total thickness of the skin the method is not appropriate to measure the transcutaneous transport of nanoparticles because it is a static arrangement. Nanoparticles do not diffuse as fast as molecules.

There was a strong need for further analytical methods that can assess the percutaneous penetration of nanoparticles. Quantitative results with low detection limits and a spatial resolution in the order of 1 µm are required to create maps and depth profiles of the distribution of nanoparticles. micro PIXE with a nuclear microprobe fulfils these requirements. In a multinational project, supported by the European Commission under the programme "Quality of Life and Management of Living Resources", eight project partners, including six nuclear microprobe laboratories, two centers for electron microscopy and several dermatological and pathological departments studied the penetration of nanoparticles under various conditions on healthy pig and human skin and on human skin with impaired barrier function. There was a strong focus on the measurements of a vast number of skin samples by nuclear microscopic techniques to assess the barrier function of skin against nanoparticles. However, a nuclear microprobe cannot analyse the penetration of nanoparticles into skin *in-vivo*. The exposed skin has to be taken from laboratory animals or volunteers. The sampling is a small punch biopsy from which freeze dried cross sections (15 µm to 30 µm thick) of the skin are prepared for nuclear microprobe measurements.

The µPIXE analysis provides several useful information. There are the elemental distributions of the physiological elements, e.g. phosphorous and sulphur, which delineates the strata of the skin. The *stratum corneum* is recognisable by a low phosphorous and a high sulphur concentration. Skin with an intact structure has a sharp transition from vital tissue into the dead horny layer of the *stratum corneum*. The borderline is the *stratum granulosum* which still consists of living cells. From the µPIXE maps elemental profiles can be extracted to get quantitative penetration profiles of the nanoparticles, e.g. from the outer skin surface, where the nanoparticles were spread, into the vital tissue beyond the *stratum granulosum*. Furthermore, the average concentration of titanium(dioxide) can be extracted from regions of interest. The regions can be chosen,

for example, comprising the vital tissue and excluding the *stratum corneum*. Thus, the concentration of nanoparticles that have passed the barrier could be extracted.

Figure 4.2 shows an example from a µPIXE analysis of a psoriatic skin sample. The characteristic of the psoriasis is the excessive skin production due to an accelerated proliferation of keratinocytes. This leads to a disturbed structure of the skin, so called psoriatic plaques, because keratinocytes turn into corneocytes already in deeper skin layers. In the PIXE maps this is expressed by sulphur rich structures (the dead corneocytes) intermingled in the phosphorous rich region (vital tissue). There is no intact barrier in form of the *stratum corneum*. The analysis shows that there is a penetration of nanoparticles up to a depth of 30 µm with only a little tail up to 40 µm. The number of penetrated particles than drops under the detection limit which is in average 0.2 µm^{-3}. The signals at 53 µm and 63 µm are close at the detection limit and might come from statistical fluctuations. At this low levels additional careful analyses of these spots are needed to give clear answers concerning possible preparation artefacts.
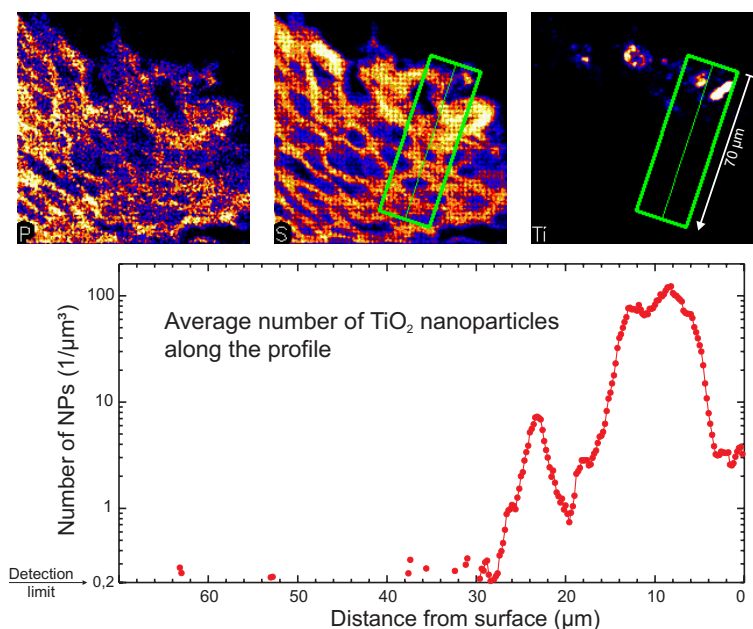

Fig. 4.2: µPIXE analysis of the penetration of TiO$_2$ nanoparticles into psoriatic skin. The elemental maps (100 µm × 100 µm) of P, S, and Ti show the impaired *stratum corneum*. From the green rectangular area a titanium profile was extracted to quantify the concentration of particles with increasing depth.

Summarising all nuclear microprobe analyses and the electron microscopy investigation we can conclude that healthy skin is an effective barrier for nanoparticles in sunscreens. The nanoparticles are mechanically spread over the skin and rubbed in the outermost layers of the *stratum corneum disjunctum* where they have no contact to vital tissue. Nanoparticles do not diffuse fast enough. In the case of psoriatic skin, the nanoparticles are rubbed into the fuzzy structure of the outer regions with contact to vital cells. Again, the nanoparticles will not diffuse deeper. The fast proliferation of the cells will transport the nanoparticles to the surface where a fast desquamation occurs.

Chapter 5

Trace Metals in Brain

The relevance of trace elements in association with neurodegenerative diseases is of growing interest since elevated concentrations of metal ions in these diseases could be linked to pathological processes [HOL07]. There are more and more studies that link redox-active metal ions – most notably aluminium, calcium, manganese, iron, copper, and zinc – to the pathology of several neurodegenerative diseases such as Alzheimer's, Parkinson's, and prion diseases, Friedreich's ataxy, amyotrophic lateral sclerosis, and multiple sclerosis [DOR04, OTE04].

The mechanism for the pathologies may particularly be bases on the oxidative potentials of the involved metals when their physiological balance is disturbed [HEN04]. It is likely that the altered homeostasis and redox activity will lead to severe cellular damage and subsequent apoptosis or necrosis. The cellular damage is mostly caused by an increased production of free radicals since metal ions, in particular iron and copper ions, catalyse radical production via the Fenton reaction. This is supported by a recent study that revealed a contribution of a metal induced oxidative stress component to neurodegeneration [MOR04]. For instance, Parkinsons disease is characterized by a selective vulnerability of the dopaminergic neurons in the *substantia nigra*, accompanied by abnormally high concentrations of iron in the affected brain areas. Therefore, iron (in its Fe^{2+} state) is believed to contribute to oxidative stress and therefore to neuronal death in the *substantia nigra*.

Therefore, a major research interest is the analysis of metal ion concentrations in particular brain regions or cell types affected by neurodegenerated disorders. A basic approach is to understand the principles of iron metabolism by a comprehensive study of which a quantitative elemental analysis on the cellular and sub-cellular level contributes complementary information for a deeper understanding. The following examples summarise the elemental analytical part of studies that were conducted in the LIPSION laboratory in close collaboration with Dr. Markus Morawski and Anja Fiedler (neuroanatomy group, Prof. Arendt, Paul-Flechsig-Institute for Brain Research of the University of Leipzig).

5.1 Neurons with a specialised extracellular matrix: the perineuronal net

An approach to a better understanding of neuropathologies is the investigation of the selective neuronal vulnerability. Focussing on the vulnerability in relation with anatomy and the regional and cellular characteristics together with the disturbed metal homeostasis, especially the iron (mis-)management, a noticeable correlation appears with the heterogeneous distribution pattern of a lattice-like neuronal coating of extracellular matrix proteoglycans, a so called perineuronal net [Tho01, Bru99]. A characteristic feature of this structure is that it ensheathes only a subpopulation of distinct types of neurons (see figure 5.1).
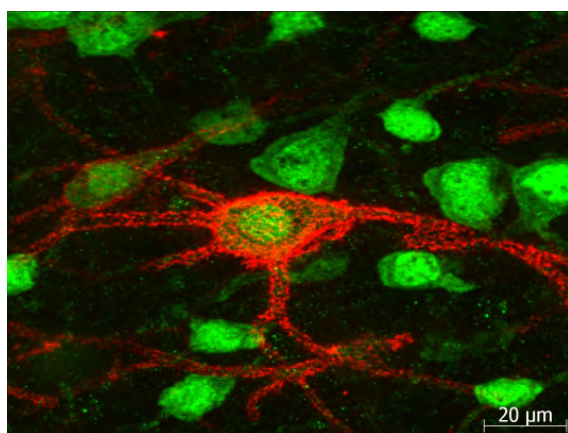

Fig. 5.1: Laser scanning microscopy image of neurons and perineuronal nets (green: neurons immunohistochemically stained with NeuN; red: perineuronal nets lectinhistochemically stained with WFA). The neuron in the center posses a distinct net, the neuron on the left side a flimsy one only. (courtesy of Anja Fiedler)

In regions with physiologically higher iron concentrations the iron is compartmentalised mainly in oligodendrocytes; it is essential for the support of axons and for the production of myelin sheath. Free excess iron ions contribute to cellular damage by catalysing oxidative stress. However, in the regions of pathologically higher iron concentrations, where a progressive loss of neurons takes place for instance in Parkinson's and Alzheimer's diseases, a particular group of neurons is not or at least very lately affected by degeneration. This group obviously posses a certain protection mechanism. Numerous indications suggested that the polyanionic extracellular matrix proteoglycans are involved in the protection mechanisms. Interestingly, this specialised form of neuronal extracellular matrix is able to bind large amounts of iron due to their negatively charged chondroitin sulfate proteoglycans. The function and a possible role in neuroprotection are subject to many-sided investigations.

According to the polyanionic character of the perineuronal nets, a possible neuroprotective effect could be based on the ability to scavenge iron ions thereby reducing the oxidative stress. The ability to scavenge cations has to be connected with a high affinity to metal ions. In order to determine the affinity, transverse sections (6 µm thick) of an adult Wistar rat were incubated with gradually increasing concentrations of colloidal iron hydroxide. The concentrations of iron bound to the perineuronal nets were analysed for the different Fe loadings in several brain regions. The result for the *cortex* is shown in figure 5.2. The distinct affinity to iron ions is shown in the sharp increase of the bound iron already at a low iron loading. The retention can be math-

ematically expressed by the Michaelis-Menten-equation for enzyme kinetics whereby the concentration of bound iron replaces the enzyme activity that is usually taken as ordinate in the theory of enzyme kinetics.
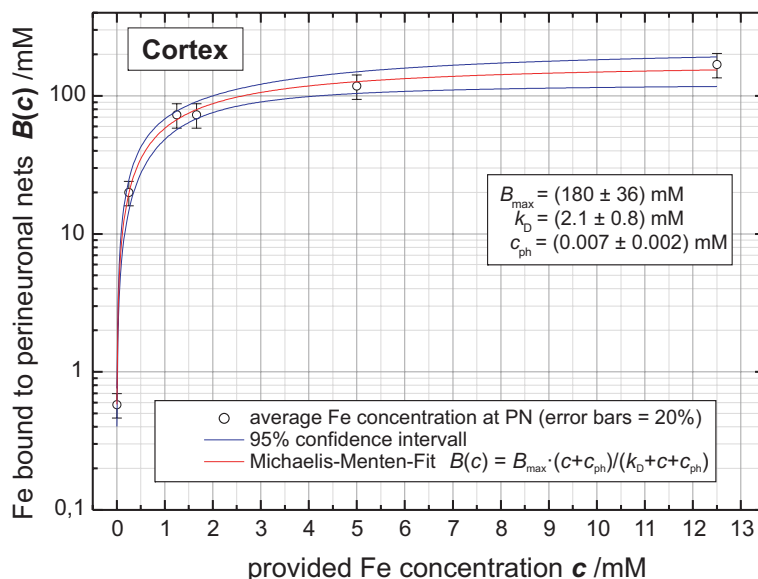

Fig. 5.2: Analysis of the affinity of perineuronal nets to iron. The dependency of the Fe-concentration bound to the PN upon the applied Fe loading follows the Michaelis-Menten equation from which the affinity can be extracted.

The study has shown that under increased ion loading the perineuronal nets attract and accumulate iron ions [REI03]. This affinity could be an auxiliary mechanism of the perineuronal net ensheathed neurons that is part of a specialised cellular iron metabolism to eliminate the excess iron. Therefore, in a follow-up study, the physiological intraneuronal concentration of iron in the cytoplasm was investigated with a special emphasis to the difference between neurons ensheathed by a perineuronal net and neurons without a net. For the analysis Wistar rat brain sections including the regions of the *substantia nigra*, *nucleus ruber*, *subiculum*, *parietal cortex*, brain stem and *cerebellum* were prepared. The challenge was to analyse the subcellular distribution of iron at physiological concentrations maintaining the high spatial resolution of 1 μm.

Normally the perineuronal nets are neither visible in optical microscopy nor in nuclear microscopy. Although, after very long acquisition times perineuronal nets seem to slightly show up via an increased contrast in the sulphur map due to their main components chondroitin sulphate proteoglycans, this is not suitable method for a fast and reliable recognition of the perineuronal nets. Other appropriate recognition techniques have to be established. The idea connects standard immunohistochemical methods with a selective elemental contrast for nuclear microscopy [MOR05]. The method can easily tag a variety of physiological structures by immune-labeling with primary antibodies in combination with a secondary antibody intensified by an elemental additive appropriate for ion beam analysis (e.g. Co, Ni, Cd, Ag, Au of highest purity). Tests have shown that there is no significant change in elemental concentrations of cells due to the immunolabeling with an elemental marker.

With this method the perineuronal nets were immunohistochemically marked with
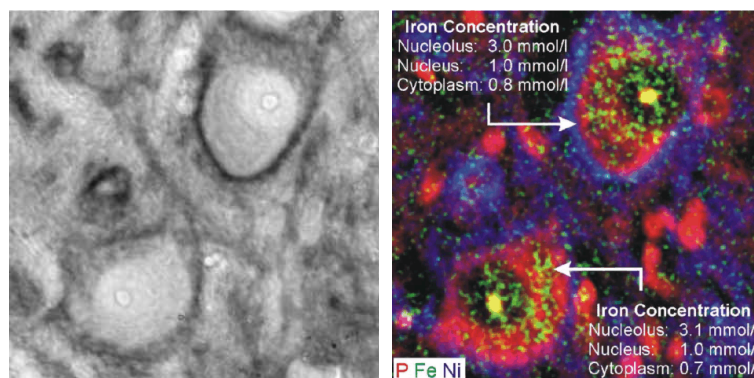
Fig. 5.3: Left: Light microscopy image (100 µm × 100 µm) of two neurons showing the dark nickel enhancement of the perineuronal net (PN). The upper neuron is enclosed by a PN, the lower one is not. Right: Nuclear microscopic elemental map of the same area as in the left image. PNs appear in the nickel distribution (Ni: blue). Cell cytoplasm can be recognized by intense phosphorus concentration (P: red). Iron is shown in green (Fe: green). The yellow areas are a co-localisation of phosphorus and iron. (courtesy of Anja Fiedler)

lectin WFA[1] and intensified by DAB-Ni[2] to facilitate the PN visualization by ion beam microscopy. Figure 5.3 gives an example of a typical analysis, here of two neurons from the *nucleus ruber*. First, in a large overview scan neurons were identified according to their shapes in the phosphorus concentration (representing the cytoplasm). The nickel-distribution revealed neurons ensheathed by a perineuronal net. The detailed analysis with high spatial resolution and sensitivity was then performed on selected neurons. Concentration values for the different cellular compartments were extracted such as for the nucleolus, the nucleus (with/without nucleolar contributions), the cytoplasm, and the total neuronal concentrations.
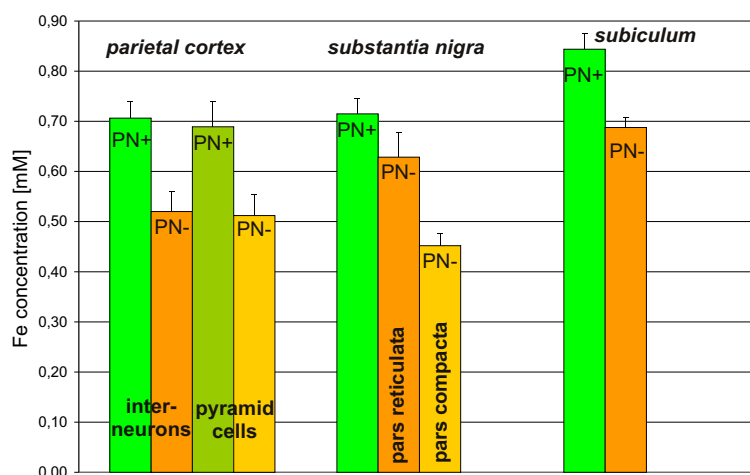

Fig. 5.4: Statistical analysis of the cytoplasmic iron concentrations of neurons with (green) and without (orange) perineuronal net for different brain regions. PN ensheathed neurons have a significantly higher Fe concentration (Student's t-test, $p < 0.02$). Error bars represent the standard errors. (courtesy of Anja Fiedler)

---

[1] wisteria floribunda agglutinin

[2] DAB-Ni: diamino benzidine with nickel as marker

The study on the intraneuronal iron content is based on the analyses of 106 perineuronal net ensheathed neurons and 121 control neurons in the aforementioned brain regions of two Wistar rats. The statistical analysis of the data revealed a slightly higher intraneuronal iron concentration in neurons ensheathed by PNs than in neurons devoid of PNs on the significance level of $p < 0.05$ (figure 5.4). It is assumed that the higher iron concentration is closely related to the concentrations of iron transport and storage proteins, especially that of the storage protein ferritin. This hypothesis is currently under investigation by molecular biological and immunohistochemical methods.

The reduced vulnerability of particular neurons might be explained by the assumption, that the PNs protect the neurons against degeneration by scavenging free iron ions and the possible conversion to non-toxic iron (Fe^{3+}), which can be stored inside the cell. This could probably delay functional changes as well as metabolic imbalances in the course of Parkinsons disease.

5.2 Metal ions in Parkinson's disease – the role of neuromelanin

Patients suffering from Parkinson's disease have an up to three fold higher iron concentration in the brain region *substantia nigra*. The reason for this pathological accumulation, obviously an altered iron homeostasis, is unknown. Presumably, the iron accumulating molecular structures, e.g. ferritin in glial cells and in particular the pigment neuromelanin in neurons play a fundamental role in the aetiology of Parkinson's disease. Neuromelanin is a dark coloured intracellular pigment appearing in a specific population of neurons (dopaminergic and noradrenergic) in senescent mammals predominantly in the *substantia nigra pars compacta* and in the *locus coeruleus*, being formed by oxidation of catecholamines. In recent years, there is increasing interest in the role of neuromelanin because of a hypothesised link between this pigment and the cell death of neuromelanin-containing neurons in Parkinsons disease (PD), due to metal ion binding of neuromelanin and a consequential generation of free radicals [Zec06]. The biology, i.e. the structure, synthesis, physiology and its role in the neuron is still not entirely understood. It is likely that, similar to other types of melanins, neuromelanin acts as a protector against free radicals by inactivating or chelating free toxic metal ions (e.g. iron, copper, calcium). However, in the case of redox-active metal ion excess, and this is controversially discussed, neuromelanin could potentiate the free radical production due to a reduced binding capacity. The role of neuromelanin in the pathology of PD is therefore an actual focus in neuroscience [Fed05].

Although many studies have been published during the last years which focus on neuromelanin and the link between iron accumulation and Parkinson's disease (recently reviewed in [Fas06]), a conclusive prove of the hypothesised link between excess iron concentrations and the aetiology of Parkinson's disease could not be given. Early studies, an energy-dispersive X-ray analysis with an electron microscope and a LAMMA study stated indeed the presence of iron in neuromelanin for the Parkinson's case and not for the control case [Jel92, Goo92]. However, all these studies lack a quantitative analysis *in-situ*.
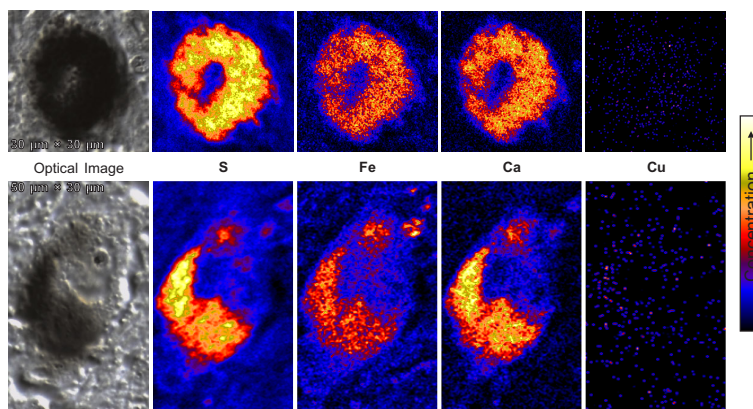
Fig. 5.5: Optical images and quantitative element maps of two neuromelanin pigmented neurons from a patient suffering from Parkinson's disease.

To our best knowledge, there is no comparative study of Parkinson's cases versus control that performed spatially resolved quantitative elemental analysis of the concentration of metal ions bound to neuromelanin *in-situ*. Nuclear microprobe analysis provides, in collaboration with the brain research institute, a unique opportunity to investigate in detail intraneuronal metal concentrations with respect to Parkinson's disease. Therefore, we launched an initial study. The *substantia nigra* of three cases with different severity of Parkinson's disease and three control cases without any history of neuropsychiatric disorders or mental impairment were taken and prepared for ion beam microanalysis. From each case about ten neuromelanin pigmented neurons, which appeared morphologically regularly shaped, were analysed in order to extract the concentration levels for metal ions. Extracellular neuromelanin resulting from degenerated neurons was excluded from the analysis because extracellular neuromelanin is continuously degraded by microglia.

For the interpretation of the results one has to take into account that the neuronal melanin content varies from cell to cell and consequently also the total metal ion content in the cell. For a specific investigation of the binding capacity of neuromelanin, it is therefore advisable to take the ratio of the metal concentrations and the melanin content, whereby the sulphur concentration was taken as a measure for the melanin content, because melanin is rich in sulphur [ODH94]. The ratio metal ion to sulphur concentration then gives the quantity that is compared between Parkinson's and control cases. Figure 5.6 shows the result for the iron content bound to neuromelanin.

The result on the iron content was most surprising. From the literature it was suggested that intraneuronal neuromelanin would bind significantly more iron in the case of Parkinson's disease. The result, however, shows no significant difference. There might be a slightly higher variability in the Parkinson's group, but there is not enough statistical power to draw conclusions on that issue. The only secured result is that the concentration ratio of iron to sulphur is about 0.1 in both groups, Parkinson's and control cases. The reasons of the unaffected iron content may be based on the selection of the pigmented neurons for analysis. We have chosen neurons for analysis which were of regular shape. This could also mean that these neurons were not or not yet affected by pathological changes and showed therefore a normal iron content. On the other
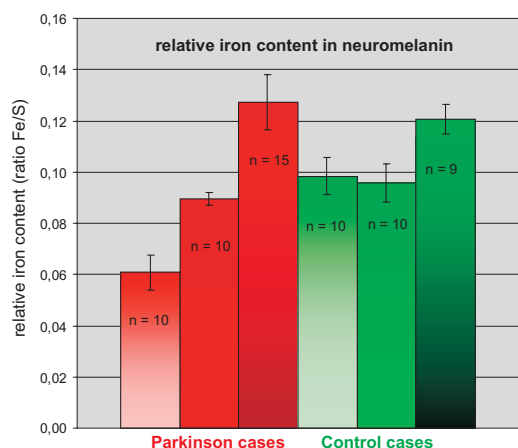
Fig. 5.6: Analysis of the iron content of intraneuronal neuromelanin of several cells for three cases with Parkinson's disease (red) and three control cases (green). The iron content of was normalized to the melanin content via the sulphur concentration. Surprisingly there is no significant difference in the iron content between the Parkinson's and control cases. Error bars indicate the standard errors. (courtesy of Nirav Barapatre)

hand, looking at the other metal concentrations we found a significant difference in the potassium and calcium content. The potassium content in intraneuronal neuromelanin was found to be five fold higher in the Parkinson's group, whereas the calcium content was 40% lower than that for the control group. Any interpretation of the varying potassium and calcium content would be speculative due to a lack on available data from other studies. There is clearly a need for further quantitative studies which shall be based on a broader random sample of Parkinson's and control cases.

The elemental analysis of trace metals in neuromelanin was also performed with very high spatial resolution of well below 0.5 µm. This resolution is adequate to study the ultra-structural elemental distribution in neuromelanin. Due to the appearance of neuromelanin as an agglomerate of microgranules with an intermingled neutral lipid component the binding and accumulation of metal ions to neuromelanin is not homogeneous which lead to a substructure in their distributions.
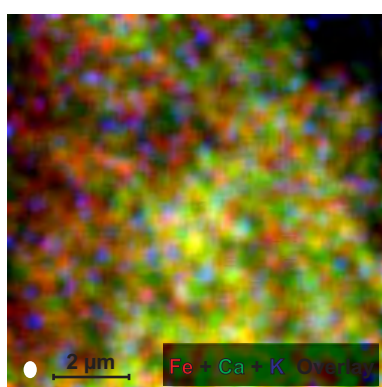

Fig. 5.7: High resolution Fe-, Ca-, K- elemental overlay map of an intraneuronal neuromelanin pigment (10 µm × 10 µm). The speckled distributions of potassium, calcium and iron on the ultrastructural level suggest different binding sites in neuromelanin for the depicted elements. The white spot represents the spatial resolution for this map which is 350 nm × 450 nm, measured on a resolution standard prior the analysis.

Figure 5.7 demonstrates this substructure for the distributions of iron, calcium, and potassium. The figure is a three element map where the three depicted elements Fe, Ca, and K are shown in red, green, and blue, respectively. Any co-localisation of two or three elements will lead to an additive colour mixing in the map and subsequently to colours such as magenta (blue+red), yellow (green+red), cyan (blue+green), or white

(all three colours). Although, there are co-localisations, especially in the middle and lower part of the map, many single colour granules show up in the left and upper part of the map where the granules are more sparsely distributed and do not row up too much. These single colour granules point to selective binding sites for metal ions within the neuromelanin. Nevertheless, the analysis of the ultrastructural appearance is very challenging for ion beam analysis and still on the edge of assured results.

Chapter 6

Low Dose Radiobiology with Single Ions

The risk assessment for ionising radiation in the medium and high dose regions is based mostly on the data derived from exposures due to accidents (Chernobyl, nuclear power plants, military) or from a survey of the victims of the nuclear explosions in Hiroshima and Nagasaki. A risk assessment for low dose exposures, as it can occur in occupational exposures, however, has to be made from epidemiological studies or from an estimated radiobiological effectiveness. The estimation results from a linear extrapolation of the high dose region into the low dose region. This approach implies a linear no threshold model of the radiobiological effectiveness [PRO93, STR04]. The linear dependency in the low dose region, however, is challenged by a variety of recent studies. The non-linear effects are attributed to several mechanisms of inter-cell communication that lead to an amplification of radiation effects due to the identical response of cells, so called Bystander cells, which were not directly affected by ionising radiation. Therefore, the generic term for these kinds of effects is Bystander effect. A recent review of Bystander effects can be found in [MOR07].

The non-linearity of the dose-effect curves measured for a variety of endpoints can be in both directions towards higher radio-sensitivity and towards lower sensitivity. The latter means less radiation response which can also be interpreted as adaptive response. In both cases, bystanding cells receive certain kinds of signals from directly affected cells informing them about harmful radiation conditions or immediately triggering cellular responses. Although a vast number of cellular responses have been tested and several mediating mechanism have been proposed, the signalling pathways are far from being unveiled [PRI07, HAM07].

Besides low intensity X-rays or low fluence alpha-sources and broad ion beams the use of micron-sized MeV ion beams for targeted irradiation of living cells in culture or tissue is a promising approach to bring new insights in low dose radiobiology [FOL05]. The ability to precisely deliver a certain amount of energy to a single cell commences at the energy that is transferred by a single ion. The positional accuracy even allows to specifically target subcellular structures, e.g. the nucleus as target or definitely exclude it from irradiation. Focussed and collimated, light and heavy ions, the options are many-sided and widely deployed for a comprehensive approach in low dose ion irradiation experiments. Around the world there are a few dedicated microbeam ir-

radiation facilities which are already fully operational, other microbeam laboratories have recently extended their facilities by special irradiation platforms and performed first radiobiological experiments. This development is continued by other labs that are developing or planning radiobiological experiments on their facilities.

The Leipzig LIPSION laboratory has a 3 MV ion accelerator with a radiofrequency ion source for H^+- and He^+-ions. The available ranges of ion energy and the corresponding LET[1] for water is given in figure 6.1. Running helium, the ion source also provides a certain albeit small proportion of He^{++}-ions. Whether this rate is adequate to provide enough beam current for the microprobe was not yet fully tested. It may help that the required beam current for single ion applications is rather low. If the ion source would provide a usable He^{++}-ion rate the range of the helium-ion energy would extend drastically and so did the usable LET range. The extended region is also shown in figure 6.1.
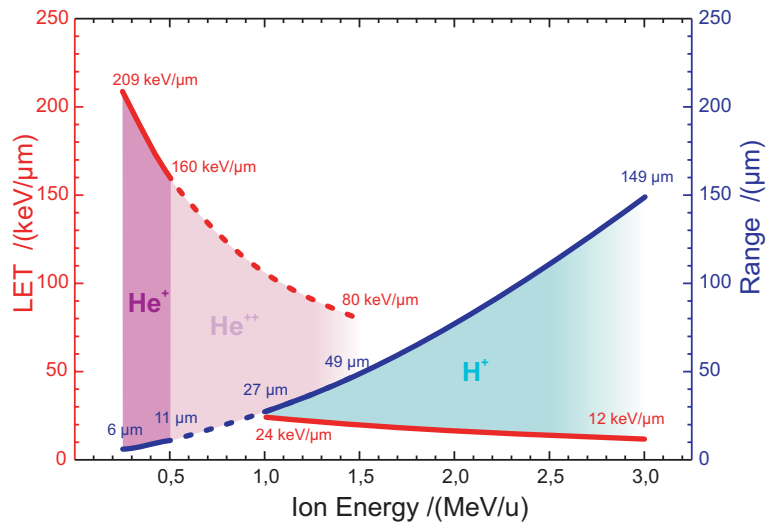

Fig. 6.1: Overview of the energies and corresponding ranges of LET and penetration depths of the ions available at the Leipzig Nanoprobe. The ion species He^{++} is also shown here, although the He^{++} yield of the ion source is very low and might not be sufficient for applications. This still needs to be tested.

We have started the first development work for an irradiation platform in 2001. Initially, the platform was an inset into the existing target chamber of the microprobe and very limited with respect to further developments, but appropriate to perform preparatory experiments. The first issue is to guide the ion beam into air without too much energy loss, and lateral straggling but maintaining the vacuum in the microprobe system without compromise. These preconditions have to be fulfilled to achieve an accuracy of the irradiation position below 1 μm. A thin window made from Si_3N_4 turned out to be a suitable exit beam window [CAL00]. We used a rectangular 100 nm thin membrane with an area of 1 mm × 1 mm.

The Petri dishes in which the cells are cultivated do also need a thin window, this is the irradiation window. It can be a thin polymer foil (polyethylene terephthalate,

---

[1]LET: linear energy transfer, the amount of energy transferred per unit distance to the irradiated medium

6 μm, 2 μm, or 0.9 μm) or again Si_3N_4 that has to be mounted leak-proof over the hole in the Petri dish bottom. The polymer foil is good for large area windows in the order of square centimeters but easily wrinkles which is a disadvantage for microscopy. The Si_3N_4 window provides a flat membrane with the disadvantage of small areas in the order of square millimeters only, but the lowest energy loss and lateral straggling compared to the thicker polymer. For irradiation the Petri dish window has to be positioned as close as possible to the beam exit window in order to reduce the air gap and the drift length which otherwise would degrade unnecessarily the hit accuracy. The distribution of ion impacts in air at the position of the Petri dish irradiation window directly behind the exit window were tested using the nuclear track detector material CR-39. The results show a hit accuracy significantly better than 0.5 μm which corresponds to the value deduced from SRIM simulations [Rei04].

Due to a missing online-microscope the first test platform did not provide cell recognition capabilities for targeted irradiation[2]. Therefore, homogeneous and patterned irradiations only were used for the first irradiation experiments.

6.1 Irradiation induced double strand breaks and heat shock protein expression

One of the first irradiation experiments was to visualise the hit position after patterned irradiation with H^+- and He^+-ions directly in the cells. This can be done by visualising direct effects of ionising radiation such as double strand breaks (DSB) of the DNA in the nucleus [Jak03]. The visualisation utilises immunohistochemistry. On the molecular level there are continuously working inspection proteins that test for DSB and tag the positions of the DSB by phosphorylation of the adjacent histone H2AX. The phosphorylated form of the histone, specified by γH2AX, is easily visualised by fluorescence labelled specific antibodies which clearly appear as fluorescence foci in confocal microscopy.

The irradiation of the cellular nuclei with 1.5 MeV He^+-ions (2 MeV before exit window) having a LET of 185 keV/ μm will create between 10 and 20 DSB per He^+-ion. This is about ten times more than the DSB induction rate of 2 MeV H^+-ions (2.25 MeV before exit window) with a LET of 16 keV/ μm [Hau04]. The irradiation was done in a pattern build up of small crosses. Each cross consisted of 7×7 pixels with a pitch of 1 μm and an intercross distance of 5 μm. The experiments then showed that the densely ionising helium ions created enough DSB and pronounced foci co-localised with the ion hit already by applying a single He^+-ion per pixel (figure 6.2 left picture). The cross in the nucleus was drawn by only 15 helium ions (two ions in the center of the cross) without any cooling at room temperature. The cross is clearly shaped according to the irradiation pattern.

Proton irradiation notably shows a different effect. Although irradiation at room temperature did create double stand breaks, which can be visualised as fluorescence foci, their positions appear relatively far from the ion hit position. The initially irradi-

---

[2]In 2007 we replaced the old target chamber by a specially designed multi-purpose target chamber with online-microscope and a platform for targeted single cell irradiation.

ated cross pattern was badly blurred. Cooling the cells close to $0\,°C$ during irradiation could diminish the blurring effects holding the foci localised to a certain degree even though the crosses are not well preserved (figure 6.2 right picture). The sparsely ionising H^+-ions do not create dense tracks of DSBs as it is known from heavier ions including helium ions. They rather create reactive oxygen species which then can induce DSBs. The ability of reactive oxygen species to diffuse prior to the creation of DSB would also explain the blurred pattern when irradiated at room temperature. Cooling the cells during irradiation, therefore, could decrease the mean free path length of reactive oxygen species which results to a less blurred formation of foci patterns.
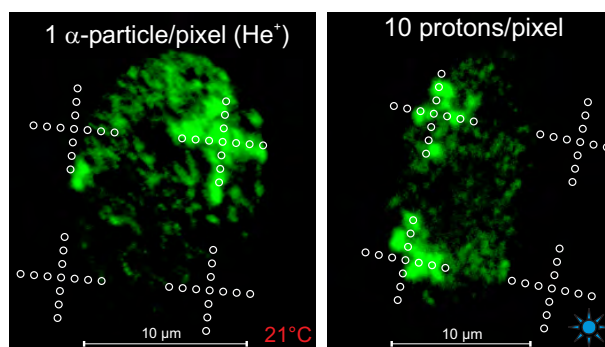

Fig. 6.2: Induction of double strand breaks in nuclei of fibroblasts after patterned irradiation with 1.5 MeV He^+- (left) and 2 MeV H^+-ions. The He^+- irradiation creates localised DSB at room temperature whereas the DSB after H^+ irradiation are much more fuzzy and actually delocalised when not cooled during irradiation.

The visualisation of double strand breaks after irradiation gives information on direct effects of ionising radiation to DNA damage, the reasons for genomic instability. This is, however, only a small part of possible influences on the complex system of cellular mechanisms. The influence on proteins and cellular organelles may even have immediate effects on the cell cycle or on vital control sequences for the cellular survival pathways. The heat shock protein HSP70 is an important cellular protein that is involved in a widespread of auxiliary and repair mechanisms, mainly expressed due to external stressors. Ionising radiation is also an external stressor. Thus, cellular HSP70 levels could also be increased after irradiation with single ions. Since triggered repair mechanisms are a secondary reaction on stress factors, the expression of HSP70 is a candidate for a sensitive measurement of bystander signals.

We therefore conducted irradiation experiments (untargeted patterned H^+- and He^+-ions) on fibroblasts with the HSP70 expression as endpoint. This endpoint also provides a simple positive control, the heat shock of the cells itself. The main conclusion we could draw was that neither the pattern nor the irradiated field appeared in the distribution of the response. The response was spread over the whole culture exceeding the irradiated area. These results confirmed the increased expression of HSP70 as indirect effect of ionising radiation for H^+-ions as well as for He^+. Furthermore, the cellular expression pattern differed considerably from that of the heat shock control. After heat shock the increasing HSP70 expression occurred mainly in the nucleus which corresponds to previous reports [WEL84, MIC97]. Whereas the irradiation caused an increased HSP70 expression not only in the nucleus but also remarkably in the cyto-

plasm of the fibroblasts. For proton irradiation, this cytoplasmic expression appeared in form of small HSP70 aggregates which seemed to intensify with increasing proton dose. Figure 6.3 shows the a typical appearance of the endpoints.
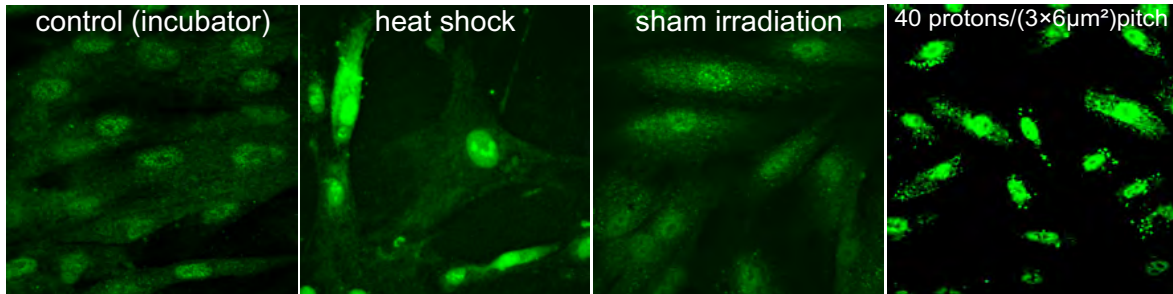

Fig. 6.3: Expression of the heat shock protein HSP70 in fibroblasts under normal conditions (control), after heat shock (30 min at 42°C), after sham irradiation (full procedure without ion irradiation) and after homogeneous irradiation with 2 MeV proton.

The expression of HSP70 was not only increased in the cells within the irradiated area (300 µm × 300 µm) but also in the bystanding cells all over the irradiation window (2 mm × 2 mm). Obviously, there must have been a response mediating intercellular signalling, either medium borne signal molecules or information exchange via gap junctions when the cells are in direct contact; even both pathways could be responsible. The response mediating factors, however, are not yet fully disclosed [Mar06, Lit06]. Thus, it would be very helpful to separate the two pathways, which is of course not easy. A first approach are medium transfer experiments that investigate the effects of culture medium mediated intercellular communication. The medium transfer experiments require two cell populations, irradiated and non-irradiated ones, in separated Petri dishes. Our approach is to realise spatially separated sub-populations of cells in a single Petri dish, a specialised Petri dish permitting structured cell growth.

6.2 Specialised Petri dishes

Investigating the signalling pathways which mediate the bystander response is also addressing the question whether the intercellular pathways for triggering the non targeted effects are cut when membrane-bound cell to cell contact proteins are blocked (e.g. connexins [Azz03]). Blocking in this sense is connected with specific agents added to the cell culture.

Another way of blocking could also be mechanically by creating micro-walls which prevent direct cell to cell contact in the Petri dish [Hoh08]. These micro-walls can be build utilizing proton beam writing [Zha05, Men07]. The principle is based on lithographic techniques where a film, sensitive to a certain kind of radiation, is partially exposed in a predefined pattern. After chemical development the pattern appears as remaining solid structure (negative stencil) or the development dissolves the pattern into the remaining film (positive stencil). In the case of proton beam writing the radiation is the scanned focussed proton beam. The film, spread over the substrate (e.g the irradiation window) can then be made of any MeV-proton sensitive material.

This is for the walls, which build up the cellular barriers, the negative photo resist SU-8, basically an epoxy resin.

Scanning the proton beam over the resist allows to directly write any shape and therefore, to create predefined compartments separated by epoxy resin walls (SU-8) walls. Technically, the specialised Petri-dishes with cellular compartments were successfully prepared. The walls were created with different heights, 10 μm, 20 μm, and 60 μm. Tests of the biocompatibility did not show any harmful effects to the cell cultures. However, fibroblasts were able to overcome the barriers after a certain period of time. Cellular barriers in form of microwalls turned out not to be suitable for the separation of cells into sub-populations.

The second approach was to achieve a structured cell growth in a Petri dish by generating cell repellent areas [Hoh08]. Therefore, the adhesion properties of the cell attaching surface in a Petri dish has to be changed. This is achieved by coating the surface with agar [Roh03]. Agar[3] is normally a gel for growing microorganisms based on a seaweed extract. The molecular structure of agar is a polysaccharide that is a kind of positive resist sensitive to proton irradiation, therefore, ideally suited to be patterned by proton beam writing. The proton irradiation cracks the polysaccharide into oligo- or monosaccharides which are soluble in water. The development step after the exposure of agar to MeV protons is therefore simply rinsing with water. The simple process of proton beam writing in agar can produce patterns for structured cell growth. Figure 6.4 shows an example of three stripes, 100 μm wide with a gap of also 100 μm, where the agar has been dissolved. The cells grow well in these stripes confined by the surrounding remaining agar.
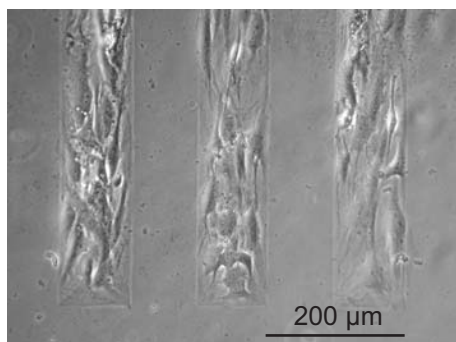

Fig. 6.4: Structured cell growth on an agar coated mylar foil: The cells grow on areas where the agar has been removed prior seeding in a three-step treatment: 1) coating the mylar foil with a thin layer of agar, 2) writing the areas by proton beam writing, 3) removing the agar in the exposed areas by rinsing with water.

The Petri dishes with structured cell growth provide sub-populations of cells in a single dish for the investigation of the irradiation induced bystander effect. When selected or all cells in one of these sub-populations are irradiated the endpoints show up in the irradiated population. When the endpoints also appear in the unirradiated sub-populations separated from the irradiated population, a signalling pathway via gap-junctions can be excluded, factors released into the medium are then responsible for triggering the bystander response. Another scenario could be the induction of endpoints only in those unirradiated sub-populations which are in contact to irradiated cells via connecting bridges. When there is no effect in isolated sub-populations, the bystander signals are then mediated via gap-junctions. A study that addresses these questions is in preparation. Some initial tests have already been done [Hoh08].

---

[3]from Malay agar-agar: jelly

Chapter 7

STIM-Tomography

High resolution STIM images can be taken from samples with thicknesses in the range of micrometers, or even tens of micrometers in the case of lyophilised biological materials. These images achieve lateral resolutions below 100 nm. They represent, however, merely a two dimensional projection of a three dimensional density distribution. This is totally adequate in most cases, such as STIM on cross sections of joint cartilage to visualise the network of single collagen fibres [Rei01]. However, when the 2D-projection is not conclusive enough or the depth information is of interest as well, then a three dimensional analysis, a tomography, is required.

The principle of STIM-tomography is based on a series of parallel beam projections of two dimensions (STIM-maps) which are taken under different orientations, i.e. by consecutively rotating the sample in small angular steps. The angular component adds the third dimension. Rotational and lateral scanning together build up a data set from which the three dimensional density distribution can be reconstructed. The mathematical concept was developed by the mathematician J. Radon and is nowadays known as Radon transformation [Rad17]. A comprehensive textbook on the Radon transformation and some of its applications is given by S.R. Deans [Dea93]. A detailed introduction with emphasis on STIM-tomography and its implementation in the LIP-SION laboratory is given by M. Schwertner [Sch02]. The implementation is based on a software package developed at the University of Melbourne by A. Sakellariou that provides a reconstruction algorithm for the qualitative reconstruction via backprojection of filtered projections (Radon transformation) as well as the iterative DISRA algorithm for a quantitative reconstruction [Sak02, Sak01].

The 3D tomographic analysis using STIM is also capable of maintaining a high spatial resolution, not at the same value as a single 2D STIM map, but in principle not far from that. Maintaining the high resolution is based on one of the major advantages when utilizing a focussed proton beam for analysis, i.e. its relatively large rigidity or large penetration depth without too much lateral straggling. Thus the lateral spatial resolution moderately decreases with increasing depth along the beam track. Over a long range the beam diameter will not widen remarkably, most of the lateral straggling appears close to the end of range of the ions where the stopping power is maximal. For STIM measurements usually the end of range is significantly larger than the thickness of the sample. Therefore, the beam spread after transmission is still small.

After a first STIM-tomographic experiment in Leipzig and the reconstruction of the

data in Melbourne the method was introduced in Leipzig. Initially a STIM tomographic experiment on a grid standard was performed to obtain the spatial resolution achievable with the tomography set-up in Leipzig [SCH06]. Furthermore, STIM-tomography was performed on three types of biological samples, articular cartilage, a zygospore, and recently on a mite.

7.1 Tests with a resolution standard

The resolution in STIM-tomography differs from that of a single 2D-projection. This is due to the merging process of reconstruction from many projections (e.g. 360 as shown in the examples below) which will accumulate any inaccuracy such as positioning inaccuracies from the stage, positional instability of the beam, misalignment of the rotation plane to the slice orientation (one of the scan directions), and bad data points resulting from missing or co-incident particle detection (sum-peak). A careful preparation and alignment prior measurement and a sophisticated data preprocessing is therefore essential for a successful reconstruction.
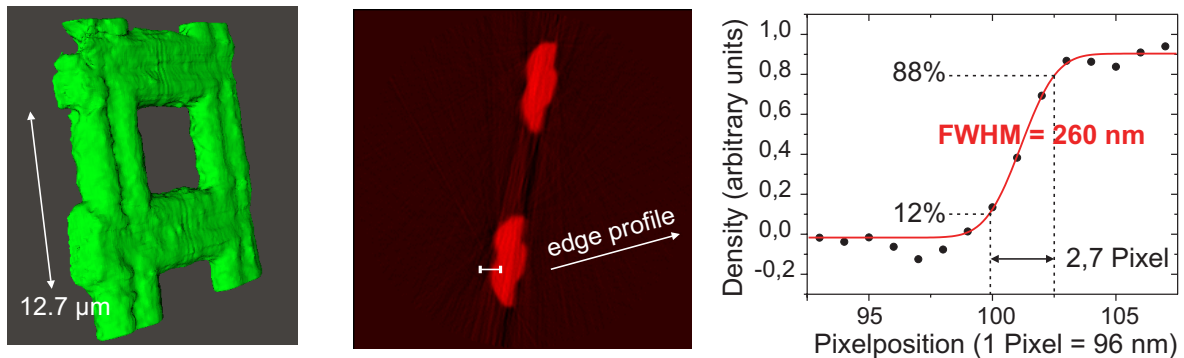

Fig. 7.1: Measurement of the spatial resolution obtained with STIM-tomography. Left: Rendering of a piece of a 2000 mesh copper grid (6,7 μm bar width). Middle: Reconstructed tomogram showing the middle horizontal slice of the grid. Right: Edge profile of the density along the path indicated in the middle picture fitted with a Gaussian function for the determination of the lateral resolution.

Figure 7.1 shows the result for a STIM-tomography on a piece of a 2000 mesh copper grid. The bar width is about 6.7 μm. The grid is a suitable microstructure with known dimensions and shape to investigate the effects of the individual steps of the preprocessing and the quality of both reconstruction algorithms, the reconstruction via backprojection of filtered projections and the DISRA algorithm.

The data set consists of 360 projections (angular step 0.5°) with 250 by 250 pixels each (24 μm × 24 μm) taken over ten hours of data acquisition with a beam diameter of about 100 nm (2 MeV H$^+$). From this experiment the reconstructed three dimensional density distribution of the grid was used to extract the resolution of the 3D image. This was done by analysing an edge profile of a bar within a reconstructed slice which yielded a resolution of (260 ± 21) nm.

The data acquisition for the STIM-tomography on the grid was done when the active compensation of varying stray magnetic fields was not yet available. Thus, beam fluctuations due the stray fields had a noticeable influence on the final resolution

in the tomogram. In the ongoing tomography experiments we expect an improvement of the resolution to values closer to 100 nm.

7.2 Application to biological samples

In Leipzig, STIM-tomography had already been applied to samples of articular cartilage [REI02] in order to reveal the arrangement of the collagenous network which can appear as cross-linked fibres or bundles of tubules [REI01]. In particular the tubular structure is hardly identifiable by single STIM-maps. STIM-tomography provides the complete and necessary three-dimensional information to reveal the structure of tubular bundles provided that the resolution is less than 200 nm. These challenging demands on the tomographic resolution arise from the sub-micron architecture of a single tubulus which has a wall thickness of about 100 nm and a diameter of less than 300 nm. Figure 7.2 shows the reconstructed density distribution within the cartilage sample. There is a heterogeneity in the extracellular matrix that is likely to be due to the collagen network, but no single fibres or tubules are visible. The resolution for this tomography is about half a micron. This is due to uncertainties in the raw data set, dominated by positional inaccuracies (dominant rotational error and a vertical drift). Therefore, the tomographic reconstruction of these tubules is subject to further STIM-tomography experiments which benefit from the new stage and goniometer.
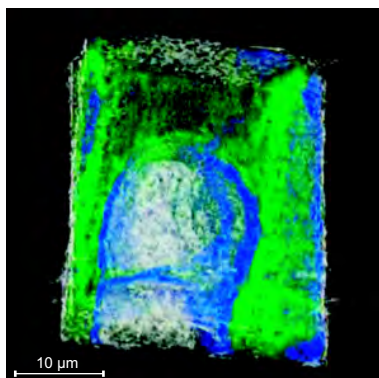

Fig. 7.2: Left: Rendering of a sample of articular cartilage (30 μm × 32 μm × 10 μm) showing a pair of chondrocytes (white) in a collagenous matrix (green). The resolution of the 3D analysis is not high enough to visualise individual collagen fibres. Blue represents the most dense part within the sample.

Another application of STIM-tomography to biological samples was the analysis of the inner structure of a fungus, a zygospore. A zygospore is a reproductive part of fungi (division: *zygomyceta*) that is formed during sexual reproduction when the tubular hyphae of complementary mating type of two zygomyceta meet. In the case of facultative biotrophic fusion parasites (order: *mucorales*) the mycoparasite sense for a host fungus to form zygospores with a subsequent cytoplasmic fusion between host and parasite [WÖS04]. This is inevitably associated with the transfer of genetic information from parasite to the host, the so called horizontal gene transfer. The horizontal gene transfer is of interest for the understanding of evolutionary jumps and phylogenetic intercrossings but it is also of great interest for biotechnological applications [WÖS96].

The physiological study of the parasexual processes within a zygospore, however, is often hampered by the highly sculptured thick wall of the mature zygospore which is opaque for light and electron microscopy. The wall obscures the key process of genetic

information transfer, the transfer of gamete which can be based on multi nuclei or single nucleus transfer. The latter is of greater importance for technological applications with a selective gene transfer.

The mycoparasite *absidia parricida* is a facultative biotrophic fusion parasite. Although it is known to undergo horizontal gene transfer by forming zygospores, the internal structure of the zygospore, multi or single nucleus fusion was not yet investigated. The zygospore of *absidia parricida* has dimensions small enough to perform a scanning transmission ion microscopic experiment which allows insights into the zygospore core (fig. 7.3).
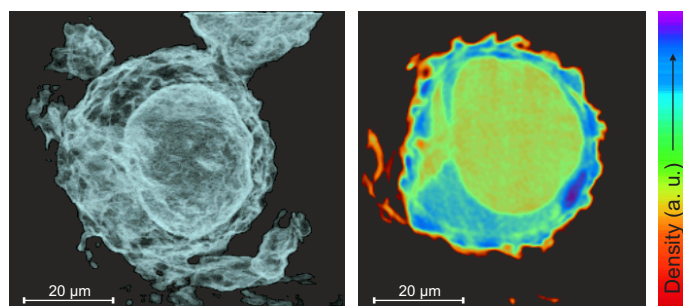

Fig. 7.3: Left: Rendering of a zygospore with internal nucleus. Right: Tomogram representing a slice through the middle of the zygospore with the remaining hyphae on the left side of the nucleus.

The figure shows a rendering of the zygospore and a tomogram of the middle horizontal slice through the nucleus. The main features are the highly sculptured surface of the thick wall and the inner nucleus. In the false colour representation of the tomogram the thick robust wall appears in blue, it has a higher density than the nucleus which appears in orange and green. The STIM-tomography measurement thus clearly shows that the zygospore has a single nucleus where the nuclei of both, parasite and host, were fused. The structure prodruding from the left side of the nucleus is possibly the remaining hyphae of the two mating fungi.

Chapter 8

Summary and Outlook

The Leipzig LIPSION laboratory, operational since August 1998, has been developed to a high performance nuclear microprobe. It provides quantitative trace element analysis with sub-micron spatial resolution, 2D- and 3D-microscopy of density distributions and the targeted irradiation of living cells with counted single ions. The analytical methods are based on particle induced X-ray emission spectrometry (PIXE), Rutherford backscattering spectrometry (RBS), scanning transmission ion microscopy (STIM) and STIM-tomography.

The specific development of the Leipzig nuclear microprobe led to an improved performance of the capabilities for trace element analysis. For sub-micron analysis the spatial resolution could be improved to 300 nm at a sensitivity of about 1 μg/g for metal ions in biological matrices; for a resolution of 1 μm the sensitivity was improved to 200 ng/g (3 μmol/l). The methods have been applied to various studies in the life sciences: environmental pollution research (single aerosol particle analysis), nanosafety research (risk through dermal uptake of nanoparticles), brain research (neuronal iron distribution), low dose radiobiology (induction of DNA double strand breaks and increased heat shock protein release after single ion bombardment), and a three-dimensional analysis of the inner structure of a fungal zygospore. For these applications the nuclear microprobe provided the required capabilities, a high sensitivity in elemental analysis, a spatial resolution in the micron or sub-micron region, and a precise delivery of energetic single ions. The broad spectrum of applications emphasises the nuclear microprobe as a unique instrument for analysis and materials modification. The LIPSION facility is certainly among the top ten nuclear micro/nanoprobe worldwide.

What is left?

The answer is: A further continuous development of the analytical and modification capabilities, instrumentations and applications of the Leipzig high energy ion nanoprobe. A few suggestions for these issues shall be shortly summarised in the following.

Microprobe performance: Although the Leipzig microprobe has reached an outstanding performance its limits in lateral resolution might not yet be reached. The main handicap is the still existing beam position inaccuracy preventing the improvement in spatial resolution. Its elimination is an indispensable major task that has to

be solved. The improvement could be as high as a factor of two in resolution.

High resolution quantitative elemental analysis is usually accompanied by low count rate due to low beam currents. This is in particular true when analysing trace element distributions with PIXE. For this case the best way to improve the performance is to increase the detection efficiency. A first step was already taken by ordering a second X-ray detector of the same model as the well established first detector. However, the new detector has to be revised by the manufacturer due to dissatisfactory performance. Finally, both detectors will mainly cover the space in front of the sample leaving only very restricted geometric conditions for further in front detectors. In the case of thin sections of biological materials, additional detector elements can be placed behind the sample to increase the detection efficiency of the system. However, additional conventional X-ray detectors with cryostats for liquid nitrogen cooling are less convenient at a multi-purpose target chamber as it is installed at the Leipzig microprobe. Very compact, low cost silicon drift detectors with an energy resolution below 150 eV @5.9 keV are available (e.g. Amptek). This type of detector can be assembled according to customer needs. Thus, an efficient additional detection system for PIXE analysis of thin biological samples could be installed in the remaining space behind the sample.

Targeted irradiation of living cells requires the precise recognition of the targets, e.g. cell nuclei or the cytoplasm of cells, and the accurate conversion into beam coordinates for the irradiation with single ions. Very recently, first targeted irradiation experiments on living cells have shown the feasibility of off-line cell recognition without any staining and the conversion into beam coordinates utilising fiducial markers on the Petri dishes. A few necessary minor improvements towards a higher degree of automation will follow soon. The next step has now to focus on the Petri-dish holder which shall include an enclosure for the cells providing an appropriate humidified atmosphere to prevent as much as possible any additional stress factors for the cells.

Ion beam microtomography, in particular STIM-tomography, has been successfully established in the Leipzig microprobe laboratory. The resolution required for the analysis of collagen networks is a remaining issue but will be available when the aforementioned deterioration factor has been eliminated. The last challenge in microtomography is the 3D elemental analysis. PIXE tomography is for that the first approach, the implementation, however, is by far more difficult than for STIM-tomography. The data acquisition time for PIXE-tomography is at least one order of magnitude longer than for STIM-tomography. Complicated ion beam sample interactions, i.e. matrix effects such as energy dependent X-ray production cross sections and X-ray attenuation, do not allow to apply standard back-projection algorithms for 3D reconstruction, instead an iterative algorithm with an initial "good guess" has to be applied. In the case of negligible matrix effects, e.g. Fe-, Cu- and Zn- analysis in biological materials, ion beam induced sample shrinkage constricts the beam dose for data acquisition and therefore resolution and sensitivity. Even with high detection efficiency a full 3D analysis of biological samples with 1 µm resolution is at the edge of feasibility but achievable for microstructures of solid state materials.

References

[Ahl07] Sarabjeet Singh Ahluwalia, Dinesh Goyal. Microbial and plant derived biomass for removal of heavy metals from wastewater. *Bioresource technology* **98** (12), 2243–2257 (2007).

[Azz03] Edouard I. Azzam, Sonia M. de Toledo, John B. Little. Expression of CONNEXIN43 is highly sensitive to ionizing radiation and other environmental stresses. *Cancer research* **63** (21), 7128–7135 (2003).

[Bet30] Hans A. Bethe. Zur Theorie schneller Korpuskularstrahlen durch Materie. *Ann. Phys.* **397** (3), 325–400 (1930).

[Bet07] A. A. Bettiol, C. N. B. Udalagama, E. J. Teo, J. A. van Kan, F. Watt. Embedded photonic structures fabricated in photosensitive glass using proton beam writing. *Nuclear Inst. and Methods in Physics Research, B* **260** (1), 357–361 (2007).

[Blo33] Felix Bloch. Bremsvermögen von Atomen mit mehreren Elektronen. *Z. für Phys.* **81** (5–6), 363–376 (1933).

[Bre96] Mark B.H. Breese, David N. Jamieson, Philip J.C. King (*eds.*). *Materials analysis using a nuclear microprobe.* John Wiley & Sons, INC. (1996).

[Bre07] M. B. H. Breese, E. Vittone, G. Vizkelethy, P. J. Sellin. A review of ion beam induced charge microscopy. *Nuclear Inst. and Methods in Physics Research, B* **264** (2), 345–360 (2007).

[Bro02] R. J. Brooks, D. E. Hole, P. D. Townsend. Ion beam induced luminescence of materials. *Nuclear Instruments and Methods in Physics Research Section B: Beam Interactions with Materials and Atoms* **190** (1), 136–140 (2002).

[Bru99] G. Bruckner, D. Hausen, W. Hartig, M. Drlicek, T. Arendt, K. Brauer. Cortical areas abundant in extracellular matrix chondroitin sulphate proteoglycans are less affected by cytoskeletal.. *Neuroscience* **92** (3), 791–805 (1999).

[But96] T. Butz, G. J. F. Legge. From micro– to nanoprobes: Auspices and horizons. *Nuclear Instruments and Methods in Physics Research Section B: Beam Interactions with Materials and Atoms* **113** (1), 317–322 (1996).

[Cal00] T. Calligaro, J.-C. Dran, E. Ioannidou, B. Moignard, L. Pichon, J. Salomon. Development of an external nuclear microprobe on th Aglae facility of the Louvre museum. *Nucl. Instr. and Meth. in Phys. Res.* **B 161–163**, 328–333 (2000).

[Chu78] W.K. Chu, J.W. Mayer, M.A. Nicolet. *Backscattering Spectrometry.* Academic Press, New York (1978).

[Coo72] J. Cookson, A. Ferguson, F. Pilling. Proton microbeams, their production and use. *Journal of Radioanalytical and Nuclear Chemistry* **12** (2), 39–52 (1972).

[Dea93] Stanley R. Deans. *The Radon Transform and Some of its Applications.* Krieger publishing company, Malabar, Florida (1993).

[Del05] Ralph J. Delfino, Constantinos Sioutas, Shaista Malik. Potential role of ultrafine particles in associations between airborne particle mass and cardiovascular health. *Environmental health perspectives* **113** (8), 934–946 (2005).

[Dol03] G. Dollinger, G. Datzmann, A. Hauptner, R. Hertenberger, H.-J. Korner, P. Reichart, B. Volckaerts. The Munich ion microprobe: Characteristics and prospect. *Nuclear Instruments and Methods in Physics Research Section B: Beam Interactions with Materials and Atoms* **210**, 6–13 (2003).

[Dor04] P. M. Doraiswamy, A. E. Finefrock. Metals in our minds: therapeutic implications for neurodegenerative disorders. *Lancet Neurology* **3** (7), 431–434 (2004).

[Doy97] B. P. Doyle, A. H. Andeweg, S. Ballestrero, J. U. M. Beer, J. E. Butler, M. B. H. Breese, S. H. Connell, M. L. Drummond, P. Formenti, I. Z. Machi. The Schonland Micro–Scanning Ion Beam Analysis Facility. *Nuclear Instruments and Methods in Physics Research Section B: Beam Interactions with Materials and Atoms* **130** (1), 37–44 (1997).

[Dym95] A. D. Dymnikov, D. N. Jamieson, G. J. F. Legge. Optimal non–linear, orthomorphic, magnetic quadrupole lens systems for ion microprobes. *Nuclear Instruments and Methods in Physics Research Section B: Beam Interactions with Materials and Atoms* **104** (1), 64–68 (1995).

[Fas06] Mauro Fasano, Bruno Bergamasco, Leonardo Lopiano. Modifications of the iron–neuromelanin system in Parkinson's disease. *Journal of neurochemistry* **96** (4), 909–916 (2006).

[Fed05] H. Fedorow, F. Tribl, G. Halliday, M. Gerlach, P. Riederer, K. L. Double. Neuromelanin in human dopamine neurons: Comparison with peripheral melanins and relevance to Parkinson's disease. *Progress in Neurobiology* **75** (2), 109–124 (2005).

[Fis85]   B. E. Fischer. The scanning heavy ion microscope at GSI. *Nuclear Instru-ments and Methods in Physics Research Section B: Beam Interactions with Materials and Atoms* **10**, 693–696 (1985).

[Fol05]   M. Folkard, K. Prise, G. Schettino, C. Shao, S. Gilchrist, B. Vojnovic. New insights into the cellular response to radiation using mi-crobeams. *Nuclear Inst. and Methods in Physics Research, B* **231** (1), 189–194 (2005).

[Fol07]   M. Folkard, Prise, K.M., B. Vojnovic. Status of charged particle microbeams for radiation biology. *Journal of Physics: Conference Series* **58** (1), 62–67 (2007).

[Goo92]   P. F. Good, C. W. Olanow, D. P. Perl. Neuromelanin–containing neurons of the substantia nigra accumulate iron and aluminum in Parkinson's disease: a LAMMA study. *Brain research* **593** (2), 343–346 (1992).

[Gur07]   A. Gurbich (16.11.2007). IBANDL: Ion Beam Analysis Nuclear Data Li-brary.
URL: *http://www-nds.iaea.org/ibandl/* .

[Ham07]   Nobuyuki Hamada, Hideki Matsumoto, Takamitsu Hara, Ya-suhiko Kobayashi. Intercellular and intracellular signaling pathways me-diating ionizing radiation–induced bystander effects. *Journal of radiation research* **48** (2), 87–95 (2007).

[Hau04]   A. Hauptner, S. Dietzel, G. A. Drexler, P. reichart, R. Krücken, T. Cremer, A. A. Friedl, G. Dollinger. Microirradia-tion of cells with energetic heavy ions. *Radiat Environ Biophys* **42**, 237–245 (2004).

[Hen04]   M. W. Hentze, M. U. Muckenthaler, N. C. Andrews. Balancing Acts – Molecular Control of Mammalian Iron Metabolism. *Cell* **117** (3), 285–297 (2004).

[Hoh08]   Marcus Hohlweg. *Entwicklung strukturierter Petrischalen und Io-nenbeschuss lebender Zellen zur Untersuchung des Bystander–Effektes unter Ausschluss von Zell–Zell–Kommunikation über Gap–Junctions: Diplomar-beit.* Diplomarbeit, Universität Leipzig, Leipzig (Januar 2008).

[Hol07]   Francisco Molina Holgado, Robert C. Hider, Alessandra Gaeta, Robert Williams, Paul Francis. Metals ions and neurode-generation. *Biometals : an international journal on the role of metal ions in biology, biochemistry, and medicine* **20** (3–4), 639–654 (2007).

[Jak03]   B. Jakob, M. Scholz, G. Taucher Scholz. Biological imaging of heavy charged–particle tracks. *Radiation research* **159** (5), 676–684 (2003).

[Jam97] D. N. Jamieson. Recent applications of nuclear microprobe analysis to frontier materials. *Nuclear Instruments and Methods in Physics Research Section B: Beam Interactions with Materials and Atoms* **130** (1), 706–716 (1997).

[Jam01] D.N. Jamieson. New generation nuclear microprobe systems. *Nucl. Instr. and Meth. in Phys. Res.* **181**, 1–11 (2001).

[Jel92] K. Jellinger, E. Kienzl, G. Rumpelmair, P. Riederer, H. Stachel-berger, D. Ben Shachar, M. B. Youdim. Iron–melanin complex in substantia nigra of parkinsonian brains: an x–ray microanalysis. *Journal of neurochemistry* **59** (3), 1168–1171 (1992).

[Joh95] Sven A.E. Johansson, John L. Campbell, Klas G. Malmqvist (*eds.*). *Particle-Induced X-Ray Emission Spectrometry (PIXE)*. Monographs on Analytical Chemistry and Its Application. John Wiley & Sons, INC. (1995).

[Kan03] J.A. van Kan, A.A. Bettiol, F. Watt. Three–dimensional nanolithography using proton beam writing. *Applied Physics Letters* (2003).

[Lit06] J. B. Little. Cellular radiation effects and the bystander response. *Mutation Research – Fundamental and Molecular Mechanisms of Mutagenesis* **597** (1), 113–118 (2006).

[Lla98] Yvan Llabador, Philippe Moretto (*eds.*). *Nuclear microprobes in the life sciences.* World Scientific Publishing Co. Pte. Ltd. (1998).

[Mal96] K. G. Malmqvist. Applications of nuclear microprobes in environmental research. *Nuclear Instruments and Methods in Physics Research Section B: Beam Interactions with Materials and Atoms* **113** (1), 336–346 (1996).

[Mar06] Maria João Santos Marques, Félix Carvalho, Carla Sousa, Fernando Remião, Rui Vitorino, Francisco Amado, Rita Ferreira, José Alberto Duarte, Maria de Lourdes Bastos. Cytotoxicity and cell signalling induced by continuous mild hyperthermia in freshly isolated mouse hepatocytes. *Toxicology* **224** (3), 210–218 (2006).

[Mei95] J. Meijer, A. Stephan, J. Adamczewski, H. Roken, H. H. Bukow, C. Rolfs. Superconducting microprobe at Bochum. *Nuclear Instruments and Methods in Physics Research Section B: Beam Interactions with Materials and Atoms* **99** (1), 423–426 (1995).

[Men07] F. Menzel, D. Spemann, S. Petriconi, J. Lenzner, T. Butz. Proton beam writing of submicrometer structures at LIPSION. *Nuclear Inst. and Methods in Physics Research, B* **260** (1), 419–425 (2007).

[Mic97] A. A. Michels, B. Kanon, A. W. T. Konings, K. Ohtsuka, O. Bensaude, H. H. Kampinga. Hsp70 and Hsp40 Chaperone Activities

in the Cytoplasm and the Nucleus of Mammalian Cells. *The Journal of Biological Chemistry* **272** (52), 33283–33289 (1997).

[Mor97] P. Moretto, Y. Llabador. The nuclear microprobe: An insight of applications in cell biology. *Nuclear Instruments and Methods in Physics Research Section B: Beam Interactions with Materials and Atoms* **130** (1), 324–334 (1997).

[Mor04] M. Morawski, T. Reinert, G. Brückner, F. Wagner, T. Arendt, W. Tröger. The Binding of Iron to Perineuronal Nets: A Combined Nuclear Microscopy and Mössbauer Study. *Hyperfine Interactions* **159** (1), 285–291 (2004).

[Mor05] M. Morawski, T. Reinert, C. Meinecke, T. Arendt, T. Butz. Antibody meets the microbeam – or how to find neurofibrillary tangles. *Nuclear Instruments and Methods in Physics Research Section B: Beam Interactions with Materials and Atoms* **231** (1), 229–233 (2005).

[Mor07] William F. Morgan, Marianne B. Sowa. Non–targeted bystander effects induced by ionizing radiation. *Mutation research* **616** (1–2), 159–164 (2007).

[Mou97] D.J.W. Mous, R.G. Haitsma, T. Butz, R.-H. Flagmeyer, D. Lehmann, J. Vogt. The novel ultrastable HVEE 3.5MV Singletron$^r mTM$ accelerator for nanoprobe applications. *Nucl. Instr. and Meth. in Phys. Res.* **B 130**, 31–36 (1997).

[Nob77] R. Nobiling, K. Traxel, F. Bosch, Y. Civelekoglu, B. Martin, B. Povh, D. Schwalm. Focussing of proton beams to micrometer dimensions. *Nuclear Instruments and Methods* **142** (1), 49–50 (1977).

[Odh94] G. Odh, R. Carstam, J. Paulson, A. Wittbjer, E. Rosengren, H. Rorsman. Neuromelanin of the human substantia nigra: a mixed–type melanin. *Journal of neurochemistry* **62** (5), 2030–2036 (1994).

[Osi07] T. Osipowicz, M. Breese. 10th International Conference on Nuclear Microprobe Technology and Applications (ICNMTA2006). *Nuclear Inst. and Methods in Physics Research, B* **260** (1), vii–viii (2007).

[Ote04] P. I. Oteiza, G. G. Mackenzie, S. V. Verstraeten. Metals in neurodegeneration: involvement of oxidants and oxidant–sensitive transcription factors. *Molecular Aspects of Medicine* **25** (1), 103–115 (2004).

[Pri03] K. M. Prise, M. Folkard, B. D. Michael. A review of the bystander effect and its implications for low-dose exposure. *Radiation protection dosimetry* **104** (4), 347–355 (2003).

[Pri06] Kevin M. Prise. New advances in radiation biology. *Occupational medicine (Oxford, England)* **56** (3), 156–161 (2006).

[Pri07] K. M. Prise, S. Burdak Rothkamm, M. Folkard, G. Kashino, C. Shao, L. Tartier. New insights on radiation–induced bystander signalling and its relationship to DNA repair. *International Congress Series* **1299**, 121–127 (2007).

[Pro93] National Council on Radiation Protection. Limitation of Exposure to Ionizing Radiation: Report. *Natl. Council Radiat. Prot.* **116** (1993).

[Prz97] W. J. Przybylowicz, J. Mesjasz Przybylowicz, V. M. Prozesky, C. A. Pineda. Botanical applications in nuclear microscopy. *Nuclear Instruments and Methods in Physics Research Section B: Beam Interactions with Materials and Atoms* **130** (1), 335–345 (1997).

[Qua07] A. Quaranta, J. Salomon, J. C. Dran, M. Tonezzer, G. Della Mea. Ion beam induced luminescence analysis of painting pigments. *Nuclear Inst. and Methods in Physics Research, B* **254** (2), 289–294 (2007).

[Rad17] J. Radon. Über die Bestimmung von Funktionen durch ihre Integralwerte längs gewisser Mannigfaltigkeiten. *Berichte Sächsische Akademie der Wissenschaften* **29**, 262–277 (1917).

[Rei01] T. Reinert, U. Reibetanz, J. Vogt, T. Butz, A. Werner, W. Grunder. Visualisation of collagen fibrils in joint cartilage using STIM. *Nuclear Instruments and Methods in Physics Research Section B: Beam Interactions with Materials and Atoms* **181**, 511–515 (2001).

[Rei02] T. Reinert, A. Sakellariou, M. Schwertner, J. Vogt, T. Butz. STIM Tomography at the Leipzig Nanoprobe LIPSION. *Nuclear Instruments and Methods in Physics Research Section B: Beam Interactions with Materials and Atoms* **190**, 266–270 (2002).

[Rei03] T. Reinert, M. Morawski, T. Arendt, T. Butz. Quantitative microanalysis of perineuronal nets in brain tissue. *Nuclear Instruments and Methods in Physics Research Section B: Beam Interactions with Materials and Atoms* **210**, 395–400 (2003).

[Rei04] T. Reinert, A. Fiedler, J. Skopek, J. Tanner, J. Vogt, T. Butz. Single ion bombardment of living cells at LIPSION. *Nuclear Instruments and Methods in Physics Research Section B: Beam Interactions with Materials and Atoms* **219**, 77–81 (2004).

[Rei06] T. Reinert, D. Spemann, M. Morawski, T. Arendt. Quantitative trace element analysis with sub–micron lateral resolution. *Nuclear Instruments and Methods in Physics Research Section B: Beam Interactions with Materials and Atoms* **249** (1), 734–737 (2006).

[Roh03] Stephan Rohr, Regula Flückiger Labrada, Jan P. Kucera. Photolithographically defined deposition of attachment factors as a versatile method for patterning the growth of different cell types in culture. *Pflügers Archiv : European journal of physiology* **446** (1), 125–132 (2003).

[Ros04] P. Rossi, D. K. Brice, C. H. Seager, F. D. McDaniel, G. Vizkelethy, B. L. Doyle. Ion beam induced luminescence of doped yttrium compounds. *Nuclear Instruments and Methods in Physics Research Section B: Beam Interactions with Materials and Atoms* **219**, 327–332 (2004).

[Rya04] C. G. Ryan. Ion beam microanalysis in geoscience research. *Nuclear Instruments and Methods in Physics Research Section B: Beam Interactions with Materials and Atoms* **219**, 534–549 (2004).

[Sak01] A. Sakellariou, D. N. Jamieson, G. J. F. Legge. Three–dimensional ion micro–tomography. *Nuclear Instruments and Methods in Physics Research Section B: Beam Interactions with Materials and Atoms* **181** (1), 211–218 (2001).

[Sak02] Arthur Sakellariou. *STIM and PIXE Tomography - The three Dimensional Quantitative Visualisation of Micro-Specimen Density and Composition.* Dissertation, MARC Melbourne, University of Melbourne-Australia (2002).

[Sch02] Michael Schwertner. *Hochauflösende Ionenstrahl-Mikrotomographie am LIPSION.* Diplomarbeit, Universität Leipzig, Leipzig (März 2002).

[Sch06] M. Schwertner, A. Sakellariou, T. Reinert, T. Butz. Scanning transmission ion micro–tomography (STIM–T) of biological specimens. *Ultramicroscopy* **106** (7), 574–581 (2006).

[Spe03] D. Spemann, T. Reinert, J. Vogt, J. Wassermann, T. Butz. Active compensation of stray magnetic fields at LIPSION. *Nuclear Instruments and Methods in Physics Research Section B: Beam Interactions with Materials and Atoms* **210**, 79–84 (2003).

[Spe05] D. Spemann, P. Esquinazi, R. Hohne, A. Setzer, M. Diaconu, H. Schmidt, T. Butz. Magnetic carbon: A new application for ion microbeams. *Nuclear Inst. and Methods in Physics Research, B* **231** (1), 433–439 (2005).

[Str04] Bundesamt für Strahlenschutz. *Umweltradioaktivität und Strahlenbelastung im Jahr 2003 – Unterrichtung durch die Bundesregierung.* (2004).

[Swa97] C. P. Swann. Recent applications of nuclear microprobes to the study of art objects and archaeological artifacts. *Nuclear Instruments and Methods in Physics Research Section B: Beam Interactions with Materials and Atoms* **130** (1), 289–296 (1997).

[Tak97] M. Takai. Recent applications of nuclear microprobe techniques to microelectronics. *Nuclear Instruments and Methods in Physics Research Section B: Beam Interactions with Materials and Atoms* **130** (1), 466–469 (1997).

[Teo07] E.J. Teo, M.B.H. Breese, A.A. Bettiol, F.J.T. Champeaux, T.L.S.L. Wijesinghe, D.J. Blackwood. Tunable colour emission from patterned porous silicon using ion beam writing. *Nuclear Inst. and Methods in Physics Research, B* **260** (1), 378–383 (2007).

[Tes95] J.R. Tesmer, M. Nastasi (*eds.*). *Handbook of Modern Ion Beam Materials Analysis.* Materials Research Society (1995).

[Tho01] K. J. Thompson, S. Shoham, J. R. Connor. Iron and neurodegenerative disorders. *Brain research bulletin* **55** (2), 155–164 (2001).

[Tow07] P. D. Townsend, M. Khanlary, D. E. Hole. Information obtainable from ion beam luminescence. *Surface & Coatings Technology* **201** (19), 8160–8164 (2007).

[Vis97] R. D. Vis. Applications of the nuclear microprobe in planetary science. *Nuclear Instruments and Methods in Physics Research Section B: Beam Interactions with Materials and Atoms* **130** (1), 587–591 (1997).

[Wat81] F. Watt, G. W. Grime, G. D. Blower, J. Takacs. A Coupled Triplft Configuration of the Oxford Microprobe. *IEEE Transactions on Nuclear Science* **28** (2), 1413–1416 (1981).

[Wat03] F. Watt, J. A. van Kan, I. Rajta, A. A. Bettiol, T. F. Choo, M. B. H. Breese, T. Osipowicz. The National University of Singapore high energy ion nano–probe facility: Performance tests. *Nuclear Instruments and Methods in Physics Research Section B: Beam Interactions with Materials and Atoms* **210**, 14–20 (2003).

[Wel84] W. J. Welch, J. R. Feramisco. Nuclear and nucleolar localization of the 72,000–dalton heat shock protein in heat–shocked mammalian cells. *J Biol Chem.* **259** (7), 4501–4513 (1984).

[Wös96] J. Wöstemeyer, A. Wöstemeyer, K. Voigt. Horizontal gene transfer in the rhizosphere: A curiosity or a driving force in evolution? *Advances in Botanical Research* **24**, 399–429 (1996).

[Wös04] J. Wöstemeyer, Ch. Schimek, K. Schultze, A. Burmester, K. Voigt. Parasexual processes in fungal host–parasite interactions. *Endocytobiosis Cell Res.* **15** (2), 477–481 (2004).

[Zec06] L. Zecca, F. A. Zucca, A. Albertini, E. Rizzio, R. G. Fariello. A proposed dual role of neuromelanin in the pathogenesis of Parkinson's disease. *Neurology* **67** (7, 2), 8–11 (2006).

[Zha05] F. Zhang, F. Sun, J.A. van Kan, P.G. Shao, Z. Zheng, R.W. Ge, F. Watt. Measurement of cell motility on proton beam micromachined 3D scaffolds. *Nuclear Inst. and Methods in Physics Research, B* **231** (1), 413–418 (2005).

[Zho04] H. Zhou, G. Randers-Pehrson, C. A. Waldren, T. K. Hei. Radiation-induced bystander effect and adaptive response in mammalian cells. *Advances in Space Research* **34** (6), 1368–1372 (2004).

[Zie] James F. Ziegler, J.P. Biersack. SRIM - The Stopping and Range of Ions in Matter.
URL: *http://www.research.ibm.com/ionbeams/* .

Appendix
Selected Publications

List of selected publications attached to the appendix

[A1] T. Butz, R.-H. Flagmeyer, J. Heitmann, D. N. Jamieson, G. J. F. Legge, D. Lehmann, U. Reibetanz, **T. Reinert**, A. Saint, and D. Spemann. The Leipzig high-energy ion nanoprobe: A report on first results. *Nuclear Instruments and Methods in Physics Research Section B: Beam Interactions with Materials and Atoms*, 161:323–327, 2000. (T.R. contributed to sample preparation, measurements, data analysis, interpretation)

[A2] J. Vogt, R.-H. Flagmeyer, J. Heitmann, D. Lehmann, **T. Reinert**, St. Jankuhn, D. Spemann, W. Tröger, and T. Butz. Solid State Analysis with the New Leipzig High-Energy Ion Nanoprobe. *Mikrochim. Acta*, 133:105, 2000. (T.R. contributed to sample preparation, measurements, data analysis, interpretation)

[A3] D. Spemann, **T. Reinert**, J. Vogt, T. Butz, K. Otte, and K. Zimmer. Novel test sample for submicron ion-beam analysis. *Nuclear Instruments and Methods in Physics Research Section B: Beam Interactions with Materials and Atoms*, 181:186–192, 2001. (T.R. contributed to measurements, data analysis, interpretation)

[A4] T. Butz, D. Lehmann, **T. Reinert**, D. Spemann, and J. Vogt. Ion Microscopy and Tomography. *Acta Physica Polonica A*, 100:603, 2001. (T.R. contributed to sample preparation, measurements, data analysis, interpretation)

[A5] S. Lebed, J. Butz, T. Vogt, **T. Reinert**, D. Spemann, J. Heitmann, Z. Stachura, J. Lekki, A. Potempa, J. Styczen, and B. Sulkio-Cleff. A novel ultra-short scanning nuclear microprobe: Design and preliminary results. *Nuclear Instruments and Methods in Physics Research Section B: Beam Interactions with Materials and Atoms*, 181:32–38, 2001. (T.R. contributed to design, measured data, interpretation)

[A6] D. Spemann, **T. Reinert**, J. Vogt, D. Dobrev, and T. Butz. Suitable test structures for submicron ion beam analysis. *Nuclear Instruments and Methods in Physics Research Section B: Beam Inter-*

actions with Materials and Atoms, 190(1):312–317, 2002. (T.R. contributed to measurements, data analysis, interpretation)

[A7] D. Spemann, **T. Reinert**, J. Vogt, J. Wassermann, and T. Butz.
Active compensation of stray magnetic fields at LIPSION.
Nuclear Instruments and Methods in Physics Research Section B: Beam Interactions with Materials and Atoms, 210:79–84, 2003. (T.R. contributed to installation, measurements, data analysis, interpretation)

[A8] T. Butz, Ch. Meinecke, M. Morawski, **T. Reinert**, M. Schwertner, D. Spemann, and J. Vogt.
Morphological and elemental characterisation with the high-energy ion-nanoprobe LIPSION.
Applied Surface Science, 252(1):43–48, 2005. (T.R. contributed to sample preparation, measurements, data analysis, interpretation)

[A9] **T. Reinert**, D. Spemann, M. Morawski, and T. Arendt.
Quantitative trace element analysis with sub-micron lateral resolution.
Nuclear Instruments and Methods in Physics Research Section B: Beam Interactions with Materials and Atoms, 249(1):734–737, 2006. (T.R. wrote, contributed to sample preparation, measurements, data analysis, interpretation)

[A10] J. Wang, P. Guo, X. Li, J. Zhu, **T. Reinert**, J. Heitmann, D. Spemann, J. Vogt, R.-H. Flagmeyer, and T. Butz.
Source Identification of Lead Pollution in the Atmosphere of Shanghai City by Analyzing Single Aerosol Particles (SAP).
Environ. Sci. Technol., 34:1900, 2000. (T.R. contributed to measurements)

[A11] J. Wang, P. Guo, X. Li, J. Zhu, **T. Reinert**, J. Heitmann, D. Spemann, J. Vogt, R.-H. Flagmeyer, and T. Butz.
Identification of air pollution sources by single aerosol particle fingerprints - micro-PIXE spectra.
Nuclear Instruments and Methods in Physics Research Section B: Beam Interactions with Materials and Atoms, 161:830–835, 2000. (T.R. contributed to measurements, data analysis)

[A12] P. Guo, J. Wang, J. Zhu, **T. Reinert**, J. Heitmann, D. Spemann, J. Vogt, R.-H. Flagmeyer, and T. Butz.
Combination of Micro-PIXE with the Pattern Recognition Technique for the Source Identification of Individual Aerosol Particles.
Appl. Spectrosc., 54(6):807–811, 2000. (T.R. contributed to measurements)

[A13] P. Guo, J. Wang, X. Li, J. Zhu, **T. Reinert**, J. Heitmann, D. Spemann, J. Vogt, R.-H. Flagmeyer, and T. Butz.
Study of metal bioaccumulation by nuclear microprobe analysis of algae fossils and living algae cells.
Nuclear Instruments and Methods in Physics Research Section B: Beam Interactions with Materials and Atoms, 161:801–807, 2000. (T.R. contributed to measurements, data analysis, interpretation)

[A14] F. Menzel, **T. Reinert**, J. Vogt, and T. Butz.
Investigations of percutaneous uptake of ultrafine TiO$_2$ particles at the high energy ion nanoprobe LIPSION.
Nuclear Instruments and Methods in Physics Research Section B: Beam Interactions with Materials and Atoms, 219:82–86, 2004. (T.R. contributed to sample preparation, measurements, data analysis, interpretation, writing)

[A15] J. Lekki, Z. Stachura, W. Dąbroś, J. Stachura, F. Menzel, **T. Reinert**, T. Butz, J. Pallon, E. Gontier, M.D. Ynsa, P. Moretto, Z. Kertesz, Z. Szikszai, and Á.Z. Kiss.
On the follicular pathway of percutaneous uptake of nanoparticles: Ion microscopy and autoradiography studies.
Nuclear Instruments and Methods in Physics Research Section B: Beam Interactions with Materials and Atoms, 260(1):174–177, 2007. (T.R. contributed to sample preparation, measurements, data analysis, interpretation)

[A16] T. Butz, **T. Reinert**, T. Pinheiro, P. Moretto, J. Pallon, Á.Z. Kiss, J. Stachura, W. Dąbroś, Z. Stachura, J. Lekki, M. Lekka, J. Hunyadi, T. Bíró, M. Sticherling, L. Van Vaeck, P. Van Royen, J.-E. Surlève-Bazeille.
NANODERM – Final Report.
URL: http://www.uni-leipzig.de/ñanoderm. (T.R. contributed to sample preparation, measurements, data analysis, interpretation, writing)

[A17] **T. Reinert**, M. Morawski, T. Arendt, and T. Butz.
Quantitative microanalysis of perineuronal nets in brain tissue.
Nuclear Instruments and Methods in Physics Research Section B: Beam Interactions with Materials and Atoms, 210:395–400, 2003. (T.R. wrote, contributed to sample preparation, measurements, data analysis, interpretation)

[A18] M. Morawski, Ch. Meinecke, **T. Reinert**, A. C. Dorffel, P. Riederer, T. Arendt, and T. Butz.
Determination of trace elements in the human substantia nigra.
Nuclear Instruments and Methods in Physics Research Section B: Beam Interactions with Materials and Atoms, 231(1):224–228, 2005. (T.R. contributed to measurements, data analysis, interpretation, writing)

[A19] M. Morawski, **T. Reinert**, Ch. Meinecke, Th. Arendt, and T. Butz.
Antibody meets the microbeam - or how to find neurofibrillary tangles.
Nuclear Instruments and Methods in Physics Research Section B: Beam Interactions with Materials and Atoms, 231(1):229–233, 2005. (T.R. contributed to measurements, data analysis, interpretation, writing)

[A20] M. Morawski, **T. Reinert**, G. Brückner, F. Wagner, T. Arendt, and W. Tröger.
The Binding of Iron to Perineuronal Nets: A Combined Nuclear Microscopy and Mössbauer Study.
Hyperfine Interactions, 159(1):285–291, 2004. (T.R. contributed to measurements, data analysis, interpretation, writing)

[A21] Ch. Meinecke, M. Morawski, **T. Reinert**, T. Arendt, and T. Butz.
Cellular distribution and localisation of iron in adult rat brain (substantia nigra).
Nuclear Instruments and Methods in Physics Research Section B: Beam Interactions with Materials and Atoms, 249(1):688–691, 2006. (T.R. contributed to measurements, data analysis, interpretation, writing)

[A22] A. Fiedler, **T. Reinert**, M. Morawski, G. Brückner, T. Arendt, and T. Butz.
Intracellular iron concentration of neurons with and without perineuronal nets.
Nuclear Instruments and Methods in Physics Research Section B: Beam Interactions with Materials and Atoms, 260(1):153–158, 2007. (T.R. contributed to measurements, data analysis, interpretation, writing)

[A23] **T. Reinert**, A. Fiedler, M. Morawski, and T. Arendt.
High resolution quantitative element mapping of neuromelanin-containing neurons.
Nuclear Instruments and Methods in Physics Research Section B: Beam Interactions with Materials and Atoms, 260(1):227–230, 2007. (T.R. wrote, sample preparation, contributed to measurements, data analysis, interpretation)

[A24] M. Morawski, A. Fiedler, **T. Reinert**, G. Brückner, and T. Arendt.
Iron compartmentalisation in the rat brain: do perineuronal net-ensheathed neurons play a special role?.
Journal of Neurochemistry, 101:35, 2007. (T.R. contributed to measurements, data analysis, interpretation, writing)

[A25] J. Tanner, D. Spemann, **T. Reinert**, J. Vogt, and T. Butz.
The Leipzig High-Energy Ion-Nanoprobe LIPSION: Design of single-ion bombardment of living cells.
Radiation Research, 158(3):372, 2002. (T.R. contributed to design, construction)

[A26] **T. Reinert**, A. Fiedler, J. Skopek, J. Tanner, J. Vogt, and T. Butz.
Single ion bombardment of living cells at LIPSION.
Nuclear Instruments and Methods in Physics Research Section B: Beam Interactions with Materials and Atoms, 219:77–81, 2004. (T.R. wrote, contributed to sample preparation, irradiation, data analysis, interpretation)

[A27] A. Fiedler, **T. Reinert**, J. Tanner, and T. Butz.
First Irradiation Experiments with Living Cells at LIPSION.
Radiation Research, 161(1):95–96, 2004. (T.R. contributed to sample preparation, irradiation, data analysis, interpretation, writing)

[A28] C. Nilsson, S. Petriconi, **T. Reinert**, and T. Butz.
Status of the new single-ion hit facility for irradiation of living cells at LIPSION.
Radiation Research, 166(4):672–673, 2006. (T.R. contributed to design, construction)

[A29] A. Fiedler, **T. Reinert**, J. Tanner, and T. Butz.
DNA double strand breaks and Hsp70 expression in proton irradiated living cells.

Nuclear Instruments and Methods in Physics Research Section B: Beam Interactions with Materials and Atoms, 260(1):169–173, 2007. (T.R. contributed to sample preparation, irradiation, data analysis, interpretation, writing)

[A30] C. Nilsson, S. Petriconi, **T. Reinert**, and T. Butz.
The new target chamber at LIPSION: The new translation stage and goniometer and the new irradiation platform for single cell experiments.
Nuclear Instruments and Methods in Physics Research Section B: Beam Interactions with Materials and Atoms, 260(1):71–76, 2007. (T.R. contributed to measurements, data analysis, interpretation)

[A31] **T. Reinert**, A. Sakellariou, M. Schwertner, J. Vogt, and T. Butz.
Scanning transmission ion microscopy tomography at the Leipzig nanoprobe LIPSION.
Nuclear Instruments and Methods in Physics Research Section B: Beam Interactions with Materials and Atoms, 190:266–270, 2002. (T.R. wrote, contributed to sample preparation, measurements, data analysis, interpretation)

[A32] M. Schwertner, A. Sakellariou, **T. Reinert**, and T. Butz.
Scanning transmission ion micro-tomography (STIM-T) of biological specimens.
Ultramicroscopy, 106(7):574–581, 2006. (T.R. contributed to sample preparation, measurements, data analysis, interpretation, writing)

The Leipzig high-energy ion nanoprobe: A report on first results

T. Butz [a,*], R.-H. Flagmeyer [a], J. Heitmann [a], D.N. Jamieson [b], G.J.F. Legge [b],
D. Lehmann [a], U. Reibetanz [a], T. Reinert [a], A. Saint [b], D. Spemann [a], R. Szymanski [b],
W. Tröger [a], J. Vogt [a], J. Zhu [a]

[a] *Fakultät für Physik und Geowissensch., Universität Leipzig, Abteilung NFP, Linnéstrasse 5, D-04103, Leipzig, Germany*
[b] *School of Physics, MARC, The University of Melbourne, Parkville, Vic. 3052, Australia*

Abstract

The high-energy ion nanoprobe LIPSION at the University of Leipzig has been operational since October 1998. Its magnetic quadrupole lens system, arranged as a separated Russian quadruplet, has been developed by the Microanalytical Research Centre (MARC), Melbourne. The ultrastable single-ended 3.5 MV SINGLETRON™ accelerator (High Voltage Engineering Europa) supplies H^+ and He^+ ion beams with a beam brightness in the range of 10–20 A rad^{-2} m^{-2} eV^{-1} [D.J.W. Mous, R.G. Haitsma, T. Butz, R.-H. Flagmeyer, D. Lehmann, J. Vogt, Nucl. Instr. and Meth. B 130 (1997) 31]. Due to this high brightness, the excellent optical properties of the focusing system of the nanoprobe and the suppression of mechanical vibrations, lateral resolutions of 100 nm for the low current mode (STIM) and 340 nm at a current of 10 pA (PIXE, RBS, SEI modes) were achieved. Further improvements are expected. © 2000 Elsevier Science B.V. All rights reserved.

PACS: 41.75.A; 72.20.M; 29.30.K
Keywords: Nanoprobes; Resolution; Medicine; Solid state

1. Introduction

In the past, ion beam techniques have been successfully applied for elemental analysis and to the determination of the density information and charge collection properties of various materials. The high-energy ion microprobes bring to these a lateral resolution down to the micrometer regime.

An increase in the spatial resolution toward the submicron range would fulfill the requirements of a wide range of applications.

With the new Leipzig ion nanoprobe we shall focus on medical problems with techniques like single ion bombardment or two- and three-dimensional high resolution investigations on biological samples as well as on problems in solid state physics. In the field of materials science a quantitative elemental as well as defect or structural analysis of complex materials would be challenging.

* Corresponding author. Fax: +49-341-97-32701; website: http://www.uni-leipzig.de/ ˜nfp/.
E-mail address: butz@physik.uni-leipzig.de (T. Butz).

These analytical possibilities are due to the ultrastable single-ended 3.5 MV SINGLETRON™ (High Voltage Engineering Europa) [1], its high brightness and the excellent properties of the focusing system of the nanoprobe produced at MARC, Melbourne.

2. The Leipzig ion nanoprobe

2.1. Laboratory

The establishment of the Leipzig Ion Nanoprobe laboratory was part of the reconstruction of a whole building. It gave the opportunity to design a new laboratory from scratch. Therefore the bedplates of accelerator and nanoprobe could be founded in greater depths (approx. 10 m) separately from the surroundings to minimize mechanical vibrations. In order to avoid thermal drifts of the system the room temperature and humidity are controlled by a powerful air conditioning system with an accuracy of ± 2 K and $\pm 1\%$, respectively.

2.2. Accelerator

A high beam brightness and a high stability of the beam energy are important for high resolution nanoprobe applications. The 3.5 MV SINGLETRON™ has a beam brightness of 10–20 A rad^{-2} m^{-2} eV^{-1}. The voltage ripple is approx. $25V_{pp}$ and the stability of the beam energy is about ± 50 eV over 5 h measured with the ^{7}Li(p,n) threshold at 1.881 MeV [1].

The ion beam supplied by the accelerator can be bent into five different beamlines by a switching magnet. An additional 90° analyzing magnet is used to direct the beam into the nanoprobe.

2.3. Brief description of the nanoprobe and its significant features

The nanoprobe, shown schematically in Fig. 1, was designed for extremely high resolution work. Extreme measures had to be adopted in providing mechanical rigidity, minimizing any scattered beam from collimators, slits or gas molecules, and providing very accurate control of the specimen.

When referred to the convergence angle of a microbeam at the specimen (the image plane), aberration coefficients for the various possible probe forming lens configurations are comparable. This means that if the brightness distribution from the accelerator was uniform with displacement and angle, each system would give similar performance.

However, the separated Russian quadruplet configuration of magnetic quadrupole lenses adopted for LIPSION has some significant advantages in practice. The first advantage is that the two stage system provides a large and symmetric demagnification factor so that the critical object collimator can be relatively large and hence scattering from its surfaces is more readily avoided. The large demagnification also makes mechanical instability at this point proportionately less important. In fact, all instabilities are less important in the first stage of the system than in the second stage.

The second advantage is that the large demagnification factor fully exploits the high brightness provided by the HVEE SINGLETRON accelerator. In particular, the peak of brightness in the
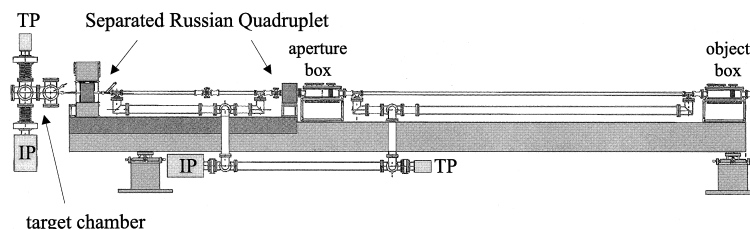

Fig. 1. Leipzig high-energy ion nanoprobe (scheme). Abbreviations: TP – turbo molecular pump, IP – ion getter pump.

paraxial region (shown by measurements published previously [2]) enables us to form finely focused probes without incurring significant penalty of aberrations.

The specifications of the LIPSION system appear in Table 1 and a first order raytrace (from program PRAM [3]) through the two stages of demagnification is shown in Fig. 2. This raytrace shows the internal crossovers in both the x–z and y–z planes and the excellent close proximity of the exit principal planes to the plane of the focused probe.

The whole system is supported on a heavy steel reinforced box girder laying on adjustable steel pedestals. The beam line instrumentation is placed in heavy multiport boxes mounted on the girder, but computer-controlled object and aperture collimator stages are mounted directly on the girder with movement through balanced bellows to isolate them from external forces. Separate microslits are also mounted on the girder. Both lens doublets are mounted on a very heavy steel baseplate which is supported by the girder with its own shock-absorbing attachment. The first doublet is adjustable, in contrast to the more critical second doublet which is more rigidly mounted on this baseplate.

Slit scattering can be minimized because the internal crossovers are situated at different distances after the first doublet. Therefore, separate slits are provided at each of the crossovers and these are adjusted to intercept any scattered beam, but not the primary beam. The beam tube is magnetically shielded using μ-metal, pumped at four points and is directly supported above the

Fig. 2. Ion optics of the LIPSION system. The vertical lines on the axis show the position of the entrance principal planes, the Gaussian image plane, and the exit principal planes, respectively. The ray which starts on the left from above the axis is in the x–z plane, the other ray is in the y–z plane. The initial ray vectors were 50 μm with a divergence of 0.05 mrad (corresponding to a 50 μm diameter aperture collimator).

large diameter pumping lines connected to an ion and a turbomolecular pump beneath the girder. This arrangement provides high pumping speed and a good vacuum of 10^{-8} mbar which is necessary for low gas scattering.

The specimen chamber is mounted on the girder; but the specimen itself is mounted on the baseplate with a very rigid steel gantry, which also incorporates the mounting of the second doublet. From this gantry, the specimen is located by means of a high precision, computer-controlled x–y micrometer-stage with DC motors and optical-encoder feedback, providing smooth total movement of 200 mm with an accuracy of 0.1 μm in the horizontal (x) and vertical (y) directions.

The specimen chamber is equipped with front and rear viewing microscopes, each with a choice of two objective lenses, which can be removed from the beam axis and accurately repositioned against stops. A 45° viewing port is also available. There is a Ge X-ray detector, a secondary electron detector, an externally controlled set of four concentric rings to support and accurately position particle detectors or other instrumentation, a computer controlled goniometer, a STIM detector and a triaxial Faraday cup, both removable from the beam path, and many electrical feedthroughs.

Table 1
Specifications of the Leipzig nanoprobe (Q1–Q4 denote the quadrupole lenses of the split Russian quadruplet downstream)

Object to aperture (m)	4.90
Aperture to Q1 (m)	0.54
Q2 to Q3 (m)	2.49
Q4 to specimen (mm)	330
Pole length of each lens (mm)	57
Spacing Q1 to Q2 and Q3 to Q4 (mm)	40
Turns per pole in Q2 and Q3	108
Turns per pole in Q1 and Q4	125
Bore radius of all lenses (mm)	6.35
Demagnification	$D_x = D_y = 82.2$
Maximum magnetic rigidity	12 amu MeV/q^2

The chamber is composed of two large sections, each with a large windowed quick-access port. The combination of turbomolecular and ion pumps provides a rapid pumpdown.

The whole described vacuum equipment and the positioning system of object and aperture diaphragms and target are fully automated. The lens currents are computer controlled and stabilized. During focusing, the program can adjust the average value and ratio of the two lens currents, thus allowing the size and the shape of the beam spot to be adjusted independently. In order to achieve the highest resolution the beam is first focused with the help of the rear optical microscope with large current at a wide object and aperture diaphragm, and then the object and aperture are reduced in size.

3. Resolution measurements on an InGaP/GaAs(0 0 1) semiconductor heterostructure

As a first application an InGaP/GaAs(0 0 1) semiconductor heterostructure has been investigated by PIXE and STIM with 2.25 MeV H^+ ions. The crystals were glued "face-to-face" and thinned down to some µm in thickness. Fig. 3 shows a scheme of the described sample. The sharpness of the interface gives a measure of the lateral resolution of the focused ion beam. Fig. 3 shows the Ga, In and As count rate of a linescan over the InGaP/GaAs interface. The FWHM of the derivative of the fitted function at the Ga count rate corresponds to a beam diameter of 340 ± 30 nm. The current for this measurements was 10 pA and the object and aperture diaphragms had a diameter of 20 and 100 µm, respectively. The resolution is a bit worse than expected, due to a small drift of the beam position during the measurements. This drift might be caused by small fluctuations of the beam energy, a problem which is still under investigation.

On the same sample, STIM measurements were performed using the µ-slits of the system and an aperture diaphragm with 10 µm in diameter. Fig. 3 shows the count rate of the ions transmitted through the InGaP layer of a linescan over the InGaP/glue interface. The beam diameter (FWHM of the derivative of the fitted function) is 100 ± 10
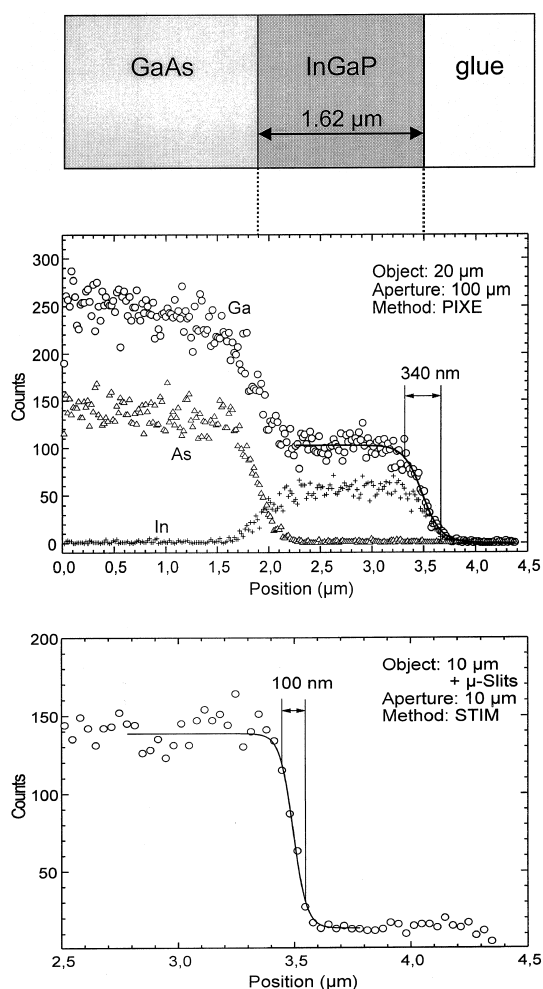
Fig. 3. Scheme of the InGaP/GaAs sample and PIXE and STIM count rates of linescans over the heterostructure with extracted resolution figures.

nm. For longer measurements the resolution deteriorates due to the beam drift mentioned above.

4. Outlook

In the future, a faceted X-ray detector in order to increase the efficiency for µ-PIXE, including PIXE tomography, and new techniques like IBIC and IL will be installed. Further investigations in order to reduce beam drifts are under way.

Acknowledgements

References

[1] D.J.W. Mous, R.G. Haitsma, T. Butz, R.-H. Flagmeyer, D. Lehmann, J. Vogt, Nucl. Instr. and Meth. B 130 (1997) 31.

[2] R. Szymanski, D.N. Jamieson, Nucl. Instr. and Meth. B 130 (1997) 80.

[3] M.B.H. Breese, D.N. Jamieson, P.J.C. King, Materials Analysis with a Nuclear Microprobe, Wiley, New York, 1996.

Solid State Analysis with the New Leipzig High-Energy Ion Nanoprobe

Jürgen Vogt*, **Rolf-Horst Flagmeyer, Johannes Heitmann, Dietmar Lehmann, Tilo Reinert, Steffen Jankuhn, Daniel Spemann, Wolfgang Tröger,** and **Tilman Butz**

Universität Leipzig, Fakultät für Physik und Geowissenschaften, Abt. Nukleare Festkörperphysik, Linnéstr. 5, D-04103 Leipzig

Abstract. The high-energy ion nanoprobe LIPSION at the University of Leipzig has been operational since October 1998. The ultrastable single ended 3.5 MV SINLETRON^{TM} accelerator supplies the H^+ or He^+ ion beam. A magnetic scanning system moves the focused beam across the sample. At present, a resolution of 150 nm in the low current mode and 300 nm at 5 pA could be achieved.

The UHV grade experimental chamber is equipped with electron-, energy dispersive X-ray-, and particle detectors. They can be used simultaneously to analyse the sample by means of PIXE (particle induced X-ray emission), RBS (Rutherford backscattering) and in the case of thin samples STIM (scanning transmission ion microscopy).

A goniometer allows the application of channeling measurements in single crystals in combination with these methods.

The detection limits depend on the elements to be analysed and range from $(1000 \cdots 1)$ µg/g relative and $(1 \cdots 0.01)$ pg absolute. The analysis is nondestructive, but the sample has to be vacuum resistant. Applications of the nanoprobe in the field of semiconductor research, biomedicine, and archaeology will be described.

Key words: Ion beam analysis; ion microprobe; solid state analysis; microanalysis.

Abbreviations: AFM: Atomic force microscopy, CCM: Channeling contrast microscopy, CSTIM: Channeling scanning transmission ion microscopy, ERD: Elastic recoil detection, IBIC: Ion beam induced charge, IBIL: Ion beam induced luminescence, PIXE: Particle induced X-ray emission, RBS: Rutherford backscattering, SEI: Secondary electron imaging, SEM: Secondary electron microscopy, STIM: Scanning transmission ion microscopy, XPS: X-ray photoelectron spectroscopy

High energy ion microprobes have made their way into several disciplines like material science, geosciences, environmental sciences, art and archaeology, bio- and medical sciences, and several others already some years ago [1]. The penetration and depth sensitivity of ions, the element specificity, the quantitation, the imaging and tomographic capabilities, and the versatility of ion microprobes are just a few important advantages of this analytical tool. The future progress depends, at least in several disciplines like semiconductor technology or biomedical applications, on the achievement of ultra-high resolution below the micrometer regime. Therefore, a new dedicated high energy microprobe with true nanoprobe capabilities was designed and installed at the University of Leipzig. This probe named "LIPSION" has been operational since October 1998. The two main parts of LIPSION are a new designed 3.5 MV ion accelerator (SINGLETRON^{TM}, HVEE, High Voltage Engineering Europa B.V.) with a full solid state power supply, an optimized high frequency ion source, and the nanoprobe. Due to the described design the accelerator has a very high energy stability $(\Delta E/E < 10^{-5})$ and beam brightness. The probe itself is equipped with a magnetic quadrupole lens system and an all-purpose measuring chamber (MARC, Microanalytical Research Centre Melbourne). Besides

---

 * To whom correspondence should be addressed

the determination of the resolution figures the probe was successfully applied to the analysis of solid state material, cartilage samples, and archaeological bones.

The Nanoprobe

The nanoprobe laboratory (Fig. 1) was specially designed for the achievement of high spatial resolution and long term stability of the probe operation. One of the key issues for the submicrometer resolution is the minimization of vibrations. The foundations of the accelerator and the nanoprobe are completely separated from each other. Both are build on 5–7 m deep pillars in a vibration absorbing layer of the soil with a heavy steel concrete table on top. Measured vibration amplitudes peak to peak are below $0.3\,\mu m$. Another important parameter is the long term stability of the air conditioning system. We achieve $\pm 2\,K$ over a week and a constant humidity of 55%, stable to better than 5%.

The Singletron^{TM} (HVEE) high energy ion accelerator is designed for very stable operation at terminal voltages from $0.8\,MV$ up to $3.5\,MV$. The ion source supplies H^+- and He^+ beams with a brightness of more than $10\,A\,rad^{-2}\,m^{-2}\,eV^{-1}$ and a current of app. $30\,\mu A$. The long term stability of the ion energy as a quantity of crucial importance for ultra high resolution work is as good as $\pm 20\,eV$ over several hours.

The parts of the nanoprobe itself and the experimental chamber are mounted on a heavy steel girder (Fig. 2) with an additional vibration isolation between the basement and the girder. The probe consists of an object-diaphragm ($300\,\mu m$ to $5\,\mu m$ diameter), an aperture diaphragm with ($300\,\mu m$ to $10\,\mu m$) diameter, a split Russian quadruplet magnetic lens system with a demagnification factor of 100 with very low aberrations, and a scanning coil system.

The vacuum inside the beamline and the measuring chamber of app. $10^{-8}\,mbar$ is provided by means of carbon-free turbopumps and ion getter pumps. During nanoprobe measurements the turbopumps have to be switched off to avoid additional vibrations.

The sample is mounted on a 3-dimensional computer controlled precision stage inside the UHV-
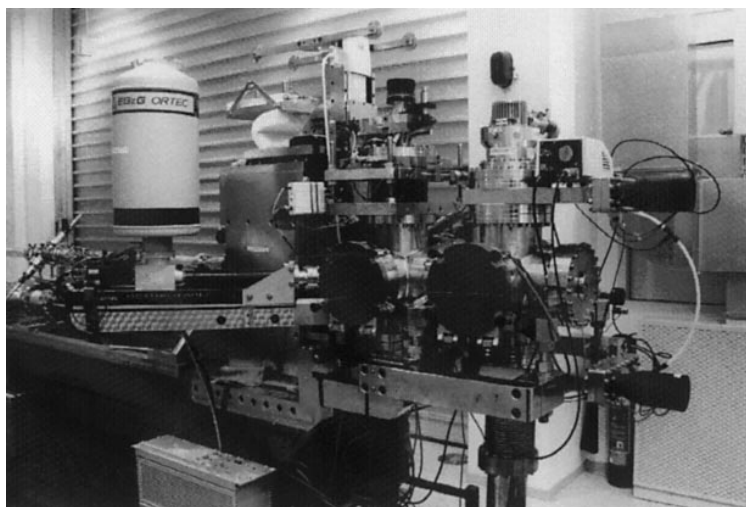
Fig. 1. Nanoprobe facility LIPSION at the University of Leipzig
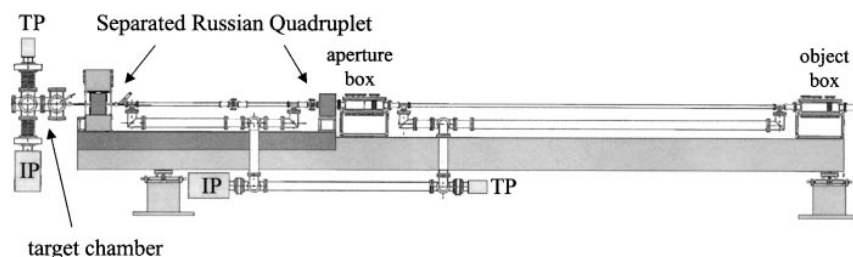
Fig. 2. Schematic of the nanoprobe

Solid State Analysis with the New Leipzig High-Energy Ion Nanoprobe   107

chamber. Samples as big as $(2 \times 2 \times 0.5)$ cm can be analysed. The proper alignment of the sample in the chamber with regard to the position of the ion beam can be carried out using a built-in optical microscope.

The UHV experimental chamber is equipped with a channeltron for the detection of ion induced secondary electrons (SEI), a high purity Ge-detector with an active area of $95\,mm^2$ and an energy resolution of $150\,eV$ at $5.9\,keV$ for PIXE, two charged particle detectors in backward direction (RBS) and one in transmission geometry for STIM.

The data collection system MPSYS (MARC Melbourne) collects and stores complete energy spectra produced by the detectors at each beam position. Four detectors can be run simultaneously. In addition, optional energy windows can be set in the spectra for real-time elemental mapping.

Analytical Methods

There are two main advantages of the high energy ion probe analysis techniques compared to competing methods, like electron microprobe or X-ray microanalysis. First, the high energy ion beam is very stiff, therefore the information volume is well defined (Fig. 3). Second, various reaction channels can be used *simultaneously* for the determination of composition and structure of the sample. Table 1 summarizes
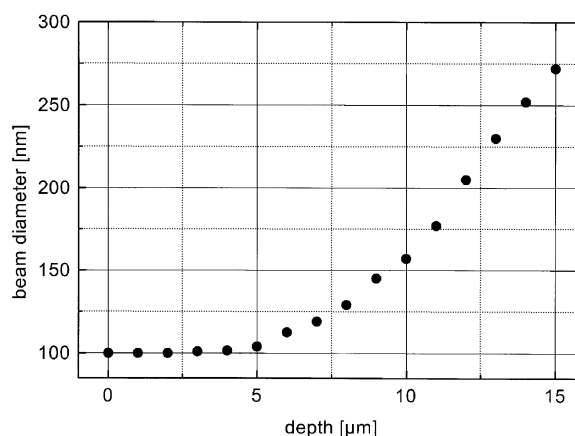
Fig. 3. Beam broadening inside the sample, SRIM96 simulation, $2.25\,MeV\ H^+$ into Si, beam diameter $100\,nm$

the pertinent characteristics and properties of the various methods.

Applications

Intercalation of Ag Into TiS$_2$

Two dimensional layered transition metal dichalcogenides like TiS_2 or TaS_2 are well known for their ability to form intercalation compounds with a large variety of atoms, or even organic molecules [2].

Table 1. Characteristics of the ion beam analytical methods available at LIPSION

| Method	Material property	Information depth ($E_{ion} = 2.5\,MeV$)	Detection limit (µg/g)	Spatial resolution (nm)	Accuracy (%)
PIXE	quantitative elemental distribution, $Z > 11$	$< 15\,µm$ for H^+	$1000 \cdots 0.3$	> 300	5
IBIL	distribution of species	app. $5\,µm$, depending on optical properties of the sample	$100 \cdots 0.5$	> 300	10
RBS	quantitative elemental distribution, $Z > 2$	$5\,µm$ for He^+, $20\,µm$ for H^+	0.5 atomic layers	> 500	3
ERD	distribution of light elements, $Z < 3$	$< 1\,µm$	$10000 \cdots 10$	> 500	3
CCM	distribution of crystal quality	$< 5\,µm$		> 300	
STIM	density distribution	only thin samples $< 30\,µm$ for H^+, $< 10\,µm$ for He^+		> 100	
CSTIM	distribution of crystal quality, imaging of single defects	only thin samples $< 30\,µm$ for H^+, $< 10\,µm$ for He^+		> 100	
IBIC	charge collection efficiency distribution	$< 50\,µm$ for H^+, $< 15\,µm$ for He^+		> 100	
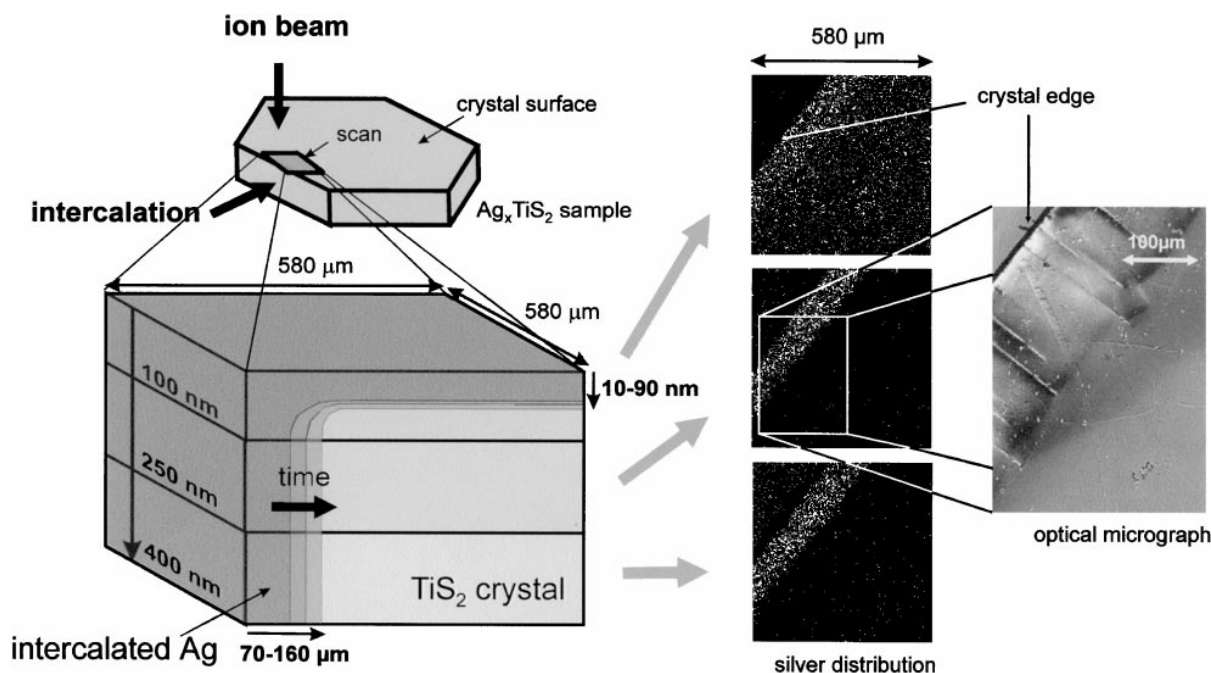
Fig. 4. 3D-distribution of Ag intercalated into TiS_2

Titanium disulfide single crystals consist of stacked layers of TiS_2 sandwiches. The titanium monolayer is covalently bound to the two sulfur layers in the sandwich, where the sandwiches are bound quite weakly to each other via van der Waals forces. The intercalate uses the van der Waals gap between the sandwiches to penetrate into the crystal.

In order to study the intercalation of Ag into this material Ag_xTiS_2 samples were prepared by electrolytic intercalation of a short circuited cell consisting of TiS_2 and silver electrodes in an $0.15\,M$ $AgNO_3$ solution [3]. The intercalation time varied from 10 min to 2.5 h.

The resulting 3-dimensional distribution of Ag was measured by means of RBS with the Leipzig nanoprobe while still at Melbourne for testing. The samples were scanned continuously with an He^+ beam with $4\,\mu m$ diameter at an energy of $2\,MeV$. The scan field has a dimension of 500 pixels × 500 pixels covering an area of $580\,\mu m \times 580\,\mu m$. For each pixel a complete energy spectrum of the backscattered particles was collected. The dose was kept as low as possible to avoid beam damage ($< 3 \cdot 10^{-3}\,nC/\mu m^2$). In this way a set of depth distributions of Ag could be obtained (Fig. 4) from which the 3-dimensional distribution was evaluated. Additional information was gathered using XPS, SEM, and AFM [4].

The RBS data exhibit a sharp intercalation front. Ag was found to be present over the whole investigated area of the crystal, but only to a depth of 100 nm. In deeper layers the intercalation was restricted to the border zone close to the crystal prism edge. The width of this zone increases with the intercalation time. After 10 min and 2.5 h, the intercalation front has moved $70\,\mu m$ and $160\,\mu m$ respectively, laterally from the crystal edge. The measured stoichiometry of the Ag_xTiS_2 changes from the range of $x = (0.38$–$0.42)$ (first stage phase; intercalation into every nth gallery is called "nth stage") in the near surface region to the range of $x = (0.14$–$0.2)$ (second stage phase) in deeper layers. Due to the combination of RBS measurements with techniques like SEM and AFM it was possible to obtain a three dimensional image of the Ag distribution in Ag_xTiS_2 in conjunction with a clear picture of the plastic and partly irreversible deformations of the host material which accompany the intercalation.

Elemental Analysis of Ancient Human Bone

The relationship between biological development, health status, and living conditions of our ancestors is of high interest for the archaeological, anthropological as well as for the medical sciences. The determination of the trace element status and the mineral density of buried bones is one of the key issues for the development of a indicator for the health status of the former population. In order to determine the elemental composition of the bones and to estimate the influence of the burial environment on the elemental content of the skeletons (diagenesis), femoral cross sections of ancient human bones of the Merowingian period (6–8th century AD) were analysed by laterally resolved PIXE.
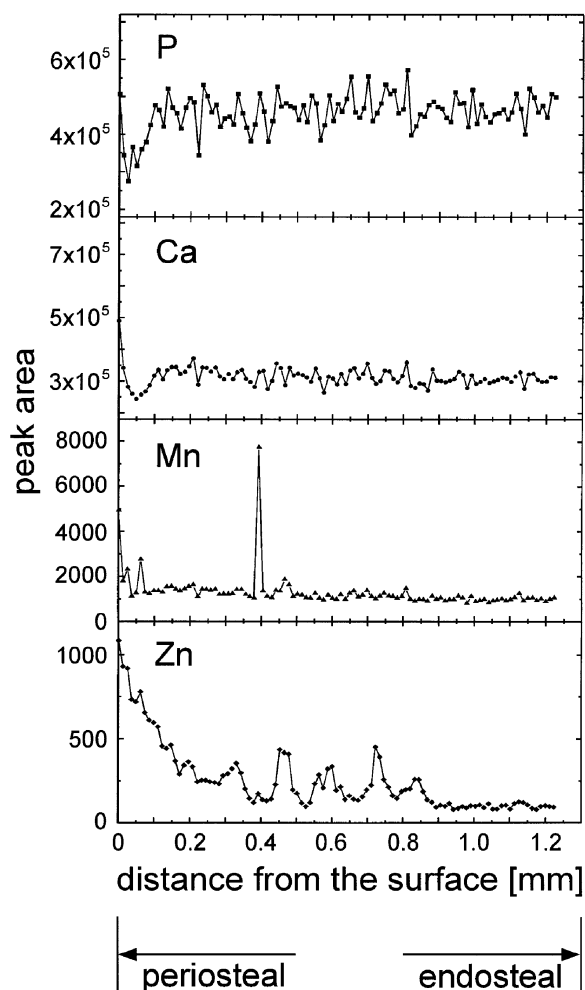
The μPIXE measurements were started at the Rossendorf nuclear microprobe using a 3 MeV proton beam of $(3 \times 3)\,\mu m^2$ at 200 pA. The cross sections (2 mm thickness) cut with a diamond saw, were scanned radially from the outer edge (periost) in the direction to the center of the bone (endost) over a distance of 1.55 mm at maximum, with 128 points for each line scan. The charge per step was 100 pC so that a total charge of 12 nC was collected per point.

A different behaviour of the radial distributions of the main and trace elements like P, Ca, Mn, and Zn was observed due to several biochemical and geochemical processes which act on bone during life and after death, respectively (Fig. 5). In the case of Zn a gradually decreasing concentration from periost to endost with peaks superimposed were observed. A possible explanation for these characteristic profiles is that Zn enrichment in the osteoblasts is superimposed onto a diffusion profile of Zn from the environment into the bone. Apparently, mineral exchange processes play a important role. In addition, the change of the ionoluminescence colour from orange to blue from the surface to the inner part of the bone cross section is a clear evidence for an ion exchange process $Ca^{2+} \rightarrow Mn^{2+}$ in the near surface layer [5]. To confirm this interpretation PIXE maps were recorded with a spatial resolution of 500 nm using the LIPSION nanoprobe at an ion energy of 2.25 MeV. They show a rather inhomogeneous distribution of manganese with a strongly decreasing concentration from the periost to the endost (Fig. 6) in agreement with the change of the luminescence colour.

These results indicate post mortem mineral exchange processes and possible further diagenetic alterations during burial of bone tissue in soil. However, these processes are limited only to the region near the surface (up to a maximum of 2 mm). Therefore, the determination of the content and the
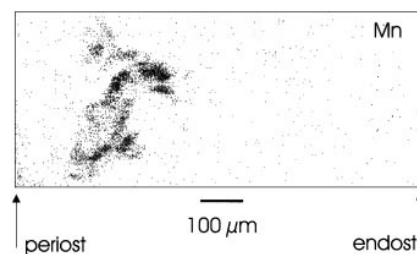
Fig. 5. Elemental distributions of P, Ca, Mn, and Zn obtained by scanning the cross section of the left femoral shaft of a male Merowingian individual

Fig. 6. PIXE-image of the distribution of Mn in the periosteal region of the cross section of the left femoral shaft of a male Merowingian individual

distribution of main and trace elements of the bones in regions free from diagenetic changes are under way.

Scanning Transmission Ion Microscopy on Cartilage Samples

Worldwide, people suffer from a degenerative disease of the joint cartilage, mainly in their hip or knee joints, called arthrosis. The basic mechanism of the initial process is still being discussed. Microscopic NMR-tomography could visualise internal structures and their early arthrotic changes in the cartilage collagenous network [6]. From this a theory was deduced that assumes a network transformation leading to a loss in mechanical stiffness and later on to the destruction of the cartilage itself. Biochemical staining pointed to calcium as a possible initiator or as an involved element. Preliminary experiments

revealed that the elemental distributions within the cartilage, especially that of calcium, compared well with NMR-microscopic pathological zones of early arthrotic changes. This stimulated further measurements and interesting interpretations of the interaction between elemental distribution and the collagenous network itself [7].

The distributions of the elements P, S, Cl, K and Ca in a 30 μm thick cartilage bit-slices were measured with μPIXE using LIPSION. From the same region STIM images were taken which represent the mass density distribution within the cartilage sample (Fig. 7). Four layers differing in mass density are clearly distinguishable, a contrast which does not exist in the case of optical microscopy.

A possible explanation of this structure could be a different ratio between collagen fibrils (forming the network) and the intercollagenous gel-like matrix in the different regions. The collagenous network changes its structure near the articular surface, where the fibrils are tangentially aligned and show a much smaller spacing. In this region a remarkable increase in the Ca and P concentration was found for samples subjected to mechanical load [8]. It is assumed that internal redistributions of Ca- and P-ions take place. Obviously, the elemental distributions are related to the density and structure of the collagenous network. Scanning transmission ion microscopy is a suitable method to visualise this network. Figure 8a shows aligned cartilage cells as an indicator for an aligned network which becomes visible at higher magnification (Fig. 8b).

In the future, a 3D-picture of the network will be obtained by stepwise rotating the sample over 180° and recording the two-dimensional map (2D projection) for each setting, in analogy to computer tomography (CT).
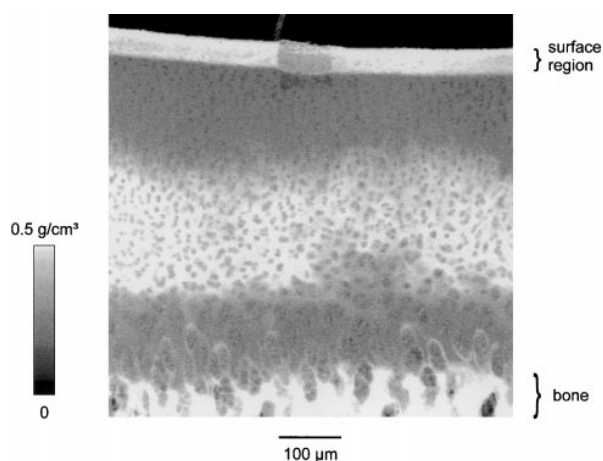
Fig. 7. $650 \times 650\,\mu m^2$ density image of a 30 μm thick, freeze dried cartilage section (pig femoral condyle), measured with STIM using protons at an energy of 2250 keV
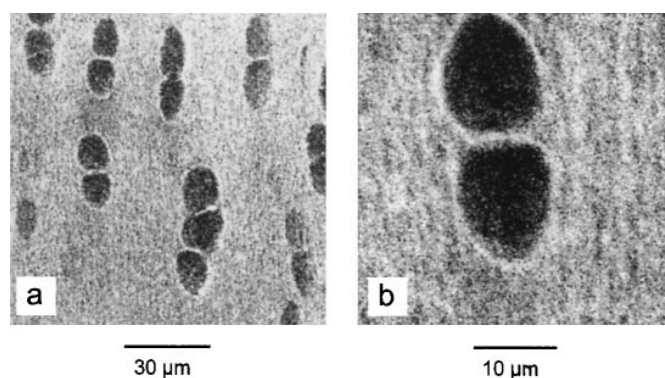

Fig. 8. (a) $110 \times 110\,\mu m^2$ STIM image of the cartilage region with aligned collagenous fibrils surrounding cartilage cells (low density area in the near surface region in Fig. 7). (b) STIM image with higher magnifications; collagenous fibrils around the two cells become visible

Conclusion

After a few month of operation, the LIPSION nanoprobe proved to be a very versatile and useful microanalytical tool for various solid samples, e.g. crystalline material as well as biological tissue, with the potential to open up new applications in the field solid state nanoanalysis.

Outlook

Furthermore, we will work on the fine tuning of the accelerator and the nanoprobe in order to reach 100 nm spatial resolution in the high current mode, suitable for RBS and PIXE, and < 50 nm in the low current transmission mode (STIM, CSTIM, STIMT).

References

[1] M. B. H. Breese, D. N. Jamieson, P. J. C. King, *Materials Analysis Using a Microprobe*. J. Wiley & Sons, New York, 1996.

[2] G. V. S. Rao, M. W. Shafer, *Intercalated Layered Materials*, D. Reichel Publishing Company, 1979.

[3] G. R. Carlow, *PhD Thesis*, Simon Fraser University, 1992.

[4] J. Heitmann, J. McCallum, W. Tröger, T. Butz, *Nucl. Instr. Meth. Phys. Res. B* (in press).

[5] D. Spemann, St. Jankuhn, J. Vogt, T. Butz, *Nucl. Instr. Meth. Phys. Res. B* (in press).

[6] W. Gründer, M. Wagner, A. Werner, *Mag. Reson. Med.* **1998**, *39*, 376.

[7] T. Reinert, T. Butz, R.-H. Flagmeyer, St. Jankuhn, W. Gründer, M. Kanowski, M. Wagner, D. Grambole, F. Herrmann, *Nucl. Instr. Meth. Phys. Res.* **1998**, *B136-138*, 936.

[8] U. Reibetanz, *Diploma Thesis*, Universität Leipzig.

Novel test sample for submicron ion-beam analysis

D. Spemann [a],[*],[1], T. Reinert [a], J. Vogt [a], T. Butz [a], K. Otte [b], K. Zimmer [b]

[a] *Nukleare Festkörperphysik, Universität Leipzig, Linnéstr. 5, D-04103 Leipzig, Germany*
[b] *Abt. Ionenstrahltechnik, Institut für Oberflächenmodifizierung e.V., Permoserstr. 15, D-04318 Leipzig, Germany*

Abstract

In order to determine the beam spot size, scan size and scanning properties of a nuclear microprobe system a novel test sample with nanometer structures for the use in submicron ion-beam analysis has been developed by the University of Leipzig and the Institute for Surface Modification (IOM). The test sample provides horizontally and vertically arranged periodic structures, which range from 4 µm to 150 nm in size. The structures have been produced in SiO_2 and Ag for topographic and elemental contrast, respectively, using electron beam lithography and various etching techniques. The test sample was investigated with a scanning electron microscope (SEM) and the high-energy ion nanoprobe LIPSION. Due to the excellent definition of the edge profiles, the ion beam spot size can be directly derived from a line scan across an edge even in the submicron regime. The structures on the test sample also allow the determination of scan sizes of a few microns. Furthermore, a special nanostructure is proposed which makes it possible to image the beam current density within a submicron beam spot directly. © 2001 Elsevier Science B.V. All rights reserved.

PACS: 06.30.Bp; 07.78.+s; 41.85.Ew; 85.40.H
Keywords: Test sample; Electron beam lithography; Submicron beam spot sizes; Properties of scanning system; Beam profile

1. Introduction

In order to fully exploit the analytical capabilities of a nuclear microprobe the accurate determination of beam spot size and scanning properties is of vital importance. Most of the standard samples used so far for this purpose (e.g.

EBEAM test sample, Chessy test sample and TEM Cu-grids) are not suitable for different reasons (material combination, design of the structures, accuracy of the edge profiles).

In recent years Wätjen and co-workers [1] developed a CRM, the first standard sample, which is especially designed for the use in nuclear microprobes. The structures provided on this sample are very suitable for beam spot sizes larger than 1–2 µm. However, this CRM does not allow to determine scan sizes of a few microns and the halo or "skirt" of beam spots in the submicron regime, which are already in application [2,3].

---

[*] Corresponding author. Tel.: +49-341-97-32706; fax: +49-341-97-32497.
E-mail address: spemann@physik.uni-leipzig.de (D. Spemann).
[1] http://www.uni-leipzig.de/~nfp

Therefore, a novel test sample has been developed by the University of Leipzig and the Institute for Surface Modification (IOM) which is especially designed for the use in ion beam analysis with submicron lateral resolution.

2. Test sample

2.1. Experimental setup

As substrate material for the test sample we used commercially available silicon wafers with a thermal oxide layer with a thickness of 800 nm. On one half of the sample chip (part 1) a 15 nm chromium layer was sputter deposited in order to avoid charge accumulation during electron beam lithography (EBL). This side is used for the fabrication of structures in SiO_2, whereas on the other half of the chip (part 2) a layer of 350 nm silver was additionally sputter deposited for the fabrication of structures with an elemental contrast.

For the EBL we utilized a JEOL JSM-6600 scanning electron microscope (SEM) which was modified for EBL with an Elphy system from RAITH GmbH. The 950 k molecular weight poly-methylmethacrylate (PMMA) resist from Allresist GmbH was spin-coated on the sample with a thickness of about 500 nm and baked at a temperature of 180°C prior to the writing process. Due to the different substrate materials as well as the variable structure sizes we applied different writing dosages of approximately 150–320 $\mu C/cm^2$ at an electron beam current of about 170 pA during EBL.

The EBL mask structures have been transferred into the silicon dioxide or silver by reactive ion beam etching (RIBE) with CHF_3 and argon sputtering. The etching was performed in a non-commercial IBE system using a Kaufman-type graphite lining ion source (ISQ150, Roth & Rau GmbH) with a beam diameter of 15 cm. A water-cooled and rotating substrate stage was used to maintain a constant sample temperature. The beam energy and the current density were set to 700 eV and 200 $\mu A/cm^2$, respectively.

2.2. Structure layout

Each test sample chip with a size of about 1×1 cm^2 consists of two parts with the same structure layout. Edges, dots as well as vertical and hori-
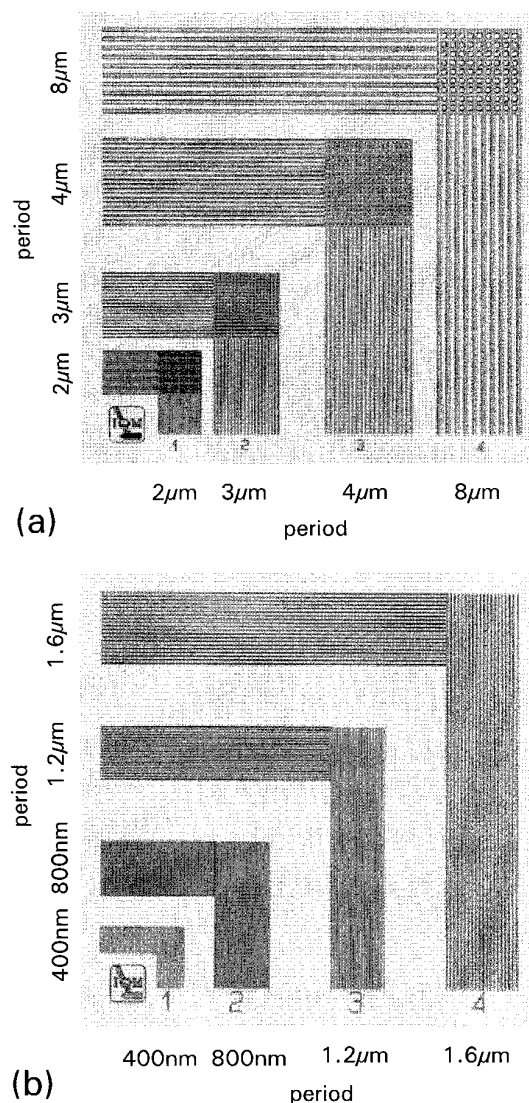
Fig. 1. Optical micrograph showing the horizontal and vertical gratings with periods as indicated in the figure: (a) structure 1 (size: 400 μm × 400 μm); (b) structure 2 (size: 200 μm × 200 μm).

Table 1
Summary of the size of the different gratings of the test sample[a]

Structure	Area	Period	Space	Line width
1	1	2 μm	1.38 μm	0.63 μm
	2	3 μm	1.8 μm	1.2 μm
	3	4 μm	2.2 μm	1.8 μm
	4	8 μm	4.1 μm	3.8 μm
2	1	400 nm	250 nm	150 nm
	2	800 nm	550 nm	250 nm
	3	1200 nm	850 nm	350 nm
	4	1600 nm	1000 nm	600 nm

[a] Note that all values have a relative uncertainty of about 5%.

zontal gratings have been chosen for the current test layout. Structure 1 with a size of about 400×400 μm^2 (see Fig. 1(a)) consists of gratings with a period ranging from 8 to 2 μm, whereas structure 2 with a size of about 200×200 μm^2 (see Fig. 1(b)) consists of gratings with a period ranging from 1600 to 400 nm (Table 1 summarizes the different gratings and their sizes). In structure 1 the gratings overlap in the right upper corner, resulting in rectangular dots with a size similar to the gratings (Fig. 2).

2.3. Results

After EBL, the PMMA-mask has been transferred into the SiO$_2$ by CHF$_3$-RIBE on part 1. This results in almost vertical side walls of the gratings without trenching and edge slopes smaller than 30 nm per 400 nm height are achieved (Fig. 3). In Fig. 4, an SEM micrograph of a cleaved grating with the smallest period of 400 nm is shown. The high aspect ratio as well as the almost vertical side walls (angle of better than 85°) can be seen clearly.
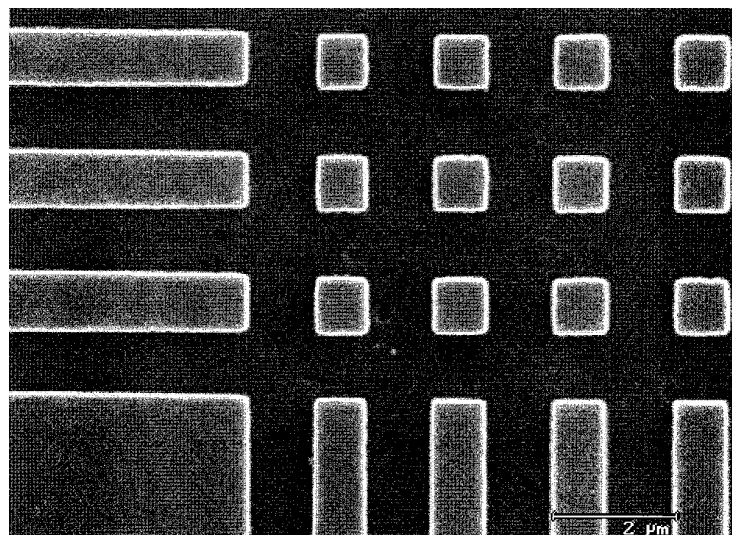
Fig. 2. Top view SEM micrograph of the gratings with a period of 2 μm. The rectangular dots formed in the region, where the horizontal and the vertical gratings overlap, are clearly visible.
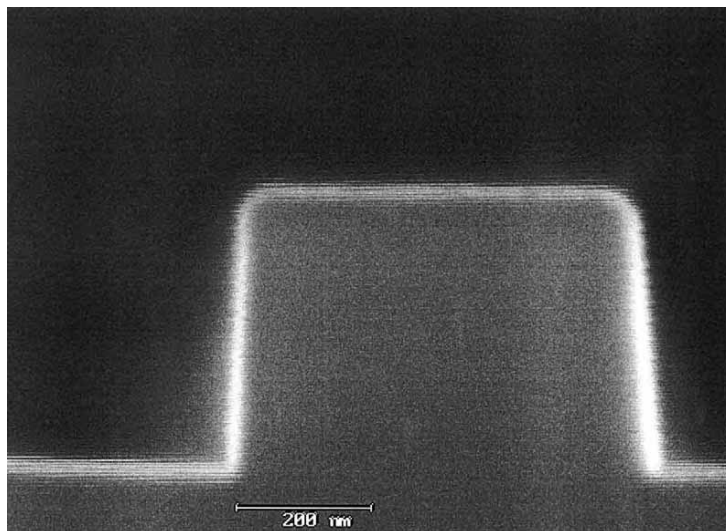
Fig. 3. SEM micrograph of a cleaved grating with a period of 1.6 μm. The edge slope smaller than 30 nm per 400 nm height is clearly visible.
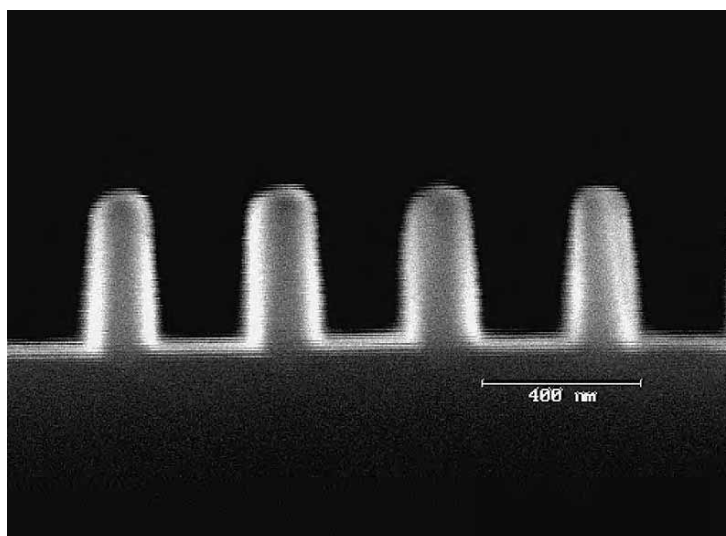
Fig. 4. SEM micrograph of a cleaved grating with a period of 400 nm. Note the high aspect ratio as well as the almost vertical side walls (angle of better than 85°).

The resist was removed by wet chemistry and O_2 plasma etching. The Cr had been removed by wet etching.

On part 2 of the sample the mask was transferred into silver by a combination of CHF_3 and argon etching. The usage of CHF_3 for the silver

sputtering is justified in order to stabilize the PMMA and, hence, to yield a higher etch selectivity. The etching time was adjusted to remove the silver in the unmasked regions completely. Due to the re-deposition of silver during sputter etching the side walls of these gratings have a slightly higher roughness compared to the structure in SiO_2.

3. Test measurements with the ion nanoprobe LIPSION

All test measurements were performed with a 2 MeV proton beam.

3.1. Scanning properties

The periodic structures provided on the test sample allow the determination of the scan size, step width and linearity of the scanning system for scan sizes from several hundreds down to a few microns. Especially the rectangular dots on structure 1 (Fig. 2) proved to be very suitable for this purpose. Due to the high yield of Ag-L-

X-rays or secondary electrons the accurate determination of the scan size takes only a few minutes.

3.2. Beam spot size

In order to determine the beam spot size we performed line scans in the *x*- and *y*-directions across the Ag-stripes of the 8 μm grating using PIXE. The collected data were fitted with an error function using NUFIT7.0 (see Fig. 5). Due to the excellent definition of the edge profiles (edge slope + irregularities < 50 nm), the beam spot size can be directly derived from the fitted data even in the submicron regime without deconvolution.

For an object and aperture size of 100 μm and a beam current of 120 pA the beam spot size was determined to be 770 and 740 nm in the *x*- and *y*-directions, respectively. Under identical experimental conditions a line scan in the *y*-direction was performed for comparison using a 2000 mesh Cu grid, which yielded a beam spot size of 920 nm, clearly underestimating the beam quality.
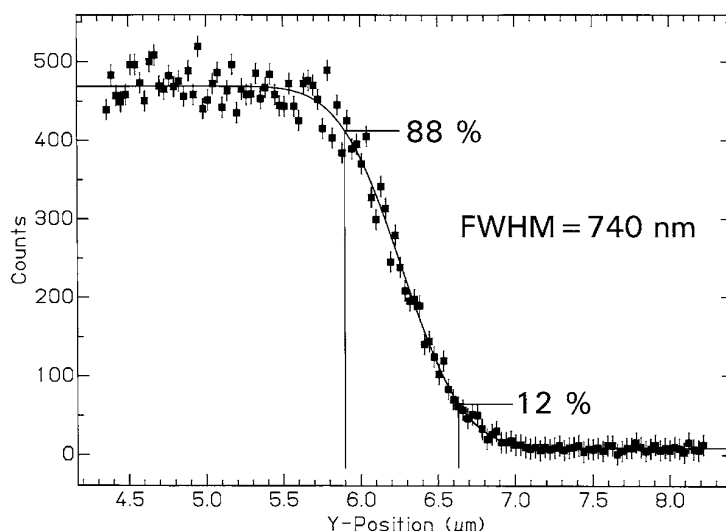
Fig. 5. PIXE line scan in the *y*-direction (object and aperture size: 100 μm, beam current 120 pA). The data were fitted with an error function yielding a beam spot size of 740 nm.
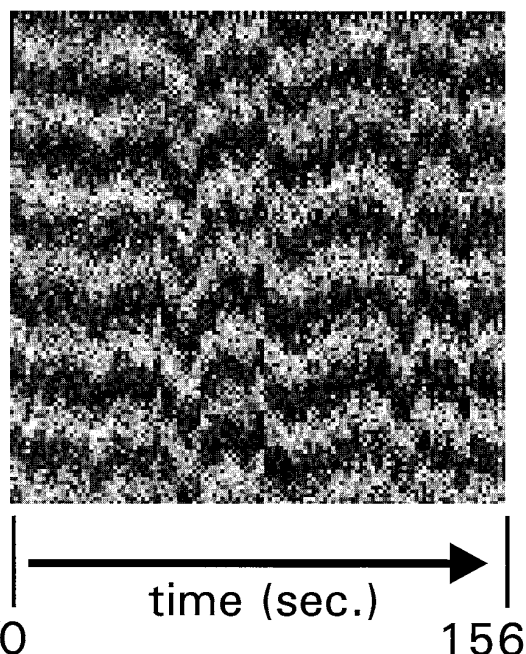
Fig. 6. Secondary electron intensity map from a raster scan in the *y*-direction across the horizontal grating with a period of 400 nm (scan size: 2.5 μm × 2.5 μm). The beam spot fluctuations in the *y*-direction during data acquisition are clearly visible.

3.3. Beam spot fluctuations

We probed fluctuations of the beam spot position using a raster scan in the *y*-direction across the horizontal grating with a period of 400 nm. Since a raster scan provides a "timescale" in the map (see Fig. 6), the beam spot fluctuations in one direction become visible as image distortions of the original structure. As can be seen in Fig. 6 the beam spot fluctuates by approximately 150 nm in the *y*-direction, most likely caused by slowly varying external magnetic fields. A complete shielding of the external magnetic fields could possibly improve the lateral image resolution by a factor of two.

4. Conclusions

A novel test sample with nanometer structures for high-resolution ion beam analysis has been
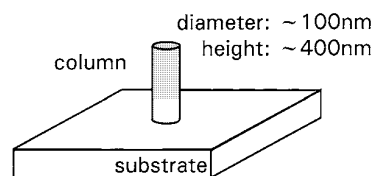
Fig. 7. Schematic drawing of a column providing elemental contrast.

developed by the University of Leipzig and the IOM. It provides periodic structures, which range from 4 μm down to 150 nm in size.

The test sample proved to be very useful for the determination of beam spot sizes in the submicron regime, of scan sizes down to a few microns and for performance tests of the high-energy ion nanoprobe LIPSION.

5. Outlook

The determination of beam profiles and beam halos in the submicron regime is hardly possible with existing standard samples and CRMs. Therefore we propose a new design for a submicron structure which allows the direct imaging of beam profiles and beam halos. The column, shown schematically in Fig. 7, acts as a probe for the beam current density within a beam spot. The elemental map obtained from a scan of the beam spot over the column gives a direct quantitative two-dimensional image of the beam current density distribution of the beam spot.

These structures are currently under development.

References

[1] U. Wätjen, C. Dücsö, A. Tajani, F. Munnik, F. Lechtenberg, Nucl. Instr. and Meth. B 161–163 (2000) 359.

[2] F. Watt, T. Osipowicz, T.F. Choo, I. Orlic, S.M. Tang, Nucl. Instr. and Meth. B 136–138 (1998) 313.

[3] T. Butz, R.-H. Flagmeyer, J. Heitmann, D.N. Jamieson, G.J.F. Legge, D. Lehmann, U. Reibetanz, T. Reinert, A. Saint, D. Spemann, R. Szymanski, W. Tröger, J. Vogt, J. Zhu, Nucl. Instr. and Meth. B 161–163 (2000) 323.

Ion Microscopy and Tomography

T. Butz, D. Lehmann, T. Reinert, D. Spemann and J. Vogt

Universität Leipzig, Fakultät für Physik und Geowissenschaften
Linnéstr. 5, 04103 Leipzig, Germany

The use of light ions for microscopy and tomography is illustrated by a variety of recent applications in materials and life sciences at the Leipzig high-energy ion-nanoprobe LIPSION with a short comparison to other microscopic techniques. The versatility of ion techniques is exemplified by Rutherford backscattering spectrometry maps of thin films of solar cell materials, particle induced X-ray emission maps of manganese in ancient human bones, particle induced X-ray emission on single aerosol particles with μm size, and scanning transmission ion microscopy and tomography on pigs knee cartilage. Finally, the design of a single ion single living cell bombardment facility is sketched for studies of the cellular response and microdosimetry.

PACS numbers: 41.75.Ak, 72.20.My, 29.30.Kv

1. Introduction

The resolution of conventional optical microscopy is limited by the photon wavelength around 1 μm. Photons do not penetrate into the sample unless it happens to be transparent. The contrast is provided by the wavelength-dependence of the absorbance/reflectivity. There is "chemical blindness", i.e. the chemical constitution is not obtained by optical microscopy. A natural extension is the use of X-rays, preferably obtained from synchrotron sources with a tunable wavelength. Such X-ray microscopes with resolutions in the order of 100 nm became feasible through the recent progress in X-ray optic devices. The penetration of X-rays is good, the generally poor contrast due to absorption can be outweighted by tremendous accuracy and, above all, by comparing images below and above absorption edges. In this way, the "chemical blindness" is overcome at the expense of sequential imaging at various wavelength. In principle, a full near edge and extended X-ray absorption fine structure (NEXAFS, EXAFS) spectrum could be recorded at each pixel thus allowing "chemical speciation". Drawbacks thus far are the large experimental effort and the lack of tunable X-ray lenses.

Using massive charged particles like electrons overcomes several of these difficulties. The optical elements in electron microscopes are very advanced and rely on electromagnetic interactions of charged particles in vacuum. At sufficiently high energy the de Broglie wavelength is short enough to allow for atomic resolution. High energy electrons do penetrate into the sample, but their lateral straggling is severe and ultrathin samples are required for ultrahigh resolution. Thus, tomography is not really feasible with electrons. The excitation of characteristic X-rays provides chemical sensitivity — simultaneously for practically all elements! A disadvantage is the large Bremsstrahlungs background which impairs the detection limits. The use of even heavier particles like protons provides good penetration, small lateral straggling compared to electrons, and chemical sensitivity with very low detection limits due to the low Bremsstrahlungs background. These are the main reasons to develop ion microscopy and tomography despite the fact that the generation of MeV proton beams is slightly more expensive than the generation of MeV electron beams, true also for ion optical devices, and despite the fact that beam diameters below 1 μm are difficult to achieve. The world record for the smallest 2 MeV proton beam is at 40 nm diameter held by the Leipzig high-energy ion-nanoprobe LIPSION [1], still far above atomic resolution. However, it is the versatility of the ion beam techniques which renders ion microscopy and tomography an invaluable tool.

2. Ion beam techniques, microscopy, and tomography

Rather than to give an introduction to all possible ion beam techniques the reader is referred to the following books: *Materials Analysis using a Nuclear Microprobe* by Breese et al. [2], *Applications of Nuclear Microprobes in the Life Sciences* by Llabador and Moretto [3], and *Particle Induced X-Ray Emission Spectroscopy (PIXE)* by Johansson et al. [4]. For the present purpose it suffices to illustrate and discuss the most important techniques shown in Fig. 1 with particular emphasis on scanned ion beams in order to produce images as shown in Fig. 2.

RBS: Rutherford backscattering spectrometry relies on the elastic scattering of light ions like protons or alpha particles from target atoms. The ions lose energy due to elastic collisions during their track into the sample and on the way out. The energy loss is measured and depends on the mass density of the target and on kinematics. Depth sensitivity is obtained via the stopping power of the target material. RBS maps are ideally suited for the investigation of the composition and homogeneity of the thickness of thin films.

ERDA: elastic recoil detection analysis relies on the detection of matrix atoms recoiling after ion collisions rather than detecting backscattered projectiles like in RBS. Thus using $\mathrm{d}E/\mathrm{d}x$ and E-detectors a simultaneous multielement analysis is possible. The special case of protons as projectiles and protons (hydrogen) in the target as ejectiles offers the advantage of coincidence detection of both particles under 90 degrees, i.e. with very low background.
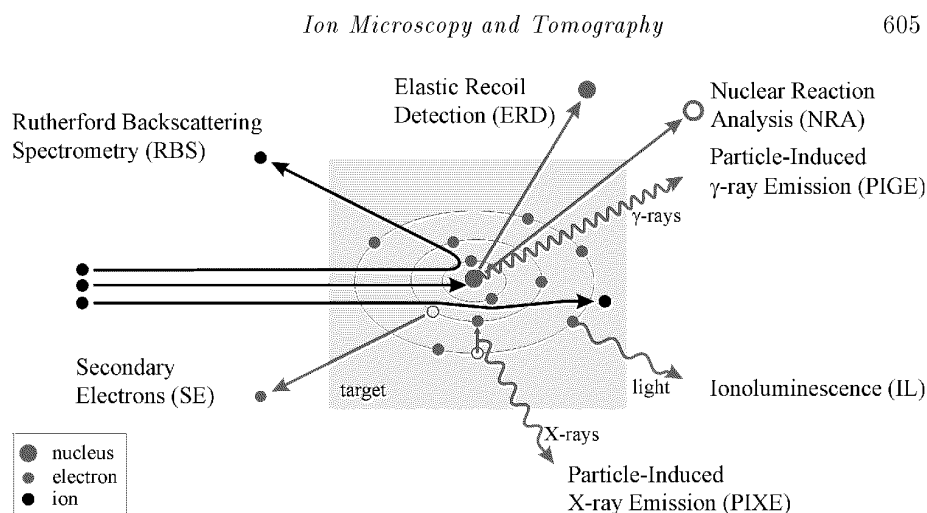
Fig. 1.   Survey over common ion beam techniques showing projectile, target atom (nucleus and electrons), ejectiles, and radiation.
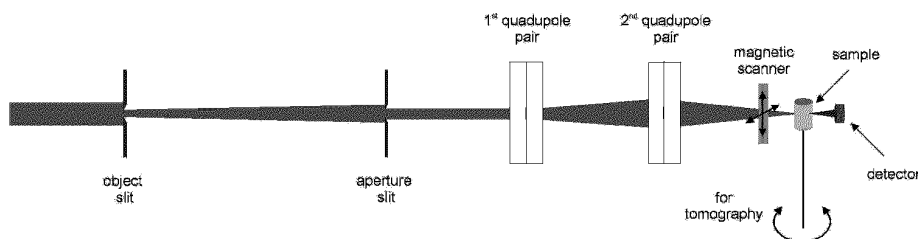
Fig. 2.   Principle of ion microscopy and tomography.

PIXE: particle induced X-ray emission relies on the measurement of characteristic X-rays excited by particle bombardment of atoms. A simultaneous multielement analysis is possible which is essentially standard-free. Detection limits in the 0.5 μg/g range are possible. PIXE-maps are an indispensible tool for the investigation of lateral inhomogeneities of stoichiometries. Unfortunately, the depth resolution is poor and — even worse — the information depth is energy dependent due to the absorption of soft X-rays in the target. Therefore, a combination of RBS, scanning transmission ion microscopy (STIM) and PIXE is often the strategy of choice.

PIGE and NRA: particle induced gamma emission and nuclear reaction analysis rely on the observation of characteristic γ-rays and particles, respectively, emitted from unstable nuclei or ejectiles produced in nuclear reactions. These techniques are particularly useful for threshold or narrow resonance reactions addressing a specific reaction at a time. Isotope specific images are obtained.

STIM: scanning transmission ion microscopy relies on the measurement of the energy of ions transmitted through the sample. Contrary to all other techniques

discussed here there are no reaction cross-sections involved in this techniques and every single particle can be detected with nearly 100% efficiency. Thus 5–7 particles per pixel are usually sufficient to obtain good quality images. Mass-density projections are generated in this way. If the sample is rotated in front of the scanned beam, a series of projections is obtained from which the 3-dimensional image can be reconstructed. A standard algorithm is the filtered Radon-backprojection.

IL: ionoluminescence is related to the well-known cathodoluminescence. With modern ultrasensitive wavelength-sensitive detection devices light emitted under ion bombardment can be used to detect trace elements in specific chemical compounds. However, quantitative analysis is difficult because there are many — often unknown — mechanisms which activate or quench light emission and spectral bands are often wide and overlapping.

SEI: secondary electron imaging relies on the detection of secondary electrons ejected under ion bombardment. The yield depends on the material and on the surface properties. Morphological images are obtained easily but are not always easy to interpret.

Summing up, there are two categories of ion beam techniques: "high-current" techniques like RBS, PIXE, PIGE, IL, SEI with typical currents in the range of 10–100 pA where radiation damage, particularly for biological samples, is an issue to be considered; "low-current" techniques like STIM or tomography with typical currents of the order of a few fA (or a countrate in the detector of several kHz for singly charged ions).

An important fact to mention is that the size of the beam spot in the limit of a small convergence angle is proportional to the square root of the spread in the beam energy and the chromatic aberration coefficient of the lens system and to the fourth root of the emittance [5]. Whereas the first two quantities can be optimized in the accelerator and lens designs, there is less freedom in optimizing the latter. The emittance is proportional to the beam current divided by the brightness. Since the reduced brightness, i.e. the brightness divided by the ion energy, is limited by the ion source, the only way to achieve ultra-high resolution is by reducing the beam current drastically.

The Leipzig high-energy ion-nanoprobe LIPSION ("lipsia" is the latin — and italian — word for linden tree where the name Leipzig came from, and "ion" is self-explanatory) was designed to achieve ultra-high resolution far below that of conventional optical microscopes, an indispensible requisite for keeping pace with the rapidly developing X-ray microscopes. A 3.5 MV ultra-stable SINGLETRON by high voltage electrical engineering (HVEE) with an RF ion source for protons and alphas is coupled to a Melbourne nuclear microprobe with a split Russian quadruplet with a demagnification in x and y of 130. The ripple is below 30 V_{pp} at 2.25 MV, the voltage and analysing magnet stability are better than 10^{-5} and great care was taken to reduce mechanical vibrations as much as possible. Up to now we have achieved about 300 nm lateral resolution for PIXE and about 80 nm
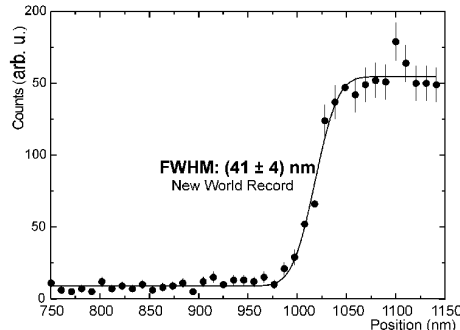
Fig. 3. Scan of ion beam over atomically sharp InGaP/GaAs semiconductor edge in STIM-mode showing beam diameter of 40 nm.

for STIM. In fact, the beam diameter is 40 nm only, as measured by a line scan over an atomically sharp semiconductor edge (see Fig. 3). At present, quasi-stationary magnetic stray fields deteriorate the resolution. We hope to achieve STIM images with a resolution better than 40 nm using an active compensation of the stray fields in the near future.

3. Examples

In the following section a few typical examples of recent activities at LIPSION are given to illustrate the power of ion microscopy and tomography. This is a rather narrow view and the reader is referred to the review books [2–4] for a broad overview.

3.1. Thin films of $Zn_{2-2x}Cu_xIn_xS_2$

Thin films of $Zn_{2-2x}Cu_xIn_xS_2$, a promising solar cell material, were produced on various substrates by pulsed laser deposition (PLD). The following fundamental questions arise: (i) does the target stoichiometry translate to the thin film and, if so, how is the homogeneity? (ii) is the film thickness homogeneous? (iii) what is the morphology (grain size, texture etc.)? (iv) what are the laterally resolved electrical properties? The last question can be answered efficiently by ion beam induced charge collection (IBIC) on contacted films, preferably also in a time-resolved mode [6]. An IBIC-facility is presently under construction at LIPSION. The morphology is usually studied by X-ray diffraction and high resolution electron microscopy (HREM). To answer the first two questions RBS and PIXE are the methods of choice. In Fig. 4 (top left) a 41 μm $\times$ 41 μm 2 MeV alpha-RBS-map is shown for a thin film with a nominal thickness of about 200 nm. Obviously, the map looks rather inhomogeneous. This could be either due to inhomogeneities in the stoichiometry or due to a variable film thickness. On the right, the "broad

608 *T. Butz et al.*
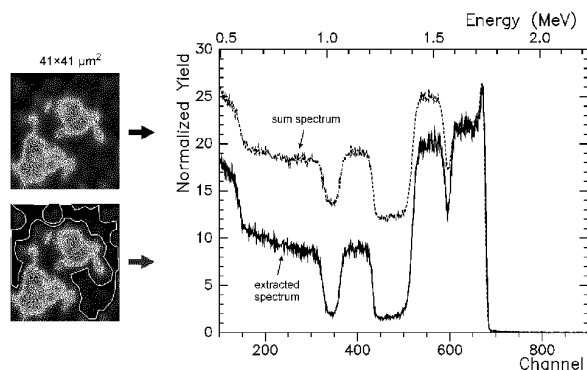
Fig. 4. Alpha-RBS-map (left top) of a thin film of $Zn_{2-2x}Cu_xIn_xS_2$ showing a rather inhomogeneous pattern; right: RBS spectrum of this area, called "sum spectrum" (dashed) and the area selected as shown in the left bottom map (solid).

field" RBS-spectrum is shown which is calculated from the map as the "sum spectrum". This alone would be rather difficult to interpret: the individual layers of In and Cu/Zn (which cannot be separated) are clearly visible (according to Z from right to left) but there is substantial intensity in between the In-region and the Cu/Zn-region where there should be none. The same holds true for the gap between the Cu/Zn-region and the S-onset. It is now possible — like in a jigsaw puzzle — to cut out regions which look relatively homogeneous (see Fig. 4 left bottom) and display the RBS-spectrum of this area alone. This results in a much improved spectrum from which the thickness of this area can be derived accurately to be 230 nm. From PIXE-maps, not shown here, we concluded that the stoichiometry of this area and that of the left-over "islands" is about the same. Thus the "islands" are indeed "rocks" of μm dimensions which very likely were sputtered as a whole by the pulsed laser deposition (PLD) process. This clearly points to an inadequate target preparation process. Needless to say that this example does not represent the present state of the art of producing PLD-films but was chosen for illustrative purposes only.

3.2. Trace elements in ancient human bone

The determination of main and trace elements in ancient human bone serves as a sort of diary for anthropologists from which information on eating habits and diseases can be derived. However, postmortem diagenetic alterations may corrupt this "diary" and it is of utmost importance to learn to what extent ions have been leached out of the bone or incorporated into the bone by mineral exchange processes or microbial influences in the burial ground. Spatially resolved IL-data on samples from a Merowingian population near Frankfurt/Main, Germany, showed that there is an intense orange luminescence in the periostal regions of the ancient bone which fades out after a few mm and turns over into a blue

luminescence, like that observed for recent bones throughout the sample [7]. The suspicion was that Mn-ions are incorporated into hydroxylapatite and we therefore took 84 μm × 84 μm maps of a region close to a pore in the bone sample. Figure 5
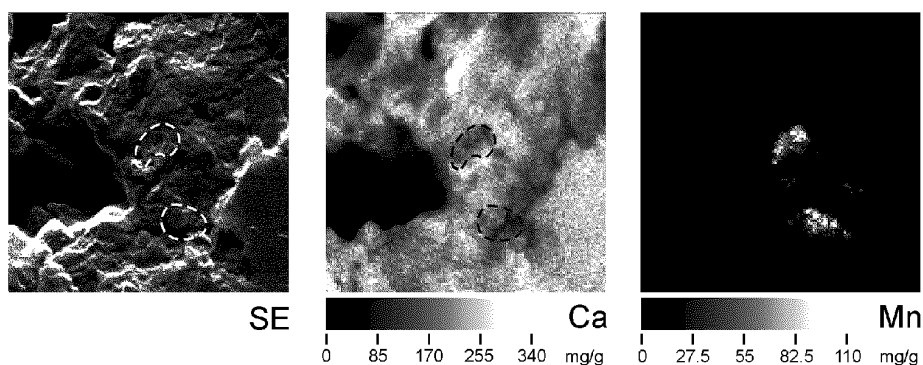

Fig. 5.   From left to right: SE-map, Ca-map, Mn-map of a sample of ancient human bone.

(left) shows an SE-map which closely resembles the Ca-map (middle) and gives an idea of the morphology. The Mn-map (right) shows two pronounced spots surrounded by clouds with unusually high Mn-concentration. However, if integrated over large areas the slight increase in the average Mn-concentration might have been overlooked with less sensitive methods than IL. At present we cannot decide whether Mn was incorporated via mineral exchange through pores or whether it is a result of the remnants of microbe colonies. In any case, the Mn-rich zone should not be considered a "virgin diary". Correlations between several trace elements indicate that in fact this outermost zone is certainly contaminated by various elements and should not be considered useful for further interpretations.

3.3. Single aerosol particles

The analysis of the composition of aerosol particles is usually carried out collecting a large amount of particles in a compactor and determining the average composition. This is rather unsatisfactory if the sources of pollution are rather diverse. In order to trace back the source of pollution the identification of individual aerosol particles — often as small as 1 μm and below — is necessary. This can be achieved by μ-PIXE. In Fig. 6 a PIXE-map (8 μm × 8 μm) of two aerosol particles from Shanghai is shown together with their spectra from which — using a fingerprint "library" established by a neural network — the type of source can be identified unambiguously: the left particle comes from a blast furnace, the right one from a cement factory [8].
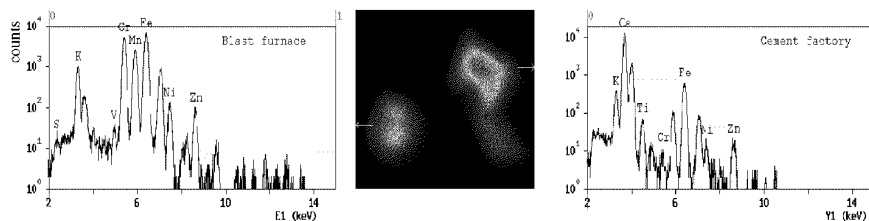
610   *T. Butz et al.*

Fig. 6.   PIXE-map of two aerosol particles of different provenance in the Shanghai area.
The insets show characteristic PIXE-spectra used as fingerprints for identification.

3.4. Cartilage

The degradation of cartilage in joints lead to a very common and painful
disease: arthrosis. At present we have no good means for an early diagnosis nor
is there a good therapy. The metabolism in cartilage proceeds via kneading (like
a sponge) since there are no vessels. Hence, the knowledge of the internal ar-
chitecture of cartilage is of crucial importance to understand its functioning and
malfunctioning. Cartilage is by no means a homogeneous substance. Under an
optical microscope cartilage cells, called chondrocytes, with typical dimensions of
10 μm are easily visible. In some areas they appear as isogonic pairs with a char-
acteristic orientation. This immediately calls for the hypothesis that the collagen
fibres are aligned in the same way. This is in fact borne out by electron microscopy
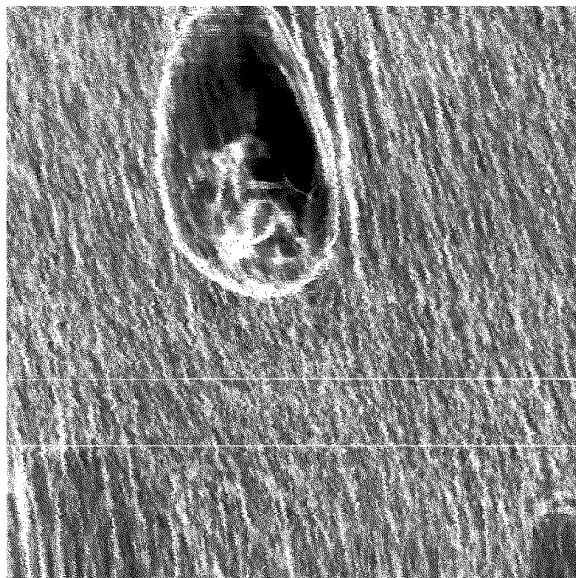
Fig. 7.   STIM-image (40 μm × 40 μm) of a thin slice of cartilage from a pigs knee
showing a chondrocyte and the well aligned collagen fibres (white).

on freeze fractured samples and was deduced as well from angle resolved nuclear magnetic resonance microscopy [9]. These collagen fibres are too small to be observable by optical microscopy, but are easily seen in ion-microscopy. Figure 7 shows a 40 μm × 40 μm STIM image of a sample from a pigs knee cartilage with a lateral resolution of 80 nm. The sample was freeze dried. The chondrocyte and intracellular structures — difficult to interpret due to the freeze drying — are clearly visible, as are the highly oriented collagen fibres [10]. It turns out that the type and degree of orientation as well as the micro-architecture of the collagen fibres varies drastically over various regions of the tibial and femoral cartilage. PIXE-maps, not shown here, exhibit μm-spots of high Ca-concentration which are not paralleled by P-spots. Their origin is not yet clear but these might be nuclei for solid particle formation which mechanically deteriorate the cartilage upon kneading. Further studies on cartilage with and without mechanical load will elucidate the transport of nutrients and metabolic products.

Finally, first ion tomographic images were obtained on a cartilage sample of dimensions 10 μm × 28 μm × 30 μm. Projections were collected every 0.5 degree for 180 degrees. Since the sample had no resemblance to a cylinder (like that shown in Fig. 2) the sinograms had to be corrected substantially using the relatively sharp contours of the chondrocyte as a sort of "fiducial marker". Figure 8 shows the reconstructed image which — unfortunately — cannot rotate on a printed paper. The big advantage of ion tomography compared to electron microscopy is that images of "thick" samples (say 30 μm tissue) can be obtained in a non-destructive manner. We hope to improve the resolution in our tomography such that individual
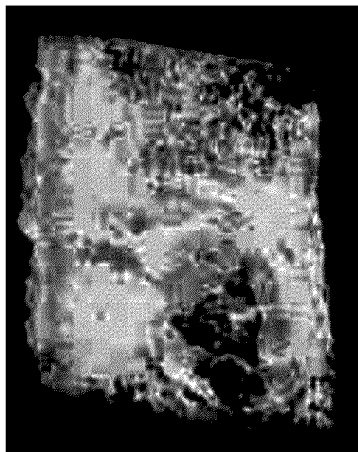

Fig. 8.   Perspective view of a cartilage slice (28 μm × 10 μm × 30 μm) obtained by ion tomography. Grey represents high density material (large energy loss), light grey represents medium density material. The low density material was omitted for the sake of clarity.

collagen fibres or eventually collagen tubes are directly visible. Tomography with an external beam would be highly desirable because the freeze drying procedure could be avoided and experiments in which the pressure on cartilage samples can be cycled would become feasible.

4. Outlook: single ion bombardment of single living cells

When counting individual particles like in STIM, when talking about external beams, and when dealing with biological material the question of targeted bombardment of a single living cell by an exactly counted number of particles comes up naturally. A single alpha particle with a few MeV traversing a cell nucleus can produce a measurable damage. A hot topic is the so-called bystander effect: a cell is hit and some of the bystanding cells respond as if they were hit, too. Questions of microdosimetry can be addressed with completely new dimensions. Consequences for radiotherapy are foreseeable. Up to now, collimated external ion beams are in use with roughly 1 μm lateral accuracy. Focused external ion beams with much better resolution and single living cell bombardment facilities are presently under construction at various places in the world [11]. A sketch of the facility at LIPSION is shown in Fig. 9. Cells are cultivated on a mini-Petri dish and the coordinates of the nuclei are recorded in a cell-observer. These dishes are then brought to the irradiation platform and mounted upright. Cells which adhere sufficiently to the mylar bottom of the dish retain their positions for a couple of minutes, as has been tested earlier. A fiducial marker on the mini-Petri dish — not
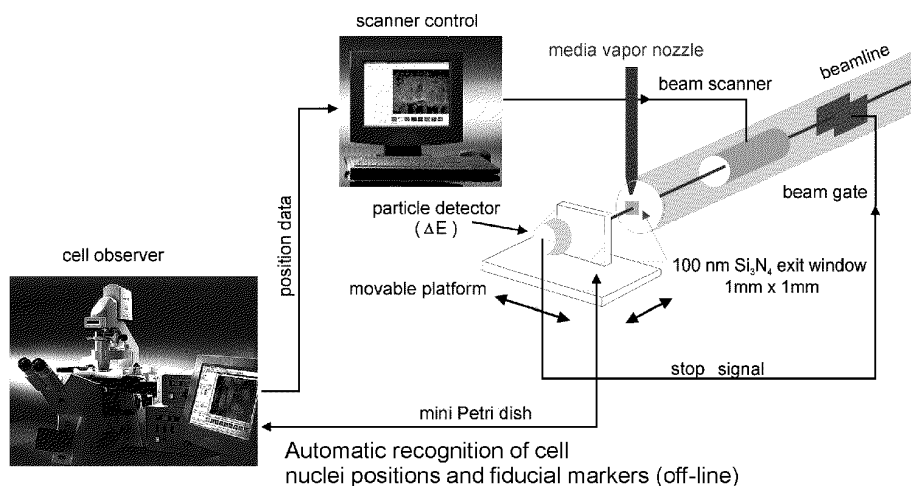

Fig. 9.   Sketch of the single ion single living particle bombardment facility at LIPSION (under construction).

in contact with the media — helps to precisely position the dish via STIM. The coordinates of the cell nuclei are transferred to the scanner and a single (or more) selected cell nucleus (or cytoplasm) is bombarded with a preselected number of particles. A particle detector behind the cells triggers the beamgate upstream and registers the energy lost in the exit window, the mylar bottom of the mini-Petri dish, the cell, and the media. After bombardment we analyze the cell culture for micronucleus formation and apoptosis off-line.

5. Acknowledgment

References

[1] D. Spemann, T. Reinert, J. Vogt, D. Dobrev, T. Butz, to be presented at the 15th Int. Conf. on Ion Beam Analysis, Cairns 2001, Australia.

[2] M.B.H. Breese, D.N. Jamieson, Ph.J.C. King, *Materials Analysis Using a Nuclear Microprobe*, Wiley, New York 1996.

[3] Y. Llabador, Ph. Moretto, *Applications of Nuclear Microprobes in the Life Sciences*, World Sci., Singapore 1998.

[4] *Particle-Induced X-Ray Emission Spectroscopy (PIXE)*, Eds. S.A.E. Johansson, J.L. Campbell, K.G. Malmqvist, Wiley, New York 1995.

[5] G.J.F. Legge, J.S. Laird, L.M. Mason, A. Saint, M. Cholewa, D.N. Jamieson, *Nucl. Instrum. Methods Phys. Res. B* **77,** 153 (1993).

[6] B.L. Doyle, G. Vizkelethy, K.M. Horn, D.S. Walsh, and P.E. Dodd, in: *Proc. 16th Int. Conf. on the Application of Accelerators in Research and Industry, Denton (USA) 2000*, CP567 AIP Press, 2001.

[7] D. Spemann, St. Jankuhn, J. Vogt, T. Butz, *Nucl. Instrum. Methods Phys. Res. B* **161-163,** 867 (2000).

[8] P. Guo, J. Wang, X. Li, J. Zhu, T. Reinert, J. Heitmann, D. Spemann, J. Vogt, R.-H. Flagmeyer, T. Butz, *Appl. Spectrosc.* **54,** 807 (2000).

[9] W. Gründer, M. Kanowski, M. Wagner, A. Werner, *Magn. Reson. Med.* **43,** 884 (2000).

[10] T. Reinert, U. Reibetanz, J. Vogt, T. Butz, A. Werner, W. Gründer, *Nucl. Instrum. Methods Phys. Res. B*, in press.

[11] 5th *International Workshop on Microbeam Probes of Cellular Radiation Response, Stresa (Italy) 2001, Radiation Protection and Dosimetry*, in press.

A novel ultra-short scanning nuclear microprobe: Design and preliminary results

S. Lebed [a,*], T. Butz [b], J. Vogt [b], T. Reinert [b], D. Spemann [b], J. Heitmann [b], Z. Stachura [c], J. Lekki [c], A. Potempa [c], J. Styczen [c], B. Sulkio-Cleff [d]

[a] *Institute of Applied Physics (IAP), UR-244030 Sumy, Ukraine*
[b] *University of Leipzig, Faculty of Physics and Geo Sciences, D-04103 Leipzig, Germany*
[c] *Institute of Nuclear Physics (INP), PL-31342 Cracow, Poland*
[d] *Institute of Nuclear Physics, University of Münster, D-48149 Münster, Germany*

Abstract

The paper describes an optimized scanning nuclear microprobe (MP) with a new ultra-short (total length of 1.85 m) probe forming system based on a divided Russian quadruplet (DRQ) of magnetic quadrupole lenses. Modern electrostatic accelerators have a comparatively high beam brightness of about 10–25 $pA/\mu m^2/mrad^2/MeV$. This allows the MP proposed to provide a high lateral resolution even with large (1%) parasitic (sextupole and octupole) pole tip field components in all lenses. The features of the design permit the MP operation in the high current and low current modes with a short working distance and inexpensive quadrupole lenses. A new quadrupole doublet design has been developed for the MP. In the present work the calculated features of the new MP are compared with preliminary experimental results obtained with a similar system (total length of 2.3 m) at the INP in Cracow. The new MP is promising for studies of solids or biological samples with high resolutions (0.08–2 μm) in both modes under ambient conditions. A vertical version of the ultra-short MP can be very useful for single ion bombardments of living cells. © 2001 Elsevier Science B.V. All rights reserved.

PACS: 2590; 2930; 2970; 2990
Keywords: Scanning nuclear microprobe; Probe forming system; Quadrupole lens; Beam brightness

1. Introduction

At present, scanning nuclear microprobes (MP) are operated in two modes [1]: the high current

* Corresponding author. Tel.: 380-542-327087; fax: 4812-371881.
E-mail address: lebed@alf.ifj.edu.pl (S. Lebed).

mode involving analysis by PIXE/RBS with a beam spot diameter (MP resolution) of 0.3–5 μm at a beam current of 100–1000 pA and the low current mode by STIM/IBIC/SEU with spatial resolution down to 30 nm at a current of fA or by using single ions.

The traditional probe forming system (PFS) is a rather long system with a total length $l > 4$ m [2,3]. As has been calculated [4–6], a short version

of optimized PFS ($l \sim 2.3$ m) based on a divided Russian quadruplet (DRQ) of magnetic quadrupole lenses with moderate demagnification ($|D_{x,y}| \cong 17$) allows operation with submicron resolutions. A horizontal MP based on a Van de Graaff (HVEC type K-3000) accelerator with this PFS was designed, constructed, installed and tested in the Institute of Nuclear Physics (INP), Cracow, Poland [7]. The MP based on the short PFS has some important advantages. It permits a considerable reduction in the limitation of the MP resolution due to extremely low sensitivity of the PFS to intrinsic and main parasitic lens aberrations [6]. The short PFS is less sensitive to mechanical vibrations. This system is especially promising for the next generation of a vertical MP with external beam for biomedical applications.

A novel post-lens beam scanning system [5,7,8] gives an additional advantage for the short MP. This short (in Z plane) ferrite-core magnetic system allows probe operation with a very short working distance (down to 8 cm). This system is well suited for studies of biological samples (cells, tissue, etc.) with high frequency beam scanning in the short MP with external beam. The focused beam could be extracted to air through a thin (0.1–10 μm) window [9–12].

The goal of the ion-optical design for the MP with novel ultra-short PFS (<2 m) is high resolution (0.08–1.5 μm) in both modes even with large sextupole and octupole components (1%) included in all lenses. The main factors that are critical for this goal to be attained are: optimized PFS configuration and high beam brightness.

In the present paper a new adjustable quadrupole doublet design is proposed for this MP.

2. Beam line optics and design features

The experimental hall of the LIPSION nanoprobe facility at the University of Leipzig has a small space of about 2 m length only for the installation of the MP with external beam downstream a switching (30°) magnet. In this case the short PFS based on a DRQ is promis-
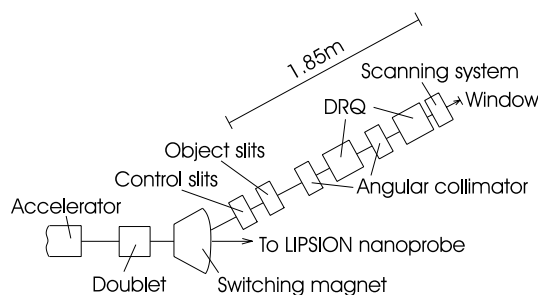

Fig. 1. Layout of the new Leipzig MP unit.

ing. The layout of the proposed unit is shown in Fig. 1.

2.1. Beam transport system

The ion-optical optimization of the beam transport system is performed for the short Leipzig MP beam line. The MP is based on a 3.5 MeV single ended accelerator (Singletron™) [13,14]. The beam envelopes along the 3 MeV proton path between the beam crossovers located outside the accelerator and the entrance to the PFS are shown in Fig. 2. The doublet of magnetic quadrupole lenses and a switching magnet serve to transport the beam crossovers (in X and Y planes) to accelerator control slits with a minimum contribution of the intrinsic aberrations to the degradation
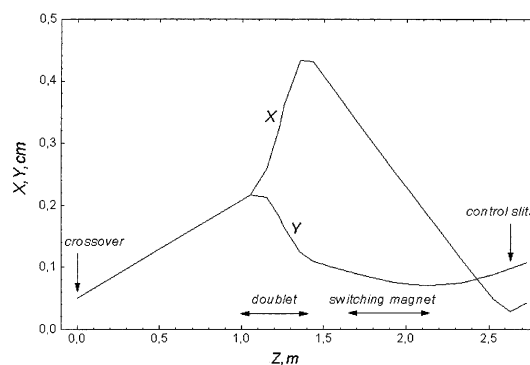

Fig. 2. Beam envelopes along the 3 MeV proton path between the beam crossover located outside the Singletron accelerator and the entrance to the PFS.

of the beam brightness [15]. At the same time the switching magnet is used for the beam analysis. The physical parameters of the doublet (dimensions and lens excitations) were determined as a result of the calculation. The following parameters were given: total length of the beam transport system (2.6 m), entrance beam emittance and physical parameters of the switching magnet.

2.2. Leipzig PFS and comparison with other systems

A lot of contemporary MPs based on magnetic quadrupole lenses employ the following PFSs: classic Russian quadruplet, long DRQ, Oxford triplet and novel quintuplet (see Table 1 and [2,3,14,16]). These systems have a rather large length (up to 10 m) with a small working distance ($8 < g < 30$ cm). The PFS's produce a high demagnification (up to 110) but at the cost of very high spherical aberration coefficients and strong sensitivity to parasitic sextupole and octupole field components in the lenses (Table 1). Therefore these lenses should be fabricated with a very low value of the pole tip field contamination (0.05–0.3%) due to main parasitic aberrations [17,18]. As a result the production of such high performance MP lenses is fairly expensive.

The Singletron and HVEC accelerators have high brightness RF ion sources (HVEE) and a perfect ion-optics design. So they can provide a paraxial proton beam of high brightness up to 25 pA/μm^2/mrad^2/MeV [15]. This allows a short DRQ system to operate with a small object slit ($\leqslant$20 μm) in the high current mode.

The microprobes based on DRQ systems are simulated using programs: SFS [19], PRAM [3] and TRANSPORT [20]. A uniform beam brightness and rectangular apertures have been assumed in all cases. The calculation of the beam spot size is based on tracing of 10,000 particles spread randomly and uniformly over the entrance phase-space determined by the object and divergence slits. S_{12} and S_{23} are the separation between the first and the second, the second and the third lenses, respectively; $S_{34} = S_{12}$ for the quadruplet system. The quintuplet system has five lenses with

the spacing between the first three lenses given by S_{12} and S_{23} [16].

The beam envelopes along a proton path for the high current mode in the short Leipzig system are shown in Fig. 3. The greatest deviation of the microbeam occurs in the third lens. This is the reason for the maximum effect of the aberrations in this lens leading to beam spot broadening in the X plane (Table 1, Fig. 3). The beam divergence in this plane is decreased by an angular collimator to reduce broadening.

The optimized short PFS is not very sensitive to the beam energy stability. As can be seen in Table 1, both short systems have fairly small chromatic aberration terms. This provides small (<5%) beam spot broadening at the target in the high current mode even with as low as 0.1% energy stability typical of the HVEC accelerator.

A figure of merit $Q = D_x D_y / (\langle x/\Theta^3\rangle\langle y/\phi^3\rangle)^{1/3}$ can be used to describe the maximum beam current for a given spot size assuming that main spherical aberration terms are dominant [16]. Table 1 shows that a novel quintuplet and short DRQ systems provide a high figure of merit Q. It should be noted that the parameter Q does not include other aberration terms. The quintuplet system, despite its high Q, has large spherical aberration cross-terms and parasitic terms. Similarly, other long systems listed in Table 1 also suffer from these terms leading to the beam spot broadening. Extreme insensitivity to the above-mentioned aberrations is the main advantage of the short DRQ system. It permits the proposed MP with an ultra-short (1.85 m) PFS to operate with a fairly high resolution of 1.5–2 μm in the high current mode (Table 2) as well as with the spatial resolution as high as 80 nm in the low current mode (Table 3) even with large sextupole and octupole components (1%) included in all lenses. This opens the way for utilisation of cost-effective lenses as focusing elements for the MP. It should be mentioned that all long PFS's with high demagnification listed in Table 1 cannot be operated with lenses of such quality. On the other hand, the short DRQ system equipped with high performance lenses (with parasitic components $\leqslant$0.3%) can provide MP resolution of ~1 μm in

Table 1
Comparison of ion-optical parameters of the short Leipzig PFS with five existing probe forming systems

Systems	Short DRQ (Leipzig)	Short DRQ (Cracow)	Long DRQ (Leipzig)	Classic RQ (MARC) [16]	Triplet (Oxford) [16]	Quintuplet (W80-56) [16]
Coupling	+A − B	+A − B	+A − B	+A − B	−A + A − B	+A + A
	+B − A	+B − A	+B − A	+B − A		−A − A + B
Overall system length (m)	1.85	2.3	9.27	8.3	7.4	4.7
S_{12} (m)	0.033	0.033	0.033	0.03	0.05	0.45
S_{23} (m)	0.535	0.64	2.45	0.03	0.05	0.60
Working distance (mm)	110	150	300	155	152	85
Quadrupole length (mm)	80	64	64	27.7	108	110
Lens bore diameter (mm)	12.7	12.7	12.7	12	15	14
Maximum pole-tip field, 3 MeV protons (T)	0.278	0.323	0.2	−0.227	0.218	0.211
Demagnification						
D_x	14	17.6	110	−25	92	−65
D_y	14	17.6	110	−25	−26	69
Rotational aberration[a] (μm/mrad^2)						
$\langle x/\phi\rho_1\rangle,\ \langle y/\Theta\rho_1\rangle$	2	2	6	−26	7; −29	—
$\langle x/\phi\rho_2\rangle,\ \langle y/\Theta\rho_2\rangle$	1	0.1	−3	63	14; −61	—
$\langle x/\phi\rho_3\rangle,\ \langle y/\Theta\rho_3\rangle$	7	13	188	−51	−20; 90	—
$\langle x/\phi\rho_4\rangle,\ \langle y/\Theta\rho_4\rangle$	−10	−15	−191	14	—	—
Chromatic aberration (μm/mrad/%)						
$\langle x/\Theta\delta\rangle$	−252	−281	−1861	130	−343	1195
$\langle y/\phi\delta\rangle$	−56	−68	−542	173	873	−98
Spherical aberration (μm/mrad^3)						
$\langle x/\Theta^3\rangle$	77	161	64270	−112	426	−2933
$\langle x/\Theta\phi^2\rangle$	5.6	26	30530	−370	207	−226
$\langle y/\Theta^2\phi\rangle$	5.6	26	30530	−370	−743	212
$\langle y/\phi^3\rangle$	2	6	4900	−262	−2197	43
Figure of merit Q	36	33	18	20	24	89
Parasitic aberration sensitivity						
Largest sextupole term (μm/mrad^2/%)	$\langle x/\Theta^2 s\rangle$ −491	$\langle x/\Theta^2 s\rangle$ −665	$\langle x/\Theta^2 s\rangle$ −41350	$\langle y/\Theta\phi s\rangle$ −827	$\langle y/\Theta\phi s\rangle$ 1733	$\langle x/\Theta^2 s\rangle$ −7411
Largest octupole term (μm/mrad^3/%)	$\langle x/\Theta^3 o\rangle$ −512	$\langle x/\Theta^3 o\rangle$ −821	$\langle x/\Theta^3 o\rangle$ 410000	$\langle y/\phi^3 o\rangle$ −1530	$\langle y/\Theta^3 o\rangle$ 18986	$\langle x/\Theta^3 o\rangle$ 48000

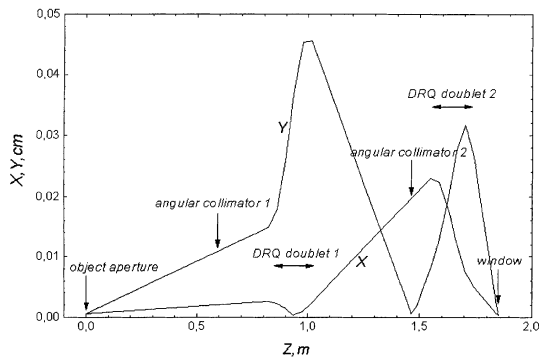[a] Experimentally verified: Classic RQ (MARC) [3]; Triplet (Oxford) [2].

Fig. 3. 3 MeV proton beam envelopes along the short Leipzig PFS in the high current mode.

the high current mode as does a long system (Table 2). Note that a standard circular aperture can be used as an object slit in the short system too.

2.3. Quadrupole doublet design

The requirements for the design and manufacture of magnetic quadrupole lenses for modern MPs imply either a high manufacture precision (3–6 μm) of a single-piece lens [21] or a high adjustment accuracy for separate components of an adjustable lens [22]. This allows a considerable increase in the MP resolution limited because of high sensitivity to intrinsic and parasitic lens aberrations (see Table 1). At the same time optimized short MP's are almost insensitive to these aberrations permitting a three times lower manufacture

precision and a significantly simpler focusing element design. Fig. 4 shows a layout of the element proposed (adjustable quadrupole doublet). The design has important adjustable parts that allow the pole tips (1) and yokes (2) to be shifted and fixed in X and Y planes by means of screws (3). The required distances between the pole tips in these planes are set by standard stencils (4). In this case the pole tip field contamination due to the above parasitic components can be reduced. The grid shadow method [23] could be used for the control and reduction of this contribution in each lens by fine doublet adjustment. In addition the neighbouring (in Z plane) pole tip pairs (1) and yokes (2) have to be manufactured from one-piece commercial iron or a special alloy. All parts are bolted together in the X, Y, Z planes as a doublet. These details of the doublet design make it possible to minimize first-order parasitic lens aberrations (translational, tilt and rotation misalignments [2]) in a single doublet. The translational and tilt misalignments can be eliminated effectively by relatively simple lens adjustments in the PFS [2]. The elimination of the rotational misalignment between lenses in PFS is a much more difficult procedure, especially for the long system with high demagnification. Long PFS's (as compared to short systems) have high sensitivity to rotational aberrations (Table 1). Nevertheless both doublets in the short system have to be mounted on special 3-D mechanical devices for their precise alignment (singly and pairwise) by the proton beam spot on the quartz target. In this way it is possible to eliminate practically the first- and second-order parasitic aberrations in the PFS that

Table 2
Calculated probe resolutions with DRQ systems in the high current mode (100 pA beam spots)

Systems	Short DRQ (Leipzig)	Short DRQ (Cracow)	Long DRQ (Leipzig)
Beam brightness (pA/μm^2/mrad^2/MeV)	18	10	18
Beam energy spread (%)	0.002	0.1	0.002
Object size (μm $\times$ μm)	10 $\times$ 10	20 $\times$ 20	100 $\times$ 100
Divergence (mrad $\times$ mrad)	0.06 $\times$ 0.35	0.063 $\times$ 0.134	0.012 $\times$ 0.016
Beam spot size (μm) with 0% parasitic aberrations in all lenses	1.0	1.2	1.1
Beam spot size (μm) with 0.3% parasitic aberrations in all lenses	1.2	1.4	2.9
Beam spot size (μm) with 1% parasitic aberrations in all lenses	1.5	1.9	Not applicable

Table 3
Calculated probe resolutions with the short Leipzig DRQ system in the low current mode with 1% parasitic aberrations included in all lenses

Object slits $d_{1x} \times d_{1y}$ (µm)	5×5	1×1
Collimating slits $d_{2x} \times d_{2y}$ (µm)	5×5	5×5
Beam size at the window $d_x \times d_y$ (nm)	380×360	80×70
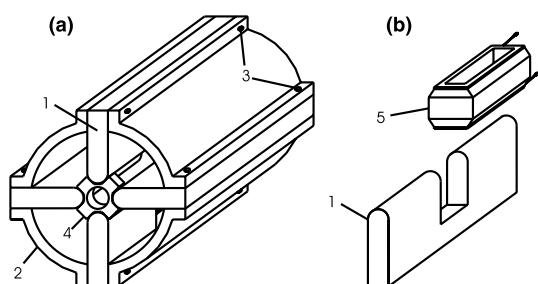
Fig. 4. (a) Layout of the doublet (quadrupole windings are removed). 1: pole tips, 2: yoke, 3: screws, 4: stencil; (b) 1: pole tip, 5: winding.

contribute to the beam spot broadening at the target.

3. Performance tests

3.1. New quadrupole doublet

The doublet (Fig. 4) was manufactured in the INP workshop. It was tested on the Cracow MP beam line as a focusing element of the PFS with a total length of 4 m and a working distance of 0.92 m. A beam spot size of 0.08×0.3 mm^2 has been achieved for a 0.8 MeV proton beam at the quartz plate behind the 0.5 mm object diaphragm. This result is in good agreement with the calculated value for the demagnification $D_x = -5.4$ and $D_y = -1.55$. The tests demonstrated good beam focusing and transport properties of the doublet.

3.2. Short Cracow PFS

In a performance test of the short Cracow PFS a resolution of 3.3 µm has been achieved for a 2.4

MeV proton beam at the copper grid placed behind the 50 µm object diaphragm and the 200 µm angular collimator [7]. This result illustrates that the PFS operates with the demagnification $D \geqslant 15$ which is in good agreement with the calculated value of $D = 17.6$ (Table 1 and [4–6]).

4. Conclusions and outlook

The authors propose a novel optimized MP with an ultra-short ($l = 1.85$ m) PFS based on a DRQ of magnetic quadrupole lenses. The system makes it possible to improve the MP resolution limited due to the intrinsic and main parasitic lens aberrations. The PFS (with modest $D_x = D_y = 14$) could provide sufficiently high MP resolutions in the high current mode (1–1.5 µm) as well as in the low current mode (down to 80 nm) even with fairly large parasitic (1%) lens aberrations. A new quadrupole doublet design has been developed for the MP. This focusing element is simpler and cheaper to manufacture than lenses for traditional long systems. The preliminary experimental tests demonstrated that the new doublet is promising as a beam transport system and a focusing element for the optimized short nuclear microprobe. It will be used to optimize the Cracow MP beam transport system. It is intended to employ a similar doublet for the beam transport in the short Leipzig MP. We are going to produce the next two doublets of improved design as focusing elements for the short Leipzig PFS in the near future.

In a performance test of the short Cracow PFS a demagnification of $D \geqslant 15$ was achieved. This experimental result is in good agreement with numerical calculations.

The new scanning nuclear microprobe has a great promise for studies of solid-state or biological samples with high resolutions in both modes under ambient conditions. It is planned to adapt the MP in Cracow to work with an external beam. We have started feasibility studies for the installation of an ultra-short horizontal MP with an external beam for biomedical applications at the LIPSION laboratory in Leipzig. A vertical version of the MP can be very useful for single ion bombardment of living cells.

Acknowledgements

References

[1] G. Legge, Nucl. Instr. and Meth. B 130 (1997) 9.

[2] G. Grime, F. Watt, Beam Optics of Quadrupole Probe-Forming Systems, Adam Hilger, Bristol, Great Britain, 1984.

[3] M. Breese, D. Jamieson, P. King, Materials Analysis Using a Nuclear Microprobe, Wiley, New York, 1996.

[4] V. Brazhnik, S. Lebed, W. Kwiatek et al., Nucl. Instr. and Meth. B 130 (1997) 104.

[5] S. Lebed, M. Cholewa, Z. Cioch et al., Nucl. Instr. and Meth. B 158 (1999) 44.

[6] S. Lebed, Nucl. Instr. and Meth. B 152 (1999) 145.

[7] S. Lebed, Z. Stachura, Z. Cioch et al., Nucl. Instr. and Meth. B 181 (2001) 95.

[8] V. Khomenko, S. Lebed, S. Mordik, Nucl. Instr. and Meth. B 130 (1997) 86.

[9] T. Calligaro, J. Dran, H. Hamon et al., Nucl. Instr. and Meth. B 136–138 (1998) 339.

[10] A. Kinomura, Y. Horino, Y. Mokuno et al., Int. J. PIXE 9 (3–4) (1999) 143.

[11] A. Sugimoto, K. Ishii, S. Matsuyama et al., Int. J. PIXE 9 (3–4) (1999) 151.

[12] T. Kamiya, T. Sakai, M. Oikawa et al., Int. J. PIXE 9 (3–4) (1999) 217.

[13] D. Mous, R. Haitsma, T. Butz et al., Nucl. Instr. and Meth. B 130 (1997) 31.

[14] T. Butz, R. Flagmeyer, J. Heitmann et al., Nucl. Instr. and Meth. B 161–163 (2000) 323.

[15] S. Lebed, Nucl. Instr. and Meth. B 155 (1999) 322.

[16] C.G. Ryan, D.N. Jamieson, Nucl. Instr. and Meth. B 158 (1999) 97.

[17] D. Jamieson, G. Legge, Nucl. Instr. and Meth. B 30 (1988) 235.

[18] D. Jamieson, J. Zhu, Y. Mao et al., Nucl. Instr. and Meth. B 104 (1995) 86.

[19] S. Lebed, A. Ponomarev, Nucl. Instr. and Meth. B 130 (1997) 90.

[20] K.L. Brown, SLAC-91, 1997.

[21] D. Jamieson, G. Grime, F. Watt, Nucl. Instr. and Meth. B 40–41 (1989) 669.

[22] V. Brazhnik, V. Khomenko, S. Lebed et al., Nucl. Instr. and Meth. B 104 (1995) 69.

[23] D. Jamieson, G. Legge, Nucl. Instr. and Meth. B 30 (1988) 235.

Suitable test structures for submicron ion beam analysis

D. Spemann [a,*], T. Reinert [a], J. Vogt [a], D. Dobrev [b], T. Butz [a]

[a] *Nukleare Festkörperphysik, Fakultät für Physik und Geowissenschaften, Universität Leipzig, Linnéstr. 5, D-04103 Leipzig, Germany*
[b] *Gesellschaft für Schwerionenforschung mbH, Planckstr. 1, D-64291 Darmstadt, Germany*

Abstract

For the precise determination of the sizes of submicron beam spots test structures with an excellent edge definition are required. For this purpose a semiconductor heterostructure consisting of an 1.62 μm GaInP epi-layer grown on (0 0 1) GaAs has been made, which provides atomically sharp edges for beam spot size measurements. Since the sample has been thinned down by standard transmission electron microscope (TEM) preparation techniques, it can be used for both PIXE and STIM. The sample has been investigated with a TEM and the ion nanoprobe LIPSION. A one-dimensional beam profile in the low current mode was determined by a STIM measurement using 2 MeV protons and yielded a FWHM of (41 ± 4) nm, which is the smallest value reported so far for high energy nuclear micro- and nanoprobes. Furthermore we present nickel nanowhiskers produced at the GSI Darmstadt by electrochemical preparation of etched ion track membranes that have been used to obtain two-dimensional images of the shapes of submicron beam spots. For these measurements a scan over a single nickel nanowhisker having a diameter of 220 nm and a height of about 6 μm was performed. © 2002 Elsevier Science B.V. All rights reserved.

PACS: 06.30.Bp; 07.78.+s; 41.85.Ew
Keywords: Test sample; Semiconductor heterostructure; Nanowhisker; Submicron beam spot sizes; Submicron beam spot shape

1. Introduction

So far, the beam spot sizes and scanning properties of nuclear microprobes have been determined using standard samples (e.g. EBEAM test sample, Chessy test sample and transmission electron microscope (TEM) Cu-grids) which are not suitable for this purpose for different reasons (material combination, design of the structures, accuracy of the edge profiles).

In 1999, a test sample dedicated for ion beam analysis was presented which proved to be useful for beam spot sizes down to a few micrometers [1], but not for submicrometer beams. However, in recent years a lot of effort has been made to optimize the design and performance of the probe forming systems of nuclear microprobes, making ion beam analysis with submicron lateral resolution applicable [2,3]. Yet, due to the lack of suitable test samples, the precise determination of submicron beam spot sizes was hardly possible. The first test sample especially designed for the use in submicron ion beam analysis was presented at the 7th ICNMTA September 2000 in Bordeaux [4].

---
* Corresponding author. Tel.: +49-341-97-32706; fax: +49-341-97-32497.
  E-mail address: spemann@physik.uni-leipzig.de (D. Spemann).
  URL: http://www.uni-leipzig.de/~nfp.

However, it cannot be used in transmission mode and does not allow to obtain two-dimensional images of the shape of a beam spot directly.

In this paper two advanced test structures are presented, which are especially suited for the determination of submicron beam spot sizes in high (PIXE) and low current mode (STIM) and for a two-dimensional imaging of the shape of a beam spot, respectively.

2. Beam spot size measurements on a GaInP/GaAs(001) semiconductor heterostructure

2.1. The design of the test sample

A suitable test structure for beam spot size measurements especially in the low current mode has to meet the following requirements: (i) it has to be transparent for an ion beam, (ii) the edges of the structure have to be exactly defined with an edge slope <5 nm which is 10% of the expected beam spot size in transmission mode, (iii) it should provide a structure which allows the precise determination of the scan size used for the beam spot size measurements to ensure that the beam spot sizes obtained are correct. Up to now there was no test sample available which meets the requirement regarding edge definition that can be used with high energy ions. Hence, it was impossible to accurately determine the beam spot size in the low current mode leading to the unsatisfactory situation that the actual beam spot size had to be estimated by many microprobe groups so far. Therefore a GaInP/GaAs(001) semiconductor heterostructure as shown schematically in Fig. 1 is presented, which

Fig. 2. TEM image of the GaInP/GaAs(001) heterostructure showing the width of the GaInP epi-layer. The upper part defines the left edge (glue-GaInP-interface). The lower part is brightness enhanced and defines the right edge (GaInP-GaAs-interface).

fulfills all the requirements stated above. It can be thinned to make it transparent for an ion beam, provides atomically sharp edges and allows the scan size calibration on the GaInP layer using PIXE.

2.2. Sample preparation

The GaInP epi-layer was grown on (001)GaAs by low pressure metal-organic vapour-phase epitaxy [5]. This layer-by-layer growth process ensures atomically sharp edges. The samples have been glued together "face to face", a cross section has been cut, which was then thinned down by mechanical grinding, polishing and Ar^+ ion milling. Due to the thinning procedures the sample has a wedge-like shape with thicknesses ranging from 10 nm to 50 μm depending on the sample position along the GaInP epi-layer. After the thinning procedure the sample was studied with a TEM. Due to its spatial resolution down to the atomic level the excellent quality of the edges could be confirmed. Furthermore using a TEM the width of the GaInP epi-layer has been determined to be 1.62 μm (see Fig. 2).

2.3. Beam spot size measurements

The beam spot size can be determined by performing several successive line scans alternating in

Fig. 1. Schematic of a cross-section of a GaInP/GaAs(001) semiconductor heterostructure. The structure provides two edges that can be used for beam spot size measurements.

x- and y-direction $(x, y, x, y, \ldots)$ across the 1.62 µm-GaInP epi-layer. This allows to check the reliability of the extracted data. For this purpose the test sample has to be rotated by 90° between the measurements to ensure that the edges are perpendicular to the scan direction. As can be seen in Fig. 2 the test sample also provides an edge perpendicular to the GaInP epi-layer. This is a result of the thinning procedure where the semiconductor heterostructure happened to break along the corresponding crystal plane leaving this edge. Therefore it is also possible to perform a two-dimensional scan over both edges, however, the accurate determination of the beam spot size from this measurement is more difficult compared to line scans.

As reported earlier the LIPSION nanoprobe still suffers from beam spot fluctuations caused by slowly varying magnetic stray fields [4], which are predominant in one direction. Therefore only one-dimensional beam profiles have been measured at the ion nanoprobe LIPSION with the beam scanned perpendicular to the direction of the beam spot fluctuations. The edge of the semiconductor heterostructure was positioned accordingly. The measurements were performed with 2.0 MeV protons using PIXE- and STIM-line scans. The scan size was determined by a PIXE-line scan across the 1.62 µm-GaInP epi-layer. The lateral positions of the As- and In-edge as indicated in Fig. 3 were derived from fits of the experimental data and the difference of the lateral positions was set to 1.62 µm.

The beam profiles were determined by scanning across the 1.62 µm-GaInP epi-layer and fitting the collected data with an error function using NUFIT7.0 (see Fig. 4). The edge used for the PIXE- and STIM-measurements was the one at the GaInP/glue-interface. Due to the excellent definition of the edge the beam profile can be directly derived from the fitted data without deconvolution.

First the beam was focused to an almost circular spot as has been confirmed by scanning over a Ni-nanowhisker (see Fig. 7(a), details are given below). Then for the following measurements the object and aperture have been replaced by successively smaller diaphragms leading to a reduc-
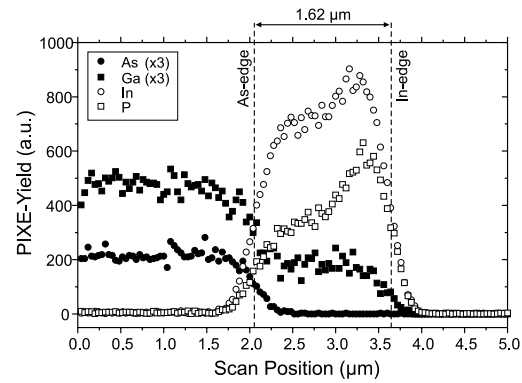

Fig. 3. X-ray yield profiles of As, Ga, In, and P obtained from a PIXE-line scan across the GaInP epi-layer (left: GaAs, right: glue). The positions of the As- and In-edge used for scan size calibration are indicated.

tion of the beam spot size. The FWHM of the beam profiles obtained in the high current mode range from (483 ± 8) nm at a beam current of 36 pA (object diaphragm: 50 µm in diameter, aperture diaphragm: 100 µm in diameter) to (267 ± 16) nm at a beam current of 1.4 pA (object diaphragm: 20 µm in diameter, aperture diaphragm: 50 µm in diameter).

In the low current mode a one-dimensional beam profile with an FWHM of (41 ± 4) nm at a beam current of 1000 ions/s was obtained as shown in Fig. 4(b) using microslits in addition to a 10 µm diaphragm as object and an aperture diaphragm of 10 µm diameter. This is the smallest one-dimensional beam profile obtained so far with a high energy nuclear micro- or nanoprobe which proves both the very good performance of LIPSION and the suitability of the semiconductor heterostructure for determining beam spot sizes far below 1 µm.

At present the spatial resolution in transmission mode is limited to ∼80 nm due to beam spot fluctuations. Therefore, in order to make full use of the small beam spot it is planned to install a system for an active compensation of the mentioned magnetic stray fields, because the shielding with mumetal turned out to be not sufficient. With this system installed the lateral resolution in transmission mode will be comparable to the beam spot size making the LIPSION nanoprobe
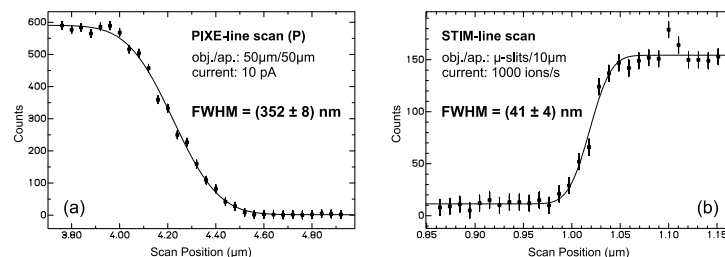
Fig. 4. Beam profiles in high and low current mode derived from line scans over the semiconductor heterostructure: (a) P-X-ray yield, (b) number of transmitted ions with low energy loss.

especially very promising for high resolution IBIC and STIM.

3. Two-dimensional imaging of the beam spot shape using a Ni-nanowhisker

3.1. The design of the test sample

As has been already proposed [4], suitable test structures for imaging the beam spot shape are free-standing columns with small diameters ($\sim$100 nm) and well defined geometry that provide both elemental and topographical contrast. The columns on the test sample should be well separated but easy to locate. These requirements can be fulfilled by free-standing Ni-nanowhiskers deposited on a Cu foil as substrate.

3.2. Sample preparation

The Ni-nanowhiskers have been produced by electrofilling of etched ion tracks in organic foils at the GSI Darmstadt. A Cu foil deposited on one side of the matrix foil acts as a support for the nanowhiskers. After electrofilling, the organic matrix has been dissolved leading to free-standing Ni-nanowhiskers. With this technique whiskers with diameters <100 nm and areal densities up to 10^8 cm^{-2} can be obtained [6].

For the measurements presented here a sample was used with a rather low areal density of 10^7 cm^{-2} which made the location of a well separated single nanowhisker much easier than in the case of higher areal densities. As a suitable compromise
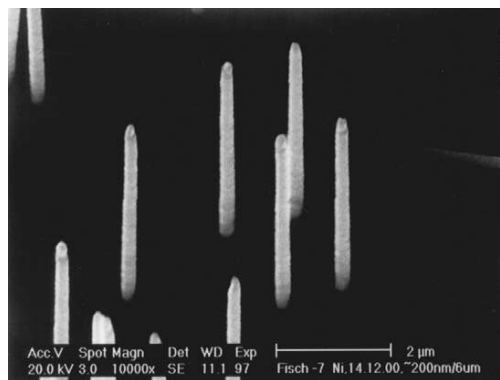
Fig. 5. SEM image of the Ni-nanowhiskers used for the imaging of the beam spot shape. The whiskers have diameters ranging from 200 to 240 nm and a length of 6 μm.

between nanowhisker diameter and stability we chose a sample with $\sim$220 nm whiskers. The size and shape of the nanowhiskers is shown in Fig. 5.

3.3. Beam spot shape measurements

The measurements have been performed with 2.0 MeV protons at the ion nanoprobe LIPSION. Since the Ni-X-ray yield from the whiskers was too low to obtain maps with good counting statistics, the secondary electrons caused by the ion bombardment were detected in the measurements described below. The high aspect ratio of the nanowhiskers ensures a good contrast with respect to the Cu-substrate for topological reasons.

In order to find a whisker which is well separated and oriented parallel to the ion beam a large scan is made first as shown in Fig. 6. As can be seen in the

SE-map, some of the whiskers are tilted, most of the whiskers are well aligned but not well separated (white spots) and some are laying on the substrate. From this map the scan region and the nanowhisker used in the beam spot shape measurements
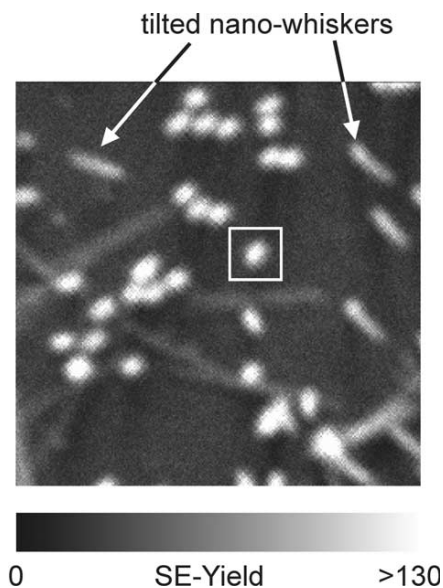
were selected as indicated by the white square in Fig. 6. Then the ion beam was scanned over this single nanowhisker using a scan size of 2.7×2.9 μm^2. The observed two-dimensional SE intensity distribution gives a measure of the convolution of the beam spot and the nanowhisker dimensions. Fig. 7(a) shows a contour plot of the SE yield for a beam spot with an current of 36 pA obtained using an object and aperture diaphragm with a diameter of 50 and 100 μm, respectively. The dashed line indicates the half of the maximum SE yield and therefore roughly represents the beam spot size. As can be seen, the beam spot is slightly more extended in the x-direction (800 nm) than in the y-direction (710 nm). Expectedly, the beam spot sizes obtained are larger then the ones measured on the semi-conductor heterostructure since no deconvolution of the beam spot and the nanowhisker dimensions has been made. Fig. 7(b) shows the same SE-map as a three-dimensional wire frame. Apart from the peak in the SE yield caused by the nanowhisker the SE yield from the Cu substrate is also not uniform. It shows minima along the scan positions with $x = 0$ and $y = 0$ which cannot be due to a shadowing of the SE detector caused by the nanowhisker alone. Since this behaviour is even more pronounced when using larger beam spots for the scanning, further studies will address the question whether the anti-scattering slits between the split Russian quadruplet lenses are responsible for this behaviour or not.
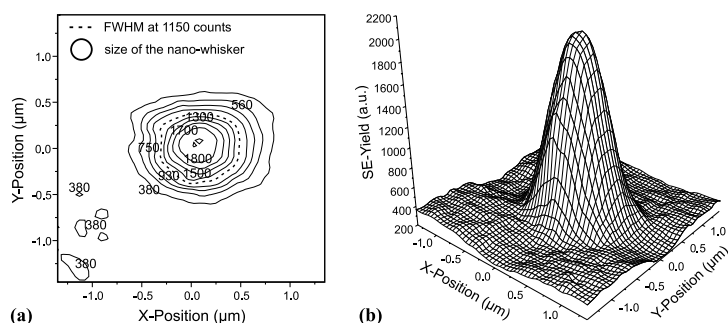

Fig. 6. SE-map showing several nanowhiskers (scan size: 21.5×23 μm^2). As can be seen, some of the whiskers are tilted, most of the whiskers are straight but not well separated and some are laying on the substrate. The scan region and the nanowhisker used in the beam spot shape measurements are indicated by the white square.

Fig. 7. SE yield distribution obtained using an object and aperture diaphragm with a diameter of 50 and 100 μm, respectively. (a): Contour plot showing the shape of the beam spot. The dashed line represents the beam spot size. (b): three-dimensional wire frame of the SE yield. Apart from the peak in the SE yield caused by the nanowhisker, the SE yield from the Cu substrate shows minima along the scan positions with $x = 0$ and $y = 0$.

4. Conclusions

The GaInP/GaAs(0 0 1) semiconductor hetero-structure presented here proved very useful for the accurate determination of beam spot sizes in the high and low current mode due to its excellent edge definition. A one-dimensional beam profile obtained in the low current mode by a STIM measurement using 2 MeV protons yielded a FWHM of (41 ± 4) nm.

Furthermore, two-dimensional images of the shapes of submicron beam spots have been obtained by scanning over a single nickel nanowhisker which acted as a small probe for the beam current density within the beam spot.

Acknowledgements

References

[1] U. Wätjen, C. Dücsö, A. Tajani, F. Munnik, F. Lechten-berg, Nucl. Instr. and Meth. B 161–163 (2000) 359.

[2] F. Watt, T. Osipowicz, T.F. Choo, I. Orlic, S.M. Tang, Nucl. Instr. and Meth. B 136–138 (1998) 313.

[3] T. Butz, R.-H. Flagmeyer, J. Heitmann, D.N. Jamieson, G.J.F. Legge, D. Lehmann, U. Reibetanz, T. Reinert, A. Saint, D. Spemann, R. Szymanski, W. Tröger, J. Vogt, J. Zhu, Nucl. Instr. and Meth. B 161–163 (2000) 323.

[4] D. Spemann, T. Reinert, J. Vogt, T. Butz, K. Otte, K. Zimmer, Nucl. Instr. Meth. B 181 (2001) 186.

[5] V. Gottschalch, R. Franzheld, I. Pietzonka, R. Schwabe, G. Benndorf, G. Wagner, Cryst. Res. Technol. 32 (1997) 69.

[6] D. Dobrev, J. Vetter, N. Angert, Nucl. Instr. and Meth. B 149 (1999) 207.

Active compensation of stray magnetic fields at LIPSION

D. Spemann [a,*], T. Reinert [a], J. Vogt [a], J. Wassermann [b], T. Butz [a]

[a] *Nuclear Solid State Physics, University of Leipzig, Linnéstr. 5, D-04103 Leipzig, Germany*
[b] *Institute for Machine Dynamics and Measurement, Vienna University of Technology, Wiedner Hauptstr. 8-10, A-1040 Vienna, Austria*

Abstract

As reported previously, slowly varying stray magnetic fields and, recently, additional 50 Hz fields deteriorate the lateral resolution in the low current mode of the high-energy ion nanoprobe LIPSION. Therefore, the active stray magnetic field compensation system AMK_5 has been installed in the LIPSION laboratory. This system utilizes six coils in a Helmholtz-arrangement and advanced technology for magnetic field sensing and signal processing for its operation and allows to reduce the stray field fluctuations to excellent ± 10 nT in all three directions for frequencies from true DC up to the kHz range. A compensation factor >100 was obtained for the vertical direction. The compensation system was also used to determine the sensitivity of LIPSION to stray magnetic fields. It was found that the sensitivity is largest for stray fields along the beam direction leading to a beam spot movement of 1.1 m/T in both horizontal and vertical direction. Thus, the residual stray field fluctuations of ± 10 nT result in beam spot movements of ± 13 nm assuming a homogeneous stray field and no contribution from stray fields outside the shielded volume. It is demonstrated that the lateral resolution of LIPSION is significantly improved by the active compensation system. However, there are still beam spot fluctuations in both vertical and horizontal direction dominated by 50 Hz components which limit the resolution in the low current mode to approximately 130 nm. The source of these fluctuations is still unclear.
© 2003 Elsevier B.V. All rights reserved.

1. Introduction

Non-static stray magnetic fields caused, e.g. by trams, power supplies, and transformer stations can lead to a significant deterioration of the lateral resolution of ion micro- and nanoprobes even at low magnitudes of ~ 1 μT [1]. As has been shown previously, the lateral resolution in the low current mode of the high-energy ion nanoprobe LIPSION is primarily limited by beam spot fluctuations caused by slowly varying stray magnetic fields [2,3] and, recently, by additional 50 Hz fields. Up to now, the beam tube of the nanoprobe has been passively shielded with Mumetal yielding a resolution of ~ 80 nm at best in the low current mode with beam spot sizes of ~ 40 nm [3] (it should be noted that those resolutions were obtained in the

* Corresponding author. Tel.: +49-341-97-32706; fax: +49-341-97-32497.
E-mail address: spemann@physik.uni-leipzig.de (D. Spemann).
URL: http://www.uni-leipzig.de/~nfp.

past when no 50 Hz contributions were present). However, it turned out to be very difficult to shield the separated Russian quadrupole lens system effectively due to its complex geometry. Since the area around the lens system is most sensitive to stray magnetic fields an effective shielding is highly desirable in order to achieve lateral resolutions comparable to the beam spot size. Therefore, a system for an active compensation of stray magnetic fields has been installed at LIPSION.

We report on the operating principle and performance of the active compensation system, its impact on the performance of LIPSION and on the residual beam spot fluctuations. All measurements have been performed using 2 MeV protons.

2. The active compensation system AMK_5

2.1. Principle of operation

The principle of operation of an active compensation system for stray magnetic fields is to measure the stray magnetic field in the x-, y- and z-direction separately and to compensate it by a magnetic field of the same magnitude but opposite direction produced using coils in a so called "Helmholtz-arrangement". In the case of a homogeneous stray magnetic field the superposition with the generated magnetic field leads to a complete compensation in theory. In practice, however, there are several handicaps for a complete compensation including the non-ideal size or position of the Helmholtz coils due to insufficient available space, distortion of the magnetic flux produced for compensation due to the ferromagnetic response within or near the coil arrangement and dephasing between stray field and generated field due to time delays in the measuring and control device. It should be noted that inhomogeneous stray magnetic fields can never be compensated completely.

The room conditions of the LIPSION laboratory allowed to install the Helmholtz-coils in an optimal size and position (see Fig. 1). The most sensitive part of the nanoprobe is near the quadrupole lenses in front of the target chamber as has been determined experimentally. Therefore, these lenses are positioned in the center of the coils. In order to obtain a large homogeneous area along the beam axis, a distance of 9.0 m was chosen between the two x-coils (36 turns each). A much smaller homogeneous area is needed for the y- and z-direction. The corresponding coils have a distance of 2.8 m in the y- and 2.4 m in the z-direction (18 turns each).

The stray magnetic field is measured in the x-, y- and z-direction with three specially developed probes mounted near the center of the Helmholtz-arrangement which have a very high sensitivity of 2 mV/nT, a signal to noise ratio >104 dB and a bandwidth in the 100 kHz range. The signals are filtered and then digitized by fast 16-bit ADC's (conversion time <3 µs). The main controller work is done by a powerful digital signal processor (DSP, TI, TMS320C40/50, 100 Mflops).

The multi-processor system of the AMK_5 provides a transient time of 8 µs for full signal throughput which effectively minimizes the dephasing mentioned above in spite of complicated and calculation intensive codes. The control signals from the DSP are amplified by three independent power amplifiers developed for high output current on inductive loads and very low phase shifts over the full operating range. A remote control allows to activate or deactivate the compensation system.

The whole system is designed to work from true DC up to the kHz-range with a compensation factor up to 100 and above, depending on the local situation. In recent years it has been installed and successively used at scanning and transmission electron microscopes. To our knowledge, the system described is the first one that has been installed at a high energy ion micro- or nanoprobe.

2.2. Performance of the AMK_5 system

Fig. 2 shows the stray magnetic field near the quadrupole lenses in front of the target chamber measured with a separate calibrated 3D-flux gate probe (time: 20 s/div, magnetic field: 100 nT/div). First, the compensation was turned off (on the right hand side of the marker). As can be seen, there is a remarkable magnetic interference in the LIPSION-lab predominantly in the z-direction with a very slow variation of the larger magni-
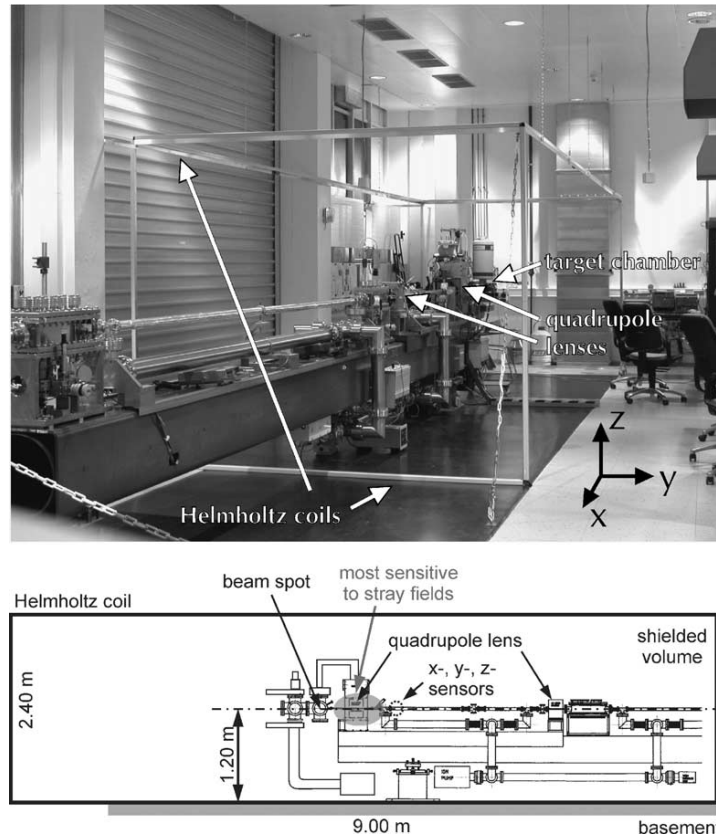
Fig. 1. Top: view of the LIPSION laboratory. Six rectangular coils (three coil pairs) for the *x*-, *y*- and *z*-direction form the Helmholtz-arrangement. The coil dimensions are: $x \times y \times z = 9.0 \text{ m} \times 2.9 \text{ m} \times 2.4 \text{ m}$. Bottom: schematic of the Helmholtz-arrangement showing the size and position of the coil pair for the *y*-direction. Note that the beam direction is along the *x*-axis.

tudes. Therefore, a successful compensation can only be achieved with a compensation system working even at true DC. At the marker position the compensation is turned on. With a smooth transition the system gets activated and suppresses any further variation of the magnetic field (left hand side of the marker). It should be noted, that the measurement was done synchronously for all three channels. The different time positions in the graphs are due to different zoom positions of the time series during readout of the oscilloscope only. The remaining fluctuations of the magnetic field are approximately ± 10 nT. Since the strongest stray field variations in the *z*-direction have magnitudes of more than ± 1.5 μT, compensation factors of more than 100 have been obtained.

3. Impact on lateral resolutions at LIPSION

3.1. Sensitivity of LIPSION to stray magnetic fields

The sensitivity of LIPSION to beam spot fluctuations caused by varying external magnetic fields has been tested by applying a magnetic field. For this purpose a 0.24 Hz triangular shaped AC was sourced separately into each of the Helmholtz coil pairs creating an extended magnetic field along the direction given by the corresponding coil pair (see Fig. 3(a)). The field strength was measured in the center of the shielded volume with calibrated magnetometers. The beam spot fluctuations caused in the horizontal (*y*) and the vertical (*z*) direction have been determined by PIXE scans
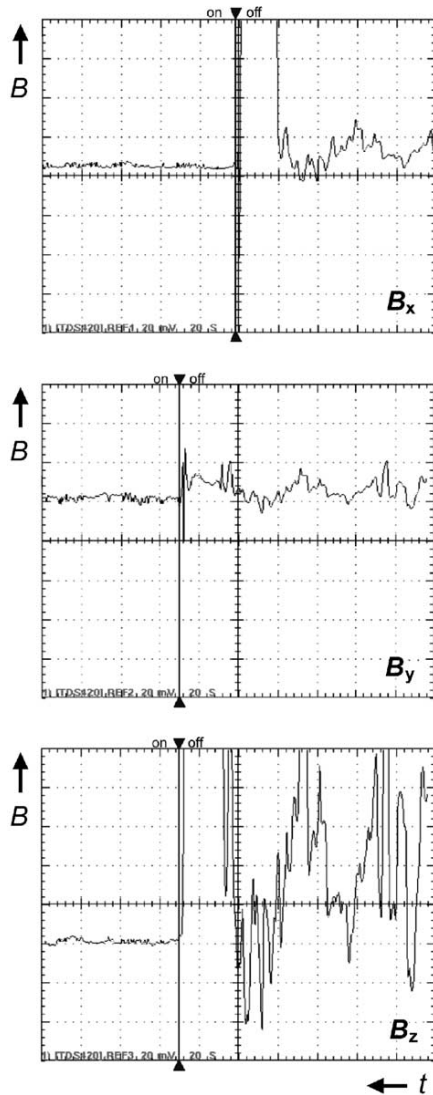
Fig. 2. Stray magnetic field in the x-, y- and z-direction in the LIPSION laboratory measured with a calibrated 3D-flux gate probe (time: 20 s/div, magnetic field: 100 nT/div). Right from marker: compensation system switched off. Left from marker: compensation system activated. The remaining fluctuation of the magnetic field is approximately ± 10 nT.

with 27 μm × 27 μm scan size on a 2000 mesh Cu grid using raster scanning in the y- and z-direction, respectively. Fig. 3(b) and (c) shows the maps for an applied magnetic field with an amplitude of $B_{0,z} = 2.32$ μT in the vertical direction. The beam

spot fluctuations of ± 1.1 μm in both scanning directions produce triangular shaped patterns in the maps. One might expect beam spot movements in the direction perpendicular to the magnetic field only. However, all magnetic fields produced in the x-, y- and z-direction resulted in a beam spot movement in both y- and z-direction, i.e. not perpendicular to the direction of the external magnetic field. Table 1 shows the beam spot movements in metres/Tesla for 2 MeV protons for all directions. The LIPSION system is most sensitive to stray fields directed along the beam direction. Furthermore, the sensitivities in the y- and z-direction differ significantly from each other. From these data it can be concluded that the residual stray magnetic field fluctuations of ± 10 nT obtained with the active compensation system in operation result in beam spot fluctuations of approx. ± 13 nm in the case of 2 MeV protons assuming spatially homogeneous fluctuating stray fields and no further contribution to beam spot fluctuations from stray fields outside the shielded volume.

3.2. Lateral resolution improvements by active compensation of stray magnetic fields

Since the expected improvement of the lateral resolution is largest in the low current mode, STIM measurements were performed on the semiconductor heterostructure described in [3] with and without active compensation. Fig. 4 shows a STIM scan over a GaAs edge (scan size: 2.4 μm × 2.4 μm) with the beam scanned in horizontal direction. First the compensation was activated (upper part of the STIM map) which results in a distortion-free image of the edge. Then the compensation was switched off (lower part of the map) leading to strong distortions in the image. In order to compare the lateral resolutions, beam profiles in the horizontal direction were extracted from the upper and lower part of the map as shown right in Fig. 4 (beam profiles in the vertical direction are similar). The lateral resolution in the low current mode using the active compensation system was determined to be (132 ± 2) nm which is not as good as expected due to residual beam spot fluctuations of approximately ± 50 nm that can be
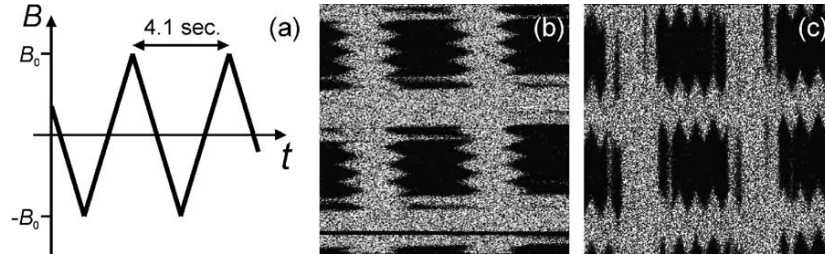
Fig. 3. Beam spot movement due to an applied triangular-shaped AC magnetic field measured by PIXE scans on a 2000 mesh Cu grid (scan size: 27 μm × 27 μm). (a) Schematic diagram of the magnetic field, (b) beam spot movement in horizontal direction, (c) beam spot movement in vertical direction.

Table 1
Beam spot movement in horizontal (Δy) and vertical (Δz) direction due to external magnetic fields in different directions for 2 MeV protons

	Magnetic field direction		
	Along beam (x)	Horizontal (y)	Vertical (z)
Δy	±1.1 m/T	±0.20 m/T	±0.47 m/T
Δz	±1.1 m/T	±0.13 m/T	±0.47 m/T

seen in the enlarged part of the STIM map. However, the beam profile from the lower part of the map appears distorted and much broader than that from the upper part which demonstrates a remarkable loss in lateral resolution when no active compensation is used. Thus, the active compensation of stray magnetic fields leads to a significant improvement of the lateral resolution in

the low current mode, where beam spot fluctuations still limit the lateral resolution. On the contrary, with active compensation the lateral resolution in the high current mode is only limited by the beam spot size.

4. Residual beam spot fluctuations

The residual beam spot fluctuations in the y- and z-direction have been determined by STIM scans over the corner of the semiconductor heterostructure (scan size: 3.0 μm × 3.0 μm). A scan speed of 350 pixels per second has been used in the z- and y-direction, respectively, in order to get information about the frequency of the fluctuations. Scanning the beam in the vertical direction over a vertical edge allows the determination of the beam
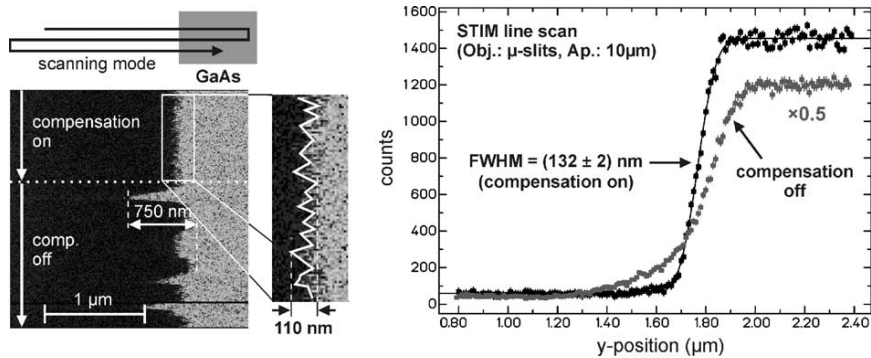

Fig. 4. STIM scan over a GaAs edge (scan size: 2.4 μm × 2.4 μm) with the beam scanned in horizontal direction. Left: STIM map taken with (upper part) and without (lower part) active compensation. The enlarged part shows residual beam spot fluctuations of approximately ±50 nm. Right: horizontal beam profiles extracted from the upper and lower part of the map.

spot fluctuations in the horizontal direction and vice versa. From the regular patterns observed in the corresponding map it could be concluded that the residual beam spot fluctuations are dominated by 50 Hz components in both horizontal and vertical direction. The source of these fluctuations is still unclear. One might think of the following sources.

4.1. Ripple on quadrupole lens current

The ripple of the Kepco MBT 36-10 MGR power supply is 0.36 mV and consists mainly of 100 Hz components. This results in a relative current fluctuation of 0.0036% for a 2 MeV proton focus. The corresponding beam spot fluctuations for the diaphragm-to-lens alignment used in the measurements shown above are 7 nm in the horizontal direction and 60 nm in the vertical direction, respectively. The latter value can be reduced by properly adjusting the height of the aperture diaphragm. Therefore, a ripple on the quadrupole lens current cannot be responsible for our beam spot fluctuations. However, the ripple will become critical if the diaphragm-to-lens misalignment is sufficiently large.

4.2. Scan system

A contribution from the scan system can be excluded, because the fluctuations are still present when a "virtual scan" is performed. For this purpose the beam is positioned on the edge of the heterostructure and a "scan" is made with the scan amplifier being switched off. Then the characteristic patterns observed in the map are only due to beam spot fluctuations.

4.3. External 50 Hz stray fields

Within the volume shielded by the active compensation system, 50 Hz stray fields are effectively reduced as can be monitored by magnetic probes.

However, the magnitude of the 50 Hz beam spot fluctuations remains unchanged. Therefore, a contribution from external stray fields seems to be unlikely. On the other hand, the 50 Hz fluctuations were not present until the end of 2001. Since no major changes whatsoever were made within the laboratory since that time, the source of the fluctuations should be external.

5. Conclusions

As could be demonstrated, the active compensation of stray magnetic fields results in a significant improvement of the lateral resolution of the LIPSION system. However, there are still beam spot fluctuations in both vertical and horizontal direction dominated by 50 Hz components which limit the resolution in the low current mode to approximately 130 nm. The source of these fluctuations is still unknown und further investigations are under way in order to further improve the lateral resolution.

References

[1] F. Watt, T.F. Choo, K.K. Lee, T. Osipowicz, I. Orlic, S.M. Tang, Nucl. Instr. and Meth. B 104 (1995) 101.
[2] D. Spemann, T. Reinert, J. Vogt, T. Butz, K. Otte, K. Zimmer, Nucl. Instr. and Meth. B 181 (2001) 186.
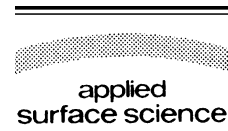[3] D. Spemann, T. Reinert, J. Vogt, D. Dobrev, T. Butz, Nucl. Instr. and Meth. B 190 (2002) 312.

Morphological and elemental characterisation with the high-energy ion-nanoprobe LIPSION

T. Butz [*], Ch. Meinecke, M. Morawski, T. Reinert,
M. Schwertner, D. Spemann, J. Vogt

*Nukleare Festkörperphysik, Fakultät für Physik und Geowissenschaften, Universität Leipzig,
Linnéstr.5, 04103 Leipzig, Germany*

Abstract

This contribution deals with the morphological and elemental characterisation with high-energy (MeV) focused ion beams (in particular protons) with special emphasis on high spatial resolution in the sub-micrometer regime and very low minimum detection limits (sub-ppm) in trace element analysis. The most important methods like particle induced X-ray emission (PIXE), Rutherford backscattering spectrometry (RBS), as well as scanning transmission ion microscopy (STIM) and STIM-tomography will be illustrated by examples from material and life sciences.
© 2005 Elsevier B.V. All rights reserved.

1. Introduction and short description of methods

In the last few years nuclear microprobes, i.e. accelerators with focused ion beams, were developed with the special focus on spatially resolved analytics. In this contribution, we present the high-energy ion-nanoprobe LIPSION in Leipzig, a "single-ended" electrostatic accelerator with 3 MV and ion optics, which yields a minimal beam diameter of 40 nm. With this system, element-specific images with a lateral resolution of 350 nm can be obtained using particle-induced X-ray emission (μ-PIXE), a high-current technique (100 pA–10 nA) [1]. Depending on the element, minimum detection limits of 0.1–10 ppm can be reached. Compared to electron-microprobes, the strongly reduced bremsstrahlung-background is advantageous, especially when dealing with heavy elements. Another high-current technique is Rutherford backscattering spectrometry (μ-RBS) [2], which is particularly well suited for thin film analysis. Here, the

* Corresponding author. Tel.: +49 341 9732701;
fax: +49 341 9732748.

E-mail address: butz@physik.uni-leipzig.de (T. Butz).

energy loss of the backscattered ion along the incoming and outgoing trajectories is measured. With comparable lateral resolution depth resolutions of 10 nm and lower using glancing incidence can be achieved. For sufficiently thin samples (e.g., 30 μm tissue) protons of 2.25 MeV can traverse the sample, and in this way scanning-transmission ion microscopy (STIM) and micro-tomography (STIM-T) are possible. Since every single proton is detected and the contrast is given by the energy loss, very low currents in the 0.1 fA range are sufficient and, hence, there are no problems with radiation damage—contrary to PIXE and RBS, even for biological samples. This is a result of the much higher penetration of protons compared to electrons. Lateral resolutions of 100 nm are possible with STIM.

All high-energy ion methods have in common that within the energy range used the stopping power is dominated by electronic stopping and approximately energy-independent (i.e., above the range of validity of the Bethe–Bloch equation), contrary to low-energy methods like SIMS, where nuclear stopping leads to sputtering. Thus, these methods are termed "non-destructive".

As an example in material science, we present the analysis of a thin film solar cell with μ-PIXE and μ-RBS. Examples in the field of bio-nano analytics come from neurosciences. The power of tomography—in print, unfortunately, only in two dimensions-is illustrated by results on cygospores.

2. An example from materials sciences: thin films

In connection with the production of thin film solar cells, we attempted to produce laterally homogeneous stoichiometric films with uniform thickness made of $Zn_{2-2x}Cu_xIn_xS_2$ on a glass substrate (SiO_2) by pulsed laser deposition (PLD). In this process, the material transfer from the target to the substrate is crucial; in addition, it must be avoided to sputter entire particles from the target onto the substrate. The analysis was carried out by the ion beam techniques PIXE and RBS [3]. The present example is intended to illustrate the power of the ion beam techniques and does not correspond to the "state-of-the-art" PLD-film preparation.

Fig. 1 shows the PIXE-maps of silicon (a) and sulphur (b), measured with 2 MeV He$^+$ ions. The dimensions are 335 μm × 335 μm. The grey scale corresponds to X-ray intensities. Dark means low intensity. Clear inhomogeneities are visible in both maps. Apparently the substrate is "invisible" at some positions. Since the sulphur intensity is high at these very same positions, one suspects that the substrate is "shaded" by the material above it. Fig. 1(c) displays PIXE-spectra of the entire film and of the "thick" particles like those displayed in Fig. 1(b) bottom (marked with a white square). The characteristic X-ray lines of Si, S, In (L), Cu and Zn are clearly visible. In addition, it is obvious from the relative intensities of the
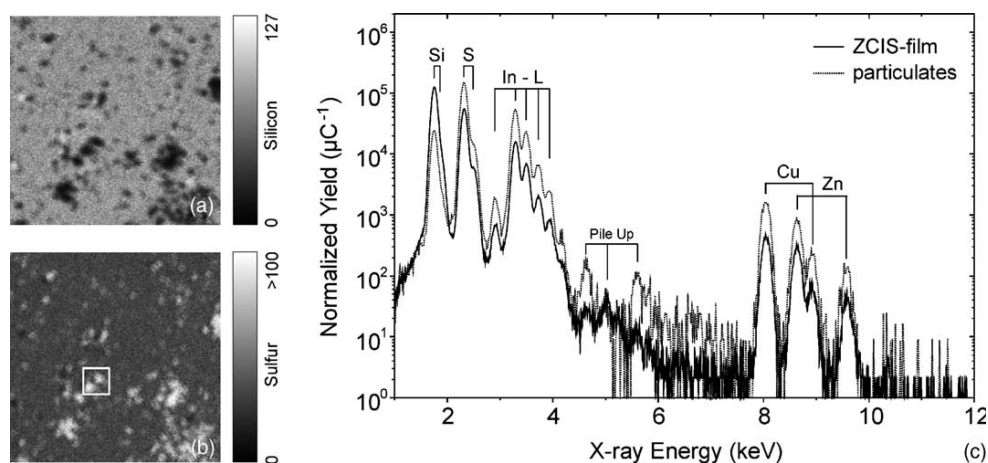

Fig. 1. (a) Silicon-map, (b) sulphur-map of a thin film of $Zn_{2-2x}Cu_xIn_xS_2$ on a glass substrate; the film is inhomogeneous and (c) PIXE-spectra of the film and the particles on the film, as shown e.g. in the white square in the sulphur map.
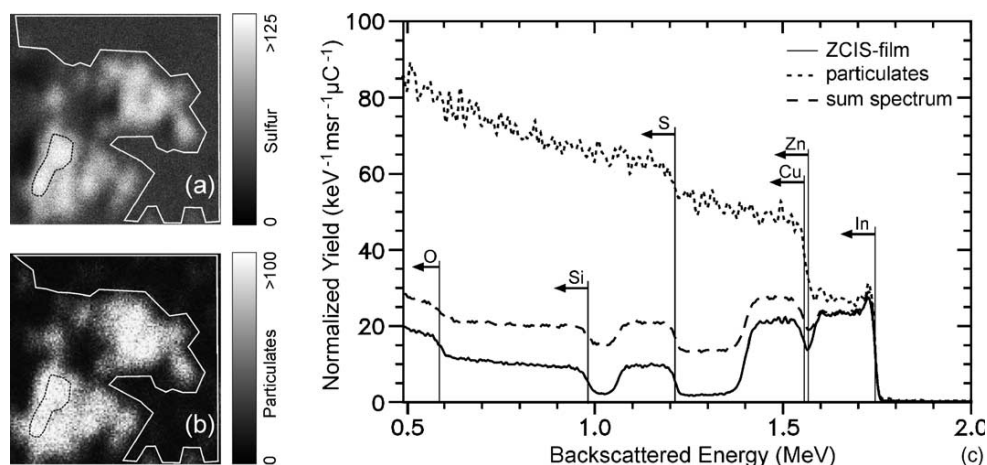
Fig. 2. (a) PIXE-map of sulphur from the small white square in Fig. 1(b), (b) RBS-map of the same region and (c) RBS-spectra of the homogeneous film (grey fretsaw region), of the particles (white fretsaw region), and the sum of both regions.

X-ray lines that the stoichiometries for the entire film and the particles are about the same. A detailed analysis of the elemental concentration requires the knowledge of the film thickness, particularly that of the particles.

Simultaneously with the PIXE-spectra we recorded RBS-spectra. Fig. 2(a) shows again the sulphur PIXE-map zoomed into the small detail of Fig. 1(b). Its dimensions are 41 μm × 41 μm. Below that in Fig. 2(b) we show the corresponding RBS-map. Bright corresponds to a large energy loss. Fig. 2(c) shows the RBS-spectra for the entire film, for the homogeneous portion of the film obtained by software-cut like fretwork, and for one or more selected particles, respectively. It is immediately possible to determine the film thickness from the energy loss provided the composition is known. It is 220 nm. One sees "from right to left", i.e. with decreasing alpha energy, first the In-peak (heaviest element), then the Cu- and Zn-peaks (unresolved in RBS), then the S-peak and, finally, the Si- and O-peaks of the substrate.

For a homogeneous film thickness, the yield between elemental peaks should vanish ideally provided the film is sufficiently thin. This is approximately the case for the "fretwork" region. On the contrary, the spectrum for the entire film exhibits a substantial yield of alphas with energies in the "forbidden" region; this unambiguously results from the "thick" particles, as demonstrated by the RBS-spectrum of the particles alone. The particles are larger than 1.5 μm.

Table 1
Elemental concentrations of Zn, Cu, In and S of a ZCIS-film, the particles on the film and of the PLD-target

| | Elemental concentrations (at.%) | | | |
	Zn	Cu	In	S
Film	18.0 ± 1.0	19.1 ± 1.0	15.5 ± 0.5	47.5 ± 1.5
Particles	14.8 ± 1.5	20.2 ± 1.5	17.5 ± 1.0	47.5 ± 2.5
PLD-target	17.5 ± 1.0	13.7 ± 1.0	16.4 ± 0.8	52.5 ± 1.5

A detailed analysis of the composition of this inhomogeneous sample is not trivial. Table 1 lists the compositions of the film, the particles and the PLD-target. The design composition was chosen as $Zn_{0.225}(Cu/In)_{0.275}S_{0.5}$. Within the uncertainty of the measurement, the sulphur concentrations agree very well and correspond to the design aim. For the Zn concentration the agreement with the design aim is less favourable, which, however, is a consequence of the target composition and not related to the Zn-transfer. The variations of the Cu-concentration are too large, even when considering uncertainties of the measurement and suggest problems with Cu-transfer. In particular, the particles are rich in Cu, compared to the target.

In conclusion, μ-PIXE combined with μ-RBS allow a detailed characterisation of thin films, which is indispensable for the further optimisation of the preparation conditions.
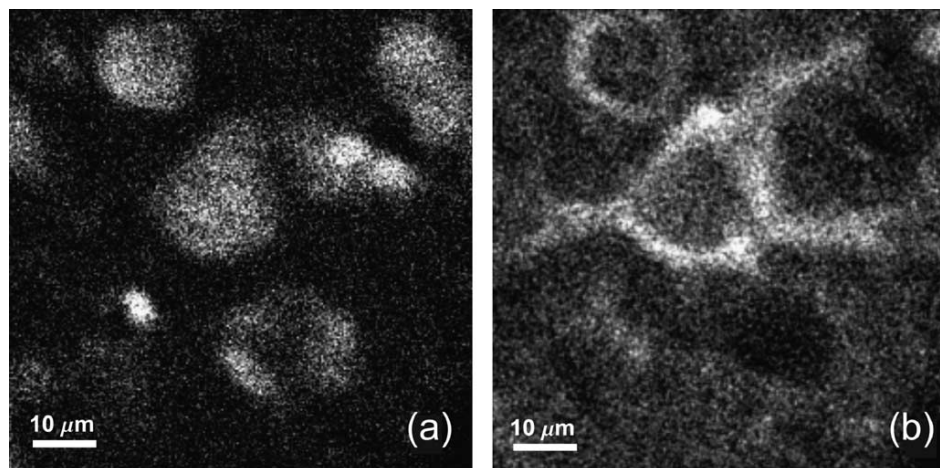
Fig. 3. PIXE-map of phosphorus (a) and of iron (b) of neurons in a brain cross-section.

3. An example from life sciences: perineuronal nets and neuromelanin

3.1. Perineuronal nets

Neurodegenerative deseases, e.g. Alzheimer's deseases play an increasingly important role, however, there is as yet no therapy despite massive efforts. In this context, it is important to investigate what protection mechanisms the organism has developed itself against—among others—oxidative stress due to metal ions. It is remarkable that in the visual and motor cortices neurons are very frequently surrounded by so-called perineuronal nets, which are good candidates for local ion homoeostasis because they are composed of large aggregated chondroitin-sulphate proteoglycans with the principal components hyaluronan and aggrecan. This prompted our investigation of the affinity of the perineuronal nets to colloidal iron by μ-PIXE. Fig. 3(a) shows the distribution of phosphorus in the substantia nigra pars compacta, which visualizes the contours of the neurons. Fig. 3(b) shows the iron distribution. The contour of the perineuronal net of a neuron slightly above the map centre with three branches is clearly visible with a further neuron above barely visible. On the contrary, the neuron below the central neuron does not exhibit a perineuronal net. A detailed investigation with various iron loads revealed that perineuronal nets can bind about a factor of 4.6 more iron than any extracellular matrix structure. This required the "soft-ware"-cutting of the contours of the perineuronal nets in the PIXE-maps, in order to deduce the iron content and to compare it with the extracellular matrix. An analysis based on the Michaelis–Menten equation yielded an affinity constant between 2.2 and 6.3 mmol/l, depending on the brain area [4]. Here, it should be stressed that μ-PIXE yields quantitative information on the elemental concentrations, contrary to staining techniques, which renders affinity studies possible.

In conclusion, our results show that perineuronal nets do have a protective action against ion-induced oxidative stress. However, it is still not clear where the elevated iron levels come from. They could be responsible for the death of neurons. Of course, the dead neurons could also be the sources and the reason for the death of neurons is still open.

3.2. Neuromelanin

In the substantia nigra pars compacta elevated iron concentrations are observed compared to pars reticulata. It was not clear whether the enrichment of iron is intra or extracellular or homogeneous [5]. There is sulphur-rich neuromelanin in the pars compacta. Hence, one would assume that it is the intracellular neuromelanin, which is primarily responsible for Fe-binding. In order to test this hypothesis element-specific images with subcellular resolution are required. Fig. 4(a–c) shows μ-PIXE maps of phosphorus, iron and sulphur. The minimum detection limits were in the
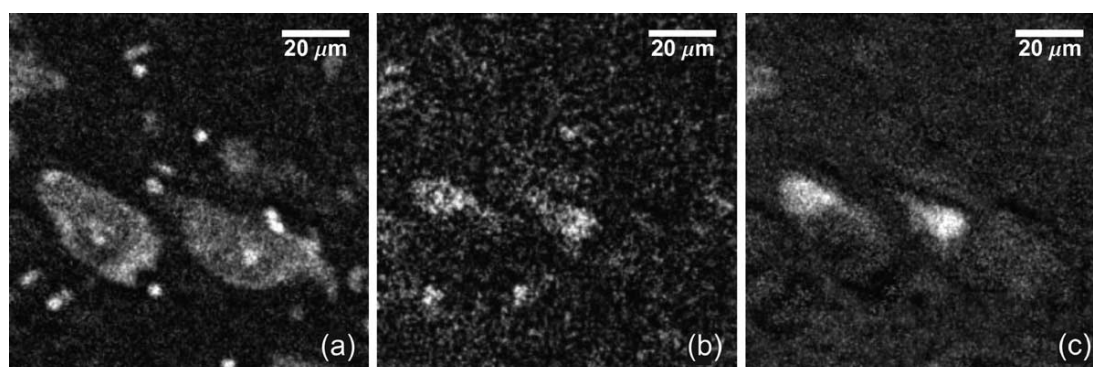
Fig. 4. PIXE map of phosphorus (a), iron, (b) and sulphur (c) of a brain section taken from the substantia nigra pars compacta. Within the neurons the iron map is correlated to the sulphur map. The small bright spots in (a) are glia cells.

range of 50 μmol/l or 3.7 μg/g. The phosphorus image exhibits the contours of two neurons (the small dots are glia cells). The correspondence between the iron and sulphur images demonstrates that neuromelanin binds iron preferentially indeed, and hence, is neuroprotective as well. A comparative study of healthy brain tissue and tissue from Parkinsonian patients revealed clear differences in the iron concentration.

This example illustrates how multi-elemental maps allow us to draw conclusions concerning the mechanisms of ion homoeostasis. It seems that oxidative stress, which can be produced by e.g. Fe, Al, Au or Zn plays an important role in neurodegenerative diseases because the organism has developed efficient protection mechanisms against it.

4. An example of μ-tomography with protons

The methods available for the three-dimensional investigation of samples with dimensions of 10–50 μm which allow the visualization of structural details with sub-micrometer resolution are rather scarce. For optically "transparent" samples, confocal laser microscopy has made astonishing progress in the last few years. For non-transparent samples, one can use either focused X-ray beams or focused proton beams. Electron-tomography is possible in principle; however, the lateral straggling of the light electrons requires sample dimensions of 100 nm or below. X-ray micro-tomography requires synchrotron sources. For biological samples wavelengths between 2.2 and
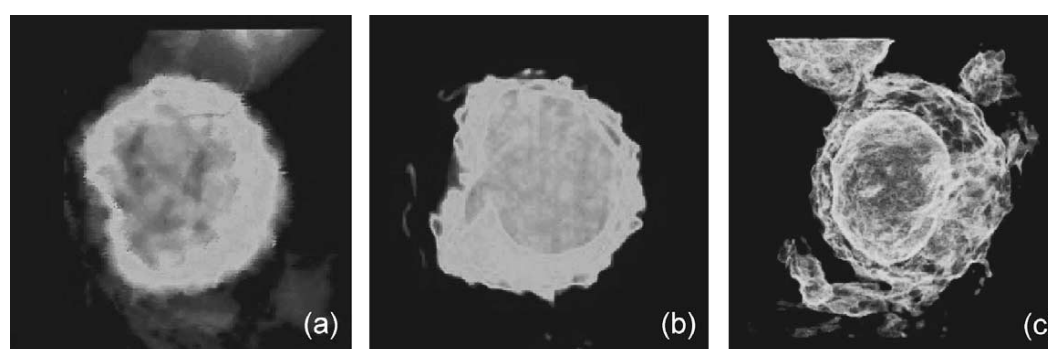

Fig. 5. (a) One of 360 projections through a cygospore capsule, (b) a cross-section through the capsule which reveals the connection of the core with the "exterior world" in the lower left corner and (c) perspective view of the capsule (in the upper left corner one can recognize the needle tip on which the capsule was mounted).

4.4 nm, the "water-window" are used. It allows spatial resolutions down to 50 nm. Because the contrast with this technique is based on absorption of X-ray quanta, relatively high fluences are required. The soft X-rays and the high fluences lead to the application of typically 10^8 Gray for tomography, which requires cryofixation of the samples. An advantage of X-ray μ-tomography is, of course, that no vacuum is required. On the contrary, proton μ-tomography requires vacuum-proof samples (it is possible to extract the proton beam through a window into air, however the slowing down of the protons in air and the lateral straggling cannot be tolerated for tomographic applications). Since the contrast in this method is based on the energy loss of the protons in transmission, very low fluences are required only. Normally, five protons per pixel are registered to calculate the median before the beam is scanned to the next pixel.

Fig. 5(a) shows one of 360 projections (the sample was rotated around $180°$ in steps of $0.5°$) of a cygospore capsule with a diameter of about 50 μm. These cygospores are of great biotechnological interest because they can reproduce themselves sexually, among others. In this way, it is possible to manipulate the cygospores genetically. The capsules were non-transparent, the microbiologists suspected several cell nuclei in an otherwise empty capsule. The energy loss data for protons immediately revealed a completely different view: the capsule was by no means empty, rather it consisted of a core similar to egg yolk with a slightly lower density than the wall. This is shown by the cross-section of Fig. 5(b). One can see that the core does not reveal internal structures within the experimental accuracy. Furthermore, the selected cross-section shows that there is but a single connection to the "exterior world". On the exterior of the capsule there are tentacles (removed for the present investigation), which mediate the sexual reproduction. Fig. 5(c) shows the three-dimensional view, whereby strong density contrasts were rendered such that the outer surface as well as the inner core are both visible. With suitable programs the capsule can be rotated around any axis, which allows us to look at all internal details.

This tomographic study required about 8 h, about half of which was mere data collection. The data analysis was based on the method of back-projection of filtered projections. Here, the stopping power was assumed to be energy-independent, an assumption which is only valid cum grano salis. Moreover, the lateral straggling should be negligible. Iterative reconstruction algorithms would be helpful; however, they were not yet required considering the achieved spatial resolution. The best value for the spatial resolution thus far was 270 nm, the limiting factor being the insufficient mechanical stability of the goniometer: it is impossible to reconstruct a "sharp" 3D-image out of 360 "shaky" projections.

5. Conclusion

The ion beam analytical methods with ions in the MeV-range normally do not belong to surface techniques (however, it is possible under certain circumstances to achieve atomic depth resolution). They are, however, indispensable for the morphological and elemental characterisation of thin films or near-surface regions, of structures in the micro- and submicro-meter regime as well as in bio-nanoanalytics. They are of course-with some reservations—non-destructive because there is practically no sputtering with MeV-ions. The reservations relate to unavoidable radiation damage, an issue, which is particularly relevant in high-current techniques.

References

[1] S.A.E. Johansson, J.L. Campbell, K.G. Malmqvist (Eds.), Particle Induced X-ray Emission Spectrometry (PIXE), Wiley, New York, 1995.
[2] W.-K. Chu, J.W. Mayer, M.-A. Nicolet, Backscattering Spectrometry, Academic Press, New York, 1978.
[3] D. Spemann, J. Vogt, T. Butz, D. Oppermann, K. Bente, Anal. Bioanal. Chem. 374 (2002) 626.
[4] T. Reinert, M. Morawski, T. Arendt, T. Butz, Nucl. Instrum. Methods B 210 (2003) 395.
[5] P.D. Griffiths, B.R. Dobson, G.R. Jones, D.T. Clarke, Brain 122 (1999) 667.

Quantitative trace element analysis with sub-micron lateral resolution

Tilo Reinert [a,*], Daniel Spemann [a], Markus Morawski [b], Thomas Arendt [b]

[a] *Nukleare Festkörperphysik, Universität Leipzig, Linnéstr. 5, D-04103 Leipzig, Germany*
[b] *Paul-Flechsig-Institut für Hirnforschung, Universität Leipzig, Jahnallee 59, 04109 Leipzig, Germany*

Available online 12 May 2006

Abstract

In recent years many nuclear microprobes have developed to sophisticated tools for elemental analysis with high resolutions down to about 1 μm. The application to trace element analysis is mainly in the field of biological and medical research. Numerous successful studies on microscopic scale structures, e.g. cells, lead to the demand for higher spatial resolution or lower detection limits. Therefore, several labs started new efforts for sub-micron resolutions, sometimes intending 100 nm.

The Leipzig microprobe laboratory LIPSION has recently improved its analytical capabilities. We are now able to perform quantitative trace element analysis with sub-micron spatial resolution (beam diameter 0.5 μm at 120 pA). As an example we give the trace element distribution in neuromelanin (intracellular pigment of neurons). Furthermore, when the scan size is reduced from cellular level, i.e. about 50 μm, to sub-cellular level of about 10 μm, the beam diameter can further be reduced by choosing smaller object diaphragms. The unavoidable reduction in beam current will not affect the mapping sensitivity unless the accumulated charge per spatial resolution is not decreased. The smallest beam diameter with analytical capabilities for elemental analysis we achieved thus far was about 300 nm in diameter. It enables an outstanding microPIXE resolution. However, some difficulties appeared in high-resolution work, which limited the acquisition time to less than 30 min.
© 2006 Elsevier B.V. All rights reserved.

PACS: 87.64.−t; 82.80.Yc; 41.75.Ak; 07.78.+S

Keywords: Trace element analysis; Sub-micron; PIXE

1. Introduction

Quantitative trace element analysis with sub-micron spatial resolution is still a developing field with manifold challenges. Studies of elemental distributions with nanometer resolution and low detections limits are already known from synchrotron X-ray fluorescent microprobes (μSXRF) [1] and from secondary ion mass spectrometry (SIMS), especially NanoSIMS [2]. The beam spots that are available for these two techniques are well below 100 nm due to nanotechnological developments in this field over the last two decades. In the beginning nineties, the high-energy ion microprobe community started thinking about pushing down the lateral resolution of focussed MeV-ion beams (mainly protons or Helium ions) from a few micron into the sub-micron or even nanometre regime [3–5]. The developments in accelerator technology [6] and microprobe lens systems [7] made this new efforts worth thinking about.

Today, several high-energy ion microprobe laboratories have reached the sub-micron scale with low beam currents (<1 pA) for analytical techniques like scanning transmission ion microscopy (STIM) or for proton beam writing (PBW). The Singapore and Leipzig groups have achieved beam spots below 50 nm [8,9]. Many other groups are currently also taking efforts to break the sub-500 nm frontiers.

Although, several groups have reported beam profile measurements with beam spots below 500 nm for high currents (>50 pA) [3,10,8] the lateral resolution is commonly not far below 1 μm in studies when particle induced X-ray emission (PIXE) and Rutherford backscattering

---

spectrometry (RBS) are used to analyse elemental distributions. What are the reasons?

Here, we report about our efforts and experiences in achieving sub-micron lateral resolution (<500 nm) in trace element analysis.

2. The Leipzig high-energy ion nanoprobe

In a previous publication the system has been described in more detail [11]. Therefore, we shortly summarize the main features only. *The laboratory*, opened in 1998, was specifically designed for high-resolution work. The accelerator and the nanoprobe are each based on deep foundations to minimize mechanical vibrations from the surrounding. The air conditioning keeps the room temperature stable with an accuracy of ± 0.5 K. *The accelerator* is the first 3.5 MV Singletron^{TM} (in-line) from the Dutch HVEE company with a relative beam energy stability in the range of 10^{-5} and a reduced beam brightness of about 20 A (rad^2 m^2 eV)$^{-1}$ [6]. *The nanoprobe* and every of its systems including the target chamber are mounted on a girder. The probe forming lens system is a separated Russian quadruplet [7] with high demagnifications of about 100, measured in both directions, which gives a nearly orthomorphic image of the circular object diaphragms (diameters of 5 μm, 10 μm, 20 μm, 50 μm, 100 μm, 150 μm, 200 μm and 300 μm and additional microslits are available). The aperture is also a circular diaphragm (5 μm, 10 μm, 20 μm, 30 μm, 50 μm, 100 μm, 200 μm and 300 μm in diameter). Additional, two pairs of anti-scattering slits can be used to intercept the scattered ions at the crossover positions between the two quadrupole-doublets. A small but very important tool had been added during the commissioning phase: a so called anti-skew lens. This is a magnetic quadrupole located directly before the last doublet, which corrects a rotational misalignment of the two doublets. The *sample positioning system* is an off-chamber computer controlled "Physik Instrumente" *x-y*-micrometer stage with an accuracy of 100 nm (DC-motors, optical encoder).

The two *detectors* for X-ray and backscattering spectrometry are a high-purity Germanium (IGLET-X, EG&G Ortec) with a solid angle of 212 msr and for RBS, an annular PIPS particle detector (AD-300-11-300-RM, Canberra) with a solid angle of 75 msr. *Mechanical vibrations* are reduced by the specific foundations and by using ion getter pumps. Influences of *external magnetic stray fields* are reduced using a mu-metal shielding of the beam tube and an active compensation system optimised for the last quadruplet, as this is the most sensitive part [12].

The latest improvements of the nanoprobe result from readjusting the aperture diaphragms and an improved focussing procedure.

3. Resolution tests

The resolution tests were performed on the Chessy test structure (Plano GmbH, Germany). It consists of a silicon substrate with 1.6 million squares (1 μm^2 each) of a thin gold layer building up chess-like fields of 10 μm × 10 μm, which build up fields of 100 μm × 100 μm and so on, resulting in a 5 mm × 5 mm chess-board like structure. Although there are other test structures with better edge definitions for sub-micron beam profile measurements, we have chosen Chessy due to its regularly one micron-sized structures with elemental contrast. The electron micrograph (see SEM image in Fig. 1) shows a very good edge definition, which is sufficient for PIXE resolution tests by mapping the characteristic gold distribution. We did not use single line scans in *x*- and *y*-direction but the horizontal and vertical lateral gold profiles over two squares extracted directly from the gold map (see Figs. 1 and 2). Line scans could possibly yield better resolutions but are less representative. The resolution values for each direction are averaged FWHM of four individual error function fits to the four edges of the two squares.

For a 500 pA, 2.25 MeV proton beam the resolution is slightly less than 1 μm^2 (0.9 μm diameter beam spot measured on a 2000 mesh Cu-rid). This is achieved with 100 μm object and 200 μm aperture diaphragms. By
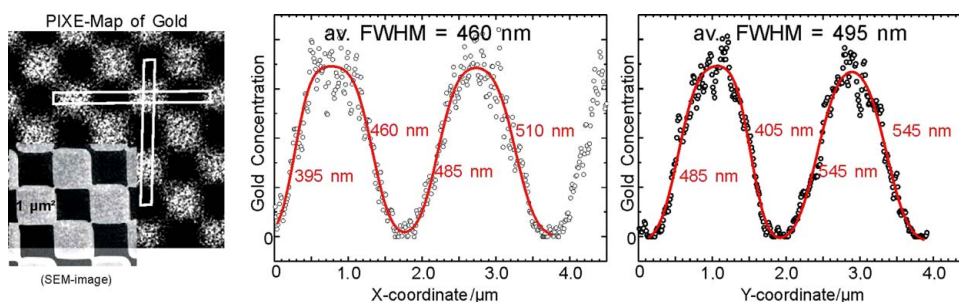

Fig. 1. Resolution measurement for elemental analysis (PIXE) on the Chessy test-structure with a 100 pA 2.25 MeV proton beam. The gold map of the 1 × 1 μm^2 squares revealed a resolution of 460 × 495 nm^2 (averaged full width at half maximum of the lateral gold profile at four square edges). The overlay on the PIXE gold-map shows the secondary electron micrograph of Chessy.
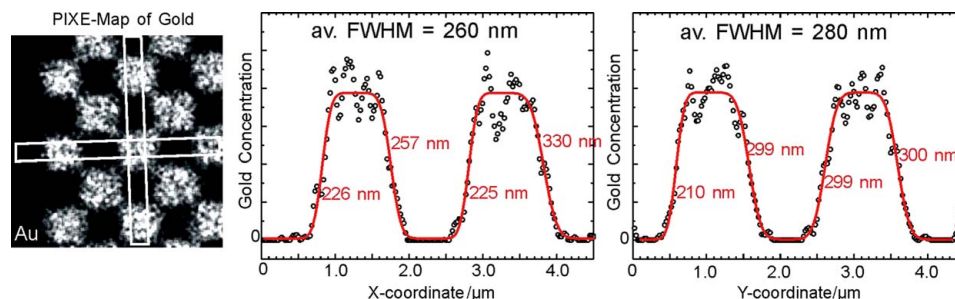
Fig. 2. Same procedures as shown in Fig. 1 carried out with a 10 pA 2.25 MeV proton beam. The resolution is 260×280 nm^2.

reducing the object to 50 µm the beam spot reduces to slightly less than 0.5 µm (460 nm × 495 nm, see Fig. 1) at 120 pA. With the 20 µm object the beam current is further reduced to 20 pA. The resulting beam spot of less than 300 nm (260 nm × 280 nm, see Fig. 2), however, could only be achieved using the second pair of anti-scattering slits, which left a beam current of 10 pA. The acquisition time for the 100 pA beam was five minutes and for the 10 pA beam was about 15 min.

Is a beam of 10 pA still applicable for trace element analysis? If we do not consider the beam current but the accumulated charge per resolution (or map pixel) then we can estimate the scan parameters for 10 pA deduced from a 100 pA beam: A scan of 50×50 µm^2 with a 0.5 µm beam (100 pA) should have 250×250 pixels (2.5 pixels per 0.5 µm beam diameter). One hour acquisition time gives a total charge of 0.36 µC or 5.8 pC per pixel which corresponds to minimum detection limits (for the whole map area) of a few µg/g for transition metals in biological samples. Accumulating 5.8 pC per pixel with a 10 pA beam over 1 h allows a mapping of nearly 80×80 pixels, which results in a scan area of 9.5×9.5 µm^2 (2.5 pixels per 0.3 µm beam diameter). This map would have the same sensitivity for mapping as the 50×50 µm^2 map but with higher spatial resolution. Improving the detection efficiency by using large solid angle X-ray detectors would also help to accept lower beam currents and thus enabling higher spatial resolution. However, with higher spatial resolution some new factors of resolution deterioration may challenge the experimenter to reach the 100 nm aim for trace element analysis with focussed proton beams.

4. Deterioration of the resolution

The resolution is not given by the beam spot dimensions alone but includes also the uncertainty of the beam position on the sample. When the beam spot is highly focussed this uncertainty can substantially deteriorate the resolution. In most cases a parasitic relative movement of the beam with respect to the sample causes this uncertainty. The reasons can be mechanical sources (vibrations in the lens system and vibrations of the sample holder, e.g. from turbo and forepumps). Also possible are influences from varying magnetic stray fields (from AC-currents or changes in DC-currents). A detailed discussion of the deteriorations in the Leipzig system was previously published [12]. Another contribution to the deterioration may come from thermal drifts of microprobe components (beam heating effects on the slits) or from the whole system itself due to changes in the room temperature. The influences of the beam on the sample can also cause a drift (e.g. spot wise heating, charging up, sample shrinkage). These influences were mostly negligible with our 1 µm beam spot but became apparent with beam spots less than 500 nm. Occasionally, we have observed longterm drifts (hours) with an amplitude of almost 1 µm. The 15 min resolution of 300 nm deteriorated to 500 nm after 45 min acquisition time. The reason of this occasional longterm drift is presently unknown, but may be caused by the sample holder stage that is located outside the chamber with a bellow-coupled feed-through and is therefore susceptible even for air convection. A new in-vacuum stage is currently being tested and intended for the newly designed analysis chamber.

5. Application to biological samples

In the last years we have undertaken several quantitative studies on elemental distributions on biological material, especially on rat and human brain [13,14]. These studies led to new demands from the neuroscience department regarding higher lateral resolution and lower detection limits.

Here, we give as an example the trace element analysis with sub-micron lateral resolution on Neuromelanin. Neuromelanin is a dark coloured intracellular pigment that appears in a specific population of neurons (dopaminergic and noradrenergic) predominantly in the *substantia nigra* and in the *locus coeruleus*. In recent years, there is increasing interest in the role of neuromelanin because of a hypothesised link between this pigment and the cell death of neuromelanin-containing neurons in Parkinson's disease (PD). The biology, i.e. the structure, synthesis, physiology and its role in the neuron is mainly unknown. It is likely that, similar to other types of melanins, neuromelanin acts
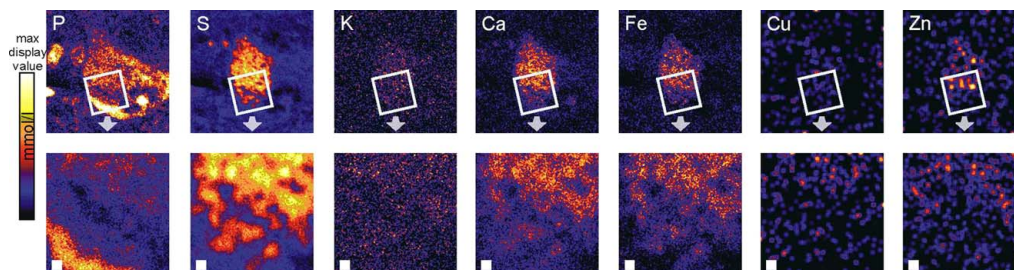
Fig. 3. Elemental maps (50×50 µm^2, top row) and a zoom-in (12.5×12.5 µm^2) of neuromelanin inside a neuron of the *substantia nigra* (healthy control). The spatial resolution is about 0.5 µm (white square in the bottom row is 1 µm^2). The maximum display values are (mmol/l): P: 420; S: 880; K: 44; Ca: 105; Fe: 145; Cu: 8; Zn: 14.

as a protector against free radicals by inactivating or chelating free toxic metal ions (e.g. iron, copper, zinc). However, in the case of redox-active metal ion excess – and this is controversially discussed – neuromelanin could potentiate the free radical production due to a reduced binding capacity. The role of neuromelanin in the pathology of PD is therefore an actual focus in neuroscience [15].

Our aim is to study the content and distribution of trace elements in neuromelanin in situ of Parkinsonian and healthy brain tissue in order to reveal any possible differences. Since the ultrastructure of neuromelanin shows different binding capacities a sub-micron elemental analysis is needed. Fig. 3 shows in the upper row the distribution of the elements P, S, K, Ca, Fe, Cu, Zn in a human neuron (non PD). The phosphorous map mainly represents the cytosolic phosphorous, thus giving an image of the cell body. Within the cell body the melanin appears due to its high sulphur content in the S-map. The ultrastructural granular shape with pigment associated lipids (cavities in the S-map) is well resolved. The elements K, Ca, Fe, (Cu) and Zn are clearly co-localized with the neuromelanin. The minimum detection limit of these elements was about 50 µmol/l (2 µg/g) in the total scan area. The lower row of Fig. 3 reveals in higher magnification the distributions of these elements in the pigment itself. The concentrations of K, Ca, Fe, Cu and Zn are higher in the sulphur containing granules of the pigment. Currently we are launching a study to investigate the change in trace element contents of neuromelanin in Parkinsonian disease.

6. Conclusion

The Leipzig high-energy ion nanoprobe is able to analyse trace elemental distributions with detection limits in the range of µg/g and with a spatial resolution of about 500 nm. By a further reduction of the resolution limiting factors, especially the longterm drifts, we expect resolutions below 300 nm in the near future. This is achievable only with sophisticated precautions against mechanical vibrations, stray magnetic fields and thermal drifts. These deterioration factors should be analysed prior to the installation of new nanoprobes to assess the necessary precautions.

References

[1] C. Mérigoux, F. Briki, F. Sarrot-Reynauld, M. Salomé, B. Fayard, J. Susini, J. Doucet, Biochim. Biophys. Acta 1619 (2003) 53.
[2] P. Hoppe, U. Ott, G.W. Lugmair, New Astron. Rev. 48 (2004) 171.
[3] G.W. Grime, M. Dawson, M. Marsh, I.C. McArthur, F. Watt, Nucl. Instr. and Meth. B 54 (1991) 52.
[4] T. Butz, G.J.F. Legge, Nucl. Instr. and Meth. B 113 (1996) 317.
[5] P.H.A. Mutsaers, Nucl. Instr. and Meth. B 113 (1996) 323.
[6] D.J.W. Mous, R.G. Haitsma, T. Butz, R.-H. Flagmeyer, D. Lehmann, J. Vogt. Nucl. Instr. and Meth. B 130 (1997) 31.
[7] A.D. Dymnikov, D.N. Jamieson, G.J.F. Legge, Nucl. Instr. and Meth. B 104 (1995) 64.
[8] F. Watt, J.A. van Kan, I. Rajta, A.A. Bettiol, T.F. Choo, M.B.H. Breese, T. Osipowicz, Nucl. Instr. and Meth. B 210 (2003) 14.
[9] D. Spemann, T. Reinert, J. Vogt, D. Dobrev, T. Butz, Nucl. Instr. and Meth. B 190 (2002) 312.
[10] D.N. Jamieson, Nucl. Instr. and Meth. B 181 (2001) 1.
[11] T. Butz, R.-H. Flagmeyer, J. Heitmann, D.N. Jamieson, G.J.F. Legge, D. Lehmann, U. Reibetanz, T. Reinert, A. Saint, D. Spemann, R. Szymanski, W. Tröger, J. Vogt, J. Zhu, Nucl. Instr. and Meth. B 161–163 (2000) 323.
[12] D. Spemann, T. Reinert, J. Vogt, J. Wassermann, T. Butz, Nucl. Instr. and Meth. B 210 (2003) 79.
[13] T. Reinert, M. Morawski, Th. Arendt, T. Butz, Nucl. Instr. and Meth. B 210 (2003) 395.
[14] M. Morawski, T. Reinert, Ch. Meinecke, Th. Arendt, T. Butz, Nucl. Instr. and Meth. B 231 (2005) 224.
[15] H. Fedorow, F. Tribl, G. Halliday, M. Gerlach, P. Riederer, K.L. Double, Prog. Neurobiol. 75 (2005) 109.

Source Identification of Lead Pollution in the Atmosphere of Shanghai City by Analyzing Single Aerosol Particles (SAP)

J. WANG,*,+ P. GUO,+ X. LI,+ J. ZHU,+,§
T. REINERT,§ J. HEITMANN,§
D. SPEMANN,§ J. VOGT,§
R.-H. FLAGMEYER,§ AND T. BUTZ§

*Shanghai Institute of Nuclear Research, CAS,
P.O. Box 800-204, 201800 Shanghai, China, and Fakultat fur
Physik und Geowissenschaften, Universitat Leipzig,
Abtelung Nukleare Festkorperphysik, Linnestrasse 5,
04103 Leipzig, Germany*

A new method combining the pattern recognition (PR) technique with micro-PIXE spectrum was used for direct assessment of lead pollution in the atmosphere of Shanghai City. Single aerosol particles (SAP) of PM$_{10}$ (<10 μm) were analyzed using the nuclear microprobe. Every particle is characterized with its micro-PIXE spectrum, which can be considered its fingerprint. The PR technique was applied to trace a lead contaminated aerosol particle back to its source. The discrimination of different pollutant sources was enhanced with investigating the individual aerosol particles. The results showed that the lead contamination from automobile exhaust should not be neglected. The lead concentration with low level was detected in most unleaded gasoline particles; however, the highest lead level of 1500 ppm was found in one of them. Furthermore, four other main pollutant sources contributing to the lead contamination in the Shanghai atmosphere were clearly identified by this method. They are the cement industry, the coal combustion, the oil combustion, and the metallurgic industry. Some other unidentified particles suggested that some more lead emitters might also exist in Shanghai.

Introduction

The lead pollution in atmospheric environment has been emphasized since the 1960s because of its potential adversity to health effects (*1*). Recent research of lead toxicity shows that lead, even at a trace level, can affect children growth and intelligence (*2*). Lead pollution has been widespread in some industrialized areas. Shanghai is a big commercialized and industrialized city in China. It has a population of 13 millions and has been developing rapidly in recent years. Atmospheric quality has been paid much attention in coordinated with the industrial activities. The high lead level in the local atmosphere turned to be a crucial environmental problem since the early 1990s (*3*). It has been improved after the local government phased out of the leaded gasoline in 1997. Even with this improvement, recent environment

* Corresponding author phone: 8621 5955 3998 ext. 276; fax: 8621 5955 3021; e-mail: spm@sinr.ac.cn.
+ Shanghai Institute of Nuclear Research.
§ Fakultät für Physik und Geowissenschaften.

survey shows that the lead pollution still widely exists in the atmosphere of Shanghai. Anthropologic lead pollution in the air is mostly derived from the industrial activity (*4*). To find ways to reduce its quantity and impacts, it requires a good understanding of the lead emitter sources.

There have been many reports on the source identification of lead contamination in the field of environmental science (*5−7*). The majority of them relied on bulk elemental analysis of filters loaded with the sampled particles, which were called by total suspended particles (TSP). Enrichment factors, chemical mass balance, relative lead concentration and isotopic ratios were the main methods used for the data procession (*7−11*). The principle for these methods was that for each measurement they could give out the relative contribution of the lead sources to the local environment. Because they measured many different particles as a whole, the ambiguities of lead pollution source identification might happen, and some minor lead sources would be lost even if a large amount of sample measurements and a time-consuming statistic data handling were used (*12*, *13*).

The limitation of the bulk analytical method can be avoided by the method of single aerosol particle (SAP) analysis (*14*). Applying this method, the size, shape, and color of the analyzed particles, which are important in aerosol studies, can be selected. Some individual particles may have their characteristic elements at concentrations lower than the detection limits of bulk analysis. However, these elements can be easily determined by single particle analysis. Although the electron microprobe can measure individual aerosol particles very efficiently, its relatively low sensitivity restricted its applications because some important trace element features in individual particles may be lost (*15*).

The development of the nuclear microprobe offers a new possibility for SAP studies. It is suitable to the individual particle analysis because it has a reasonable spatial resolution (1 μm), high sensitivity, and versatile analytical techniques (*16*, *17*). These advantages give micro-PIXE analysis a unique role in determining low levels of trace elements, such as lead in a SAP (*18*). The PIXE spectrum pattern was considered the fingerprint of the particle. A method of pattern recognition (PR) was developed for the identification of the spectrum pattern. The strategy for the fingerprint classification and identification was used to identify each measured aerosol particle.

There are two steps for the identification of lead contaminated particles in the atmosphere. At first, a set of particles PM$_{10}$ (<10 μm) was collected from the probable lead emitter sources in Shanghai City. Micro-PIXE analysis was performed on these single particles one by one. Their spectra were recorded into a database as a fingerprint library of the local lead pollution sources. Then, another set of SAP (also PM$_{10}$) was collected from the center of the city. These environmental monitor samples were analyzed by the same way, and the PR method was used to compare their spectra with those in the library and to identify the origins of these lead contaminated particles.

Materials and Methods

Sample Collection and Preparation. The TSP source samples were collected from 20 industrial trails, such as ferrous and nonferrous smelters, iron and steel plants, oil and coal combustors, cement factories, building construction sites, and automobile exhaust gases, etc. These sources were thought to contribute most of the aerosol particles floating in the atmosphere over the Shanghai City. The environmental monitor samples were collected in the atmosphere 2 m above

the ground at the city center. Hence, they represented the most harmful particles of risk to the urban residents.

A cascade impact sampler (model HY-1) was used, and single particles were collected on polystyrene fibrillate filters. Ninety-seven percent of the particles were smaller than 10 μm, and 70% of them were smaller than 3 μm. Several methods for SAP sample preparation had been reported in our earlier works (*19*). However, none of them could separate small particles (<3 μm) clearly, and only groups of SAP had been measured (*20*). To measure the single particles one by one, it was essentially important to isolate the particles from each other on a thin foil. The isolated particles should be close enough to be found easily during a beam scanning. Keeping these requests in mind, a new method for SAP sample preparation was developed.

A solution of nylon powder in isobutyl alcohol was prepared at a temperature of 80 °C. A droplet of the solution was dropped onto a rotary beaker of deionized water at room temperature. The droplet stretched, and a very thin (0.2 μm) nylon foil was formed on the water surface. Just after the formation of the foil (in a few seconds), the collected single particles were dispersively dropped from the filter onto the sticky foil by a small shaker. After 5 min of solidification, the foil attached on a stainless steel frame was taken out of the water. The single particles were separately embedded in the thin, taut, and flat nylon foil. After 24 h baking at a temperature of 60 °C, the SAP sample was ready for individual particle analysis by the nuclear microprobe.

Single Aerosol Particles (SAP) Measurement by the Nuclear Microprobe. A reliable and efficient experiment for SAP analysis demanded good performances of the nuclear microprobe. Because most of the particles were smaller than 3 μm, both high spatial resolution and high beam current were needed. The Leipzig nuclear microprobe, LIPSION satisfied the experimental requirements. A detailed description of LIPSION could be found elsewhere (*21*). A 100 μm object diaphragm and a 100 μm aperture diaphragm were used to produce a focused beam spot with 1 μm size and 80 pA beam current. Random beam scanning and two stations list mode were used for the PIXE and RBS data acquisition (*22*). The micro-PIXE spectrum provided the major information for PR identification. The RBS spectrum was used for judgment of some ambiguous results coming from PIXE alone. The particles were so small that this analysis could be considered thin target measurements. The beam charge was collected with a downstream Faraday cup. There were no conductive coating on the sample surface and no data correction for the effects of the particle matrix and shapes. A 20 nC integrated beam charge was required for each particle measurement. Each single particle measurement took about 15 min. The accelerator and the microprobe of LIPSION performed in a very stable working condition. Both the high stability of the beam and the high precision of the sample displacement made the SAP measurements very efficient.

Figure 1 shows a micro-PIXE spectrum of an individual particle coming from leaded gasoline. A rough assessment of the chemical composition in a single particle could be achieved simply by visual inspection of its spectrum feature. In the source identification of SAP, one is mostly interested in whether a given particle has the same composition as a known source particle, rather than the quantitative chemical composition of the particle. From this point of view, we propose the application of pattern recognition to the identification of individual aerosol particles by directly using their micro-PIXE spectra.

Spectrum Identification with Pattern Recognition (PR). The principle of the pattern recognition technique has been described in detail elsewhere (*23*, *24*). Here, a brief description of the method and its application to PIXE spectrum was presented as followings.
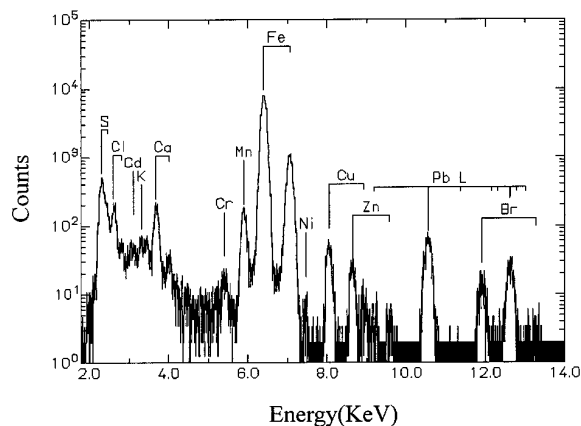

FIGURE 1. A PIXE spectrum of an individual aerosol particle coming from leaded gasoline.

A PIXE spectrum can be treated as an *n*-component column vector in an *n*-dimensional Euclidean space. In pattern recognition, two PIXE spectra are considered similar if the Euclidean angle between the two spectrum vectors in the *n*-dimensional Euclidean space is close to zero. The discriminative function is defined as below:

$$\cos \theta = \vec{X} \cdot \vec{Y} / [(\vec{X} \cdot \vec{X})(\vec{Y} \cdot \vec{Y})]^{1/2}$$

Here $\vec{X}$ and $\vec{Y}$ are the transposes of $\vec{X}$ and $\vec{Y}$, respectively. The numerator is the dot product of the two vectors, and the denominator is the product of their magnitude. The cos θ means the degree of similarity for the two spectra. Its value will be close to 1 if the two PIXE spectra have similar features. The value of cos θ is independent of the intensities of the spectra.

The PR program for the SAP identification was developed on a personal computer. The flowchart of the program was shown in Figure 2. All the PIXE spectra of the particles from the lead emitter sources were stored as a database of reference spectra patterns. Any unknown spectrum could be identified with the program in 0.1 s. The PR program ran with graphic user interface (GUI). It was easy to operate even for inexperienced persons.

Results and Discussion

Fingerprints of Emitter Source. The discrimination of different pollutant sources was enhanced by investigating single aerosol particles (SAP). Two hundred SAPs from emitter sources were analyzed. About 60 particles had detectable lead. Their micro-PIXE spectra were classified according to the corresponding pollutant sources. Each source had its typical fingerprint and some subfingerprints with different characterization of PIXE spectra. These lead contaminated particles could be classified into six categories. They were the cement industry, the automobile exhaust using both leaded and unleaded gasoline, the oil combustion, the coal combustion, and the metallurgic industry. Their average elemental concentrations were analyzed with the program TTSPM (*25*).

Six typical elemental profiles of the lead emitter sources were shown in Figure 3. Each source was featured with its characteristic elements. The main feature of high calcium concentration (35.5%) was found in cement source. The 280 ppm lead concentration in cement source came from its raw materials in the processing. High iron concentration could be found in the particles from the steel smelters. The lead (810 ppm) and some other toxic elements such as cadmium (<10 ppm) were also found in these industrial pollutant sources. They came from the raw materials used. Figure 4
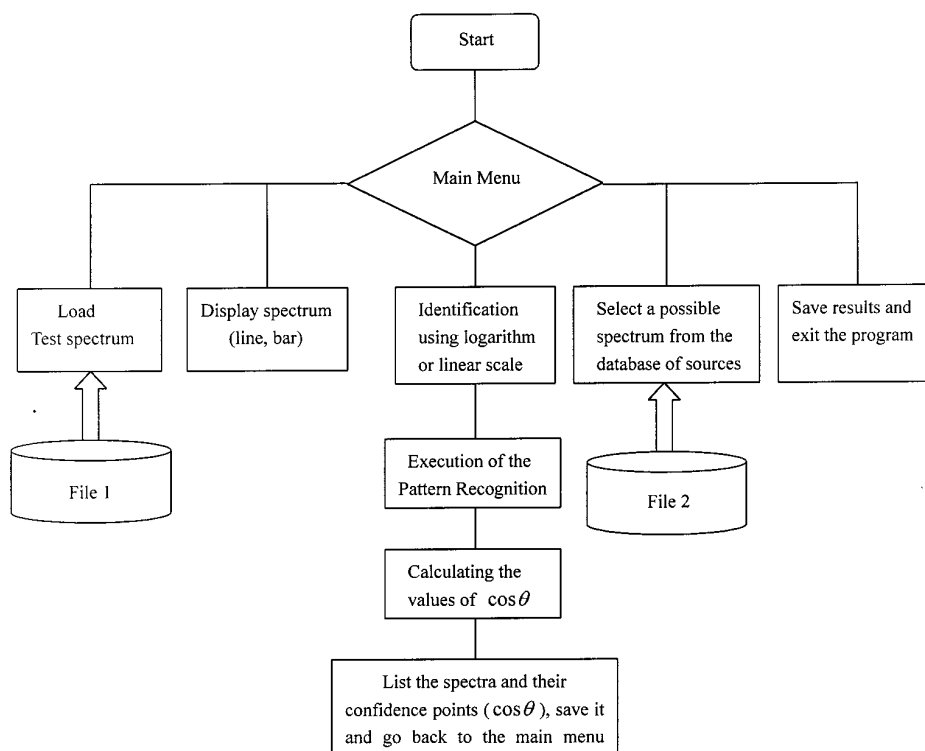
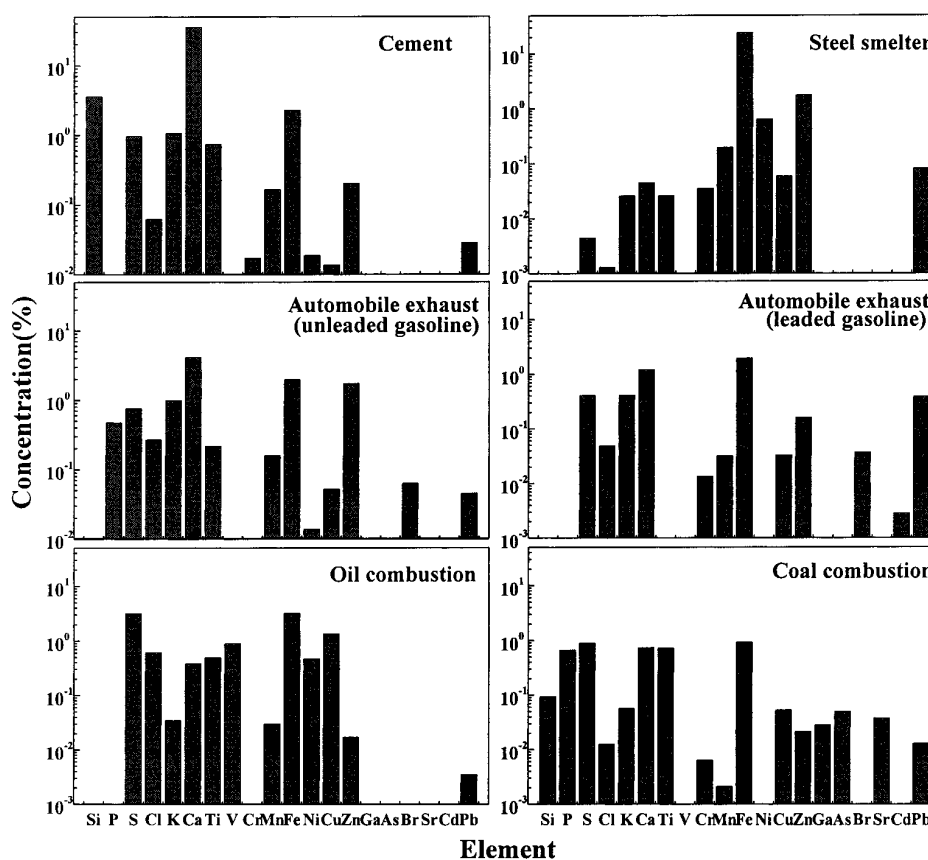FIGURE 2. The flowchart of the pattern recognition program.

FIGURE 3. Six typical elemental profiles of the lead emitter sources.
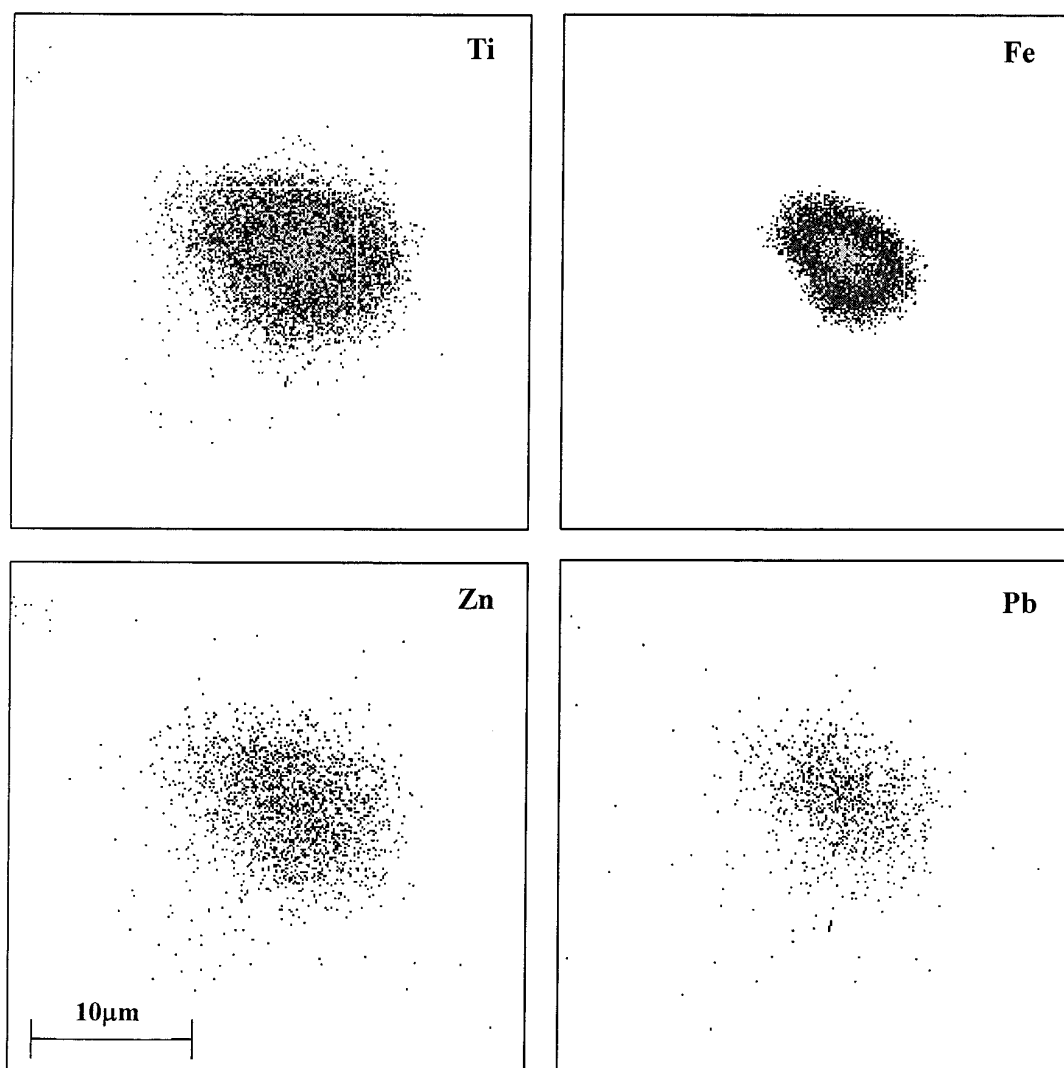
FIGURE 4. The elemental distribution maps of an individual particle from a steel smelter.

showed the elemental distribution maps of titanium, iron, zinc, and lead in an individual particle from the steel smelter. The scan size was 30 μm $\times$ 30 μm. It showed from the maps that these elements seemed to be homogeneously distributed in the individual particle.

The individual particles from automobile exhaust using both leaded and unleaded gasoline were measured as different categories of the pollutant sources. The average lead concentration (3800 ppm) in the particles from leaded gasoline was much higher than that of the particles from the other lead pollutant sources. It seemed to dominate the lead input into the atmosphere. Low lead concentration in average (450 ppm) was detected in the particles from unleaded gasoline. However, the lead value of each particle varied wildly from a few tens to hundreds ppm. It was surprising to detect a particle having 1500 ppm lead concentration. The lead in the particles from unleaded gasoline is derived from the crude oil. It was different from the situation of leaded gasoline, in which lead had been added to the oil as the lead-based antiknock compounds. The toxic metal cadmium was also found in the particles from leaded gasoline. Bromine and chlorine could be found in particles from automobile exhaust using both leaded and unleaded gasoline. It was a feature used to distinguish them from other lead pollutant sources.

The elemental distribution maps from an individual particle of automobile exhaust using leaded gasoline were shown in Figure 5. The distribution of manganese, iron, and zinc in the particle seemed to be homogeneous, but the lead seemed not. This observation indicated that lead is attached at the surface of the particle during combustion. It had been clear that many toxic elements having boiling points below the normal combustion temperature were volatilized in the process of combustion (26). They condensed onto the surrounding particles after cooling, and thus it was expected that the surfaces of the particles from automobile exhaust were enriched with these elements. The lead distribution of these particles were quite different from that of the particles from the steel smelter (Figure 4). The biological toxicity of SAP depended upon the toxic element concentration and its distribution profile in the particle. The lead enrichment at the particle surface would make it more soluble than that buried in the particle. Therefore, it would be more harmful to the local residents (27).

The characteristic elements for SAPs from oil combustion were vanadium, nickel, and copper. Those from coal combustion were arsenic and strontium. They contained relatively low lead at concentrations of 40 and 130 ppm, respectively. The pollutant source of coal combustion included some subfingerprints, which depended upon the chemical composition of raw coal used and the type of the combustion process.
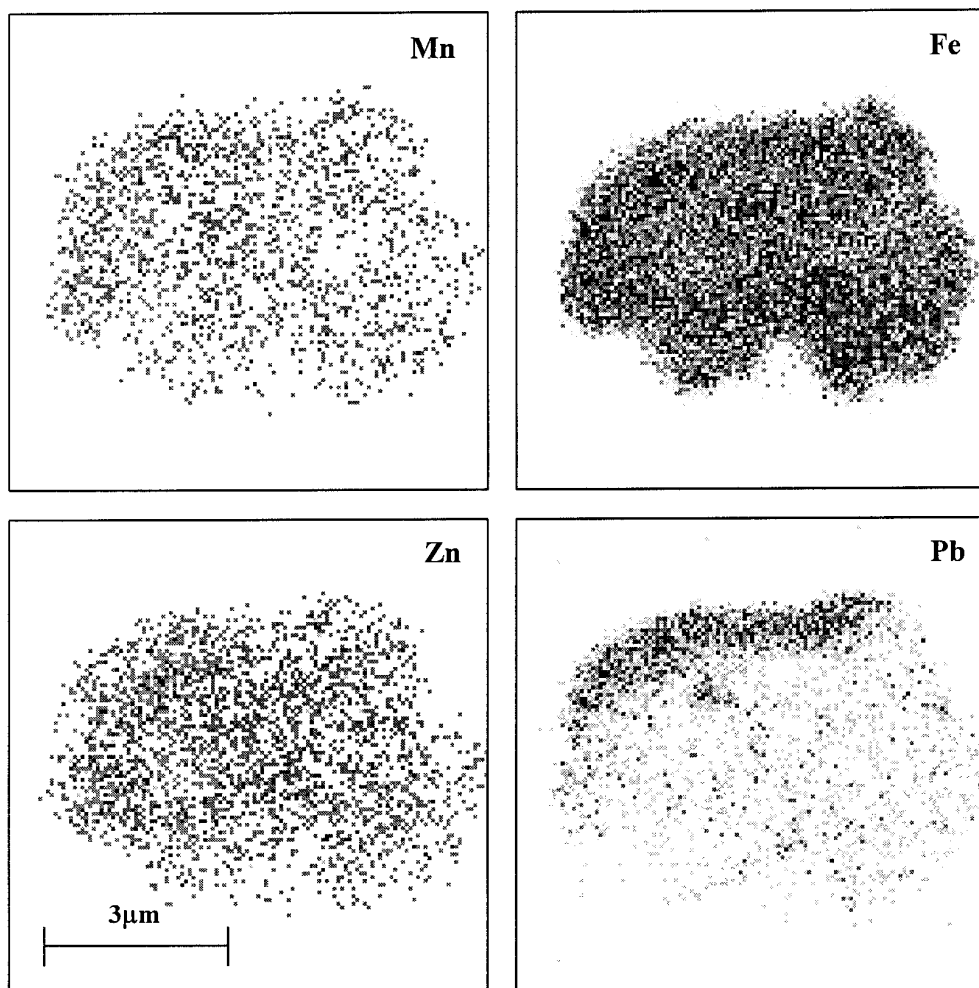
FIGURE 5. The elemental distribution maps of an individual particle from leaded gasoline.
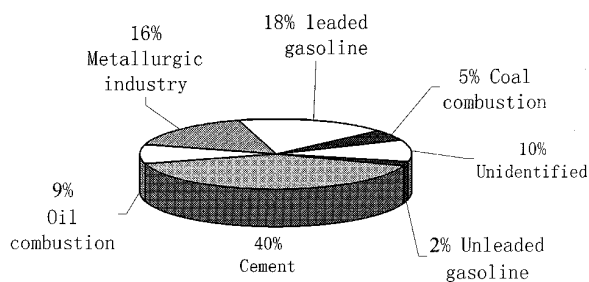

FIGURE 6. The origins of lead contaminated particles in the atmosphere of Shanghai City.

Environmental Samples Identification. Five hundred SAPs of environmental monitor samples were collected from the center of Shanghai. These samples were analyzed with the same facilities as before. Their micro-PIXE spectra were compared with the spectra of the pollutant source particles by the PR program. The origins of these particles were then identified. About 50 lead contaminated particles were found in the environmental samples. These particles belonged to seven categories of pollution sources. They were the cement industry, automobile exhaust using both leaded and unleaded gasoline, oil combustion, coal combustion, the metallurgic industry, and some unidentified sources. Figure 6 showed the relative contributions of these lead pollution sources to the local atmosphere. About 40% of lead contaminated particles were derived from the cement industry. It was true

because the municipal construction had been the largest business in the city recently. About 20% of them came from automobile exhaust due to the heavy traffic in the sampling area. Most of them belonged to the leaded gasoline category. Shanghai government had phased out of the leaded gasoline since 1997. However, the SAP analyzing results indicated that the contribution of the leaded gasoline still dominated the lead input to the local atmosphere. Shanghai is a busy metropolis. A lot of vehicles transit through the city from other areas, where the leaded gasoline is still used. The illegal supply of the leaded gasoline in the city might be continued. Another reason for the high contribution of the leaded gasoline might be the earlier lead contaminated particles blown up by the heavy traffic.

About 10% of the lead contaminated particles could not be identified. It was suggested that they might come from other lead pollution sources, which had not yet included in our investigation list. It gave hints for discovering new lead pollutant sources.

In conclusion, the discrimination of different pollutant sources could be enhanced by the combination of SAP analysis and pattern recognition technique. The features of SAPs were characterized with their micro-PIXE spectra. The original source of any SAP could be recognized by its spectrum pattern in comparing with the source spectra, which had been compiled in a library. The results showed that the automobile exhaust still contributed most of the lead pollution to the Shanghai atmosphere, though the usage of

leaded gasoline had been officially prohibited for 2 years in the city. Another important lead contributor in the city was the cement industry. Although its average lead concentration was not so high, more attention must be paid on it because a large amount of lead containing SAPs were given out from the cement factories.

Acknowledgments

Literature Cited

(1) U.S. Environmental Protection Agency. Air Quality Criteria for Lead; EPA 600/8-83-028a-d; Environmental Criteria and Assessment Office, Office of Research and Development: Research Triangle Park, NC, 1986.

(2) Centers for Disease Control. *Preventing Lead Poisoning in Young Children: A Statement by The Centers for Disease Control*; U.S. Department of Health and Human Services: Atlanta, GA, October 1991.

(3) Chen, M.; Chen, J.; Li, D. *Shanghai Environmental Sciences (in Chinese).* **1997**, *10*, 15.

(4) Mackenzie, A. B.; Farmer, J. G.; Sugden, C. L. *Sci. Total Environ.* **1997**, *203*, 115.

(5) Hamelin, B.; Ferrand, J. L.; Alleman, L.; Nicolas, E.; Veron, A. *Geochim. Cosmochim. Acta* **1997**, *20*, 4423.

(6) Kersten, M.; Dieter, C.; Schonberg, G.; Thomsen, S.; Anagnostou, C.; Sioulas, A. *Environ. Sci. Technol.* **1997**, *31*, 1295.

(7) Adgate, J. L.; Willis, R. D.; Buckley, T. J.; Chow, J. C.; Watson, J. G.; Rhoads, G. G.; Lioy, P. J. *Environ. Sci. Technol.* **1998**, *32*, 108.

(8) Fergusson, J. E.; Kim, N. D. *Sci. Total Environ.* **1991**, *100*, 125.

(9) Hunt, A.; Johnson, D. L. I.; Watt, J. M.; Thomton, I. *Environ. Sci. Technol.* **1992**, *26*, 1513.

(10) Hunt, A.; Johnson, D. L. I.; Watt, J. M. *Environ. Sci. Technol.* **1993**, *138*, 183−206.

(11) Wang, Y. E.; Willis, R. D.; Buckley, T. J.; Rhoads, G. G.; Lioy, P. *J. Appl. Occup. Environ. Hyg.* **1996**, *11*, 199.

(12) Cohen, D. D.; Bailey, G. M.; Kondepudi, R. *Nucl. Instr. Meth.* **1996**, *109/110*, 218.

(13) Marcazzan, G. M. B. *X-ray Spectrum.* **1998**, *4*, 247.

(14) Grime, G. W. *X-ray Spectrum.* **1998**, *4*, 221.

(15) Grieken, R. V.; Hoornaert, S.; Gysels, K.; Osan, J.; Worobjec, A. *Proceedings of the 6th International Conference on Nuclear Microprobe Technology and Applications*; Oct 11−16, 1998; Spier Estate, S. Africa.

(16) Hickmott, D. D.; Herrin, J. M.; Abell, R.; George, M.; Stimac, J.; Gauerke, E. R.; Denniston, R. F. *Nucl. Instr. Meth.* **1997**, *130*, 564.

(17) Orlic, I.; Osipowicz, T.; Watt, F.; Tang, S. M. *Nucl. Instr. Meth.* **1995**, *104*, 630.

(18) Olech, M.; Kwiatek, W. M.; Dutkiewicz, E. M. *X-ray Spectrum.* **1998**, *4*, 232.

(19) Sha, Y.; Gu, Y.; Liu, G.; Wang, A.; Zhang, P.; Zhu, J.; Shi, J.; Yang, S.; Liu, P.; Li, X. *Nucl. Instr. Methods* **1996**, *109/110*, 79.

(20) Sha, Y.; Shi, J.; Gu, Y.; Zhu, J.; Li, X. *Nucl. Sci. Techniques* **1996**, *7*, 61.

(21) Mous, D. J.; Haitsma, R. G.; Butz, T.; Flagmeyer, R.-H.; Lehmann, D.; Vogt, J. *Nucl. Instr. Meth.* **1997**, *130*, 31.

(22) O'Brien, P. M.; Moloney, G. *Nucl. Instr. Meth.* **1993**, *77*, 52.

(23) Tou, J. T.; Gonzales, R. C. *Pattern Recognition Principles*; Addison-Wesley Publishing Co.: 1974.

(24) Yin, L. I.; Seltzer, S. M. *Adv. X-ray Anal.* **1990**, *33*, 603.

(25) Wu, K.; Zhu, J.; Lu, R.; Yang, F. *Nucl. Instr. Meth.* **1995**, *104*, 196.

(26) Jaksic, M.; Watt, F.; Grime, G. W.; Cereda, E.; Braga, G. M.; Valkovic, V. *Nucl. Instr. Meth.* **1991**, *56/57*, 699.

(27) Linton, R. W.; Loh, A.; Natusch, D. F. S. *Science* **1976**, *191*, 852.

Identification of air pollution sources by single aerosol particle fingerprints – micro-PIXE spectra

J. Wang [a], P. Guo [a], X. Li [a], J. Zhu [a,b,*], T. Reinert [b], J. Heitmann [b], D. Spemann [b], J. Vogt [b], R.-H. Flagmeyer [b], T. Butz [b]

[a] *Shanghai Institute of Nuclear Research, Chinese Academy of Sciences, P.O. Box 800-204, 201800 Shanghai, People's Republic of China*
[b] *Fakultät für Physik und Geowissenschaften, Abteilung Nukleare Festkörperphysik, Universität Leipzig, Linnéstr. 5, 04103 Leipzig, Germany*

Abstract

A new method for direct assessment of air pollution is developed by using nuclear microprobe techniques to analyse single aerosol particles (SAP). Every particle is characterized by its PIXE spectrum which can be considered to be its fingerprint. The strategy for fingerprint classification and identification is used to trace a measured aerosol particle to its original source. Most of the particles have a size of up to 3 μm. The particles are separately attached to a clean thin foil. The Leipzig Nanoprobe, LIPSION, is used for this study. There are two steps in the new method. First, collect samples from different sources, measure them and compile their characteristic spectra into a library. Then, assess the environmental samples by comparing their spectra with those in the library. An artificial neural network (ANN) package is used for spectrum comparison. © 2000 Elsevier Science B.V. All rights reserved.

PACS: 07.79.–v; 06.60.Ei; 07.05.Mh; 89.60.+x
Keywords: Single aerosol particle; Nuclear microprobe; PIXE; Artificial neural network

1. Introduction

Atmospheric environmental pollution is a global problem because aerosol particles can be transported over long distances and they have impacts on the global climate [1]. One of the major goals of environmental pollution monitoring and controlling is to identify the pollution sources and find ways to reduce their impacts. There have been many reports on the IBA applications to air pollution assessment, the PIXE technique in particular has been used widely and routinely for this purpose. Most of them used the bulk analysis of the total suspended particles (TSP) loaded on filters. Because many different particles are measured as a whole, ambiguities of pollution source identification occurred even if a large amount of sample measurements and a time consuming statistical data handling were used [2,3].

The limitation of the bulk analytical method can be avoided by the method of single aerosol particle (SAP) analysis. Applying this method, the size, shape and colour of the analysed particles,

---
* Corresponding author. Tel.: +86-21-5955-3998; fax: +86-21-5955-3021.
E-mail address: iamzhu@hotmail.com (J. Zhu).

which are important in aerosol studies, can be selected. The characteristic elements of some individual particles may be at concentrations lower than the detectable limits of bulk analysis. However, these elements can be easily determined by single particle analysis. Although the electron microprobe can measure SAP very efficiently [4], its relatively low sensitivity restricted its applications, because some important trace element features in SAP may be lost.

A nuclear microprobe is suitable for SAP analysis, because it offers a reasonable spatial resolution (1 μm), high sensitivity and versatile analytical techniques [5,6]. It has been proved that the PIXE results of single particle analysis agree with those of bulk analysis to a tolerance of 10–20% [7,8]. Because of the geometrical and morphological factors of individual particles, the traditional quantitative PIXE analysis programs cannot be used with good accuracy [9]. Some calculation methods which try to reduce these effects have been discussed [10]. However, we can recognize each particle directly by its spectrum instead of its chemical composition. The spectrum pattern can be considered to be each particle's fingerprint. The strategy for the fingerprint classification and identification can be used to identify each measured aerosol particle. Based on the artificial neural network (ANN) technique, a pattern recognition procedure is developed for the identification. There are two steps in the procedure. First, a set of particles collected from different pollution sources is analysed by the nuclear microprobe. Their single particle PIXE spectra are recorded in a database as a fingerprint library of the pollution sources. Then, the environmental particles are measured with the same facilities. Their identification is performed by the ANN program when it reads the spectra of the particles.

2. SAP measurement

2.1. SAP sample preparation

The pollution source samples were collected from industrial excrements, such as ferrous or nonferrous smelters, iron and steel plants, oil or coal combustors, cement factories, building construction sites, vehicle exhausted gas and soil dusts. They contribute most of the aerosol particles floating in the atmosphere over Shanghai city. The environmental monitor samples were collected at the city centre.

A cascade impact sampler (model HY-1) is used and SAPs are collected on polystyrene fibre filters. 97% of the particles are smaller than 10 μm and 70% of them are smaller than 3 μm. Several methods for SAP sample preparation have been reported in our earlier work [11]. However, none of them could separate small particles (<3 μm) clearly and only groups of SAP had been measured [12]. In order to measure single particles one by one, it is essential to isolate the particles from each other on a thin foil. The isolated particles should be close enough to be found easily during a beam scanning. Keeping these requirements in mind, a new method for SAP sample preparation was developed.

A solution of nylon powder in iso-butyl alcohol was prepared at a temperature of 80°C. A droplet of the solution was dropped onto a rotary beaker of deionized water at room temperature. The droplet spread out and a very thin (0.2 μm) nylon foil was formed on the water surface. Just after the formation of the foil (in a few seconds), the collected single particles were dropped dispersively from the filter onto the sticky foil by a small shaker. After five minutes solidification, the foil attached to a stainless steel frame was taken out of the water. The single particles were separately embedded in the thin, clean and taut nylon foil. After 24 h baking at a temperature of 60°C, the SAP sample was ready for single particle analysis by the nuclear microprobe.

2.2. SAP measurement by the nuclear microprobe

Because most of the particles are smaller than 3 μm, both high spatial resolution and high beam current are needed. The Leipzig nuclear microprobe, LIPSION, satisfied the experimental requirements. A detailed description of LIPSION can be found in another contribution to this conference [13]. A 100 μm object diaphragm and a 100 μm aperture diaphragm were used to

produce a focused beam spot with 1 μm size and 80 pA current. A 50 nC integrated beam charge was required for each particle measurement.

Much experimental time was spent on searching for isolated small particles. A proper searching procedure was important for high experimental efficiency. At first, a large scan was needed to survey the sample in order to find areas where the isolated small particles were accumulated. Fig. 1 shows a PIXE image in a large scanning area $(28 \times 28 \ \mu m^2)$, in which several isolated small particles were closely situated. The coordinates of each small particle in the large scanning area were digitized and recorded for further small scans. A small scanning area (6–10 μm) was set up and one or more isolated particles were moved into the area. Fig. 2 shows nine examples of PIXE images in the small scan area. The high stability of the beam and the high precision of the sample positioning made the SAP measurements very efficient. In average, a total of 15 min was needed to search for and to measure each of the single particles. It is

economically acceptable for an enlarged investigation.

The characteristic PIXE spectrum of each particle was extracted from raw data according to the particle shape. Fig. 3 shows a PIXE spectrum extracted from a particle excreted by a vehicle burning leaded petrol. A rough assessment of chemical composition in a single particle could be achieved simply by visual inspection of its spectral features. Hence, one could estimate the possible source of a particle from its spectrum provided that the spectral features of particles from all sources had been learnt beforehand. In order to do this, an ANN program called PATTERN was used.

3. Spectrum identification with ANN technique

The ANN attempts to simulate the function of the human brain for qualitative assessment. It has been applied successfully to the interpretation of various spectra in the fields of infrared [14,15],
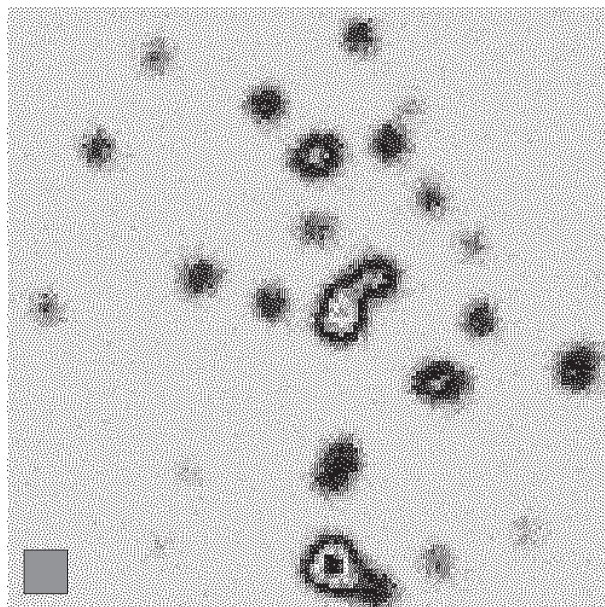

Fig. 1. PIXE image in a medium-sized $(28 \times 28 \ \mu m^2)$ scanning area, in which several isolated small aerosol particles are closely situated. A 2 μm square mark is presented at the bottom left of the area.
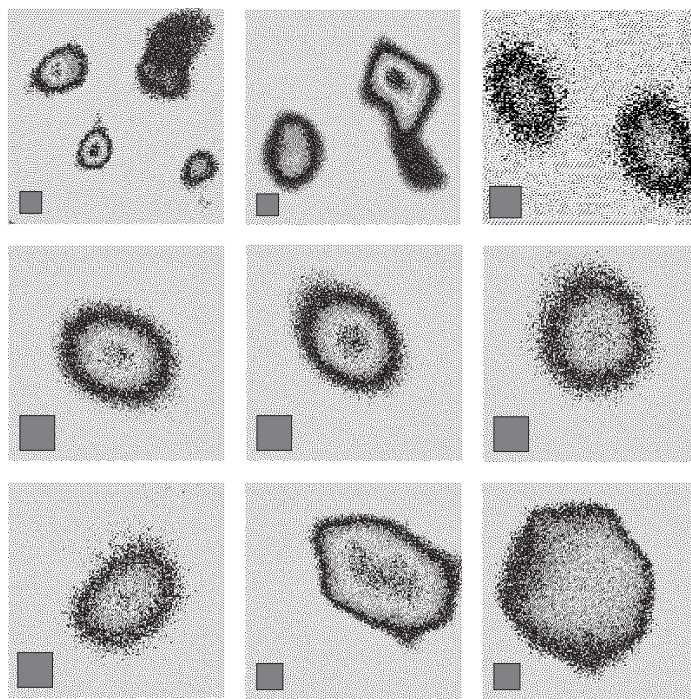
Fig. 2. Nine examples of PIXE images in small scan areas (6–10 μm), in which one or more isolated small aerosol particles are covered. A 1 μm square mark is presented in each area showing the size of the particles.
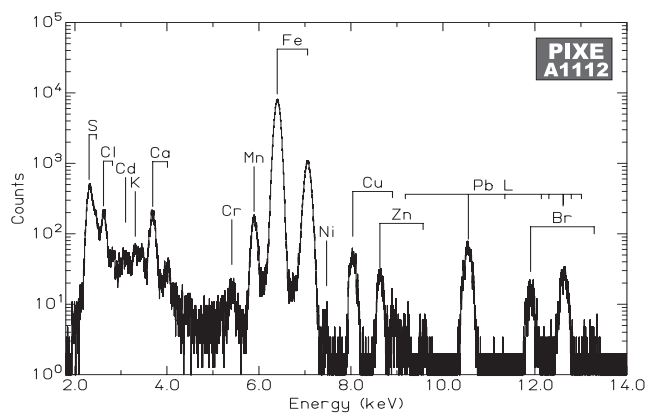

Fig. 3. PIXE spectrum extracted from a single aerosol particle excreted by a vehicle burning leaded petrol. Harmful elements Pb, Br and Cd can be seen in the spectrum.

ultraviolet [16], gamma-ray [17], and X-ray [18,19] spectroscopy. An extensive description of ANN by McClelland and Rumelhart is available [20].

An artificial neuron receives signals from external sources or from other neurons and produces one output value that can be used as an input to

other neurons or an output result of the network. The topology of an ANN depends on the complexity of application. A three-layer architecture (input, middle and output) is used in this work. The input layer contains 1024 neurons corresponding to 1024 channels of a spectrum. The output layer contains N neurons corresponding to the number of reference patterns (pollution sources). Each of the neurons in the output layer produces an output value 1 or 0 (>0.7 or <0.3).

Like a real brain, an ANN has to take a training course before doing any identification jobs. The purpose of the network training is to find the right combination of all parameters in a network which can produce a desired output code for every reference pattern. While the network reads a reference pattern, the modifications of the parameters take place in the backward direction, that is from the output layer to the input layer. After several periods of modification and regressions, the final total error for all of the input patterns reaches a low criterion. The training course is then finished and all the "knowledge" learned in the course is stored in a matrix. The neural network is now able to perform a reliable identification job for any unknown input pattern. Only when an unknown spectrum fits one of the reference patterns well enough, does its corresponding neuron give out a value of 1. All others give an output of 0.

4. Results and discussion

74 SAPs from pollution sources were measured. Their PIXE spectra were classified according to the corresponding sources. 12 reference spectrum patterns characteristic of their sources were recognized and used for the ANN training. 309 environmental monitoring particles were collected at the city centre of Shanghai. The environmental samples were measured with the same facilities. Their PIXE spectra were read by the network and their origins were then identified.

The apportionment of the air pollution sources in Shanghai resulting from the network identification is presented in Fig. 4. The cement industry contributes one-third of the aerosol particles in the region. It is true that municipal construction has
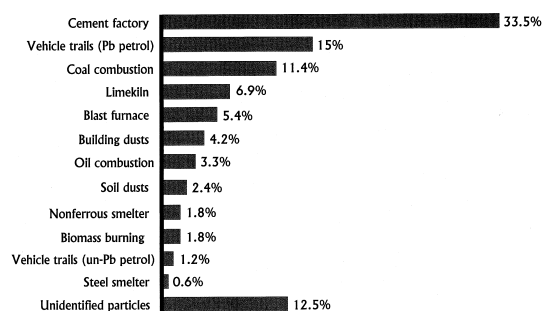

Fig. 4. Apportionment of single aerosol particles in Shanghai according to their origins.

been the largest business in the city recently. Due to the heavy traffic in the city, the gas exhausted by vehicles is the second largest contributor to the local air pollution. Surprisingly, it was discovered that the solid particles excreted by the vehicles contained obviously high levels of the harmful elements lead, cadmium and bromine (Fig. 3). Most vehicles in Shanghai are still burning leaded petrol.

In this investigation, 12.5% aerosol particles could not be identified. It was suggested that they might come from pollution sources other than those considered. By means of the pattern recognition in the ANN program, the unidentified particles could be clustered into nine species, which was useful for seeking new pollution sources.

5. Conclusion

From the point of view of environmental monitoring, 12 pollution sources and a few hundred particle samples are not enough for an accurate investigation in a large industrial city like Shanghai. This work is the beginning of a project dealing with ecological research and environmental conservation. It provides a new method for air pollution source identification and apportionment by direct SAP analysis and ANN assessment. A nuclear microprobe with micrometre spatial resolution, a bright and stable ion beam and precise sample placement is able to perform the single particle analysis efficiently enough for an enlarged investigation.

The result of the preliminary trial of this method with aerosol samples from Shanghai showed that more than one-third of the particles floating in the city atmosphere originated from the cement industry. 15% of the solid particles contained high levels of the harmful elements lead, cadmium and bromine. These particles have been excreted by traffic.

Acknowledgements

References

[1] R.J. Charlson, J. Langner, H. Rodhe, C.B. Leovy, S.G. Garren, Tellus AB 43 (1991) 152.

[2] D.D. Cohen, G.M. Bailey, R. Kondepudi, Nucl. Instr. and Meth. B 109/110 (1996) 218.

[3] G.M.B. Marcazzan, X-Ray Spectrum 27 (4) (1998) 247.

[4] R.V. Grieken, S. Hoornaert, K. Gysels, J. Osan, A. Worobjec, in: Proceedings of the Sixth International Conference on Nuclear Microprobe Technology and Applications, Spier Estate, South Africa, 11–16 October 1998.

[5] D.D. Hickmott, J.M. Herrin, R. Abell, M. George, J. Stimac, E.R. Gauerke, R.F. Denniston, Nucl. Instr. and Meth. B 130 (1997) 564.

[6] I. Orlic, T. Osipowicz, F. Watt, S.M. Tang, Nucl. Instr. and Meth. B 104 (1995) 630.

[7] W. Maenhaut, R. Salomonovic, J. Ptasinski, G.W. Grime, Nucl. Instr. and Meth. B 130 (1997) 576.

[8] F. Gerab, P. Artaxo, E. Swietlicki, J. Pallon, Nucl. Instr. and Meth. B 136/138 (1998) 318.

[9] M. Jaksic, I. Bogdanovic, E. Gereda, S. Fazinic, V. Valkovic, Nucl. Instr. and Meth. B 77 (1993) 505.

[10] S. Zhou, I. Orlic, J.L. Sanchez, C.L. Lee, F. Watt, in: Proceedings of the Sixth International Conference on Nuclear Microprobe Technology and Applications, Spier Estate, South Africa, 11–16 October 1998.

[11] Y. Sha, Y. Gu, G. Liu, A. Wang, P. Zhang, J. Zhu, J. Shi, S. Yang, P. Liu, X. Li, Nucl. Instr. and Meth. B 109/110 (1996) 79.

[12] Y. Sha, J. Shi, Y. Gu, J. Zhu, X. Li, Nucl. Sci. Techniques 7 (1) (1996) 61.

[13] T. Butz, R.-H. Flagmeyer, J. Heitmann, D.N. Jamieson, G.J.F. Legge, D. Lehmann, U. Reibetanz, T. Reinert, A. Saint, D. Spemann, R. Szymanski, W. Tröger, J. Vogt, J. Zhu, Nucl. Instr. and Meth. B 161–163 (2000) 323.

[14] K. Tanabe, T. Tamura, H. Uesaka, Appl. Spectroscopy 16 (5) (1992) 807.

[15] M. Meyer, T. Weigelt, Anal. Chim. Acta 265 (2) (1992) 183.

[16] C.R. Mittermayr, A.C.J.H. Drouen, M. Otto, Anal. Chim. Acta 294 (2) (1994) 227.

[17] Z. Cheng, M. Li, S. Xu, Nucl. Tech. (in Chinese) 19 (8) (1996) 449.

[18] A.L. Allanic, J.Y. Jezequel, J.C. Andre, Anal. Chem. 64 (21) (1992) 2618.

[19] M. Bos, H.T. Weber, Anal. Chim. Acta 247 (1) (1991) 97.

[20] J.L. McClelland, D.E. Rumelhart, Parallel Distributed Processing, vol. 1, MIT Bradfort Press, Cambridge, 1986.

Combination of Micro-PIXE with the Pattern Recognition Technique for the Source Identification of Individual Aerosol Particles

P. GUO,* J. WANG, X. LI, J. ZHU, T. REINERT, J. HEITMANN, D. SPEMANN, J. VOGT, R.-H. FLAGMEYER, and T. BUTZ

Shanghai Institute of Nuclear Research, CAS, P.O. Box 800-204, 201800 Shanghai, China (P.G., J.W., X.L., J.Z.); and Fakultät für Physik und Geowissenschaften, Universität Leipzig, Abteilung Nukleare Festkörperphysik, Linnestr. 5, 04103 Leipzig, Germany (J.Z., T.R., J.H., D.S., J.V., R.-H.F., T.B.)

In order to identify the sources of individual aerosol particles, we developed an identification system based on the combination of the micro-PIXE (particle-induced X-ray emission) technique with the pattern recognition (PR) technique. It uses the micro-PIXE spectrum of an individual aerosol particle as its fingerprint to identify the origin of the particles. A total of 294 micro-PIXE spectra of individual aerosol particles, collected at Shanghai City in China, were applied to test the PR system. These particles were collected from several pollution sources and a local environment monitor site. Most of the environment particles were identified, and the most probable sources were assigned by the PR system. It was found that cement factories and vehicle exhaust are the major contributors. About 14% of the particles from the environment monitor site could not be identified by their spectra. They might have come from some other sources we have not yet investigated. The validity and the efficiency of the system are evaluated and discussed. It is demonstrated that the combination of micro-PIXE with the pattern recognition technique offers a new, powerful tool for the source identification of individual aerosol particles.

Index Headings: **Individual aerosol particles; Pattern recognition technique (PR); Micro-PIXE.**

INTRODUCTION

One of the major problems in air pollution studies is the source identification of airborne particles. Although bulk analytical methods, such as broad-beam particle-induced X-ray emission (PIXE), using multivariate statistics techniques constitute a useful tool for identifying sources of the aerosol particles, they still have some limitations that can be avoided by single-particle analysis. The association of certain elements on a particular particle can be observed directly by single-particle measurement. Some elements tend to occur at relatively high concentration in a small particle. However, in a bulk measurement the concentration of these elements may be at a level lower than the detection limit. If these particles are measured individually, the associated elements can be determined easily. More advantages of the single particle analysis have been discussed by Van Espen,[1] Orilic,[2] and Grime.[3] Some successful analyses of individual airborne particles by nuclear microprobes have been reported.[4–7] The difficulty in accurate quantification of the element concentration in a single particle has been discussed by Jaksic et al.,[8] Bogdanovic et al.,[9] and Orilic et al.[10] To facilitate the source identification, a large-scale investigation of individual aerosol particles should be undertaken. Converting these spectra into exact element concentration is a difficult and time-consuming task. An ideal method should be rapid, automated, and relatively inexpensive.

Two samples with similar chemical composition should have similar spectral patterns. Therefore, the micro-PIXE spectra of individual aerosol particles can be used as the fingerprints of their chemical composition. In the source identification of an individual aerosol particle, one is mostly interested in whether a given particle has a spectral pattern similar to that of a known source particle, rather than its quantitative chemical composition. From this point of view, we propose the application of a pattern recognition technique for the identification of individual aerosol particles by using their micro-PIXE spectra. This approach essentially emulates visual inspection of the spectral features by a spectroscopist, but places the inspection on a more quantitative basis. It can be easily implemented with a personal computer. The pattern recognition approach has been adopted in practical applications of many analytical spectroscopy techniques.[11–13]

A set of individual aerosol particles from seven pollution sources was analyzed by a nuclear microprobe. Their micro-PIXE spectra were used to establish a fingerprint database for the pollution sources. Other individual aerosol particles were collected from a local environment monitor site and were analyzed with the same facilities. These particles were identified for their origins by comparing their micro-PIXE spectrum patterns with those in the fingerprint database by using the pattern recognition technique.

EXPERIMENTAL

Sample Collection and Preparation for Nuclear Microprobe Analysis. The pollution source samples of individual aerosol particles were collected from seven industrial plumes, such as ferrous smelters, oil and coal combustors, cement factories, construction sites, vehicle exhaust, and soil dusts. They contribute the majority of the aerosol particles floating in the atmosphere over Shanghai City. The environmental monitor samples were collected at the city center.

A cascade impact sampler (Sierra Anderson Instruments, Inc., Model HY-1) was used, and the aerosol particles were collected on thin polystyrene fiber filters. Ninety-seven percent of the collected particles are smaller
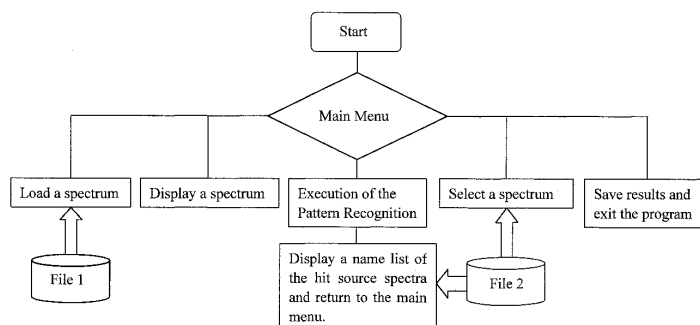
FIG. 1. The flow chart of the spectrum pattern recognition system. File 1: the spectrum files of individual aerosol particles; File 2: the spectrum files in the database of pollution sources.

than 10 μm and 70% of them are smaller than 3 μm. Several methods for the preparation of individual aerosol particles have been reported in our earlier work.[14] However, none of them could separate small particles (<3 μm) clearly, and only the groups of the aerosol particles were measured.[15] In order to measure the single particles one by one, it is essential to isolate the particles from each other on a thin foil. Furthermore, the isolated particles should be close enough to be found easily during a beam scanning. Keeping these requirements in mind, a new method for the preparation of individual aerosol particles was developed.

A solution of nylon powder in iso-butyl alcohol was prepared at a temperature of 80 °C. A droplet of the solution was dropped onto a surface of deionized water contained in a rotating beaker at room temperature. The droplet stretched, and a very thin (0.2 μm) nylon foil formed on the water surface. Just after the formation of the foil (in a few seconds), the collected single particles were dropped dipersively from the sampling filter onto the sticky foil by a small shaker. After five minutes of solidification, the foil attached on a stainless steel frame was taken out of the water. The single particles were separately embedded in the thin, taut, and flat nylon foil. After 24 h drying at a temperature of 60 °C, the individual aerosol particle was ready for single particle analysis by nuclear microprobes.

Nuclear Microprobe Irradiation and Spectra Acquisition. A reliable and efficient experiment for individual aerosol particle analysis demands good performance from the nuclear microprobe. Because most of the particles are smaller than 3 μm, both high spatial resolution and beam current are needed. The Leipzig nuclear microprobe, LIPSION, satisfied the experimental requirements. A 100 μm object diaphragm and a 100 μm aperture diaphragm were used to produce a focused beam spot with 1 μm size and 80 pA current for most single-particle measurements. The particles were so small that they could be considered as thin targets. The 2.25 MeV protons could penetrate all the particles. The beam charge
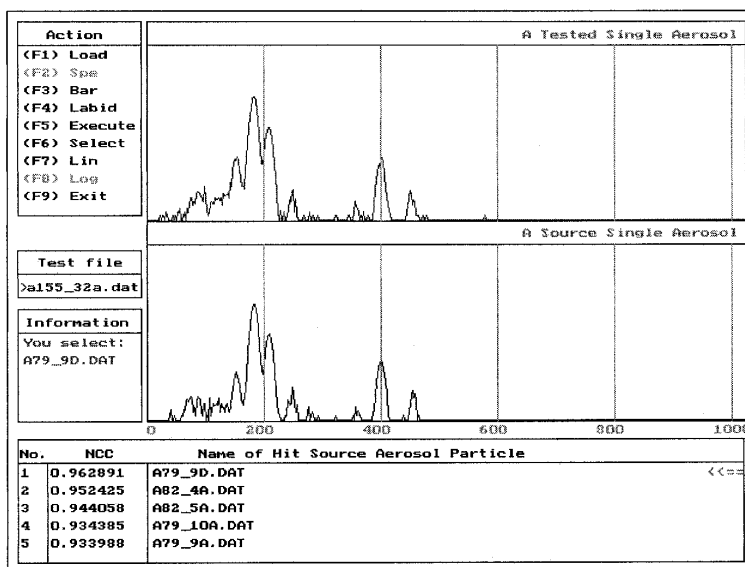

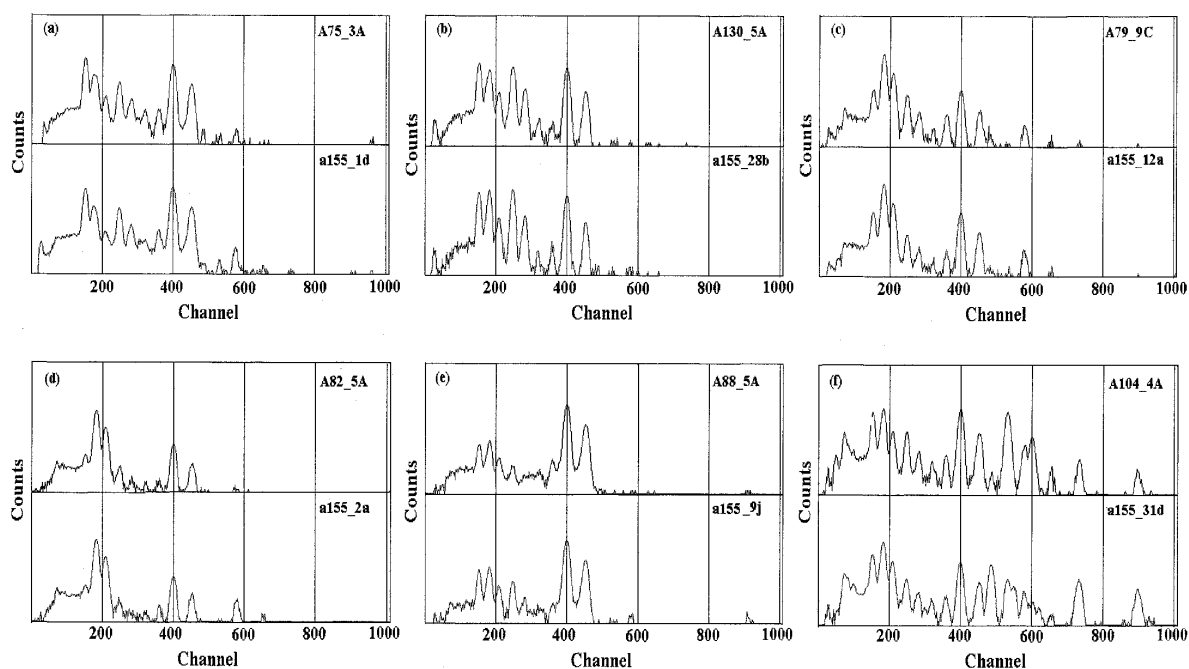FIG. 2. The program menu on the screen. NCC in the bottom window shows the values of cos θ.

Fig. 3.   Six pairs of the PIXE spectra of the particles from the pollution sources (top) and an unknown individual aerosol particle (bottom), which is recognized by this system as a particle from the top pollution source. (**a**) A75_3A is from soil dusts; (**b**) A130_5A is from coal combustors; (**c**) A79_9C is from cement factories; (**d**) A82_5A is from construction sites; (**e**) A88_5A is from ferrous smelters; and (**f**) A104_4A is from vehicle exhaust.

TABLE I.   Values of cos θ derived from the micro-PIXE spectra of 12 typical individual aerosol particles. All spectra were taken under identical conditions and with similar counting statistics. Here part A is for the shape method and part B is for the peak intensity method. Two spectra having very similar patterns should have a value of cos θ near 1. A discriminate threshold of 0.95 is used in this table to indicate the strong correlation between two samples.[a]

	A75_3a	A155_1d	A130_5a	A155_28b	A79_9c	A155_12a	A82_5a	A155_2a	A88_5a	A155_9j	A104_4a	A155_31d
	(A) Values of cos θ for the shape method											
a75_3a												
A155_1d	**0.98**											
A130_5a	0.94	0.94										
A155_28b	0.93	0.92	**0.98**									
A79_9c	0.92	0.90	0.93	0.93								
A155_12a	0.93	0.90	0.93	0.93	**0.98**							
A82_5a	0.86	0.82	0.87	0.87	0.93	0.94						
A155_2a	0.85	0.81	0.85	0.85	0.94	0.93	**0.98**					
A88_5a	0.93	0.93	0.88	0.85	0.82	0.85	0.80	0.78				
A155_9j	0.93	0.93	0.91	0.89	0.85	0.88	0.82	0.80	**0.97**			
A104_4a	0.86	0.87	0.84	0.83	0.84	0.85	0.79	0.80	0.80	0.81		
A155_31d	0.84	0.83	0.82	0.82	0.86	0.86	0.81	0.82	0.76	0.77	**0.95**	
	(B) Values of cos θ for the method of peak intensities											
A75_3a												
A155_1d	**0.97**											
A130_5a	0.93	0.92										
A155_28b	0.94	0.93	**0.96**									
A79_9c	0.93	0.93	0.91	0.93								
A155_12a	0.93	0.91	0.90	0.91	**0.98**							
A82_5a	0.87	0.88	0.87	0.87	0.93	0.93						
A155_2a	0.83	0.85	0.82	0.83	0.91	0.93	**0.98**					
A88_5a	0.91	0.90	0.87	0.90	0.89	0.91	0.91	0.86				
A155_9j	0.93	0.93	0.92	0.93	0.93	0.94	0.93	0.91	**0.97**			
A104_4a	0.90	0.89	0.85	0.86	0.93	0.91	0.81	0.79	0.80	0.85		
A155_31d	0.90	0.87	0.83	0.83	0.93	0.91	0.80	0.78	0.78	0.82	**0.95**	

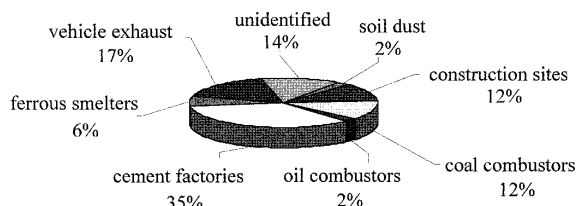[a] Values of cos θ that are above the discriminate threshold appear in boldface.

Fig. 4. The contribution of the pollution sources to the local atmosphere in Shanghai.

was collected by a downstream Farady cup. There was no conductive coating on the sample surface. No data correction for the effects of the particle matrix and shape was applied. A 20 nC integrated beam charge was used for each particle measurement. Much experimental time was spent on searching for isolated small particles. A proper searching procedure was important for the high efficiency of this work. At first, a large area scan (70 μm) was needed to find areas where the isolated small particles were present. The coordinates of each small particle in the scanning area were digitized and recorded for further small area scans (6–10 μm). The three-dimensional movement of the sample stage was digitally controlled. The accuracy of the sample displacement was better than 1 μm. One or more isolated small particles were covered by the beam within the scanning area. We measured 294 isolated individual aerosol particles. Each single particle measurement took about 15 min. The accelerator and the microprobe of LIPSION performed under a very stable working condition. The high stability of the beam and the high precision of the sample displacement made the individual aerosol particle measurements very efficient. The characteristic spectrum of each single particle was extracted from the data according to the particle shape in the small scanning area.

PATTERN RECOGNITION SYSTEM

Principle of the System. The principle of the pattern recognition technique has been described in detail elsewhere.[13] Here we only briefly introduce the method and its application to PIXE spectra.

A PIXE spectrum can be treated as an *n*-component column vector in a Euclidean space. For the pattern recognition, two spectrum vectors are considered similar if the Euclidean angle between the two vectors is small enough. The discriminative function of two spectrum vectors is defined as below:

$$\cos \theta = \vec{X}'\cdot\vec{Y}/[(\vec{X}'\cdot\vec{X})(\vec{Y}'\cdot\vec{Y})]^{1/2} \qquad (1)$$

Here $\vec{X}'$ and $\vec{Y}'$ are the transposes of $\vec{X}$ and $\vec{Y}$, respectively. The numerator is the dot product of the two vectors, and the denominator is the product of their magnitudes. The value of cos θ will be close to 1 for two PIXE spectra with similar features, and it is independent of intensities.

There are two ways to transform a spectrum into a Euclidean vector; one is according to the spectrum shape, and the other is by the intensity of each peak in the spectrum. A set of 25 peaks was set up for the vector in our work. The peak intensities were acquired by using the
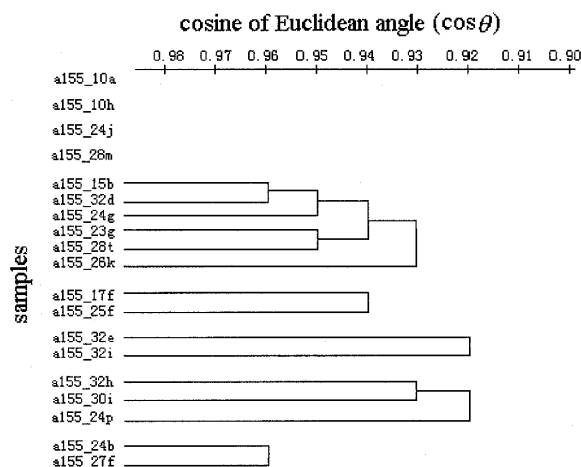

Fig. 5. The clustering results of some unidentified particles.

program AXIL. If a peak in the spectrum is lower than the detection limit, the corresponding intensity is zero. The method of the spectrum shape is simple and quick; however, the peak intensity method is favorable to some trace element features.

Implementation. A program to identify a PIXE spectrum of an individual aerosol particle has been developed on a personal computer. The flow chart is shown in Fig. 1. The identification of an individual aerosol particle by its observed PIXE spectrum pattern follows this process. At the start, the main menu (Fig. 2) is shown on the screen. The user first selects a file name with the function key F1 "Load" to enter a spectrum, which will be displayed on the screen instantly. Next, F5 "Execute" can be used to calculate the values of cos θ between the loaded spectrum and each of the spectra from the fingerprint database. Then a name list of the hit source spectra will be presented at the bottom of the screen. Finally, the user can use F6 "Select" to choose a satisfactory source spectrum from the list and to display the spectrum on the screen for comparison. The system contains all the spectra of the source particles as a fingerprint database. The user can add or delete any of the source spectra in the database. Both logarithmic and linear scales are used for the spectrum display and comparison. The logarithmic scale is more sensitive to trace element features of the particles. The PIXE spectrum has high background at the low-energy region because of *bremsstrahlung*. The pattern recognition algorithm may misunderstand a spectrum with high background, especially when the peak signals are very low. To tackle this problem, we used a background subtraction procedure before the spectrum comparison.

RESULTS AND DISCUSSION

We measured 294 individual aerosol particles. Among them, 74 particles are from seven pollution sources. The other particles are from a local environment monitor site. The spectral patterns can be considered as the fingerprints of the individual aerosol particles.

Figure 3 shows six pairs of spectra for comparison.

Each pair contains two spectra; one is a typical spectrum from a pollution source, and the other is an unknown spectrum from the monitor site. By visual inspection, it is obvious that the two spectra in each pair have similar features, which implies similar chemical composition. The spectra in different pairs have different features of their sources.

To illustrate the validity and efficiency of the pattern recognition technique, we applied Eq. 1 to some typical PIXE spectra of particles. The values of cos θ were evaluated for all possible pairs of the spectra and are presented in a triangular matrix shown in Table I. Here part A is for the shape method and part B is for the peak intensity method. A discriminate threshold of 0.95 is used in this table to indicate the strongly correlated samples. For example, the value of cos θ between a75_3a and a155_1d is 0.98, which means that the particle a155_1d came from the pollution source a75_3a. The result of the calculation coincides with the visual inspection in Fig. 3.

The results of source identification are shown in Fig. 4. The cement factory is the primary source of pollution. This is a result of municipal construction in this region of Shanghai in recent years. The second large pollution source in the region is the heavy traffic. About 14% of the aerosol particles have not been identified by this system. They do not originate from the pollution sources we have investigated. This observation suggests that they might come from other pollution sources. If we set the threshold of discrimination (value of cos θ) to 0.92, some unidentified particles are clustered into nine categories by means of the pattern recognition system. Figure 5 shows the clustering results. These nine sources were not defined in our study. This result is useful in the search for new pollution sources.

CONCLUSION

A graphical user interface program for the identification system of aerosol particles based on PIXE spectra has been developed. The combination of the micro-PIXE with the pattern recognition technique for the source identification of individual aerosol particles is efficient and easy to operate even for an inexperienced person. According to the results of identification, we could see that seven types of pollution sources were not enough for the identification of all aerosol particles in Shanghai. Some new pollution sources can be found by clustering the unidentified particles.

1. P. Van Espen, Mikrochim. Acta **114/115,** 129 (1994).
2. I. Orlic, Nucl. Instr. And Meth. B **104,** 602 (1995).
3. G. W. Grime, X-ray Spectrom. **27,** 221 (1998).
4. N. E. G. Löwenstam, J. Pallon, and H. C. Hansson, J. Aerosol Sci. **19,** 1031 (1988).
5. P. Artaxo, W. Maenhout, H. Storms, and R. Van Grieken, J. Geophys. Res. **95,** 16971 (1990).
6. P. Artaxo, M. L. C. Rabello, F. Watt, and G. Grime, Nucl. Instr. Meth. B **75,** 521 (1993).
7. G. W. Grime and F. Watt, Nucl. Instr. Meth. B **75,** 495 (1993).
8. M. Jaksic, I. Bogdanovic, E. Gereda, S. Fazinic, and V. Valkovic, Nucl. Instr. Meth. B **77,** 505 (1993).
9. I. Bogdanovic, M. Jaksic, S. Fazinic, and V. Valkovic, Nucl. Instr. Meth. B **85,** 732 (1994).
10. I. Orilic, T. Osipowicz, F. Watt, and S. M. Tang, Nucl. Instr. Meth. B **104,** 630 (1995).
11. E. K. Kemsley, S. Ruault, and R. H. Wilson, Food Chem. **54,** 321 (1995).
12. M. Twomey, G. Downey, and P. B. McNulty, J. Sci. Food Agric. **67,** 77 (1995).
13. L. I. Yin and S. M. Seltzer, Advances X-Ray Anal. **33,** 603 (1990).
14. Y. Sha, Y. Gu, G. Liu, A. Wang, P. Zhang, J. Zhu, J. Shi, S. Yang, P. Liu, and X. Li, Nucl. Instr. Meth. B **109/110,** 79 (1996).
15. Y. Sha, J. Shi, Y. Gu, J. Zhu, and X. Li, Nucl. Sci. Techn. (in Chinese), **7,** 61 (1996).

Study of metal bioaccumulation by nuclear microprobe analysis of algae fossils and living algae cells

P. Guo [a], J. Wang [a], X. Li [a], J. Zhu [a,*], T. Reinert [b], J. Heitmann [b], D. Spemann [b], J. Vogt [b], R.-H. Flagmeyer [b], T. Butz [b]

[a] *Shanghai Institute of Nuclear Research, CAS, P.O. Box 800-204, 201800 Shanghai, People's Republic of China*
[b] *Fakultät für Physik und Geowissenschaften, Universität Leipzig, Abteilung Nukleare Festkörperphysik, Linnéstr. 5, 04103 Leipzig, Germany*

Abstract

Microscopic ion-beam analysis of palaeo-algae fossils and living green algae cells have been performed to study the metal bioaccumulation processes. The algae fossils, both single cellular and multicellular, are from the late Neoproterozonic (570 million years ago) ocean and perfectly preserved within a phosphorite formation. The biosorption of the rare earth element ions Nd^{3+} by the green algae species *euglena gracilis* was investigated with a comparison between the normal cells and immobilized ones. The new Leipzig Nanoprobe, LIPSION, was used to produce a proton beam with 2 μm size and 0.5 nA beam current for this study. PIXE and RBS techniques were used for analysis and imaging. The observation of small metal rich spores (< 10 μm) surrounding both of the fossils and the living cells proved the existence of some specific receptor sites which bind metal carrier ligands at the microbic surface. The bioaccumulation efficiency of neodymium by the algae cells was 10 times higher for immobilized algae cells. It confirms the fact that the algae immobilization is an useful technique to improve its metal bioaccumulation. © 2000 Elsevier Science B.V. All rights reserved.

PACS: 07.79.–v; 89.60.+x; 01.30.Cc
Keywords: Metal bioaccumulation; Algae fossil; Green algae; Microscopic analysis; PIXE

1. Introduction

It has been known for some time that heavy metal ions are accumulated by microorganisms, such as bacteria, fungi and algae. The biosorption of microorganisms is a valuable means to remove metal ions from water [1]. The metals of interest for biosorption can be divided basically in two groups. One group comprises toxic metals that must be extracted from effluents due to their toxic actions on the environment [2]. The second group is constituted by noble metals. In the case of noble metals, their recovery from the solutions is interesting because of their strategical value [3]. The phenomenon of metal bioaccumulation was used

_____
* Corresponding author. Tel.: 86-21-5955-3998, ext. 267; fax: 86-21-5955-3021.
E-mail address: iamzhu@hotmail.com (J. Zhu).

by paleogeological scientists to explain the origin and evolution of some mineral deposits [4].

A good understanding of the biosorption processes facilitates the application of the procedure in the area of wastewater treatment and in the mining industry. However, the metal transport mechanism by the microorganisms is still not clear. A number of controversial possibilities of the biosorption processes have been reported. Some suggested that the metal ion removal was being effected by a simple process of adsorption onto the surface of algae [5–7]. However, many other facts in contrast to the behavior of surface adsorption have been observed [8–10]. These observations led to the conclusion that the biological activity of algae cells played an important role in the metal bioaccumulation [11]. The absorption occurred through interaction of metal ions with some functional groups either intracellular or on the exterior wall of the cell [12].

In order to characterize the location of the binding sites and the mechanism of metal ion transportation, further experiments are needed. The nuclear microprobe provides an ideal means for locating the sites of metal accumulation in microorganisms. It has been used to study nickel microscopic distributions in leaves of hyperaccumulator plants [13,14]. Its ability of microscopic analysis was further demonstrated by the measurements of single phytoplankton cells [15] and single microfossils [16].

The goal of this work is to study the metal bioaccumulation by measurements of metal distribution patterns in algae with the nuclear microprobe. Both, algae fossils and living algae cells were investigated. The algae fossils have single cellular or multicellular structures. The living green algae cells were treated in different ways. Because the accumulative quantities of the interesting metals are relatively low and the distribution pattern is in size of a cell, a nuclear microprobe with high spatial resolution and high analytical sensitivity is necessary for the microscopic investigation of the metal bioaccumulation. The Leipzig nanoprobe, LIPSION, consisting of a 2-stage MARC microbeamline MPU-3 and a dedicated Singletron™ manufactured by HVEE was used to produce submicron beams of high energy ions with high beam current and excellent energy stability. A detailed description of LIPSION can be found in another contribution to this conference [17].

2. Metal distribution in algae fossils

2.1. Sample description

The algae fossils were recently discovered in Southern China [18]. They lived in the late Neoproterozoic (570 million years ago) ocean and were perfectly preserved within a phosphorite mineral formation. The algal thalli range from undifferentiated single cellular species to diverse multicellular algae. The discoidal parenchymatous single cellular thalli are morphologically simple (bottom right of Fig. 1). Spicules and filaments surrounding the cellular periphery were exquisitely preserved. The multicellular algae fossils are characterized by tissue differentiation and distinct reproductive structures similar to the *corposporangia* and *spermatangia* of living algae. The sizes of both algae species range from 200 to 800 μm.

The fossil samples were prepared by cutting the phosphorite in slices with a thickness of about 100 μm. The slices were then glued on a piece of glass. The surface of the samples was ground and polished to form a final thickness of 40 μm. It was not necessary to cover the samples with a conductive layer since the phosphorite matrix has good conductivity.

2.2. Measurements and results

A 200 μm object diaphragm and a 200 μm aperture diaphragm were selected to produce a focused proton beam with 2 μm size and 0.5 nA beam current. A pair of post scanning coils with 128 turns was used for a maximum scan size of 800 μm for the 2.25 MeV proton beam. PIXE and RBS techniques were used for the element analysis and for sample imaging. In order to reduce the intense X-ray counting rates caused by calcium in the matrix, a 16.5 mg/cm^2 aluminium filter and a 54 μm Mylar sheet were inserted in front of the X-ray detector. With the filter, the average X-ray

counting rate was below 1000 cps which is ideal for the two station list mode data acquisition.

The single cellular algae fossils were embeded in the phosphorite which has a high concentration of manganese in contrast with the low manganese concentration in the fossils. It formed very sharp boundaries between the mineral and the fossil in the element distribution map of manganese (top left of Fig. 1, the scan size of each map was 600 µm × 600 µm). Some other metal accumula-

tive patterns were also presented in Fig. 1. It was obvious that the algal thallus absorbed a large amount of metals like barium, strontium, iron and calcium from its surroundings. The absorbed strontium seemed homogeneously distributed throughout the thallus. However, the barium ions penetrated the epidermic wall and were only preserved within the parenchyma of the thallus. There was a small amount of barium in the wall. Both the fossil and the mineral contained a high density
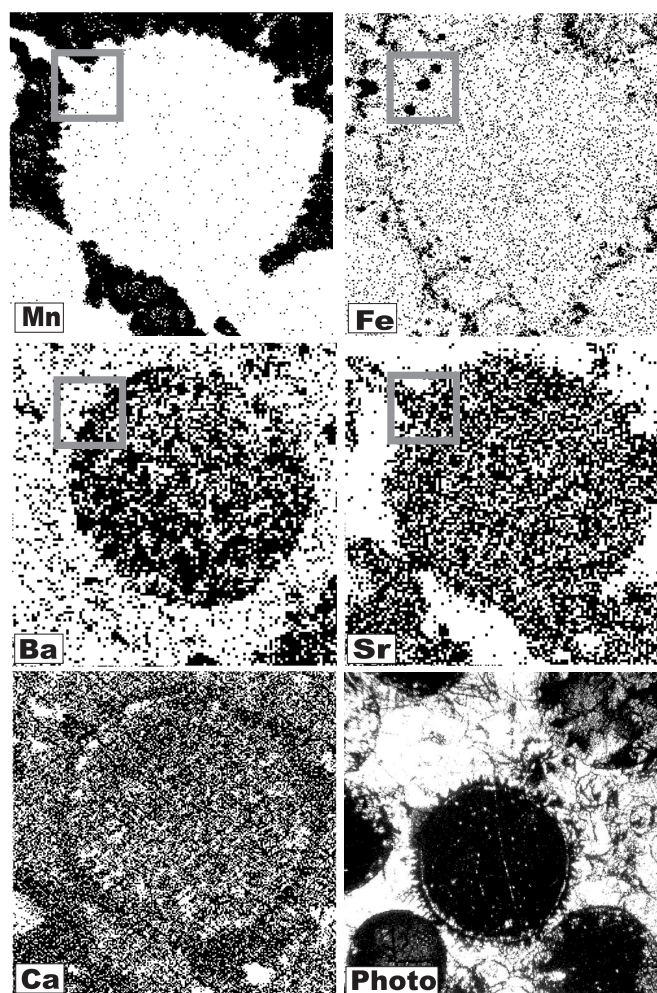
Fig. 1. Element distribution maps of a single cellular alga fossil in a 600 µm × 600 µm scan area. Three iron rich spores exist at the top left surface. A square in this region is marked for a zoom-in scanning area displayed in Fig. 2. The optical image of the thallus is presented in the bottom right picture.

of calcium, but more calcium was on the epidermic wall than inside the thallus. The iron distribution map in Fig. 1 showed an interesting pattern. The spiculate membrane of the discoidal thallus was rich with iron in forms of cystic spores. There were three iron rich spores on the upper left surface of the thallus. In order to have a close look of their location, we made another zoom-in-scan of 120 μm × 120 μm which is marked in Fig. 1. The corresponding element distribution maps in the zoom-in area are displayed in Fig. 2. It is evident by closely looking at the element maps that the iron rich cystic spores are located at the wall of the algal thallus. The iron transport in certain bacteria is well understood [19,20]. Some selective carrier ligands excreted from the cells scavenged the metal ions and formed extremely stable complexes with Fe^{3+}. These ligands bound to specific receptor sites at the cell surface. The observation of iron rich spores on the microfossil surface proved the existence of Fe^{3+} bound ligands in the cell membrane.

The cystic spores containing high metal concentration were also found in the multicellular algae fossils.

3. Metal ion biosorption of living algae cells

3.1. Sample preparation

It is clear that the transport of elements by living organisms has influenced the established ecosystem of the earth surface for some billion years. Among the 92 elements in the periodic table, 30 have been found to be involved in the natural biosorption. However, following the industrialization, more elements, especially the rare earth elements, have participated in the ecologic circulation. In order to gain better understanding of the rare earth metal bioaccumulation, we selected the uptake of trivalent neodymium ions by the green algae species *euglena gracilis* 277 as our object of
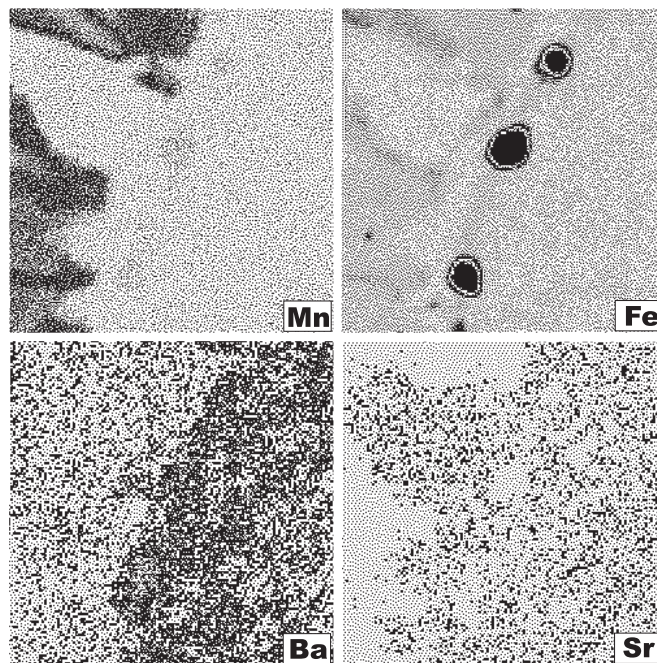

Fig. 2. The element distribution maps in the top left square of Fig. 1. The scan size is 120 μm × 120 μm. Iron rich spores are located at the thallus membrane.

investigation. The immobilization technique has been used to increase the efficiency of the metal bioaccumulation [10]. Thus, for comparison, some samples of the *gracilis* cells were immobilized before biosorption.

Cultivation. An inoculum of the *gracilis* cells was added to a suitable nutrients medium and agitated for three periods of 12 h illumination and 12 h darkness at room temperature. The cultured cells were harvested by centrifugation, washed three times with deionized water, dialyzed against the water and lyophilized for storage.

Immobilization. 20 ml of solution containing 25% glutaraldehyde ($CHO(CH_2)_3CHO$) was added to 2 g of the centrifuged cells. The mixture was then extensively agitated for 10 min. The immobilized *gracilis* cells thus formed were washed, centrifuged and stored for neodymium biosorption.

Biosorption. The *gracilis* cells were placed directly in contact with solutions containing 50 mg/l neodymium ions. After 30 min biosorption, the biomass was removed by centrifugation, washed and suspended in deionized water.

Freezedrying. A droplet of the cell suspention was put onto a very thin nylon foil which was attached to a stainless steel frame. The production of the thin foil was described in another contribution to this conference [21]. After 1 h drying in fresh air, the cells were killed and freezedried.

3.2. Measurements and results

The same experimental setup as before was used except the thickness of the aluminium absorption filter was reduced to 5.1 mg/cm^2, less than one third of the original one. The reason for that was because the *gracilis* cells were so small (< 10 μm) that they could be considered a thin target. The 2.25 MeV protons could fully penetrate the sample. Most of the *gracilis* cells were connected in chains, but there were some single isolated cells. 47 ordinary and 35 immobilized *gracilis* cells have been measured. The PIXE and RBS spectra of the cells were extracted from the raw scanning data according to their shapes. The intensity of neodymium L-X-rays was used to measure its concentration and to produce the element
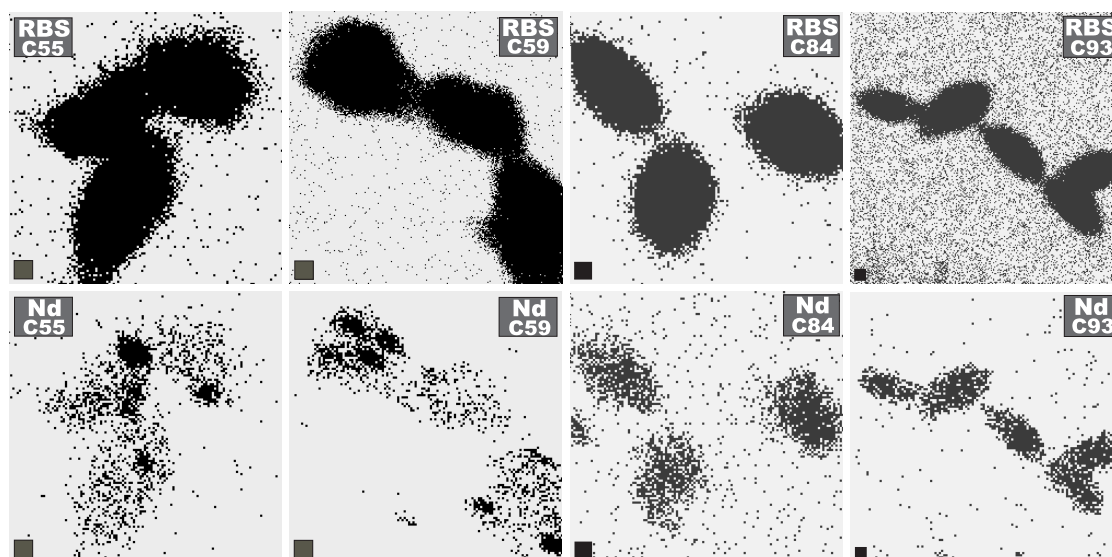

Fig. 3. Four examples of the Nd distribution patterns in the *gracilis* cells. Top row: RBS patterns. Bottom row: Nd PIXE maps. Sample C55 and C59 are ordinary cells, but sample C84 and C93 have been immobilized. A 2 μm × 2 μm square scale is attached at the bottom left corner of each map.

distribution map of the cells. The relative biomass of the cells could be estimated by their potassium contents. The semi-quantitative analytical program TTSPM [22] was used to calculate the concentration ratio of neodymium to potassium. The RBS yields in the cells were much higher than that of PIXE. Therefore, it was favourable for cell imaging.

Fig. 3 shows four examples of the neodymium distribution patterns in *gracilis* cells. Samples C55 and C59 are ordinary cells, but samples C84 and C93 have been immobilized before putting them into the neodymium solution. The distinct difference of the Nd maps between the two groups shows that the ordinary *gracilis* preserved less neodymium inside the cells but kept a high density of the metal in some cystic spores on their surface. We did not find neodymium rich spores in the immobilized *gracilis* cells. However, these cells could absorb much more neodymium which was homogenously distributed inside the cells. The concentration ratios of Nd^{3+} to K^+ were 0.018 for ordinary cells and 0.26 for immobilized cells. It is apparent that the metal bioaccumulation of immobilized *gracilis* cells was ten times more efficient than that of ordinary ones.

4. Discussion and conclusion

The transport of metal ions both intercellular and extracellular is governed by a combination of biological, chemical, kinetic and thermodynamic processes [8]. The cell membrane is the initial barrier for metal ion uptake, but some specific channels and pumps in the membrane provide pathways for metal ions in or out. In the biological process, the metal ions can be carried and transferred by many different organic ligands, e.g., humic acids. The carrier ligands are often bound in some functional groups at the cell surface or inside the cells. Metabolic activity of living cells is responsible for the synthesis of the carrier ligands and the ion channels and pumps. Some metals are essential for microbial growth and division, but an excess of these elements can be toxic. Their equilibrium is established by the cellular immune system. Excessive metal ions can be excreted by metabolism of the microorganisms. However, the breakdown of the immune system occurs when their metabolic activities are stopped by the immobilization treatment. The metal accumulation in the algae cells is thus out of control. The bioaccumulation efficiency of the rare earth metal neodymium by the green algae species *euglena gracilis* can be ten times higher if the algae activity is stopped by immobilization.

References

[1] J.M. Wood, H.K. Wang, Environ. Sci. Technol. 18 (1984) 106.
[2] P.O. Harris, G.J. Ramelow, Environ. Sci. Technol. 24 (1990) 220.
[3] D.W. Darnall, B. Greene, Environ. Sci. Technol. 20 (1986) 206.
[4] Z. Dai, C. Ren, Q. Zhao, P. Wang, F. Yang, Nucl. Instr. and Meth. B 104 (1995) 619.
[5] M. Tsezos, B. Volesky, Biotechnol. Bioeng. 23 (1981) 583.
[6] A. Nakajima, T. Horikoshi, T. Sakaguchi, J. Appl. Microbiol. Biotechnol. 16 (1982) 88.
[7] A.B. Norberg, H. Persson, Biotechnol. Bioeng. 26 (1984) 239.
[8] H. Siger, Metal Ions in Biological Systems, vol. 18, Marcel Dekker, New York, 1984, p. 223.
[9] B. Yang, I. Fang, M. Hao, Science Bulletin (in Chinese, abstract in English), 43 (1998) 7.
[10] A.C.A. Costa, S.G.F. Leite, Biotechnol. Lett. 13 (1991) 559.
[11] M. Hosea, B. Greene, Inorganica Chimica Acta 123 (1986) 161.
[12] R.H. Crist, K. Oherholser, N. Shank, M. Nguegen, Environ. Sci. Technol. 15 (1981) 1212.

[13] W. Przybylowicz, C. Pineda, V. Prozesky, J. Mesjasz-Przybylowicz, Nucl. Instr. and Meth. B 104 (1995) 176.

[14] U. Krämer, G. Grime, J. Smith, C. Hawes, A. Baker, Nucl. Instr. and Meth. B 130 (1997) 346.

[15] J. Pallon, M. Elfman, P. Kristiansson, K. Malmqvist, E.Granéli, A. Sellborn, in: Proceedings of Sixth International Conference on Nucl. Microprobe Technol. & Appl., Spier Estate, S. Africa, 11–16 October 1998.

[16] J. Zhu, C. Yang, R. Lu, K. Sheng, Y. Wang, N. Homman, K. Malmqvist, Nucl. Instr. and Meth. B 104 (1995) 402.

[17] T. Butz, R.-H. Flagmeyer, J. Heitmann, D.N. Jamieson, G.J.F. Legge, D. Lehmann, U. Reibetanz, T. Reinert, A. Saint, D. Spemann, R. Szymanski, W. Tröger, J. Vogt, J. Zhu, Nucl. Instr. and Meth. 161–163 (2000) 323.

[18] S. Xiao, Y. Zhang, A.H. Knoll, Nature 391 (1998) 553.

[19] J. Neilands, Chem. Scripta 21 (1983) 161.

[20] U. Förstner, G. Wittman, Metal Pollution in the Aquatic Environment, Springer, New York, 1979.

[21] J. Wang, P. Guo, X. Li, J. Zhu, T. Reinert, J. Heitmann, D. Spemann, J. Vogt, R. Flagmeyer, T. Butz, Nucl. Instr. and Meth. 161–163 (2000) 830.

[22] X. Wu, J. Zhu, R. Lu, F. Yang, Nucl. Instr. and Meth. B 104 (1995) 196.

Investigations of percutaneous uptake of ultrafine TiO$_2$ particles at the high energy ion nanoprobe LIPSION

F. Menzel [*], T. Reinert, J. Vogt, T. Butz

Nukleare Festkörperphysik, Fakultät für Physik und Geowissenschaften, Universität Leipzig, Linnéstr. 5, 04103 Leipzig, Germany

Abstract

Micronised TiO$_2$ particles with a diameter of about 15 nm are used in sunscreens as physical UV filter. Due to the small particle size it may be supposed that TiO$_2$ particles can pass through the uppermost horny skin layer (*stratum corneum*) via intercellular channels and penetrate into deeper vital skin layers. Accumulations of TiO$_2$ particles in the skin can decrease the threshold for allergies of the immune system or cause allergic reactions directly. Spatially resolved ion beam analysis (PIXE, RBS, STIM and secondary electron imaging) was carried out on freeze-dried cross-sections of biopsies of pig skin, on which four different formulations containing TiO$_2$ particles were applied. The investigations were carried out at the high energy ion nanoprobe LIPSION in Leipzig with a 2.25 MeV proton beam, which was focused to a diameter of 1 μm. The analysis concentrated on the penetration depth and on pathways of the TiO$_2$ particles into the skin. In these measurements a penetration of TiO$_2$ particles through the *s. corneum* into the underlying *stratum granulosum* via intercellular space was found. Hair follicles do not seem to be important penetration pathways because no TiO$_2$ was detected inside. The TiO$_2$ particle concentration in the *stratum spinosum* was below the minimum detection limit of about 1 particle/μm^2. These findings show the importance of coating the TiO$_2$ particles in order to prevent damage of RNA and DNA of skin cells by photocatalytic reactions of the penetrated particles caused by absorption of UV light.

© 2004 Elsevier B.V. All rights reserved.

1. Introduction

Micronised TiO$_2$ particles used in sunscreens as physical UV filters are suspected to pass through the horny *s. corneum* into vital skin layers via intercellular channels, hair follicles, and sweat glands. But this penetration is undesirable because of the risk of damage of DNA and RNA by photocatalytic effects of the TiO$_2$ after absorption of UV light [1], which can be prevented by coating of the particles. Furthermore, the particles can activate the immune system and accumulations of these particles in the skin can decrease the threshold for allergies [2]. The function of the *s. corneum* as a barrier against dermal uptake of ultrafine particles was the subject of several investigations, which came to different conclusions

---

[*] Corresponding author. Tel.: +49-341-973-2707; fax: +49-341-973-2497.

E-mail address: fmenzel@physik.uni-leipzig.de (F. Menzel).

concerning the penetration depth of the particles [3,4]. Most of these studies used the method of tape stripping, which only concerns the *s. corneum* and which is relatively imprecise in comparison with the spatially resolved ion beam analysis. We investigated the percutaneous penetration of TiO_2 of cross-sections of pig skin with the ion beam analysis methods PIXE, RBS, ERDA, STIM and SEI.

2. Materials and methods

For the study, cross-sections of pig skin were investigated, which shows many parallels to human skin [5], treated with four different formulations containing micronised TiO_2 particles. The used formulations were the commercial product Eucerin® Micropigment Creme 15 (5% TiO_2 concentration) from the Beiersdorf company, a liposome dispersion (18% TiO_2 concentration) from Dr. C. Bennat [6], which contains Phospholipon® 90 G and Tioveil AQ-N from Tioxide Specialties Ltd., (Billingham, UK), a formulation denoted SG1101 (4.5% TiO_2 concentration) from Prof. Dr. C. Müller-Goymann, similar to a commercial sunscreen, also containing Tioveil AQ-N, and the pure predispersion Tioveil AQ-N (40% TiO_2 concentration). The size of the TiO_2 particles was determined with TEM. They were lanceolate in shape, 45–150 nm long and 17–35 nm wide.

Skin areas at the backs of the pigs were cleaned with wash lotion, shaved and disinfected with alcohol. Then the formulations were applied by allergy test plasters (1 cm^2) and fixed with covering plasters. The samples were taken 8, 24 and 48 h later. After putting down the pigs punch biopsies were taken and plunged into liquid nitrogen. From the biopsies 20 and 30 μm thick cryosections were sliced and freeze-dried.

PIXE, RBS, STIM, ERDA and SEI measurements were carried out on the skin sections with a 2 and 2.25 MeV proton beam focused to 1 μm. For the ion beam measurements the current was about 100 pA (for STIM about 1 fA) and a charge of about 0.1–1 μC was collected. The images of elemental distributions resulting from PIXE have a resolution of 1–2 μm.

3. Hydrogen content

To evaluate the RBS data a hydrogen to carbon relation R_{HC} of the sample material must be known or it has to be assumed. For the skin samples, usually an R_{HC} of 20:10 is assumed. However, we tried to get a more precise relation by a combination of ERDA and RBS measurements. Therefore, a 6 μm thick mylar foil with known composition was investigated as a reference sample. With the number of protons $N_{(p,p)}$ recoiled from hydrogen atoms in ERDA, the charge Q from RBS, and the hydrogen area density n_H the factor k in the following formula was determined.

$$N_{(p,p)} = kQn_H.$$

Then the first value for n_H of the skin sample was determined by this relation and the values of $N_{(p,p)}$ and Q obtained from the ERDA and RBS measurements of the skin. With the n_H and the atom area density ρ_A, also obtained from RBS, a new R_{HC} was calculated. However, this calculation is based on the values for Q and ρ_A from the original assumption of R_{HC}. Therefore the RBS spectrum was re-evaluated with the new R_{HC} to determine new values for Q and ρ_A. This iteration was carried out until the differences of Q and ρ_A between two iteration steps were less then 1%.

For the two skin samples characterized by this way new R_{HC} values of 16:10 and 11:10 were determined after 11 iteration steps, which were used in a new evaluation of the PIXE data of these samples. The newly determined concentrations in mmol/l are between 5% and 10% higher than the concentrations based on the assumed R_{HC} of 20:10. To prove these results, the R_{HC} of three skin biopsies were determined by a chemical procedure to be 16.6:10–18:10.

4. Skin structure

Different layers of the skin and their components were identified by images of element and density distributions. The 15 μm thick *s. corneum* consisting of dead and horny keratinocytes is easily identified as an area of high density (Fig. 1) and high amounts of sulphur and chlorine (Fig.
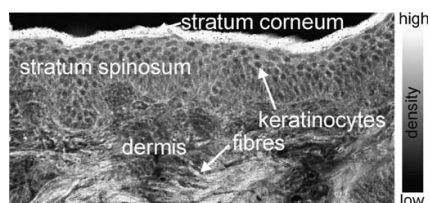
Fig. 1. STIM image of pig skin exposed to Eucerin® Micropigment Creme 15 for 8 h (409 μm × 199 μm). The *s. granulosum*, located between *s. corneum* and *s. spinosum*, could not be identified in this image.

2(b) and (c)). The *s. spinosum* is characterized by its high concentration of phosphorus (Fig. 2(a)) and the elliptical structures of the keratinocytes at the density images (Fig. 1). In the dermis, an irregular element distribution and long structures of fibres could be identified (Fig. 1). The 5–10 μm thick *s. granulosum*, located between *s. corneum* and *s. spinosum*, is characterized as the region of increasing phosphorus concentration until reaching a constant level [7]. It could be identified very well in diagrams of element concentrations along a traverse with our resolution (Fig. 3).
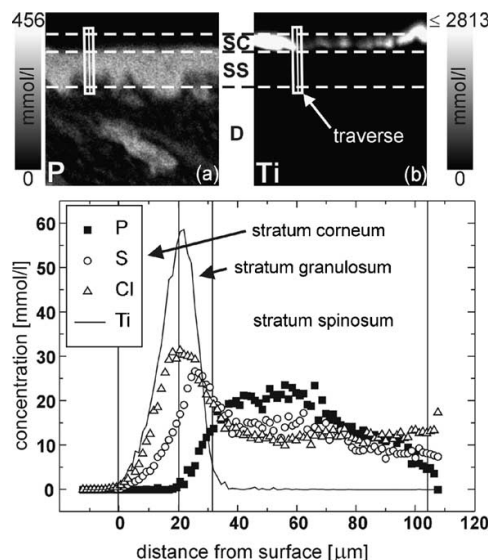
Fig. 3. Top: (a) P and (b) Ti distribution of skin exposed to SG 1101 for 24 h (315 μm × 315 μm) with marked traverse through *s. corneum* (SC), *s. granulosum*, *s. spinosum* (SS) and the dermis (D); bottom: diagram of element distribution along the traverse.
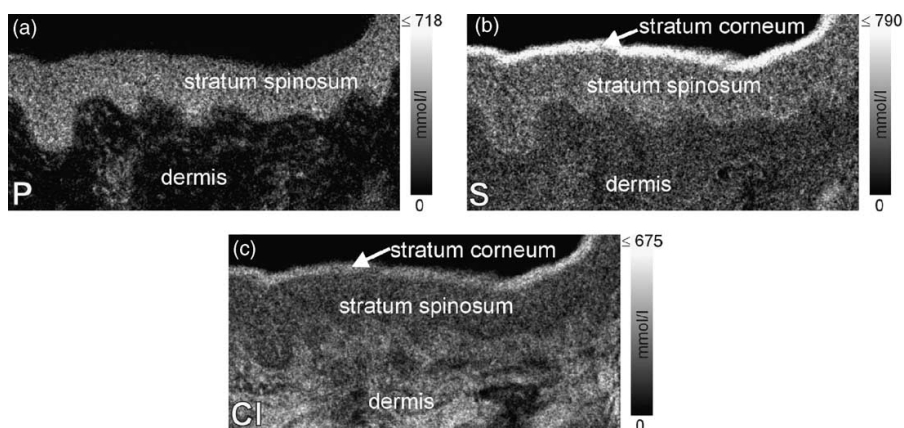

Fig. 2. Concentration maps for (a) P, (b) S and (c) Cl of pig skin exposed to Eucerin® Micropigment Creme 15 for 8 h (400 μm × 190 μm).

5. Titanium dioxide penetration

The ion beam analysis concentrated on the outer layers of skin, the epidermis. Titanium concentration in the skin layers was determined in regions of interest (see Fig. 4). As can be seen in Table 1, for all penetration times and for all four formulations titanium was found in high concentrations at the skin surface and in the *s. corneum*. A penetration into the *s. granulosum* was also observed in most samples with the help of tra-

verses (see Fig. 3). However, there was no evidence of penetration into the *s. spinosum*.

Hair follicles were located in some of the investigated cross-sections. However, there the titanium concentration was below the detection limit. Then, we always had elliptical cross-sections and never exactly parallel to the follicle. Thus, we could analyse these elliptical regions only.

In some samples titanium accumulations in the dermis were detected. However, they were identified as preparation artefacts by inspecting both
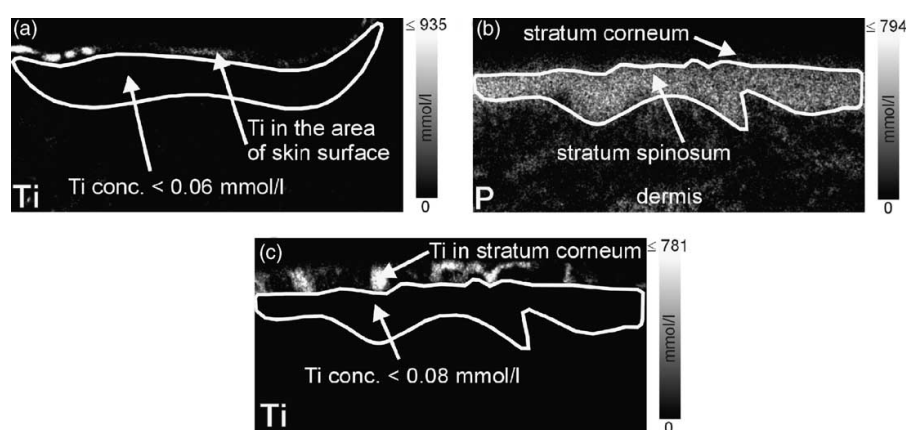

Fig. 4. (a) Ti map from the scan area of Fig. 2 (Eucerin® Micropigment Creme 15); (b) P and (c) Ti maps of skin exposed to SG1101 for 8 h (400 μm × 203 μm). The Ti concentration in the marked area of *s. spinosum* is below the detection limit.

Table 1
Titanium detection in the epidermal layers after application of the formulations for different application times

	s. corneum	s. granulosum	s. spinosum
Eucerin® (8 h)	+	○	−
Eucerin® (24 h)	+	○	−
Eucerin® (48 h)	+	○	−
Liposome dispersion (8 h)	+	○	−
Liposome dispersion (24 h)	+	−	−
Liposome dispersion (48 h)	+	−	−
SG1101 (8 h)	+	○	−
SG1101 (24 h)	+	○	−
SG1101 (48 h)	+	−	−
Tioveil AQ-N (8 h)	+	○	−
Tioveil AQ-N (24 h)	+	○	−
Tioveil AQ-N (48 h)	+	○	−

"+" means >200 mmol/l, "○" means between 0.2 and 200 mmol/l; and "−" means <0.2 mmol/l Ti concentration (minimum detection limit varies between 0.03 and 0.2 mmol/l).

sides, front and back, of the samples with PIXE, RBS and SEI.

6. Conclusion

It has been proved that micronised TiO$_2$ particles from all used formulations penetrated through intercellular spaces in the *s. corneum* into the living *s. granulosum* within the first 8 h after application. This shows the importance of coating the TiO$_2$ particles in order to prevent damages from cell components by photocatalytic reactions. Furthermore, it follows that sunscreens with physical UV filters have also potential to cause allergies.

Titanium spots in the *s. spinosum* and underneath were clearly identified as preparation artefacts by SEI and RBS measurements on both sides of the samples. In the present study no titanium was found in the hair follicles.

References

[1] R. Dunford, A. Salinaro, L. Lezhen, N. Serpone, S. Horikoshi, H. Hidaka, J. Knowland, FEBS Lett. 418 (1997) 87.
[2] B. Granum, P.I. Gaarder, E.-C. Groeng, R.-B. Leikvold, E. Namork, M. Løvik, Toxicol. Lett. 115 (2001) 171.
[3] F. Pflücker, V. Wendel, H. Hohenberg, E. Gärtner, T. Will, S. Pfeiffer, R. Wepf, H. Gers-Barlag, Skin Pharmacol. Appl. Skin Physiol. 14 (2001) 92.
[4] M.-H. Tan, C.A. Commens, L. Burnett, P.J. Snitch, Australas. J. Dermatol. 37 (1996) 185.
[5] W. Meyer, Hautarzt 47 (1996) 178.
[6] C. Bennat, Dissertation, TU Carolo-Wilhelmina zu Braunschweig, Gemeinsame Naturwissenschaftliche Fakultät, 1999.
[7] Ph. Moretto, J.E. Surleve-Bazeille, D. Licu, C. Michelet, P. Stoedzel, Nucl. Instr. and Meth. B 158 (1999) 386.

On the follicular pathway of percutaneous uptake of nanoparticles: Ion microscopy and autoradiography studies

J. Lekki [a,*], Z. Stachura [a], W. Dąbroś [b], J. Stachura [b], F. Menzel [c],
T. Reinert [c], T. Butz [c], J. Pallon [d], E. Gontier [e], M.D. Ynsa [e], P. Moretto [e],
Z. Kertesz [f], Z. Szikszai [f], A.Z. Kiss [f]

[a] *Henryk Niewodniczański Institute of Nuclear Physics PAN, Radzikowskiego 152, 31-342 Kraków, Poland*
[b] *Jagiellonian University, Medical College, Św. Anny 12, 31-008 Kraków, Poland*
[c] *Universität Leipzig, Fakultät für Physik und Geowissenschaften, Nukleare Festkörperphysik, Linnéstraße 5, 04103 Leipzig, Germany*
[d] *Lund Institute of Technology, Physics Department, Division of Nuclear Physics, Sölvegatan 14, 221 00 Lund, Sweden*
[e] *Centre d'Etudes Nucleaires de Bordeaux-Gradignan (CNRS - IN2P3), 33-175 BP 120 Le Haut-Vigneau, Gradignan cedex, France*
[f] *Institute of Nuclear Research of the Hungarian Academy of Sciences, Bem ter 18/C, 4001 Debrecen, Hungary*

Available online 14 February 2007

Abstract

We report on the visualization of the penetration of sunscreen formulations containing TiO_2 nanoparticles (about 20 nm primary particle size) into hair follicles of both human and porcine skin using the complementary methods of ion microscopy (PIXE, RBS, STIM) and autoradiography. Particles were found as deep as approx. 400 μm in the follicle, obviously introduced mechanically rather than by a diffusive process. No particles were observed in vital tissue nor in sebaceous glands.
© 2007 Elsevier B.V. All rights reserved.

1. Introduction

Sun screens with physical UV-filters commonly use TiO_2 and ZnO with primary particle sizes as low as 20 nm. There is concern that such particles could penetrate the *stratum corneum* and reach vital tissue via the transcellular, the intercellular, and the transfollicular pathway. If they reached the dermis, these particles would become systemic. Since ZnO and in particular TiO_2 are chemically rather inert, the cellular response to them would represent at least a constant burden to the immune system as long as the clearance is not known.

Therefore the EC-funded project NANODERM has been launched where several techniques like high resolution transmission electron microscopy (HRTEM), ion microscopy (PIXE, RBS, STIM) and autoradiography were applied to visualize the eventual particle penetration through the *stratum corneum* into vital skin regions, complemented with cellular response investigations in vitro and in vivo. In this paper we focus on the follicular pathway using PIXE, RBS, and STIM techniques which have already proven very useful [1,2], and autoradiography. It should be mentioned that *in vitro* studies using Franz-cells occasionally report on dermal penetration of nanoparticles [3]. However, such studies are of the integral input/output type which do not yield information on possible pathways [4,5]. Therefore, studies which visualize possible pathways are of utmost importance.

* Corresponding author.
  E-mail address: Janusz.Lekki@ifj.edu.pl (J. Lekki).

2. Results and discussion

2.1. Ion microscopy

Ion microscopy measurements have been carried out by six research groups of the consortium. The main experimental technique was Proton Induced X-Ray Emission (PIXE), providing elemental maps with high sensitivity and a micrometer lateral resolution. Typical energy of the proton beam was 2–2.5 MeV at beam currents of the order of 100 pA. For normalization purposes, rutherford backscattering spectrometry (RBS) was applied. Furthermore, scanning transmission ion microscopy (STIM), using a proton beam reduced to intensities of a few thousand particles per second, delivered valuable data of density contrast maps with resolution down to 50 nm.

The following formulations were used: hydrophobic basisgel, isopropylmyristate gel, microemulsion gel, and polyacrylate gel each containing 5 wt% TiO_2 particles (Eusolex T-2000, approx. 20 nm lateral and approx. 100 nm length primary particle size, coated). These formulations were topically applied to porcine and human skin with about 2 mg/cm^2 by gentle rubbing. Various exposure times ranging from 30 min up to 48 h were used. Subsequently biopsies (3 and 5 mm diameter) were taken and shock-frozen in liquid N_2 chilled isopentane. Thin cross-sections (approx. 20 μm) were obtained using a cryo-microtome.

From the wealth of data obtained by the NANODERM consortium [6] it turned out that neither the particle shape, nor the formulation, nor the exposure time had a significant effect on the nanoparticle penetration. The penetration was restricted to the *stratum corneum disjunctum*, i.e. the uppermost 3–5 corneocyte layers, or equivalently, a few μm only. Since we never observed a diffusion pathway, we believe that the particles were introduced mechanically. Details of this study will be published in forthcoming papers.

On the contrary, nanoparticles were found several 100 μm deep in hair follicles by μPIXE, in some cases even at 400 μm. Fig. 1 shows a sagittal cut through a hair follicle of porcine skin which was exposed to isopropylmyristate gel containing TiO_2 nanoparticles and subsequently washed with water. In this figure, the PIXE-maps for P (red), S (green) and Ti (blue) are superimposed.[1] Ti is clearly observed on top of the *stratum corneum* as well as in the follicle surrounding the hair. The left and right images are identical with the Ti colour code overmodulated to better visualize the Ti spots. The highest concentration in the spot above the hair reached values around 2.5 mg/g, i.e. more than a factor of 1000 above the minimum detection level.

We believe that the mechanical movement (tensile and compressive) of skin and hair during topical application

is responsible for the deep penetration. We also observed follicles without TiO_2, as proposed by Lademann et al. [7,8]. A representative example of a *transverse* cut through a hair follicle is shown in Fig. 2. A commercial formulation (Eucerin micropigment 25 lotion) was topically applied to porcine skin for about 30 min and subsequently cleaned with ethanol. This formulation contained circular platelets of TiO_2 with lateral dimensions around 20 nm, looking very much like P25 from Degussa (www.degussa.com). The weak peak where Ti X-rays are expected is very likely due to pile-up from the intense sulphur peak.

Lademann et al. [7,8] report on a specific transport mechanism in follicles is described which would favour particle sizes between 300 nm to 600 nm. However, our particles were more than an order of magnitude smaller and, hence, do not support this mechanism. We believe that it is the formulation (containing nanoparticles) which is actually pushed into the follicle and the particle diameter is less important provided there are no geometrical constraints. Lademann [8] also reported a mechanism why some follicles are "blocked" by sebum and corneocytes and, hence, stay free from particle penetration. An alternative explanation would be that the spreading of the formulations is rather inhomogeneous – as was usually the case, observed in numerous elemental maps measured – and therefore some follicles were not exposed at all while others were. It should be mentioned that the ion microscopy studies did never detect nanoparticles in vital tissue surrounding the follicle.

2.2. Autoradiography

A further technique which visualizes nanoparticles in tissue and which is ultra-sensitive is autoradiography. Radiolabeling of TiO_2 crystals was performed by proton irradiation of chemically pure TiO_2 (rutile, particle size of about 20 nm, trade name: R-HD2, Huntsman). The radioactive ^{48}V isotope with $T_{1/2} = 15.97$ d, was produced via the nuclear reaction $^{48}Ti(p,n)^{48}V$. A pill of 100 mg pressed TiO_2 nanoparticles was wrapped in 0.05 mm Al foil and irradiated with 17 MeV protons for 24 h with a proton beam current of 1 μA. Two days after irradiation, when most short-living parasitic activities have decayed, the total activity of the target was 85 MBq. From that 1 Bq activity corresponds to 1.176 ng of TiO_2. The radioactive vanadium is assumed to reside on Ti-sites in TiO_2 nanoparticles. ^{48}V nuclei decay by β^+- or EC-transitions predominantly to the 2295.6 keV level of ^{48}Ti (with a maximum energy of positrons of 1720 keV) and deexcite to the titanium ground level by a cascade of two gamma transitions, 1312.1 keV (0.975 transitions per decay) and 983.5 keV (one transition per decay). In autoradiography experiments, the location of TiO_2 nanoparticles was detected by exposure of freshly prepared Hypercoat LM-1 nuclear emulsion (Amersham) with decay positrons. In further experiments the location and amount of TiO_2 was monitored by detecting the cascading gamma rays with a large HPGe detector (with an

---

[1] For interpretation of the references in colour in this figure legend, the reader is referred to the web version of this article.
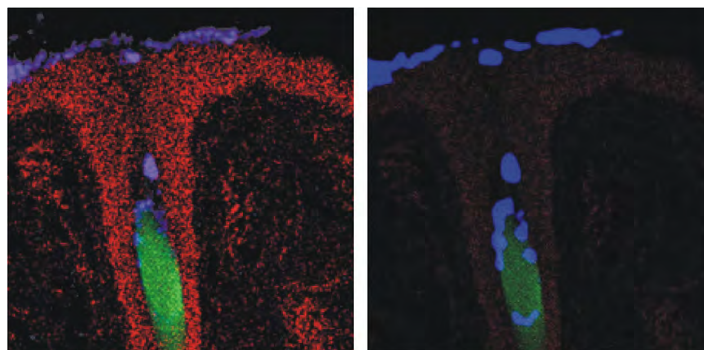
Fig. 1. Sagittal cut through a hair follicle of porcine skin exposed to a formulation containing nanosized TiO_2 . PIXE-data were taken with 2.25 MeV protons at 100 pA and a charge of 0.5 μC. The scan size is 400 μm × 400 μm, we had 256 × 256 pixels and a lateral resolution around 1 μm. The formulation with nanoparticles is deeply pushed into the follicle.
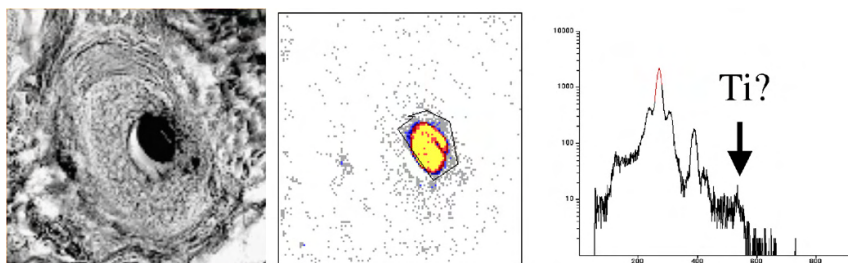

Fig. 2. Transverse cut through a hair follicle of porcine skin exposed to Eucerin micropigment 25 lotion for 30 min, than cleaned with ethanol. Left: STIM before PIXE, scan size 365 × 380 μm². Middle: PIXE-map with region of interest around the hair (sulfur rich). Right: PIXE-spectrum from region of interest clearly showing the Ti-peak around channel 550.

efficiency multiplied by the solid angle of 1.5% of 4π for 1 MeV γ-rays). The detection limit with the HPGe detector was less than 0.03 ng of TiO_2. In the experiments with the nuclear emulsion the detection limit was considerably smaller, however difficult to evaluate.

The activated TiO_2 was carefully mixed with hydrophobic basisgel (German Pharmaceutical Codex) at a concentration of 5% by weight. Large pieces of human skin samples (3 cm × 5 cm) were delivered 2–3 h after surgery of breast cancer. The samples were exposed to the radioactive formulation by gentle rubbing it to the outer part of the skin. After 2 h of exposure the formulation was carefully washed from the skin with ethanol or with ethanol and soap water until no activity was detectable in wadding pads. It was measured that after such a washing procedure still about 5 μg of TiO_2 per 1 cm² of skin was present in the samples (corresponding to 1–2%). After this procedure several biopsies were taken from the skin sample and fixed for 24 h in formalin, then dried, dipped in paraffin and cut with a microtome *perpendicular* to the skin surface into 5 μm thick slices. These slices were stretched on a microscopy glass, covered with the nuclear emulsion and left in the dark for exposure for more than two weeks. After fixation and development the emulsion was investigated with an optical microscope and compared with the underlying image of the skin slice (stained or unstained). Fig. 3 shows a transversal cut through skin containing a hair follicle. This figure clearly shows that TiO_2 "decorates" the hair in the follicle. Since every single positron track is visible (see Fig. 4), radiolabelled nanoparticles are surrounded
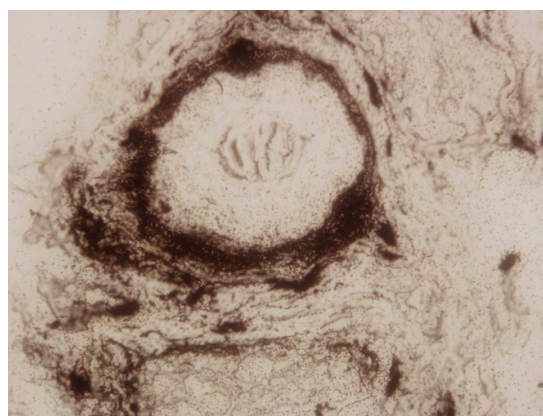

Fig. 3. Part of the autoradiography image of a hair follicle follicle (image size 300 × 220 μm²). Dark with positron "halo" is due to radiolabelled TiO_2.
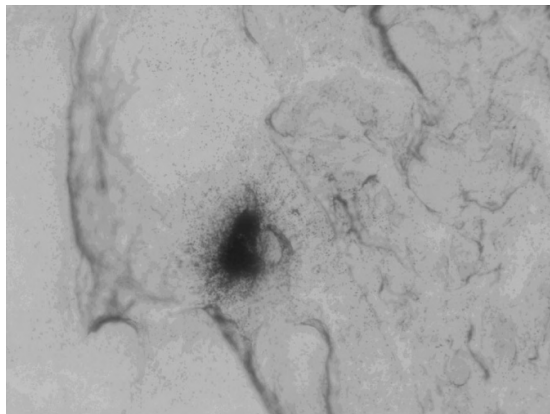
Fig. 4. Autoradiography showing a skin furrow follicle (image size $600 \times 450 \ \mu m^2$); note that individual positron tracks are visible.

by a "halo" of long tracks of the highest energy positrons and thus unambiguously discriminated from "cold" dust particles.

It should be mentioned that "hot" particles are also observed further away from the follicle in vital tissue. However, it should not be concluded that these particles went there *in vivo* because for a transversal cut contaminations are unavoidable.

Biopsies for the investigation with the HPGe detector were cut into 5 μm thick slices *parallel* to the skin surface. Even with a large effort it was not possible to obtain a flat skin surface. Therefore, slices taken even from a deeper cut still could contain some pieces of the skin surface. Slices taken randomly from different depths of skin were measured in a close geometry with the detector, three consecutive slices simultaneously (i.e. equivalent to a 15 μm thick slice). The amount of TiO_2 detected in the measured slices showed unexpected irregularities with respect to the depth, i.e. a sudden increase in activity compared to neighbouring slices. A detailed analysis of neighbouring skin slices via autoradiography showed that this was due to a skin furrow and not due a sebaceous gland.

3. Conclusions

In conclusion, we have shown with two different techniques, namely μPIXE/RBS/STIM and autoradiography, that formulations containing nanoparticles such as TiO_2 with primary particle sizes around 20 nm can be pushed

into hair follicles as deep as several 100 μm. Occasionally, follicles which were devoid of nanoparticles were observed.

The ultimate sensitivity of autoradiography with [48]V-labelled nanoparticles is, unfortunately, obstructed by contamination problems which are difficult to solve. If the microemulsions would be soaked into a greater depth of several tens of micrometers, the topmost slices with the thickness of the range of the positrons could be removed after the label has completely decayed; in this way any possible contamination during cutting would be removed as well. Unfortunately, we did not succeed in soaking microemulsions into thick tissue yet.

Since we never observed nanoparticles in vital tissue surrounding the follicle, we do not consider the transfollicular pathway a possible route of concern for the incorporation, let alone the systemic incorporation. Another question is the clearance of such formulations containing nanoparticles from follicles. A plausible time scale would be related to sebum production and/or hair growth. The future fate of such nanoparticles might become relevant from an eco-toxicological point of view.

References

[1] B. Forslind, M. Lindberg, G.M. Roomans, J. Pallon, Y. Werner-Linde, Microsc. Res. Tech. 38 (4) (1997) 373.
[2] Ph. Moretto, J.-E. Surlève-Bazeille, D. Licu, C. Michelet, P. Stoedzel, Nucl. Instr. and Meth. B 158 (1999) 386.
[3] M.H. Tan, C.A. Commens, L. Burnett, P.J. Snitch, Australas. J. Dermatol. 37 (1996) 185.
[4] F. Pflücker, H. Hohenberg, E. Hölzle, T. Will, S. Pfeiffer, R. Wepf, B. Diembeck, H. Wenck, H. Gers-Barlag, Int. J. Cosmetic Sci. 21 (6) (1999) 399.
[5] C. Bennat, C.C. Müller-Goymann, Int. J. Cosmetic Sci. 22 (2000) 271.
[6] 2nd Annual Report of NANODERM, QLK4–CT–2002-02678; E. Gontier, M.D. Ynsa, J. Hunyadi, B. Kiss, K. Gáspár, T. Pinheiro, J.N. Silva, P. Filipe, J. Stachura , W. Dabros, T. Reinert, T. Butz , Ph. Moretto, J.-E. Surlève-Bazeille, submitted for publication.
[7] J. Lademann, H.J. Weigmann, Ch. Rickmeier, H. Barthelmes, H. Schaefer, G. Müller, W. Sterry, Skin Pharm. Appl. Skin Physiol. 2 (1999) 247.
[8] J. Lademann, Presentation at the Bundesinstitut für Risikobewertung, Berlin, 28.3.2006, <http://www.bfr.bund.de/cm/232/risikobewertung_von_nanopartikeln_in_kosmetischen_produkten.pdf>.

NANODERM

Quality of Skin as a Barrier to ultra-fine Particles

QLK4-CT-2002-02678

Final Report - Summary

2007

Authors:

      Tilman Butz (Coordinator)

      Tilo Reinert

      Teresa Pinheiro

      Philippe Moretto

      Jan Pallon

      Árpad Zoltán Kiss

      Jerzy Stachura

      Wojciech Dąbroś

      Zbigniew Stachura

      Janusz Lekki

      Malgorzata Lekka

      Janos Hunyadi

      Tamás Bíró

      Michael Sticherling

      Luc Van Vaeck

      Pieter Van Royen

      Jean-Etienne Surlève-Bazeille

Summary

Standard methods in dermal penetration research are tape stripping of the stratum corneum and static Franz-diffusion cells on excised skin. Both methods do not visualize penetration pathways and both techniques can over- and underestimate actual penetration. It is unclear to what extent these techniques can be applied to the study of dermal penetration of nanoparticles, e.g. TiO_2 with dimensions in the range of 20 nm which is widely used in sunscreens with physical UV-filters. On the contrary, high resolution transmission electron microscopy (HRTEM) on ultra thin skin cross-sections visualizes individual nanoparticles but suffers from a very limited field of view. There are several preparation steps involved in preparing ultra thin skin cross-sections with the possibility of preparation artefacts. Thus, there are controversial reports on HRTEM studies of dermal penetration of nanoparticles and novel microscopic techniques are required in order to clarify the situation. A relatively new and promising application is confocal laser scanning microscopy which, however, requires a fluorescent label with the associated problem of the stability of the label.

The **objective of the NANODERM project** was to complement **HRTEM** studies with another technique, namely **ion beam analysis** (PIXE: Particle Induced X-Ray Emission; RBS: Rutherford Backscattering Spectrometry; STIM: Scanning Transmission Ion Microscopy), in order to **visualize putative pathways of nanoparticles** in skin cross-sections.

The advantage of these techniques is that very few sample preparation steps are required and thus the risk for preparation artefacts is reduced. A further advantage is that preparation artefacts, should they occur, can be easily identified, contrary to HRTEM. Moreover, larger samples can be analyzed in order to get an overview over large areas; subsequently one can zoom into a region of interest. A disadvantage is that individual nanoparticles cannot be visualized and the measurements are time-consuming. A further disadvantage is that the sample integrity can suffer if too high currents are used for PIXE; therefore the samples have to be analyzed by STIM, a technique which uses currents of about 0.1 fA before and after the PIXE measurement to ensure sample integrity.

A third technique was applied which has not been used thus far for dermal penetration studies: **autoradiography** using skin cross-sections and nuclear microemulsions. For these studies we used TiO_2 and the radiolabel 48-V. This methods has extreme sensitivity.

Biopsies from **porcine skin** and **healthy human skin** from volunteers (male and female, coloured and caucasian, different ages), as well as from **human foreskin transplanted to SCID-mice** were studied. In addition, healthy human **skin ex-**

plants from surgery was used for autoradiography. Biopsies from patients suffering from **psoriasis** were included in the study.

Several pre-treatments of the skin were applied: cleaning with ethanol, excess water exposure, partial tape stripping. **Various dermatological formulations** (mainly carbomergel, polyacrylategel, hydrophobic basisgel, isopropylmyristategel, microemulsion) containing TiO_2 nanoparticles (mainly Eusolex T-2000) and the **commercially available products** Eucerin Micropigment Crème 15 (Beiersdorf), Eucerin Micropigment Lotion 25 (Beiersdorf), Avène 50 (Pierre Fabre), and Anthelios XP SPF60 (Roche Posay) were applied topically to the skin with about 2 mg/cm^2 under non-occlusive, semi-occlusive, and occlusive conditions. Exposure times varied from 30 minutes to 48 hours.

In all but a few cases Ti was detected **on top of the stratum corneum and in the topmost layers of the *stratum corneum disjunctum*** for healthy skin. Frequently the nanoparticles were aggregated. In most cases Ti-spots in vital tissue could be identified as preparation artefacts. **In none of the roughly 500 images a coherent pathway of nanoparticles was observed, let alone a concentration profile characteristic of diffusive transport**. Hence, we conclude that the TiO_2 nanoparticles are penetrated into the topmost 3-5 corneocyte layers by mechanical action and no diffusive transport takes place. Thus, penetration studies with static Franz-diffusion cells do not seem adequate for nanoparticles. Clearance is expected to proceed via desquamation.

There is **deep penetration into hair follicles, but not into vital tissue**. Clearance is expected to proceed via sebum excretion.

No new species were detected by static Secondary Ion Mass Spectrometry (S-SIMS) and Laser Modulated Mass Spectrometry (LMMS) due to the interaction of the formulations with coated TiO_2 nanoparticles without and with UV-light.

The **interaction of cells** with TiO_2 nanoparticles both coated and uncoated was studied both ***in-vitro*** and ***in-vivo*** by **immuno-histochemical methods** and **Atomic Force Microscopy**. The cellular response to TiO_2 nanoparticles was found to depend on the cell type; various endpoints were examined. The elasticity of cells was affected by uncoated TiO_2 nanoparticles and UV-light. Radical scavengers suppressed the change in elasticity. The relevance of these observations on the cellular level is still an open question because the exposure is rather low, if it exists at all. Nevertheless, we conclude that for the sake of safety, direct contact of skin cells with TiO_2 nanoparticles should better be avoided, e.g. application of sunscreens into open wounds is not recommended.

The situation with **psoriatic skin** is less clear. Instead of a *stratum corneum* of about 10 – 15 µm thickness, psoriatic skin has a *stratum corneum* of about 100 µm thickness with corneocytes and vital keratinocytes intermingled. Here, there is no real barrier and TiO_2 nanoparticles can come into direct contact with vital cells. However, we have no evidence that the TiO_2 nanoparticles become systemic.

Summing up, we do not expect any health effects for the topical application of sunscreens containing TiO$_2$ nanoparticles (especially when coated) on healthy skin which are related to the particulate state.

The **life cycle** of TiO$_2$ nanoparticles was not examined in the present project and **ecotoxicological aspects** as well as possible subsequent absorption via other ports of entry should be considered in the future.

There are still a few open questions concerning e.g. sunburned skin with skin detachments - a typical misuse of sunscreens - or **atopic skin**. Furthermore, the role of **microlesions** is unclear.

Maybe the largest uncertainty is related to the fact that two recent publications demonstrated that mechanical flexion of skin can greatly enhance the penetration.

A standardized apparatus for mechanical flexion should be developed.

Finally, each method has detection limits and long-term exposure might still lead to appreciable absorption. Thus the **biokinetics**, possible translocation and accumulation into secondary organs, and the excretion should be investigated.

Last but not least, although TiO$_2$ nanoparticles of much smaller dimensions than 20 nm, say e.g. 2 nm, are not in use in sunscreens, it is conceivable that they might nevertheless be present and adsorbed onto larger particles, a phenomenon well known in aerosol studies. Whether they can be isolated and whether they are more soluble in body fluids than their larger counterparts remains to be investigated.
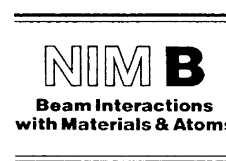
Quantitative microanalysis of perineuronal nets in brain tissue

Tilo Reinert [a,*], M. Morawski [b], T. Arendt [b], T. Butz [a]

[a] *Nukleare Festkörperphysik, Universität Leipzig, Linnéstr. 5, 04103 Leipzig, Germany*
[b] *Paul-Flechsig-Institut für Hirnforschung, Universität Leipzig, Jahnallee 59, 04109 Leipzig, Germany*

Abstract

The relevance of the perineuronal nets (specialised extracellular matrix surrounding a part of the neurons in brain tissue) as a possible protection of neurons against oxidative stress induced by metal ions (e.g. Al, Fe, Cu and Zn) is an actually discussed hypothesis. It is assumed that the perineuronal nets are able to bind metal ions and thus reduce the oxidative stress to neurons. Therefore, we used nuclear microscopy (μPIXE) in order to investigate the concentration and distribution of iron in rat brain loaded with colloidal iron with special emphasis to the perineuronal nets in the extracellular matrix. The elemental microanalysis was performed on 6 μm thin resin embedded sections. The perineuronal nets accumulated more Fe than other extracelullar matrix components leading to well defined, neuron-related structures in the Fe maps. In order to quantify the affinity, the iron accumulations in the perineuronal nets were analysed for different Fe loadings.

We present first results that support the hypothesis that perineuronal nets act as chemical protection mechanism against oxidative stress due to their ability to bind metal ions.
© 2003 Elsevier B.V. All rights reserved.

PACS: 07.78.+S; 41.75.Ak; 87.22.J; 87.64.t
Keywords: Neuronal nets; Brain; Metal ions; PIXE

1. Introduction

In 1893 the neuroscientist Camillo Golgi discovered in brain tissue of a cat a morphological structure, the perineuronal net, which was denied on the basis of an ideological conflict by Santiago Ramón y Cajal, who also observed this structure, but took it for a fixation artefact. After Cajal's statement only a few scientists continued to work in this field and after the 1930s the perineuronal net was forgotten [1]. However, the advances in histochemical and immunocytochemical methods [2–4] brought back the perineuronal net and new scientific interests on it.

The perineuronal net (PN), originally described as "finely reticular covering of finely granular aspect adhering intimately to the surface of the cell body and proximal dendrites, excluding the axon initial segment, of certain cells in the adult brain" [5], is nowadays morphologically well known, but its functions and physiology are still largely unknown [6,7]. The PN consists mainly of hyaluronic acid, glycoproteins and sulphated proteoglycans

---
* Corresponding author. Tel.: +49-341-9732706; fax: +49-341-9732497.
E-mail address: reinert@physik.uni-leipzig.de (T. Reinert).
URL: http://www.uni-leipzig.de/~nfp.

which are highly negatively charged. Therefore, the perineuronal nets are believed to have, besides other physiological functions, neuroprotective effects against ions of trace redox-active transition metals, especially Fe- and Cu-ions that catalyse free radical production.

The critical role of metal ions in the pathogenesis of neurodegenerative disorders, such as Parkinson's disease, Alzheimer's disease, amyotrophic lateral sclerosis and prion diseases, has been elucidated in recent years and is reviewed by Perry et al. [8]. The findings link the neurodegenerative processes to increased oxidative stress caused by free radicals. The physiological function of the PNs could be, besides a stabilisation of the synapses, maintaining a neuroprotective chemical barrier against metal mediated free radicals.

The aim of this study is to assess the strength of the barrier by quantifying the iron concentration in the PNs and in the extracellular matrix depending on different iron loadings in rat brain.

2. Sample preparation

The brain of an adult Wistar rat was analysed in a series of transverse sections. For the study, the rat was anaesthetised with pentobarbital (50 mg/kg) and transcardially perfused with saline containing heparin, followed by fixative (4% paraformaldehyde in a 0.1 M cacodylate buffer (pH 7.2–7.4)).

The brain was removed from the skull and (3–5) mm thick blocks were prepared. Thereafter, the blocks were postfixed overnight at 4 °C in the same fixative. The blocks were dehydrated in increasing concentrations of ethanol and after repletion in methylbenzoate, the samples were embedded in paraffin, and cut into 6 μm thick sections through the brain region of interest (approx. Bregma −5.80 mm, Fig. 1) including the nucleus ruber (red nucleus), the subiculum and the cerebral cortex. These sections were deparaffinised with xylene and rehydrated in decreasing concentrations of ethanol. After rinsing the sections in bi-distilled water they were incubated in colloidal iron hydroxide (CIH) solutions (modified after [9]) at a pH level of 1 and washed in 5% acetic acid. For the study, six different CIH solutions (2%, 10%, 13%, 20%, 40% and 100%) were used to load the brain sections with colloidal iron. The colloidal iron was stained by the Prussian blue reaction. Thus, the perineuronal nets were clearly visualised, enabling easy determination of the desired scan region (see Fig. 2).

The sections were then rinsed twice in bi-distilled water, dehydrated in increasing ethanol concentrations, cleared in xylene, embedded in Entellan and coversliped. Some of the sections were counterstained with nuclear fast red to visualise additional morphological structures. However, it turned out that staining with Prussian blue is well suited for PN recognition. After 24 h the coverslips were removed and the object slides were cooled
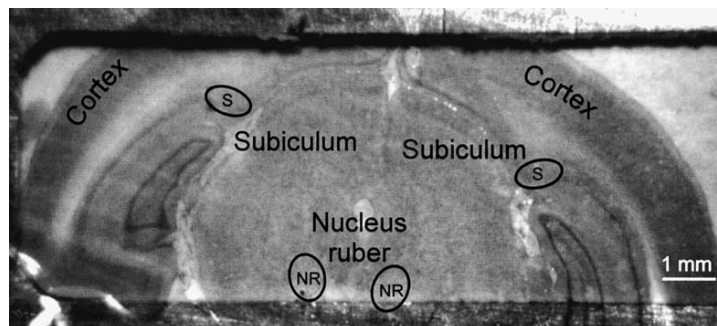

Fig. 1. Photograph of an Entellan embedded 6 μm thin section of rat brain, mounted onto a sample holder. The regions of interest are: (1) Nucleus ruber (NR): region with almost all neurons having PNs; (2) Cortex: moderate amount of PNs; (3) Subiculum (S): large amount of PNs.
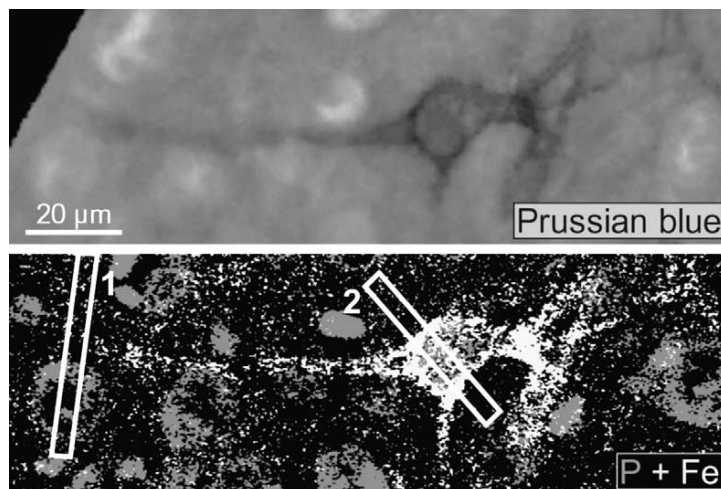
Fig. 2. Top: Microscopic image (150 μm × 50 μm) of a perineuronal net loaded with 40% colloidal iron hydroxide and stained with Prussian blue. Bottom: Corresponding phosphorus (grey) and iron (white) distribution map. The neurons can be localised by their P-rich somata. One neuron possesses a perineuronal net that clearly shows iron accumulation. From the regions 1 and 2 elemental profiles of P, Fe and K were extracted (see Fig. 3).

down (−80 °C) and the embedded sections were peeled off with the assistance of a razor blade.

It has to be noted, that the main interest is in quantifying the iron concentration. Therefore, the standard histological methods were applied accepting a potential alteration in concentrations of unbound elements.

3. Experimental

The nuclear microscopy was carried out at the Leipzig microprobe laboratory LIPSION [10] using a 2.25 MeV proton beam focused to approximately 1 μm spot size at beam currents of about 100 pA. Particle induced X-ray emission (PIXE) was used to analyse the elemental distributions, especially phosphorus (cell indicator) and iron. Simultaneously, Backscattering spectrometry (BS) was used to obtain information on the matrix composition (elements C, N, O and H indirectly), on the sample thickness and on the accumulated beam charge by fitting the BS-spectrum (yielded from the total scanned area) using the RUMP code [11].

The analysis of the hydrogen content is not straightforward and obviously an uncertainty in microbeam analysis as often stated and discussed (for example in [12]). However, the uncertainty has no crucial influence on the fitted data leading to an uncertainty in the range of a few percent. Since hydrogen is always present in organic material a ratio between carbon and hydrogen of 0.5 (C_5H_{10}) was assumed for the embedded brain tissue.

The information on matrix composition and accumulated charge was used as input for quantitative analysis in the PIXE data analysis program GeoPIXE II. This software package enables quantitative elemental imaging and has various image processing tools for μPIXE measurements [13]. Thus, elemental profiles and average concentrations in carefully selected regions of interest were extracted (Figs. 3 and 4). In order to determine the region of the perineuronal net (PN) a threshold iron concentration of 40% of the maximum value was chosen. This threshold defined regions (PN in Fig. 4) well matching the perineuronal net (in fact the prominent Prussian blue staining). The region defining the extracellular matrix (ECM) was chosen outside the PNs and
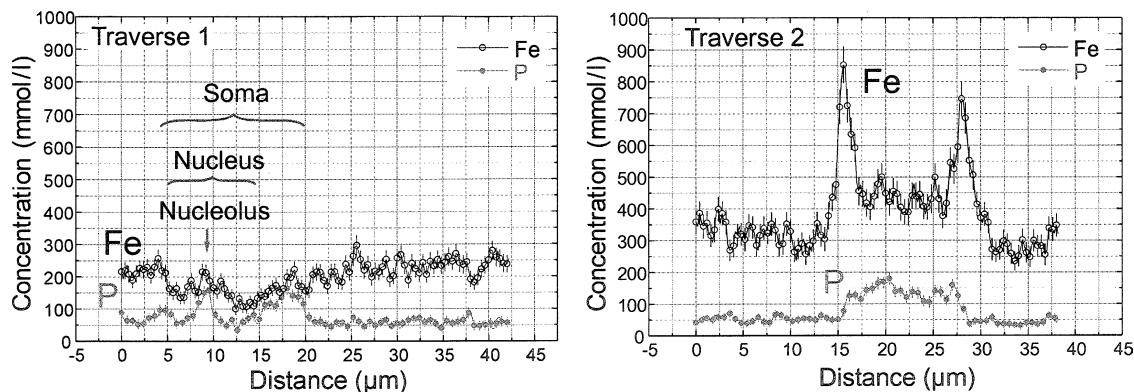
Fig. 3. Elemental profiles of Fe and P across the somata of neurons without (traverse 1) and with perineuronal net (traverse 2) extracted from Fig. 2 (40% CIH). The perineuronal net shows a manifold higher iron concentration than the surrounding extracellular matrix.
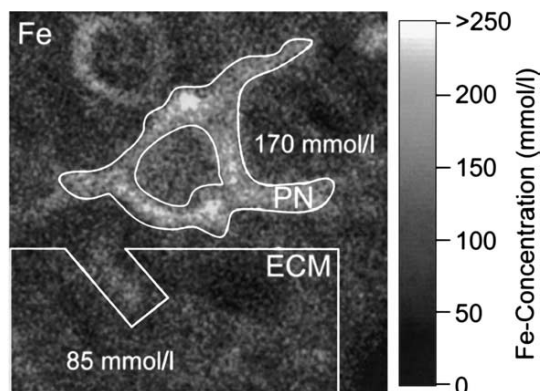

Fig. 4. Distribution map of iron. The quantitative concentrations were extracted from the marked regions.

outside the somata represented by higher phosphorus concentrations (ECM in Fig. 4).

4. Results and discussion

As expected, the iron distribution matches exactly the distribution of the Prussian blue stained colloidal iron demonstrating the perineuronal nets (Fig. 2). The phosphorus distribution shows the distribution of the somata of the neurons by highlighting the cytosol and if present the nucleolus. The nucleus itself contains less phosphorus.

The superposition of the Fe- and P-distribution clearly demonstrates neurons with and without PNs. Taking a traverse across the two types of neurons the different ability to bind iron becomes apparent and more important, quantifiable (Fig. 3).

Table 1 shows the iron concentrations in the extracellular matrix (ECM) and in the perineuronal nets (PN) of the subiculum as well as their ratios depending on the initial load with colloidal iron hydroxide. In the control and in the case of the lowest CIH loading where no PN could be seen, the intracellular iron concentration was analysed. Starting with a CIH load of 10% the PNs could be recognised and therefore be analysed. With this relatively moderate loading the ratio between the Fe concentration in the PN and in the ECM is the highest compared to the ratios at increased loadings. This successively decreasing ratio can be explained by an increasing saturation of the PN. In the case of the highest CIH loading the ratio approaches 1, i.e. the PN is nearly totally saturated.

As can be seen in Fig. 5 the relation between the ratio and the initial CIH loading can be described mathematically by a hyperbolic function with an offset of 1. The same result can be concluded from the concentrations of the measurements in the regions of the nucleus ruber and the cortex.

Table 1

Concentration of Fe in perineuronal nets (PN) and in the surrounding extracellular matrix (ECM) after different colloidal iron hydroxide load (CIH) analysed in the subiculum

CIH load (%)	Fe conc. (mmol/1)		Ratio
	PN	ECM	PN/ECM
0 (control)	$(3 \pm 0.3)^a$	1.26 ± 0.23	–
2	$(52 \pm 6)^a$	65 ± 5	–
10	263 ± 98	62 ± 15	4.2 ± 1.9
13	284 ± 34	86 ± 2	3.30 ± 0.4
20	307 ± 97	110 ± 14	2.8 ± 1.0
40	457 ± 145	213 ± 20	2.1 ± 0.7
100	800 ± 118	551 ± 48	1.5 ± 0.5

The factor of higher accumulation in the PN is also given. The stated errors are the standard deviations of the average values from three measurements per CIH loading.

[a] Since in the control and the 2%-CIH loading no PN became visible, the Fe-concentration in the somata were analysed instead.
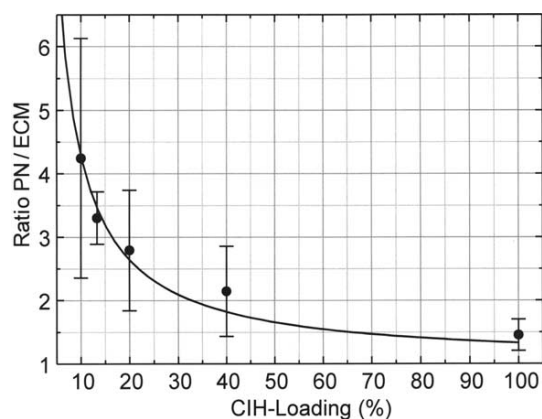
Fig. 5. The relation between the initial colloidal iron hydroxide loading and the ratio of concentrations perineuronal net/extracellular matrix. It can be described by a hyperbolic function with an offset of 1.

5. Conclusion

The spatially resolved, quantitative nuclear microscopy was successfully used to investigate the accumulation of iron in perineuronal nets in rat brain. It could be clearly shown that the perineuronal net has the ability to bind a large amount of iron concentrated close to the neuron. This affinity is not related to the iron rich granules reported by Thong which are believed to be associated to neuromelanin [14].

Nuclear microscopy enables further investigations of perineuronal nets, especially affinity studies for various metal ions. Additionally, this study will be expanded to human brain.

Acknowledgements

References

[1] R. Spreafico, S. De Biasi, L. Vitellaro-Zuccarello, J. History Neurosci. 8 (2) (1999) 179.

[2] G. Seeger, K. Brauer, W. Härtig, G. Brückner, Neuroscience 58 (2) (1994) 371.

[3] T. Murakami, M. Kosaka, H. Sato, A. Ohtsuka, T. Taguchi, Arch. Histol. Cytol. 64 (3) (2001) 313.

[4] G. Brückner, A. Bringmann, G. Koppe, W. Härtig, K. Brauer, Brain Res. 720 (1–2) (1996) 84.

[5] C. Golgi, Rendiconti della Reale Accademia dei Lincei (21 maggio) 2 (1893) 443.

[6] H. Takahashi-Iwanaga, T. Murakami, J. Neurocytol. 27 (1998) 817.

[7] M.R. Celio, I. Blümcke, Brain Res. Rev. 19 (1994) 128.

[8] G. Perry, L.M. Sayre, C.S. Atwood, R.J. Castellani, A.D. Cash, C.A. Rottkamp, M.A. Smith, CNS Drugs 16 (5) (2002) 339.

[9] W. Graumann, S.W. Clauss, Acta Histochem. 6 (1958) 1.

[10] J. Vogt, R.-H. Flagmeyer, J. Heitmann, D. Lehmann, T. Reinert, St. Jankuhn, D. Spemann, W. Tröger, T. Butz, Mikrochim. Acta 133 (2000) 105.

[11] L.R. Doolittle, Nucl. Instr. and Meth. B 9 (1985) 344.

[12] M. Maetz, W.J. Przybylowicz, J. Mesjasz-Przybylowicz, A. Schüßler, K. Traxel, Nucl. Instr. and Meth. B 158 (1999) 292.

[13] C.G. Ryan, Nucl. Instr. and Meth. B 181 (2001) 170.

[14] P.S.P. Thong, F. Watt, D. Ponraj, S.K. Leong, Y. He, T.K.Y. Lee, Nucl. Instr. and Meth. B 158 (1999) 349.

ELSEVIER

Determination of trace elements in the human substantia nigra

M. Morawski [a,*], Ch. Meinecke [b], T. Reinert [b], A.C. Dörffel [a], P. Riederer [c], T. Arendt [a], T. Butz [b]

[a] *Paul-Flechsig-Institut für Hirnforschung, Universität Leipzig, Jahnallee 59, 04109 Leipzig, Germany*
[b] *Fakultät für Physik und Geowissenschaften, Universität Leipzig, Linnéstraße 5, 04105 Leipzig, Germany*
[c] *Klin. Neurochemie, Abt. Psychiatrie, Universität Würzburg, Füchsleinstraße 15, 97080 Würzburg, Germany*

Available online 23 March 2005

Abstract

"The gain in brain is mainly in the stain" was long time a key sentence for research in neurodegenerative disease. However, for a quantification of the element concentrations (especially iron) in brain tissue, standard staining methods are insufficient. Advanced physical methods allow a quantitative elemental analysis of brain tissue. The sophisticated ion beam analysis provides a quantitative determination of elemental concentrations with a subcellular spatial resolution using a scanning proton beam focussed down to below 1 μm that induces characteristic X-rays in the specimen (PIXE – particle induced X-ray emission).

Histochemical and biochemical determinations of total iron content in brain regions from idiopathic Parkinson's disease have demonstrated an increase of iron in parkinsonian *substantia nigra pars compacta* but not in the *pars reticulata*, however without a clear cellular classification.

For the first time, we have differentially investigated the intra- and extraneuronal elemental concentrations (especially iron) of the human *substantia nigra pars compacta* versus *pars reticulata* with detection limits in the range of 50 μmol/l. Thus, we could compare the neuronal iron concentration in human brain sections of healthy and parkinsonian brain tissue. Clear differences in the iron concentration and distribution could be disclosed. Additionally, we could show in situ that the increased intraneuronal iron content is linked to neuromelanin.
© 2005 Elsevier B.V. All rights reserved.

PACS: 07.78.+S; 41.75.Ak; 87.22.J; 87.64.t

Keywords: Life sciences; Brain research; Parkinson's disease; Neuromelanin; Iron; Nuclear methods; PIXE; Substantia nigra pars compacta pars reticulata

* Corresponding author. Tel.: +49 0341 97 25757; fax: +49 0341 97 25729.
  E-mail address: morm@medizin.uni-leipzig.de (M. Morawski).

1. Introduction

Iron is the most abundant transition metal in the brain. Iron is found in active centres of many enzymes. It is a principal component of cytochromes and the iron–sulphur complexes of the oxidative chain and is therefore important for producing adenosin triphosphate (ATP). Also, the synthesis of neuronal transmitters depends on iron. Iron is a cofactor for the generation of dopamine, which highly decreases in idiopathic Parkinson's disease (PD). Furthermore there is an intense iron staining in areas that receive GABAergic (γ-aminobutyric acid) innervation suggesting a possible relationship between iron and the neuronal transmitter GABA. But up to now there is no quantified and no sufficient cellular assignment of the iron. Generally, iron is permanent complexed with proteins, but can also be present in a *labile iron pool* (LIP) of chelatable and redox-active iron [10]. In general, iron is considered as a most potent toxin.

Roughly twenty neurodegenerative disorders are associated with possible metal involved pathologies. Among them, the iron-related diseases of the brain take the biggest part (15 neurodegenerative disorders) [3]. Abnormally increased non-heme iron levels in brain areas were correlated with PD as demonstrated in a multitude of publications (for review see [5]).

These increased brain tissue iron levels have been concerned as a key generator of reactive oxygen species which damage molecules, e.g. proteins, lipids, carbohydrates and nucleic acids [16]. Oxidative stress, which is sequentially formed through increased iron induced processes (e.g. Fenton reaction), is broadly believed to be one of the major causes responsible for neuronal cell death in PD (for review see [11]). Due to these facts it is of essential significance to get specific information on the exact concentrations of iron on cellular or even subcellular levels.

For this experiment, the technique of X-ray and nuclear microscopy (e.g. μPIXE) is a versatile tool to investigate the concentration and spatial distribution of iron [8,14,15].

To our knowledge, we are the first to investigate differentially the intra- and extraneuronal elemental concentrations (especially iron) in the human brain and in particular in the human *substantia nigra pars compacta* versus *pars reticulata* of PD and healthy control brains. We were able to reach detection limits in the range of 50 μmol/l with μPIXE. Therefore, we could compare the neuronal iron concentration in human brain sections of healthy and parkinsonian brain tissue as well as the concentration of the subcellular iron bound to neuromelanin.

2. Sample preparation

For brain sections analysis of human midbrain encompassing the *substantia nigra pars compacta* and *pars reticulata* of idiopathic Parkinson's disease patients and non-demented controls were used. The sections were prepared without any staining to determine the native iron content in the PD and control brains. Twelve brains from patients with PD (aged 75 ± 5 years, $n = 6$) and controls (aged 68 ± 4 years, $n = 6$) were obtained at autopsy (Brain Bank of the University of Leipzig).

Brains obtained at autopsy were fixed by immersion in 4% formalin (4% aqueous solution of HCHO) for 1 week or longer. The tissue was rinsed under running tap water and conventional protocols for paraffin embedding and block mounting were used. The tissue was cut into 6 μm thick sections. These sections were deparaffinised with xylene and rinsed with ethanol to bring it into toluene. Then the slices were embedded in mounting medium (DePeX®, Merck) and coverslipped. After 24 h the samples were immerged into toluene to remove the coverslip. The embedded sections were peeled off to mount them on the sample holder for microbeam analysis.

3. Experimental

In this study, exclusively 6 μm thick unstained human brain slices embedded in DePeX® were investigated.

The analysis of the brain sections were performed at the ion beam laboratory LIPSION [9] (University of Leipzig). We used a 2.25 MeV proton beam at 120 pA with a beam diameter below

1 μm. Particle induced X-ray emission (PIXE) was used to analyse the elemental distributions of minor and trace elements, especially phosphorus (cell indicator), sulfur (melanin indicator) and iron. Simultaneously, proton backscattering spectrometry (BS) was used to obtain information on the matrix composition (elements C, N, O), on the sample thickness and on the accumulated beam charge by fitting the BS-spectrum using the RUMP code [2] including the non-Rutherford cross sections for C, N, O [1,13]. The determination of the hydrogen content was carried out according to the description in [12]. The information on the matrix composition and on the accumulated charge was used as input for quantitative analysis in the PIXE data analysis program GeoPIXE II [17]. The intraneuronal, extraneuronal and melanineous elemental profiles and average concentrations of the *substantia nigra pars compacta* (*SN pc*) and *pars reticulata* (*SN pr*) were extracted. One to four different cell containing areas per case and part of *substantia nigra* (*SN pc* and *SN pr*) were measured.

4. Results and discussion

The level of total iron in the *SN* in PD brains have been reported to be 1.3 up to 3.4 times higher than that in the *SN* of healthy controls (for review

see [5,6]). In our investigation, we found a 1.7 times increase in total iron of PD *SN's*. The total iron content of *SN* in PD and healthy controls are given in Table 1. In addition, the data were separated in extraneuronal iron content (any non-neuronal cell body containing tissue), intraneuronal iron content (only neuronal cell bodies) and melanin iron content (iron in overlap to neuromelanin in dopaminergic *SNpc* neurons) of the *pars compacta* and the *pars reticulata* in PD and healthy controls.

In healthy controls the iron concentration in the *pars reticulata* is greater than in the *pars compacta*. This relation is inverted in PD (Fig. 1).

Table 1
Iron content of *SN* in healthy controls and PD

Iron concentration [mmol/l]		Control	Parkinson's disease
PC	Total	7.8	14.3
	Extraneuronal	6.2 ± 1.3	8.5 ± 1.7
	Intraneuronal	15.2 ± 3.2	25.0 ± 6.6
	Melanin[*]	20.5 ± 3.8	41.4 ± 5.6
PR	Total	10.7	16.7
	Extraneuronal	7.6 ± 1.0	13.8 ± 6.7
	Intraneuronal	8.1 ± 1.4	14.8 ± 7.3
	Melanin	–	–
SN	Total (PC + PR)[*]	9.3 ± 1.2	15.5 ± 3.0

Differentiated data of extraneuronal-, intraneuronal- and melanin- iron content of the *SN pars compacta* and the *SN pars reticulata* in non-demented controls and PD. Data are mean values ± SEM.
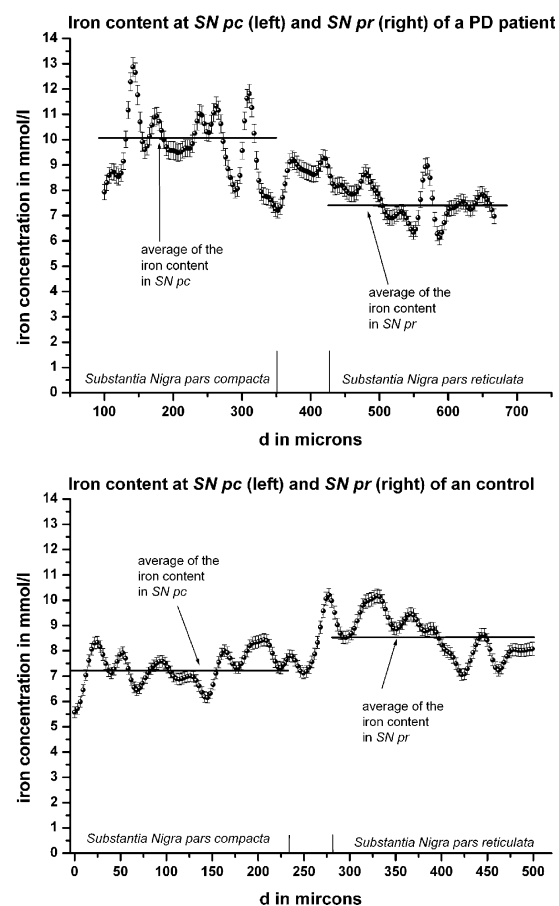[*] Significance $p < 0.05$ (students *t*-test).

Fig. 1. The integral iron distribution along a traverse. The traverse was set to the whole *SN* including *SNpc* and *SNpr*.
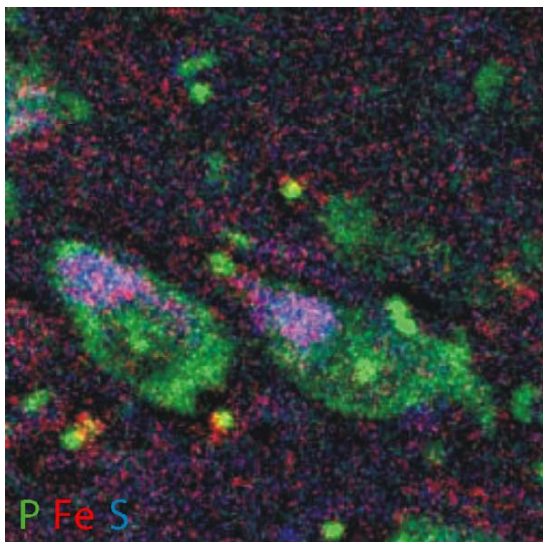
Fig. 2. Three-element map of P, Fe, S of a human *SNpc* neuron in PD. Phosphorus (green), iron (red) and sulphur (blue) is shown. The neurons can be localised by its phosphorous rich somata. The violet colour is an overlap of red and blue which shows a clear spatial correlation of iron and sulphur, i.e. the binding of iron to neuromelanin.

The intraneuronal iron concentration of PD neurons is increased in comparison to the healthy tissue, which is possibly caused by the ability of neuromelanin to bind iron [4]. The ability of neuromelanin to bind iron is shown in a three-elements map (Fig. 2). The spatial distributions of iron (red), phosphorous (green), which indicates the soma of the neuron, and sulphur (blue) are overlaid. The violet colour as an overlap of red and blue demonstrates that the increased iron concentration in dopaminergic neurons in *SNpc* is caused by the iron-rich neuromelanin.

A detailed analysis of the neuromelanin of the parkinsonian and healthy *SNpc* revealed the suggested increased iron content in the PD group (Table 1).

The elevated variation of the mean iron concentration values is in all probability caused by the different stages of the disease and the varying ages of the patients.

5. Conclusion

The first µPIXE study of human *Substantia nigra* affected by idiopathic Parkinson's disease yielded quantitative elemental maps from which differences in the iron content to non-demented controls could be spatially resolved.

The data determined by a multitude of different groups with a variety of histochemical, biochemical and spectrometric techniques revealed a consistent overall increase of *SN* iron in PD. Our data support these findings. Beyond this, our study gives a detailed analysis of the relation between the extraneuronal-, intraneuronal- and melanin related iron content in a direct comparison of *SNpc* to *SNpr*. Griffiths' questions about "the cellular and subcellular distributions of iron" and his statement that they "are also uncertain" [6] can now be answered in more detail.

In the numerous studies most attention is drawn to non-neuronal cells in order to explain the iron content in *SN* [7]. Here, we could show that even the neurons in the *SN* contain a non-negligible amount of iron, which underlies the same shift typical described under PD pathological conditions. Furthermore, we could show that the neurons of the *SN pars reticulata* accumulate more iron. A possible explanation is: the highly increased activation of microglia leads to a loss of extracellular matrix thereby decreasing the iron binding capacity which releases more free iron to the *SN pars reticulata*. A detailed study about this subject is currently underway.

References

[1] R. Amirikas, D.N. Jamieson, S.P. Dooley, Nucl. Instr. and Meth. B 77 (1993) 110.

[2] L.R. Doolittle, Nucl. Instr. and Meth. B 9 (1985) 344.

[3] P.M. Doraiswamy, A.E. Finefrock, Lancet Neurol. 3 (2004) 431.

[4] K.L. Double, D. Ben Shachar, M.B. Youdim, L. Zecca, P. Riederer, M. Gerlach, Neurotoxicol. Teratol. 24 (2002) 621.

[5] M.E. Götz, K. Double, M. Gerlach, M.B. Youdim, P. Riederer, Ann. N.Y. Acad. Sci. 1012 (2004) 193.

[6] P.D. Griffiths, B.R. Dobson, G.R. Jones, D.T. Clarke, Brain 122 (1999) 667.

[7] J.M. Hill, R.C. Switzer III, Neuroscience 11 (1984) 595.

[8] A. Ide-Ektessabi, T. Kawakami, F. Watt, Nucl. Instr. and Meth. B 213 (2004) 590.

[9] J. Vogt, R.-H. Flagmeyer, J. Heitmann, D. Lehmann, T. Reinert, St. Jankuhn, D. Spemann, W. Tröger, T. Butz, Mikrochim. Acta 133 (2000) 105.

[10] O. Kahhlon, Z.I. Cabantchik, Free Radic. Biol. Med. 33 (2002) 1037.

[11] D. Kaur, J. Andersen, Ageing Res. Rev. 3 (2004) 327.

[12] F. Menzel, T. Reinert, J. Vogt, T. Butz, Nucl. Instr. and Meth. B 219–220 (2003) 82.

[13] E. Rauhala, Nucl. Instr. and Meth. B. 12 (1985) 447.

[14] T. Reinert, M. Morawski, T. Arendt, T. Butz, Nucl. Instr. and Meth. B 210 (2003) 395.

[15] M.Q. Ren, W.Y. Ong, X.S. Wang, F. Watt, Exp. Neurol. 184 (2003) 947.

[16] P. Riederer, E. Sofic, W.D. Rausch, B. Schmidt, G.P. Reynolds, K. Jellinger, M.B. Youdim, J. Neurochem. 52 (1989) 515.

[17] C.G. Ryan, Nucl. Instr. and Meth. B 181 (2001) 170.

Antibody meets the microbeam – or how to find neurofibrillary tangles

Markus Morawski [a,*], Tilo Reinert [b], Christoph Meinecke [b], Thomas Arendt [a], T. Butz [b]

[a] *Paul-Flechsig-Institut für Hirnforschung, Universität Leipzig, Jahnallee 59, 04109 Leipzig, Germany*
[b] *Nukleare Festkörperphysik, Universität Leipzig, Linnéstr. 5, 04103 Leipzig, Germany*

Available online 23 March 2005

Abstract

In biomedical research the distributions of physiologically or pathologically active elements around or in a certain structure (e.g. tangles, plaques or different cell types) are often of great interest. Therefore, μPIXE analyses are applied to yield quantitative and spatially resolved concentration images of the elements of interest. However, the localisation of the structures to be examined is sometimes scarcely practicable or even impossible. This paper proposes a method of localising the areas of interest for μPIXE analysis. The method is based on the application of a suitable antibody tagged with a single elemental marker (e.g. Ni, Co, Cd, Ag or Au). The antibody then binds selectively to the structures of interest. The elemental marker is detectable via μPIXE, thus, showing finally the structure of interest via the bound antibody. The versatility of the antibodies in combination with the easily applied marker facilitates the localisation of a variety of structures in both light microscopy and μPIXE-imaging. The method is demonstrated on several cellular and subcellular structures in the brain. The elemental concentrations of two consecutive slices, one stained with Ni-enhanced antibody, the other unstained control, are compared to show the feasibility of trace elemental analysis for particular elements in spite if immunohistochemical structure identification. It has to be stated that the proposed technique will not work for free diffusing elements (like Na, Cl, K and Ca) whose concentrations can be altered by wet sample preparation.
© 2005 Elsevier B.V. All rights reserved.

---

[*] Corresponding author. Tel.: +49 0341 97 25757; fax: +49 0341 97 25729.
  E-mail address: morm@medizin.uni-leipzig.de (M. Morawski).

1. Introduction

The metal metabolism in the brain is receiving growing interest, since it has been linked to Alzheimer's disease (AD), Parkinson's disease (PD) [1–4] and other neurodegenerative diseases. Metals supposed to be involved in these pathological processes are Al, Ca, Mn, Fe, Cu, Zn and Pb [2,5,6]. The associated mechanisms are supposed to be located in the oxidative potential and physiological imbalance of the involved metal ions [7,4]. Alterations in their homeostasis, redox activity and sequestration can result in an increased free radical production with profound cellular consequences, including cytotoxicity with subsequent apoptosis or necrosis. Additionally, recent findings enforce the evidence of neurodegenerative processes to oxidative stress caused by metal induced free radicals [8,9].

These results indicate a direct correlation between metal abnormalities and the increased oxidative damage found in neurodegenerative diseases. Therefore, it is of vital importance to gain precise information on the concentrations of metals on preferably cellular or even subcellular levels with an unambiguous correlation to the different cell types and structures.

For this exercise the technique of nuclear microscopy (μPIXE) is a versatile tool to investigate the concentration and distribution of different metals below the 100 μmol/l ($\sim$1 μg/g) level [10–12]. However, the localisation of the structures to be examined is sometimes scarcely practicable or even impossible. Furthermore, the prior standard histochemical staining can lead to misinterpretations of the elemental concentrations due to overlapping elemental content [13].

We therefore combine the technique of nuclear microscopy (μPIXE) and the immunohistochemical (IHC) antibody marking with metal enhancement. In the IHC techniques an antibody is used to link a cellular antigen specifically to a stain that can be more readily seen with a light microscope (LM, Fig. 1). IHC provides a wide range of specimen source, antigen availability, antigen–antibody affinity, antibody type, and detection enhancement methods. The method is based on the application of a suitable antibody tagged with a single elemental marker (e.g. Ni, Co, Cd, Ag or Au). The marker is detectable via PIXE, thus, showing finally the structure of interest via the bound antibody (Ni-maps in Fig. 1). The versatility of the antibodies in combination with the easily applied marker facilitates the localisation of a variety of structures in both light microscopy and μPIXE-imaging.

2. Materials and methods

2.1. Sample preparation

Brains from patients with AD and PD were obtained at autopsy (Brain Bank of the University of Leipzig). The AD case met the criteria for definite diagnosis of Alzheimer's disease according to Ref. [14]. The diagnosis was based on the NIA-Reagan Institute Criteria for the neuropathological assessment of AD [15,16]. The Ethical Committee of the Leipzig University has approved the case recruitment. Brains are fixed by immersion in 4% formalin for 1 week or longer. Conventional protocols for paraffin embedding were used to cut sections of 6 μm thickness from the *frontal-*, *temporal-cortex* and *substantia nigra*.

2.2. Immunohistochemistry

The sections were treated according to standard IHC protocols for each antibody: preincubation, incubation with the primary antibody followed by the secondary antibody. Table 1 gives the antibodies together with the associated structures. The colour was developed using diaminobenzidine (DAB) as chromogen with nickel as enhancer. The sections were mounted on object-slides with Entellan® (Merck, Germany). The regions of interest were cut out and mounted as self-supporting target for ion beam analysis.

2.3. Ion beam analysis

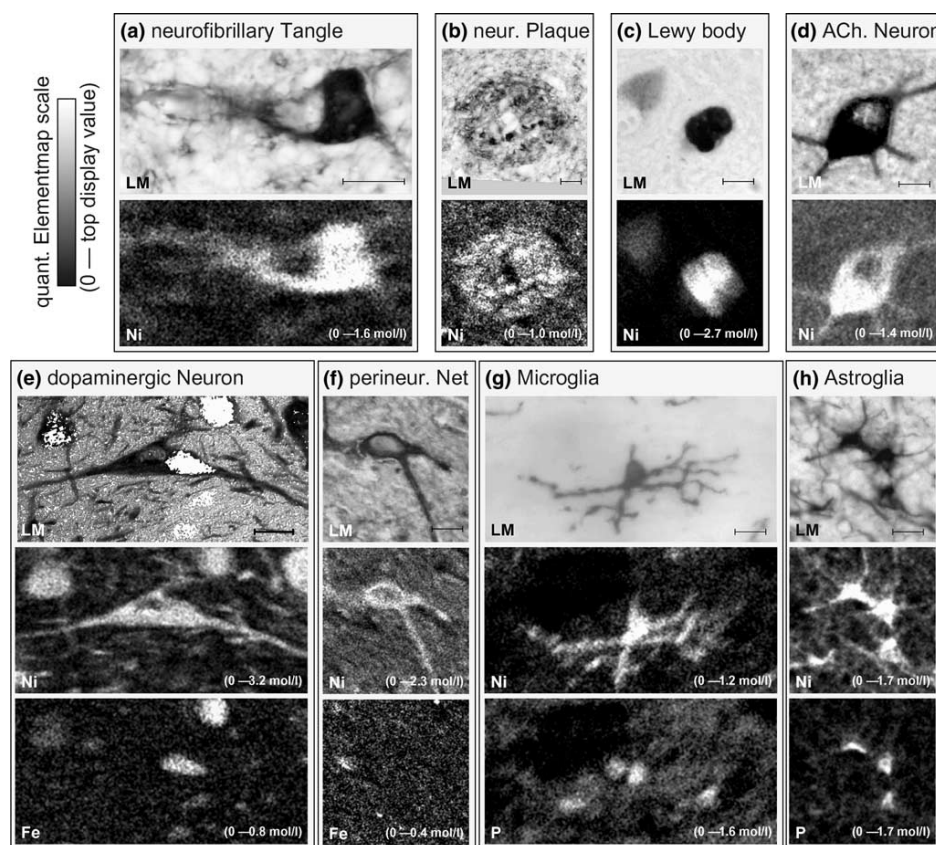The spatially resolved elemental analysis (μPIXE) was carried out at the Leipzig microprobe

Fig. 1. Examples of different immunohistochemically localised structures visible in light microscopy (LM) and in the Ni-image using nuclear microscopy for elemental analysis (Scale bar is 10 μm). Images of selected elements are exemplarily given to show the possibility of spatially resolved trace elemental analysis. For a detailed discussion see Section 3.2 in this paper.

laboratory LIPSION using the standard experimental set-up as described in more detail in Ref.

Table 1
Overview of the characterised structures and the appropriate antibodies

Structures of interest	Antibody used
(a) Neurofibrillary tangles	PHF-τ (AT8)
(b) Neuritic plaques	PHF-τ (AT8)
(c) Lewy bodies	Synuclein-1
(d) Cholinergic neurons	Choline acetyl-transferase
(e) Dopaminergic neurons	Tyrosin hydroxylase
(f) Perineuronal nets	Chondroitin-sulphate proteoglycane
(g) Microglia	Histocompatibility complex class II
(h) Astroglia	Glial-fibrillary acidic protein

[12]. Shortly summarised, we used a 100 pA, 2.25 MeV proton beam with a spot size of about 1 μm in diameter.

After localising the IHC marked structures via the light microscope in the analysing chamber the region of interest was positioned in the beam axis. Simultaneously, Particle Induced X-ray Emission (PIXE) and backscattering spectrometry were used to analyse the elemental distributions and the matrix composition, respectively. The rapidly developing nickel image in the PIXE maps ensures the correct scan position and allows optimizing the scan parameters for analysing the structure. For the quantitative elemental analysis we used the GeoPIXE software package [17].

3. Results and discussion

3.1. Structure recognition

All used antibodies are well described in a multitude of publications and show in every case used here the typical appearance under light microscopy observation (LM images in Fig. 1).

In detail, (a) and (b) anti-AT8 antibody which recognizes the phosphorylated residue of the τ-protein by showing neurofibrillary tangels and neuritic plaques in AD; (c) anti-synuclein-1 marks aggregated synuclein represented in Lewy bodies in PD; (d) anti-choline acetyl-transferase (ChAT) presents neurons utilising acetylcholine as transmitter; (e) anti-tyrosine hydroxylase (TH) displays dopaminergic neurons in the human brain; (f) anti-chondroitin-sulphate proteoglycane (CSPG) antibody reliably labels perineuronal nets in the human brain; (g) anti-histocompatibility complex (HLA)–DP, –DQ, –DR antibodies principally label many macrophages, in the human brain exclusive represented by ramified and activated microglia; (h) anti-glial fibrillary acidic protein (GFAP) demonstrates astrocytes in the human brain.

3.2. Image interpretation of Fig. 1

(a) We found the tangles. Their trace elemental concentrations are still of great interest since it is known that different elements (Fe, Cu and even Al) contribute to the aggregation of the τ-protein [18], the main constituent of the tangles which is one of the major pathologies of AD. (b) The neuritic plaques are a different manifestation of the aggregated τ-protein only. Therefore, the interpretation is similar to (a). (c) The aggregation of α-synuclein leads to the formation of Lewy bodies in PD. In this context copper is also discussed to play a promoting role in a recent publication [19]. (d) One of the early effects or an initial reason in the Alzheimer's disease is the degradation of cholinergic neurons in the forebrain. Thus, studies in order to quantify the trace elemental distributions could yield interesting results. (e) The displayed dopaminergic neuron contains an accumulation of neuromelanin (in the LM image enhanced to white for better visibility), the end product of the catecholamine metabolism. Neuromelanin is known to bind large amounts of iron, which is clearly shown in the iron map. (f) The localisation of perineuronal nets using nickel enhanced IHC with no need to use the iron containing Prussian blue standard stain [12] allows to investigate the native iron binding to the perineuronal nets under pathological and healthy conditions. (g) and (h) These images show an astroglia and an activated microglia which normally can not be distinguished from astroglia or ramified microglia in the phosphorous map. Usually the phosphorous map is used to localise the cell bodies. However, it cannot differentiate between the glia cell types.

3.3. Trace element analysis and immunohistochemistry

In standard staining methods the purity of chemical agents is mostly not a crucial factor for successful staining. However, the purity can be of utmost importance if trace element analysis is needed. In this study the nickel enhanced DAB staining was prepared using nickel ammonium sulphate with a purity of +98% to show in principle the technique (pictures in Fig. 1). For trace element analysis the metal enhancer has to be of very high purity. For Co, Ni, Ag and Cd chloride- and sulphate-salts are available with a purity of 99.999%. With this purity the analysis of elements of pathological interest (e.g. above mentioned metals) is possible. Fig. 2 gives two PIXE-spectra to compare the elemental content of an unstained section with the consecutive section marked with a Ni-enhanced antibody (anti-GFAP) reaction. There is no significant change in trace element concentration due to immunohistochemistry except the intentional Ni enhancement. This example also shows the difficulty for a Cu analysis using Ni as enhancer due to the X-ray line overlap of the Cu-K_α with the Ni-K_β lines. Table 2 gives an overview of antibody metal enhancers with respect to their suitability for elemental analysis.

The free diffusing elements like Na, Cl, K and extracellular Ca cannot be analysed using wet sample processing techniques. However, most of the other elements of interest are mainly bound to
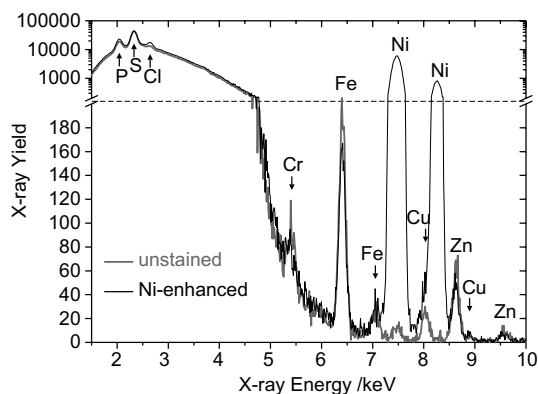
Fig. 2. PIXE-spectra of an unstained section and of the consecutive section marked with a Ni-enhanced antibody (anti-GFAP) reaction. There is no significant change in the concentrations of the elements of interest due to immunohistochemistry except the intentional Ni enhancement.

Table 2
Overview of available metal markers for antibody enhancement and their suitability (+) and inadequacy (−) due to X-ray line overlapping for elemental analysis

Marker	Element of interest				
	P	Mn	Fe	Cu	Zn
Co	+	−	−	+	+
Ni	+	+	+	−	+
Ag	+	+	+	+	+
Cd	+	+	+	+	+
Au	−	+	+	+	−

proteins and therefore fixed to a certain matrix structure (e.g. <2% free Fe).

4. Conclusion

The results show that for spatially resolved analysis of elements (e.g. P, Fe, Cu, Zn) using μPIXE the immunohistochemistry, enhanced with a specific metal (Ni), is a suitable and versatile tool to assist the localisation and differentiation of particular structures not only in the brain but in every biological tissue where antibodies are available. The principle was demonstrated with nickel. Other elements are feasible as well if X-ray line overlaps have to be avoided. For example cobalt, cadmium, gold and silver are applicable. With a suitable (overlap-free) metal enhancer detection limits below 50 μmol/l (<1 μg/g) are achievable.

References

[1] G.M. Bishop, S.R. Robinson, Q. Liu, G. Perry, C.S. Atwood, M.A. Smith, Dev. Neurosci. 24 (2002) 184.
[2] P.M. Doraiswamy, A.E. Finefrock, Lancet Neurol. 3 (2004) 431.
[3] M.E. Götz, K. Double, M. Gerlach, M.B. Youdim, P. Riederer, Ann. NY Acad. Sci. 1012 (2004) 193.
[4] K.J. Thompson, S. Shoham, J.R. Connor, Brain Res. Bull. 55 (2001) 155.
[5] P.I. Oteiza, G.G. Mackenzie, S.V. Verstraeten, Mol. Aspects Med. 25 (2004) 103.
[6] P. Zatta, R. Lucchini, S.J. van Rensburg, A. Taylor, Brain Res. Bull. 62 (2003) 15.
[7] M.W. Hentze, M.U. Muckenthaler, N.C. Andrews, Cell 117 (2004) 285.
[8] Y. Ke, Q.Z. Ming, Lancet Neurol. 2 (2003) 246.
[9] M. Morawski, M.K. Brückner, P. Riederer, G. Brückner, T. Arendt, Exp. Neurol. 188 (2004) 309.
[10] J. Makjanic, B. McDonald, F. Watt, Nucl. Instr. and Meth. B 130 (1997) 439.
[11] J. Makjanic, F. Watt, Nucl. Instr. and Meth. B 150 (1999) 167.
[12] T. Reinert, M. Morawski, T. Arendt, T. Butz, Nucl. Instr. and Meth. B 210 (2003) 395.
[13] J.P. Landsberg, B. McDonald, F. Watt, Nature 360 (1992) 65.
[14] G. McKhann, D. Drachman, M. Folstein, R. Katzman, D. Price, E.M. Stadlan, Neurology 34 (1984) 939.
[15] The National Institute on Aging, and Reagan Institute Working Group on Diagnostic Criteria for the Neuropathological Assessment of Alzheimer's Disease, Neurobiol. Aging 18 (Suppl. 4) (1997) S1.
[16] K.L. Newell, B.T. Hyman, J.H. Growdon, E.T. Hedley-Whyte, J. Neuropathol. Exp. Neur. 58 (1999) 1147.
[17] C.G. Ryan, Nucl. Instr. and Meth. B 181 (2001) 170.
[18] C. Haase, J.T. Stieler, T. Arendt, M. Holzer, J. Neurochem. 88 (6) (2004) 1509.
[19] S. Turnbull, B.J. Tabner, O.M. El Agnaf, S. Moore, Y. Davies, D. Allsop, Free Radical Biol. Med. 30 (2001) 1163.

© Springer 2005

The Binding of Iron to Perineuronal Nets: A Combined Nuclear Microscopy and Mössbauer Study

M. MORAWSKI[1], T. REINERT[2], G. BRÜCKNER[1], F. E. WAGNER[3], Th. ARENDT[1] and W. TRÖGER[2],*

[1]*Paul Flechsig Institute für Hirnforschung, Universität Leipzig, Leipzig, Deutschland*
[2]*Fakultät für Physik und Geowissenschaften, Universität Leipzig, Linnestraße 5, 04103, Leipzig, Deutschland; e-mail: troeger@physik.uni-leipzig.de*
[3]*Physik-Department E15, Technische Universität München, 85747 Garching, Deutschland*

Abstract.   A specialized form of extracellular matrix (ECM) surrounds subpopulations of neurons termed 'perineuronal nets' (PNs). These PNs form highly anionic charged structures in the direct microenvironment of neurons, assumed to be involved in local ion homeostasis since they are able to scavenge and bind redox-active iron ions. The quantity and distribution of iron-charged PNs of the extracellular matrix in the rat brain areas of the cortex and the red nucleus was investigated using the powerful combination of Particle-Induced X-ray Emission (PIXE) and Mössbauer spectroscopy. These studies reveal that the iron is bound to the PNs as Fe(III). PNs in both brain regions accumulate up to three to five times more Fe^{3+} than any other tissue structure in dependency on the applied Fe concentration with local amount maximums of 480 mmol/l Fe at PNs.

Key Words: brain research, iron, life sciences, Mössbauer effect, particle induced X-ray emission, perineuronal nets.

1. Introduction

Perineuronal nets (PNs) are a lattice-like amassment of extracellular matrix (ECM) components, originally described by Golgi [20] as a reticular structure covering the cell bodies and proximal dendrites of certain neurons. They are formed on different types of neurons in certain regions of the brain of many vertebrate species including man [3, 8]. PNs are molecularly heterogeneous, consisting primarily of chondroitin-sulphate proteoglycans (CSPG) of the aggrecan family complexed with hyaluronan [1, 8, 12].

The glycosaminoglycan chains (GAG) of PNs provide a highly negatively charged structure in the direct microenvironment of neurons that might be

---

* Author for correspondence.

involved in local ion homeostasis since it can act as 'spatial buffer' for physiologically relevant ions of calcium, potassium and sodium around highly active types of neurons [8]. The GAG might also interact with ions involved in the generation of oxidative stress such as Fe^{3+}. PNs might be able to reduce the local oxidative potential in the neuronal microenvironment through scavenging and binding of redox-active Fe^{3+} and therefore providing some neuroprotection to those neurons which are ensheathed by PNs.

Iron is the most abundant transition metal in the brain, and in biology in general. It is found in active centers of many enzymes. It is a principal component of cytochromes and the iron-sulphur complexes of the oxidative chain and therefore important for producing adenosine triphosphate (ATP). Also the synthesis of neuronal transmitters is iron-dependent. Iron is a cofactor for the generation of dopamine, which decreases in Parkinson's disease (PD). The capability of iron to catalyse the generation of free radicals by the Fenton reaction in biological systems is well investigated (for a review see [4]). Generally, iron is almost always complexed with proteins, but usually about 2% of iron ions can also be present in a labile iron pool (LIP) of chelatable and redox-active iron [6]. The LIP comprises both ionic forms of iron (Fe(II) and Fe(III)) associated with different ligands such as organic anions, polypeptides and membrane components. Furthermore, it reacts with hydrogen peroxide and superoxide to form highly reactive hydroxyl radicals causing lipid peroxidation, DNA strand breaks and degradation of biomolecules [5] and is supposed to play a major role in Alzheimer's disease (AD) [11]. Post mortem studies in AD brain tissue display a disturbance in the iron distribution and a pathological increase in neuritic plaques [7].

In a previous study, we could show that in AD brains cortical areas highly enriched in PNs are less frequently affected by neurofibrillary degeneration while PNs are much less abundant in vulnerable areas [2]. Moreover, we could extend the findings on the presumptive neuroprotective capacity of ECM components by demonstrating that neurons associated with PNs are less frequently affected by lipofuscin accumulation than neurons devoid of PNs [8]. In the present study, we investigate these potential neuroprotective effects of PNs for iron ions by studying the iron binding capacity using PIXE and the chemical state of the bound iron using Mössbauer spectroscopy.

2. Experimental

2.1. ION BEAM ANALYSIS

The Ion beam analysis was carried out at the Leipzig microprobe laboratory LIPSION [14] using a 2.25 MeV proton beam focused to approximately 1 μm spot size at beam currents of about 100 pA. Particle Induced X-ray Emission (PIXE) was used for simultaneous multi-elemental analysis of the elements

THE BINDING OF IRON TO PERINEURONAL NETS

above sodium in the periodic table. The elemental distributions, especially of phosphorus (cell indicator) and iron were analysed. Simultaneously, Rutherford Backscattering Spectroscopy (RBS) was used to obtain information on the matrix composition, on the sample thickness and on the accumulated beam charge by fitting the RBS-spectrum (yielded by the total scanned area) using the RUMP code [13].

Since hydrogen is always present in organic material, a ratio between carbon and hydrogen of 0.5 (C_5H_{10}) was assumed for the brain tissue. The information on matrix composition and accumulated charge was used as input for the quantitative analysis by the PIXE data analysis program GeoPIXE II. This software package allows quantitative elemental imaging and various image processing tools for μPIXE measurements [10].

2.2. MÖSSBAUER SPECTROSCOPY

^{57}Fe Mössbauer spectra were measured at room temperature (RT), 160 K and 4.2 K for a cortex and a red nucleus specimen. The absorbers had a thickness of 123 mg/cm^2 for the cortex and of 142 mg/cm^2 for the red nucleus sample. The source of ^{57}Co in rhodium was always kept at the temperature of the absorber. All isomer shifts will be given as measured, i.e., with respect to the source having the same temperature as the absorber. The spectra were fitted with appropriate superpositions of Lorentzian lines allowing for a Gaussian distribution of the magnetic hyperfine field or the electric quadrupole splitting, respectively.

3. Results

In the present study, we analysed the iron binding capacity of perineuronal nets as well as the chemical state of the bound iron in rat brain.

3.1. ION BEAM ANALYSIS

The PN ensheathed neurons are explicitly different from the neurons devoid of PNs, which are clearly identifiable by the superposition of the cellular P – and Fe – distribution (Figure 1). In general the phosphorus map demonstrates the localisation of the cell somata of all cells by highlighting the cytosol.

Elemental profiles and average concentrations in selected brain regions of interest were extracted. In order to determine the region of the PN, a threshold iron concentration of 40% of the maximum value was chosen. The region defining the neural tissue devoid of cell bodies and PNs, the so-called neuropil, was chosen outside the PNs and outside the somata of PN-devoid neurons
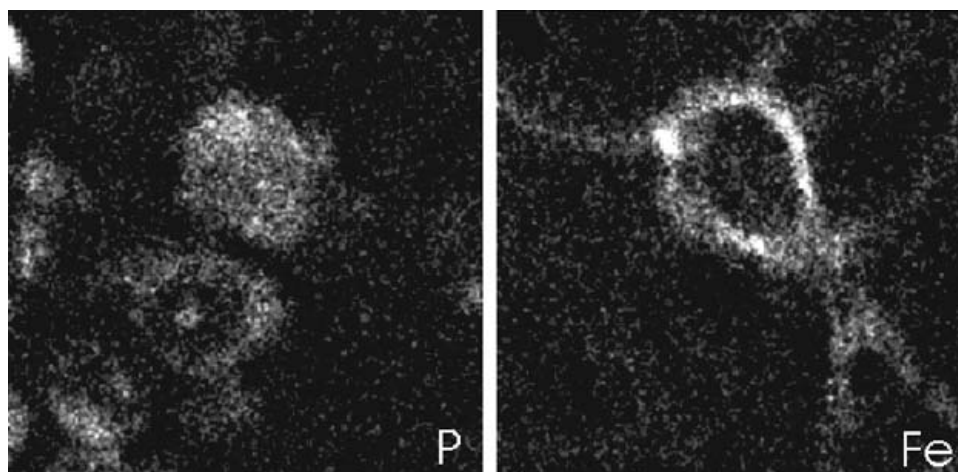
Figure 1. PIXE phosphorus (*left*) and iron (*right*) distribution map. The neurons can be localised by their P-rich somata. One neuron possesses a perineuronal net that clearly shows iron accumulation. 50μn $\times$ 50 μm.
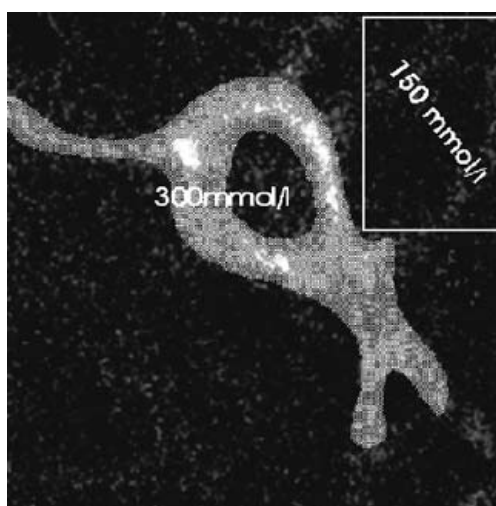

Figure 2. Distribution map of iron. The regions are marked from which the quantitative concentrations were extracted.

represented by higher phosphorus concentrations (Figure 2). PNs accumulate three to five times more iron than any other tissue structure in the investigated brain areas depending on the applied Fe concentration (Figure 3). For a detailed description see [9].

3.2. MÖSSBAUER SPECTROSCOPY

The Mössbauer spectra of both the cortex and the red nucleus specimen exhibit six-line magnetic hyperfine patterns at 4.2 K and quadrupole doublets at 160 K and RT. Spectra of the cortex material taken at 4.2 K and 160 K are shown in Figure 4. The magnetic hyperfine patterns were fitted allowing for a Gaussian distribution of the magnetic hyperfine fields. The median field values were found

THE BINDING OF IRON TO PERINEURONAL NETS
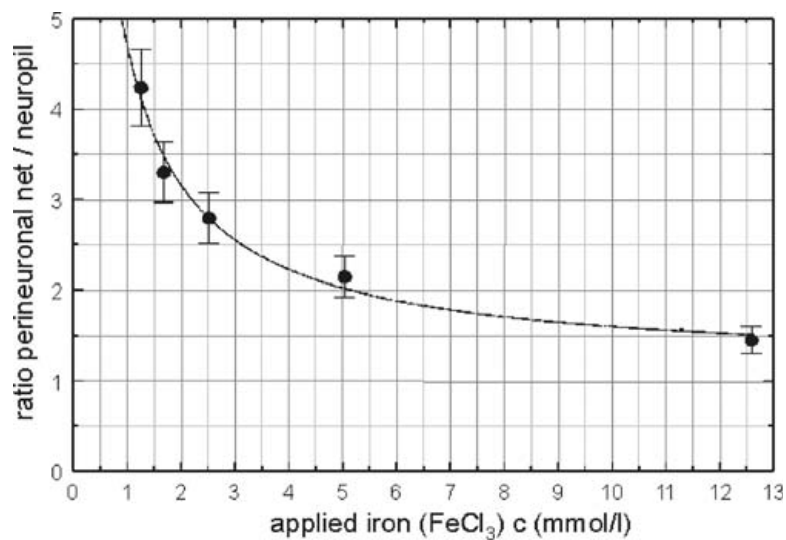
Figure 3. The relation between the initial $FeCl_3$ loading and the ratio of concentrations perineuronal net/neuropil. It can be described by a hyperbolic function with an offset of 1.
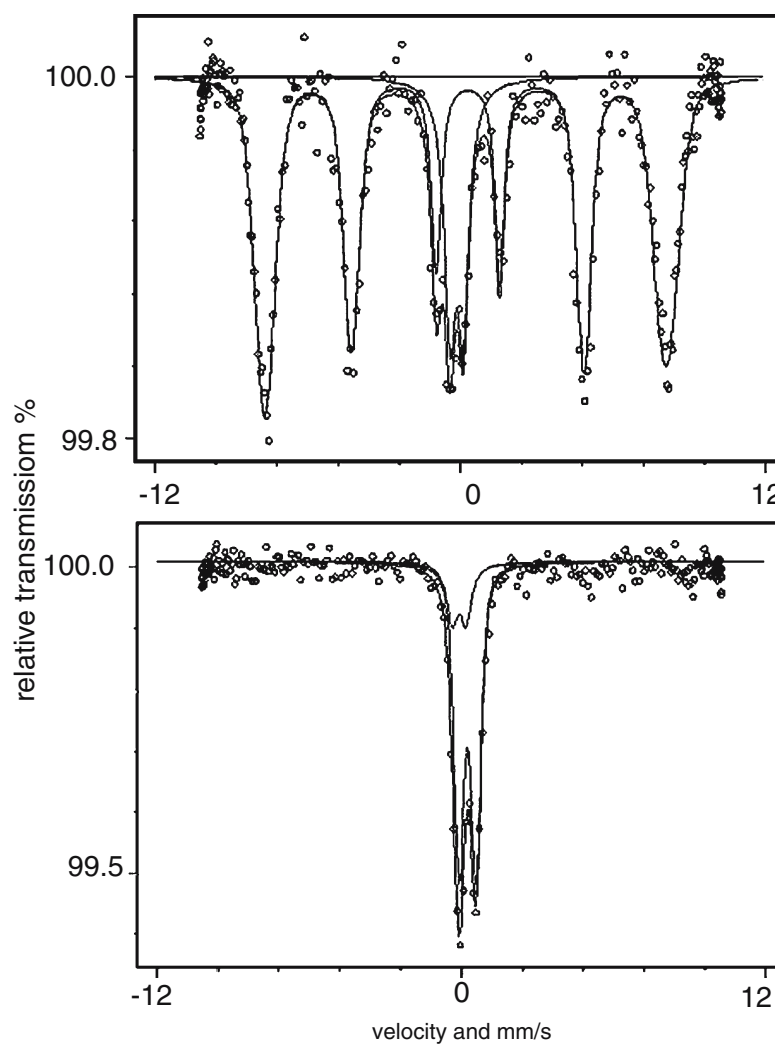

Figure 4. Mössbauer spectra of the cortex specimen taken at 4.2 K (*top*) and at 160 K (*bottom*).

to be 48.9(1) and 49.0(1) T for the cortex and the red nucleus, respectively, with variances of 2.2(1) and 1.9(1) T. The isomer shifts of 0.24(1) mm/s of the magnetically split patterns are typical for trivalent iron. The quadrupole splittings in the magnetic patterns are close to zero.

The quadrupole doublet visible in the 4.2 K spectra (Figure 4) has a shift of $-0.14(2)$ mm/s and a splitting of 0.55(2) mm/s. It is attributable to iron impurities in the beryllium window of the proportional counter and thus has no relation to the properties of the iron in the brain samples. When this component is properly taken into account in the fitting of the spectra taken at 160 K and RT, the quadrupole doublets of the iron in the brain specimens all have median isomer shifts of 0.23(2) mm/s, while the quadrupole splittings have median values of 0.68(2) mm/s and variances of near 0.3 mm/s. The Mössbauer spectra show no trace of divalent iron, which would be expected to give rise to a quadrupole doublet with a shift of about 1 mm/s and a splitting of more than 2 mm/s.

4. Discussion

The locally resolved, quantitative nuclear microscopy was successfully used to investigate the accumulation of iron in PNs in rat brain. It could be shown that PNs have a higher ability to bind a large amount of iron concentrated close to the neuron than any other tissue components in the rat brain.

The Mössbauer spectra of both the cortex and the red nucleus specimen show that the iron is bound to the extracellular matrix as an Fe(III) oxihydroxide. The magnetic hyperfine splitting observed at 4.2 K reveals magnetic ordering at low temperatures. At 160 K the iron exhibits only a quadrupole doublet and hence is already paramagnetic or superparamagnetic. This behaviour is similar to that observed, for instance, for iron in ferritin [15–17] or ferrihydrite [18, 19]. In ferritin the iron forms oxidic Fe(III) clusters of about 8 nm size which begin to exhibit superparamagnetic relaxation effects at about 10 K and exhibit completely collapsed spectra above about 50 K [18, 19]. More details on the state of the iron in the brain specimens might therefore be obtained by a more detailed study of the temperature dependence of the Mössbauer spectra between 4.2 K and about 100 K.

THE BINDING OF IRON TO PERINEURONAL NETS

Interdisziplinäres Zentrum für Klinische Forschung (IZKF) Leipzig at the Faculty of Medicine of the University of Leipzig (C1).

References

1. Brückner G., Bringmann A., Härtig W., Köppe G., Delpech B. and Brauer K., *Exp. Brain Res.* **121** (1998), 300–310.
2. Brückner G., Hausen D., Härtig W., Drlicek M., Arendt T. and Brauer K., *Neuroscience* **92** (1999), 791–805.
3. Celio M. R. and Blümcke I., *Brain Res. Brain Res. Rev.* **19** (1994), 128–145.
4. Connor J. R., Menzies S. L., Burdo J. R. and Boyer P. J., *Pediatr. Neurol.* **25** (2001), 118–129.
5. Halliwell B., *Drugs Aging* **18** (2001), 685–716.
6. Kakhlon O. and Cabantchik Z. I., *Free Radic. Biol. Med.* **33** (2002), 1037–1046.
7. Lovell M. A., Robertson J. D., Teesdale W. J., Campbell J. L. and Markesbery W. R., *J. Neurol. Sci.* **158** (1998), 47–52.
8. Morawski M., Brückner M. K., Riederer P., Brückner G. and Arendt T., *Exp. Neurol.* **188** (2004), 309–315.
9. Reinert T., Morawski M., Arendt T. and Butz T., *Nucl. Instr. Meth. B* **210** (2003), 395–400.
10. Ryan C. G., *Nucl. Instr. Meth. B* **181** (2001), 170–179.
11. Smith M. A., Nunomura A., Zhu X., Takeda A. and Perry G., *Antioxid. Redox. Signal.* **2** (2000), 413–420.
12. Yamaguchi Y., *Cell. Mol. Life Sci.* **57** (2000), 276–289.
13. Doolittle L. R., *Nucl. Instr. Meth. B* **9** (1985), 344.
14. Vogt J., Flagmeyer R. H., Heitmann J., Lehmann D., Reinert T., Jankuhn S., Spemann D., Tröger W. and Butz T., *MiKrochim. Acta* **133** (2000), 105.
15. St. Pierre T. G., Dickson D. P. E., Webb J., Kim K. S., Macey D. J. and Mann S., *Hyperfine Interact.* **29** (1986), 1427.
16. Bell S. H., Weir M. P., Dickson D. P. E., Gibson J. F., Sharp G. A. and Peters T. J., *Biochimica et Biophysica Acta* **787** (1984), 227.
17. Dickson D. P. E., *Hyperfine Interact.* **111** (1998), 171.
18. Jambor J. L. and Dutrizac J. E., *Chem. Rev.* **98** (1998), 2549.
19. Murad E., Bowen L. H., Long G. J. and Quin T. G., *Clay Minerals* **23** (1988), 161.
20. Golgi C., *Rendiconti della Reale Accademia dei Lincei (21 maggio)* **2** (1893), 443–450.

Cellular distribution and localisation of iron in adult rat brain (*substantia nigra*)

Ch. Meinecke [a,*], M. Morawski [b], T. Reinert [a], T. Arendt [b], T. Butz [a]

[a] *Institute for Experimental Physics II, Faculty for Physics and Geosciences, University of Leipzig, Linnéstr. 5, D-04103 Leipzig, Germany*
[b] *Paul-Flechsig-Institute for Brain research, University of Leipzig, Jahnallee 59, D-04109 Leipzig, Germany*

Available online 11 May 2006

Abstract

Iron appears to be one of the main factors in the metal induced neurodegeneration. Quantitative information on cellular, sub-cellular and cell specific distributions of iron is therefore important to assess.

The investigations reported here were carried out on a brain from an adult rat. Therefore, 6 μm thick embedded, unstained brain sections containing the midbrain (*substantia nigra*, *SN*) were analysed.

Particle induced X-ray emission (PIXE) using a focussed proton beam (beam – diameter app. 1 μm) was performed to determine the quantitative iron content on a cellular and sub-cellular level.

The integral analysis shows that the iron content in the *SN pars reticulata* is twice as high than in the *SN pars compacta*.

The analysis of the iron content on the cellular level revealed no remarkable differences between glia cells and neurons. This is in contrast to other studies using staining techniques.
© 2006 Elsevier B.V. All rights reserved.

PACS: 07.78.+s; 41.75.Ak; 87.64.−t

Keywords: Iron; PIXE; Brain research; *substantia nigra*; Life sciences

1. Introduction

Iron is essential for nearly all living organisms since it is involved in a variety of physiological processes, e.g. oxygen transport and electron transfer, redox/non-redox reactions as well as other cell functions. In the brain, iron is an important co-factor for the generation of dopamine and several cellular and intracellular processes e.g. tyrosine hydroxylase.

In recent years many investigations account for the iron metabolism in brain tissue due to its link to neurodegenerative diseases [1,2]. According to a well established theory [3,4] a dysfunction in the iron-homeostasis can result in an increased production of free radicals (Fenton reaction) which can lead to oxidative stress and finally to cell death [3]. This is discussed to be one of the major causes for the neuronal cell-death in the *substantia nigra pars compacta* (*SN pc*) in Parkinson's disease (PD). It is well known from different experiments (μPIXE, histochemistry, MRI) that the iron content in the *SN* of PD patients [2,5,6] is elevated.

In numerous histochemical studies iron has been localised in non-neuronal cells in the *SN* [7,8]. New results using ion beam analysis (PIXE) on human brain tissue show that also neurons in the *SN* contain a non-negligible amount of iron [5]. This study compares quantitatively the cell-specific iron content of neurons and glia cells in the brain of an adult rat. It analyses the total iron distribution and does not distinguish between the different charge states of the iron.

2. Sample preparation

To analyse the iron distribution in the *substantia nigra*, a series of transverse brain sections (adult Wistar rat) was

---

* Corresponding author. Tel.: +49 341 9732707; fax: +49 341 9732708.
  E-mail address: meinecke@physik.uni-leipzig.de (Ch. Meinecke).

prepared. For this study, the rat was anaesthetised with CO_2 and transcardially perfused with saline containing heparin, followed by a fixative (4% paraformaldehyde in a 0.1 M cacodylate buffer (pH 7.2–7.4)). After removing the brain from the skull, app. 5 mm thick blocks were prepared and post-fixed overnight in the same fixative. These blocks were dehydrated in increasing concentrations of ethanol and after repletion in methylbenzoate the sample were embedded in paraffin and cut into 6 μm thick brain sections containing the *substantia nigra* (app. Bregma −5.20 mm). These thin sections were deparaffinised with xylene and rinsed with ethanol. Then the brain sections were embedded in DePeX® (Merck, Germany) and coverslipped. After 24 h the coverslips were removed by immersion into toluene. After this procedure the brain sections were peeled off and mounted on sample holders for ion beam analysis.

3. Experimental

The spatially and elementally resolved nuclear microscopy was performed at the Leipzig microprobe laboratory LIPSION. The experimental set-up for biological applications as described in [9] was used. In these particular experiments, a 2.25 MeV proton beam of app. 120 pA for the quantitative analysis (PIXE) of the iron content in the *substantia nigra* was used. For this purpose the diameter of the focussed proton beam was app. 1 μm. The cellular distribution of the iron content was analysed using μPIXE.

The matrix elements, sample thickness and accumulated beam charge were obtained from back scattering spectrometry. For this purpose the RUMP-code [10], including the Non-Rutherford cross sections for C, N and O [11] was used. In addition, the hydrogen content was determined according to the description in [12]. The information on the accumulated charge and composition of the matrix was used as input for the quantitative elemental evaluation in the μPIXE data analysis program GeoPIXE II [13]. The cellularly resolved elemental profiles and average concentrations of the *substantia nigra pars compacta* and *pars reticulata* were extracted from scans on the scale of 30 μm × 30 μm and with an accumulated charge of app. 1.2 μC.
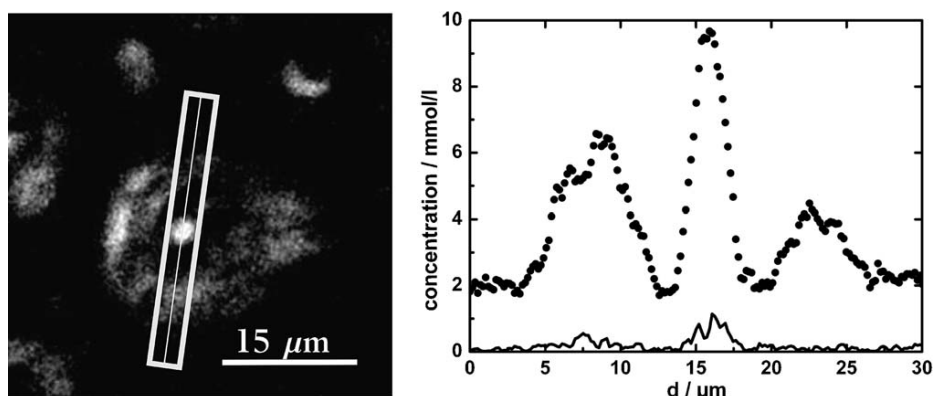

Fig. 1. Left: phosphorous map of a scan of a neuron (phosphorous used as indicator for the cell). The iron and phosphorous concentration profiles were determined along the traverse (grey box). Right: elemental concentration profile of a neuron (solid line: iron concentration, dots: phosphorous concentration).
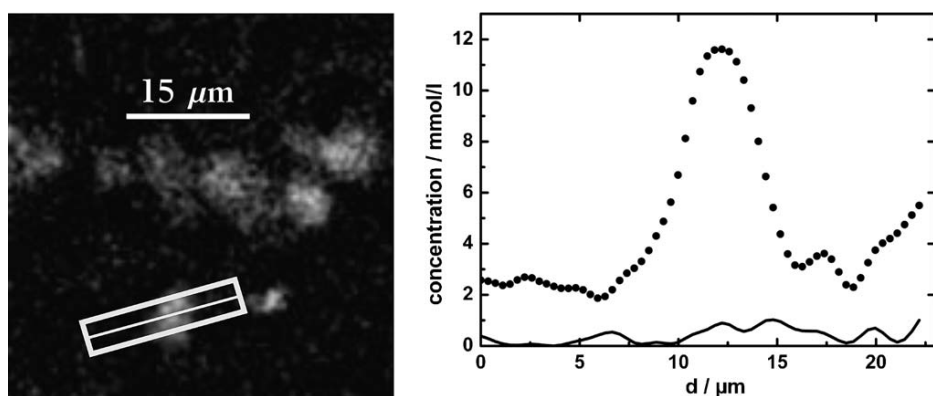

Fig. 2. Left: phosphorous map of a scan of a glia cell. The iron and phosphorous puncentration profiles were determined along the traverse (grey box). Right: elemental concentration profile of a glia cell (solid line: iron concentration, dots: phosphorous concentration).

The cell types can be distinguished according to their size and shape. Therefore, the phosphorous-map which shows the soma of cell was used. Neurons are larger than 15 μm in diameter, with a low phosphorous concentration in the nucleus, but often a phosphorous rich nucleolus inside the cell nucleus (see Fig. 1). Glia cells are smaller in size (app. 5 μm) and do not exhibit the cell nucleus in the phosphorous-map (see Fig. 2). Due to this identification of the cell by their soma, the phrase "intracellular" means "somatic". Extracellular (non-somatic) concentrations were extracted from areas excluding the cell bodies (soma of the cell).

4. Results and discussion

It should be mentioned that the embedding resin did not show a detectable PIXE-peak in the energy range of interest, i.e. it did not contain detectable amounts of iron.

First, the relation between the integral iron contents in the *SN pc* and in the *SN pr* was determined be to app. 1:2 (see Fig. 3). The diagram shows the trend of the distribution of the iron content along a traverse starting in the *cerebral pedunculus* (*cp*). In Table 1 the quantitative integral iron content is given. The relation between the extracellular (non-somatic) iron contents in the *SN pc* and in the *SN pr* is 1:2.

The relation of the iron content in glia cells (somatic) of the *SN pc* versus the *SN pr* is app. 1:2 (see Table 1). In contrast to the glial iron distribution, the somatic neuronal iron content of *SN pc* versus *SN pr* shows no significant difference ($p < 0.05$).

There is no significant difference between the glia cell related iron concentration and the neuronal iron content in the *SN pc* ($p < 0.05$) as well as in the *SN pr* ($p < 0.05$).

The intraneuronal iron content (somatic) with respect to the extracellular iron content (non-somatic) in both parts of the *substantia nigra* exhibits no significant difference ($p < 0.05$). Fig. 1 shows that in the nucleolus a high iron content is located but the intraneuronal iron content (aver-
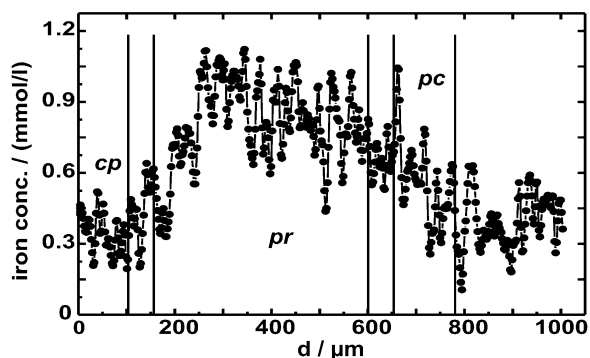
Table 1
Quantitative results of the integral, neuronal, glial and extracellular iron content of the *SN pc* and the *SN pr*. Data are mean values ± standard deviation. (Significance test – Student's *t*-test with a significance level of $p < 0.05$.) The last column gives the number of measurements (*n*) used for statistical analysis

Iron concentration (mmol/l)	*pc*	*pr*	Difference significant	Number (*n*) of measurements
Integral	0.40 ± 0.10	0.86 ± 0.22	Yes	13
Neuronal	0.58 ± 0.25	0.84 ± 0.36	No	10
Glial	0.50 ± 0.20	1.13 ± 0.57	Yes	22
Extracellular	0.44 ± 0.07	0.95 ± 0.25	Yes	13

aged over the entire cell) is equal to the extraneuronal (non-somatic) iron concentration.

The glia cell related (somatic) iron content shows no significant difference ($p < 0.05$) to the extracellular (non-somatic) iron concentration.

The significance was calculated using a *t*-test with a significance level of $p < 0.05$.

5. Conclusion

The quantitative analysis shows that the relation between the integral iron content in the *SN pars compacta* and the *SN pars reticulata* is app. 1:2. This relation is corroborated by different studies [14].

The intracellular (neuronal and glia cell related) iron content as well as the extracellular iron content in the *pars reticulata* is twice as high as in the *pars compacta*. These results corroborate other experiments which investigated the human *substantia nigra* [5].

The investigations of the cellular iron content suggested that neurons and glia cells do not differ significantly in their iron concentrations. This is in contrast to numerous histochemical studies, which explain the increased iron content in the *SN pr* as non-neuronal iron [7,8,15]. In this work we could show that neurons and glia cells acquire nearly the same amount of iron. According to our present investigations the results which were based on histochemical investigations of the cellular iron distribution in the brain should be reconsidered and reviewed regarding their validity. However, to confirm these results, further investigations in this field are needed, e.g. a larger number of measurements or using different methods (e.g. histochemistry).

Fig. 3. The integral iron concentration profile of the *substantia nigra* (rat); *cerebral pedunculus* (*cp*), *SN pars reticulata* (*pr*), *SN pars compacta* (*pc*).

References

[1] J.C. Sipe, P. Lee, E. Beutler, Dev. Neurosci. 24 (2002) 188.
[2] D. Berg, M. Gerlach, M.B.H. Youdim, K.L. Double, L. Zecca, P. Riederer, G. Becker, Neuroscience 79 (2001) 225.
[3] M. Gerlach, D. Ben-Shachar, P. Riederer, M.B.H. Youdim, J. Neurochem. 63 (1994) 793.
[4] M.B.H. Youdim, P. Riederer, Sci. Am. 276 (1997) 52.
[5] M. Morawski, Ch. Meinecke, T. Reinert, A.C. Dörffel, P. Riederer, T. Arendt, T. Butz, Nucl. Instr. and Meth. B 231 (2005) 224.

[6] E.M. Haacke, N.Y.C. Cheng, M.J. House, Q. Liu, J. Neelavalli, R.J. Ogg, A. Khan, M. Ayaz, W. Kirsch, A. Obenaus, Magn. Reson. Imaging 23 (2005) 1.

[7] G.L. Erb, D.L. Osterbur, S.M. LeVine, Dev. Brain Res. 93 (1996) 120.

[8] J.M. Hill, R.C. Switzer III, Neuroscience 111 (1984) 595.

[9] T. Reinert, M. Morawski, T. Arendt, T. Butz, Nucl. Instr. and Meth. B 210 (2003) 395.

[10] L.R. Doolittle, Nucl. Instr. and Meth. B 9 (1985) 344.

[11] R. Amirikas, D.N. Jamieson, S.P. Dooley, Nucl. Instr. and Meth. B 77 (1993) 110.

[12] F. Menzel, T. Reinert, J. Vogt, T. Butz, Nucl. Instr. and Meth. B 219–220 (2003) 82.

[13] C.G. Ryan, Nucl. Instr. and Meth. B 181 (2001) 170.

[14] J.R. Connor, S.A. Benkovic, J. Comp. Neurol. 338 (1) (1993) 97.

[15] J.R. Connor, S.L. Menzies, S.M. St Martin, E.J. Mufson, J. Neurosci. Res. 27 (4) (1990) 595.

Intracellular iron concentration of neurons with and without perineuronal nets

Anja Fiedler [a,b,*], Tilo Reinert [b], Markus Morawski [a], Gert Brückner [a], Thomas Arendt [a], Tilman Butz [b]

[a] *Paul Flechsig Institute for Brain Research, University of Leipzig, Jahnallee 59, D-04109 Leipzig, Germany*
[b] *Institute for Experimental Physics II, University of Leipzig, Linnéstrasse 5, D-04103 Leipzig, Germany*

Available online 16 February 2007

Abstract

Neurodegenerative diseases like Parkinson's disease, Alzheimer's disease and Huntington's disease are characterized by abnormally high concentrations of iron in the affected brain areas. Iron is believed to contribute to oxidative stress by catalysing radical generation and subsequently causing neuronal death.

Interestingly, subpopulations of neurons are less vulnerable against degeneration. One of these subpopulations possesses a specialized extracellular matrix arranged as a perineuronal net (PN), a structure with poorly understood functions.

In order to differentiate between neurons with and without PN according to their iron concentrations we have performed a $\mu PIXE$ study at the Leipzig LIPSION laboratory. PN-ensheathed neurons in selected brain areas were detected by lectin-histochemical staining with *Wisteria floribunda* agglutinin (WFA). The staining was intensified by DAB-*nickel* by an established method enabling the visualisation of the PNs by nuclear microscopy.

The cellular concentration of iron in the rat brain was about 1 mmol/l (ca. 30 µg/g dw). First results of subcellular analysis showed that the intracellular iron concentration of PN-ensheathed neurons tends to be slightly increased in comparison to neurons without PNs. The difference in intracellular iron concentrations could be an effect of the PNs.
© 2007 Elsevier B.V. All rights reserved.

1. Introduction

Iron is involved in neurodegenerative diseases like Alzheimer's disease (AD), Parkinson's disease (PD), Huntington's disease (HD), neurodegeneration with brain iron accumulation (NBIA), progressive supranuclear palsy (PSP), and amyotrophic lateral sclerosis [1–3]. Iron is believed to contribute to oxidative stress by catalysing the generation of free radicals [4,5]. Especially the highly reactive hydroxyl radical (OH) leads to dramatic cell damage and can result in neuronal cell death [6]. Interestingly, there are subpopulations of neurons which are less vulnerable against degeneration. One subpopulation possesses a specialized extracellular matrix arranged as a perineuronal net (PN) [7–9]. A PN consists of chondroitin sulphate proteoglycans and hyaluronic acid in connection with tenascin-R, providing a highly negative charge [10,11]. Due to the polyanionic character of the PN it has the ability to bind large amounts of iron [12]. Thus, PNs could probably have neuroprotective effects by binding and scavenging redox-active iron ions, thus, reducing the oxidative stress in the cellular microenvironment.

---
* Corresponding author. Address: Paul Flechsig Institute for Brain Research, University of Leipzig, Jahnallee 59, D-04109 Leipzig, Germany. Tel.: +49 341 9732706, fax: +49 341 9732708.
E-mail address: afiedler@uni-leipzig.de (A. Fiedler).

Neuropathological changes could be reflected by the distribution of iron in the brain. Therefore, quantitated cellular and subcellular iron levels are meaningful for the insights in the selected vulnerability between PN-ensheathed and PN-lacking neurons. The quantitative method particle induced X-ray emission (PIXE) is an extremely useful technique for scientific examinations in brain by spatially resolving iron and other elements of interest on subcellular levels. The quantitative results contribute to a better understanding of pathological changes in iron related neurodegenerative diseases [13–18]. Synchrotron based analysis techniques have an even lower detection limit (X-ray fluorescence (SR-XRF)) or are sensitive to the chemical state (X-ray absorption spectroscopy (XANES, EXAFS)), but with remarkable lower spatial resolution [19,20].

2. Materials and methods

2.1. Sample preparation

The animals (rats) used in this study were treated in agreement with the German law on the use of laboratory animals and followed the ethical guidelines of the Laboratory Animal Care and Use Committee at the University of Leipzig.

One adult male Wistar rat was deeply anaesthetized with CO_2 and transcardially perfused with saline containing heparin, followed by fixative (4% paraformaldehyde (PFA) and 0.1% glutaraldehyde in 0.1 M phosphate buffered saline (PBS), pH 7.4). The perfusion conserves the morphological structure of the brain tissue without shrinkage and red blood cells containing hem-iron are thoroughly washed out.

The brain was removed from the scull, divided frontally into three blocks and was post-fixed in 4% PFA in 0.1 M PBS, pH 7.4, over night at room temperature. The blocks were dehydrated in increasing concentrations of ethanol and after repletion in methylbenzoate, the samples were embedded in paraffin and cut into 5 μm thick sections through the brain regions of interest including the parietal cortex, the subiculum, the substantia nigra, the red nucleus and several nuclei from cerebellum/brainstem. The sections were mounted on glass slides, deparaffinized with xylene, rehydrated in decreasing concentrations of ethanol and transferred into Tris buffered saline (TBS, pH 7.4).

2.2. Lectin-histochemistry

The brain sections were lectin-histochemically stained with the *N*-acetylgalactosamine-specific, biotinylated *Wisteria floribunda* agglutinin (WFA), a reliable marker for PNs (Bio-WFA; Sigma, Germany; 1:250) [21], over night at room temperature. The lectin binding sites were then revealed with peroxidase-conjugated streptavidin (ExtrAvidin®, Sigma, Germany; 1:1000) by 1 h incubation at room temperature. The labelling was enhanced by 3,3′-diaminobenzidine (DAB) and nickel (high purity grade of 99.999% to avoid metal contamination; Sigma) resulting in a black reaction product. The nickel is used as a marker facilitating the localisation of PNs in both light microscopy and μPIXE-imaging [13]. The brain slices were embedded in mounting medium (DePeX®, Merck). After 24 h the embedded sections were peeled off to mount them on the sample holder for microbeam analysis.

To prove that the preparation and staining procedure does not effect the intracellular iron concentration, unstained paraffin-embedded sections were prepared and measured in parallel. Additionally, 10 μm thick brain slices from a fresh, unfixed rat brain were cut on cryomicrotome, mounted on glass slices, embedded in DePeX after air-drying and mounted on sample holder to measure the tissue iron concentration. In both controls, the paraffin embedded and cryo cut sections, the iron concentration in the total scan area was equal to that of the stained samples.

2.3. Ion beam analysis

The spatially resolved elemental analysis was carried out at the Leipzig ion nanoprobe LIPSION [22] using a 2.25 MeV proton beam focussed to 1 μm spot size at a current of 1 nA. The extra- and intracellular distribution of especially Fe and other elements like P, S, Ni, Cu and Zn were recorded by Particle induced X-ray emission (PIXE). Because the phosphorus map displays the cell somata and the nickel map ensures PN-positive neurons, the correct scan position and optimal scan parameters for the analysing structure could be adjusted. Backscattering spectrometry (BS) was simultaneously used to obtain information on the matrix composition (C, N, O and H indirectly), on the sample thickness and the accumulated beam charge using the RUMP code for BS-spectrum fitting. Due to the chemical composition of the embedding medium DePeX, a mixture of polystyrene (C_8H_8) and the plasticizer di-butylphtalate ($C_{16}H_{22}O_4$) a ratio between carbon and hydrogen of 1:1 ($C_{10}H_{10}$) for the embedded brain slices was assumed. For quantitative analysis of the PIXE data we used the GeoPIXE II software package [23]. Thus, elemental profiles and concentrations in regions of interest (cytoplasm, nucleus, nucleolus, PN) were extracted.

3. Results

3.1. Spatially resolved element distribution in PIXE maps

Due to the fact that more than 95% of the iron ions in the cell are bound to iron storage and iron transport proteins (ferritin, hemosiderin, transferrin) [24], the concentration of free iron which potentially was washed out during sample preparation was disregarded in the concentration analysis. The preparation and staining procedure did not change the intracellular iron concentration compared to unfixed, cryomicrotome cut, unstained brain slices.

Table 1
MDL for several elements analysed by PIXE measurements of PN-stained neurons by a collected charge of 10 μC

MDL	P	S	Cl	K	Ca	Cr	Mn	Fe	Ni	Cu	Zn
μg/g	2.0	1.6	1.4	1.0	0.77	0.3	0.27	0.25	0.55	0.79	0.82
μmol/l	59	45	36	23	17	5	5	4	9	11	11

With a spatial resolution of 1 μm the elements in brain slices can be analysed in a high trough-put using beam currents up to 1 μA. Using a reduced current of 250 pA the spatial resolution is 0.5 μm. The MDL for iron and further elements of interest from neurons analysed by PIXE by a collected charge of 10 μC are given in Table 1. The MDL of iron is 4 μmol/l (∼0.25 μg/g dry weight), respectively.

Typical elemental PIXE maps of two WFA-DAB-Ni stained neurons in rat brainstem after investigations with nuclear microscopy (current: 600 pA, charge: 5.5 μC) are given in Fig. 1. The PNs are selectively visualized by the nickel map (concentration Ni_{PN}: ∼69 mmol/l). The cytoplasm can be recognized by an intense concentration of phosphorus (concentration $P_{cytoplasm}$: ∼50 mmol/l). The nucleus had a lower concentration of phosphorus ($P_{nucleus}$: ∼41 mmol/l). A low concentration of sulphur was found in the cell nucleus ($S_{nucleus}$: ∼51 mmol/l). The merged three elemental map of phosphorus (red), nickel (blue) and iron (green) impressively shows the subcellular distribution of iron with a spatial resolution of approximately 800 nm and a MDL of 14 μmol/l. The cellular iron concentration (0.86 mmol/l) assembles the cytoplasmic iron (0.8 mmol/l), the iron of the nucleus (1.05 mmol/l) and of the nucleolus (2.08 mmol/l). Thereby, the iron concentration in the nucleolus, a special RNA-producing site in the nucleus, is remarkably increased and reflected in yellow colour due to the overlay of iron and phosphorus. The extracellular PNs did not show an increased iron concentration compared to the total intracellular iron concentration, even they are able to bind large amounts of iron [12].

The subcellular distribution of several elements can also be plotted in an elemental profile along a traverse using the GeoPIXE II software (Fig. 2). The subcellular compartments determine the element distribution and can sharply be delimited from each other. The nucleolus seems to be of specific structure and density because of the striking element composition. The marginal nickel peaks reflect the PN. At the position of the PN, where the nickel enhanced DAB staining is most pronounced, the iron concentration is *not* elevated. This is an additional proof that there are no iron impurities from the nickel/DAB staining.

Variations in the localisation of iron were not only constricted to several compartments (cytoplasm, nucleus and nucleolus), but also present inside a compartment itself. Especially in the cytoplasm iron was locally accumulated seeming to have any prominence in this cellular region (Fig. 5).

Iron seems to be bound to proteins (probably ferritin) or other structures like nucleic acids resulting in punctiform iron spots resolved to a size of approximately 0.8 μm.
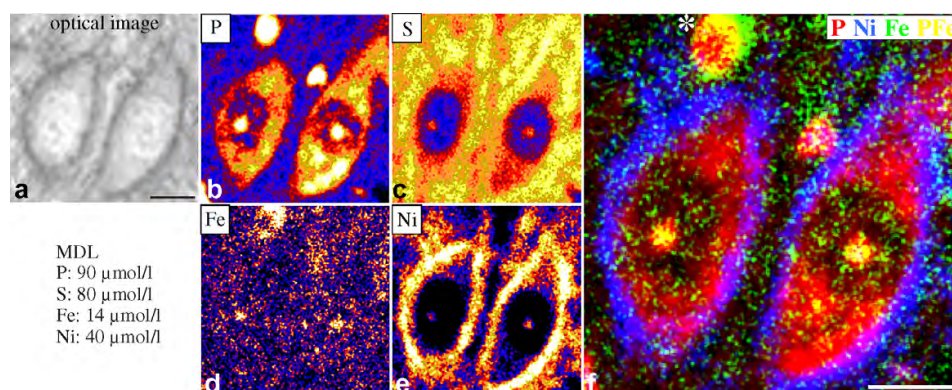

Fig. 1. Elemental PIXE maps (b–f) of two PN-ensheathed neurons in the brainstem. (a) Optical image of the analysed neurons stained for PNs (WFA-DAB-Ni, black pigment) surrounding the cells. (b) The phosphorus map indicates the cytoplasm of the cells as well as the intranuclear nucleolus. (c) Sulphur nearly omits the nuclei in contrast to the extracellular matrix. (e) In the nickel map the PNs are selective recognizable due to the Ni-enhanced staining of the PNs. (f) Three elemental map of phosphorus (red), nickel (blue) and iron (green). A co-localization of phosphorus and iron is reflected in yellow coloured regions, especially the nucleolus in both neurons (yellow). Total cellular iron concentration of the right neuron (0.86 mmol/l) is contributed by the cytoplasm (0.8 mmol/l), the nucleus (1.05 mmol/l) and the nucleolus (2.08 mmol/l). The iron concentration of the surrounding PN was the same as of the cell. The merged map also reveals an iron-rich glia cell (asterisk), probably an oligodendrocyte, because this cell type is believed to store the highest cellular iron concentrations. Collected charge: 5.5 μC. Beam current: 600 pA. Spatial resolution: 800 nm. Scale bar: 10 μm. (For interpretation of the references in colour in this figure legend, the reader is referred to the web version of this article.)
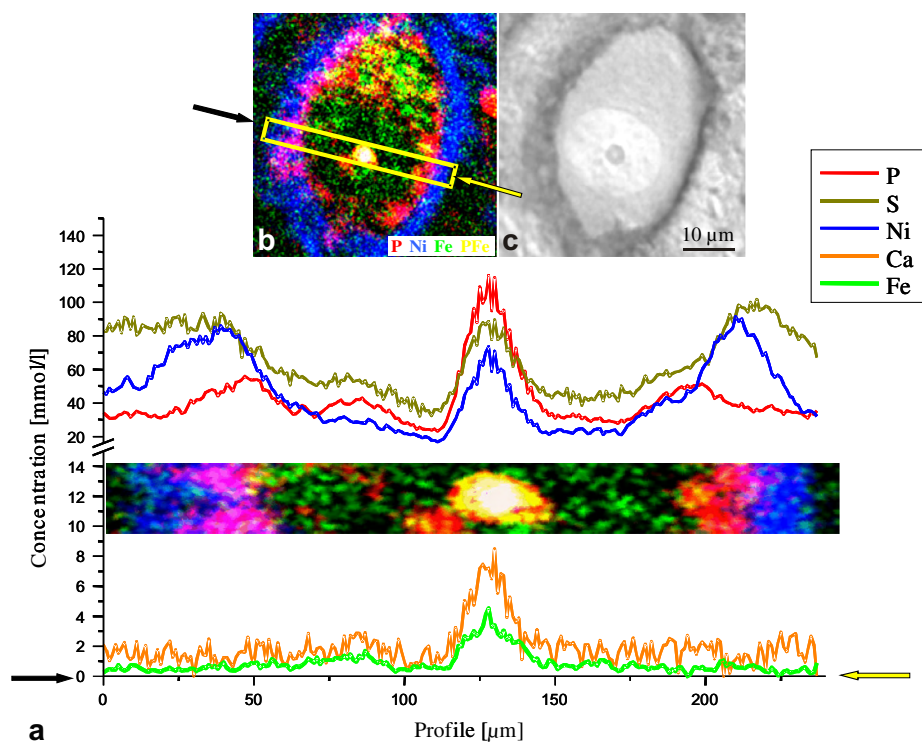
Fig. 2. (a) Elemental profiles of P, S, Ni, Cu and Fe along a traverse through a PN-ensheathed neuron of the brainstem using GeoPIXE II. (b) Merged PIXE elemental map containing phosphorus (red), nickel (blue) and iron (green) of the profiled neuron. (c) Optical image of the analysed neuron (WFA-DAB-Ni stained PN, black pigment). (For interpretation of the references in colour in this figure legend, the reader is referred to the web version of this article.)
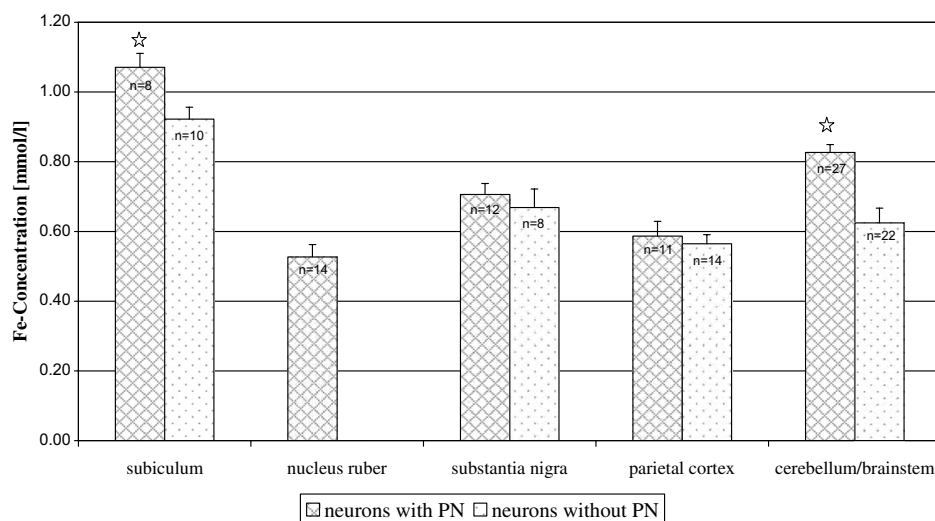
Fig. 3. Cellular iron concentration of neurons with and without a PN constituted for the examined brain regions. Asterisk: significance $p < 0.05$ students t-test. Error bar: standard error.

3.2. Intracellular iron concentration of PN-ensheathed neurons-first results

Altogether, 72 neurons with a PN and 54 neurons without a PN were examined, whereby in the region of the red nucleus only neurons with a PN could be found (Fig. 3). Depending on the examined brain areas the total cellular iron concentration varies between 0.53 mmol/l (red nucleus) and 1.07 mmol/l (subiculum) in average. The PN-ensheathed neurons in the subiculum and in nuclei of cerebellum/brainstem showed a significant increase in intracellular iron compared to neurons without a PN (significance $p < 0.05$ student's t-test). The difference between the two neuronal populations was not significant in the substantia nigra and the parietal cortex, but also tends to be increased if surrounded by a PN.

The iron concentration in the nucleus and the cytoplasm tends to be increased in neurons with a PN when all analysed neurons were evaluated, disregarding their localization in the brain (Fig. 4). However, only in the nucleolus of the PN-surrounded neurons the iron concentrations differs significantly. Nevertheless, the small volume the nucleolus contributes to the whole cell has no decisive influence on the total amount of cellular iron.

4. Discussion

The most conspicuous compartment in the cell was the nucleolus. The densely packet structure inside the nucleus is the production site of ribosomal RNA. Ribosomal RNA is extremely abundant in neurons and is providing the greatest amount of iron binding sites among cytoplas-
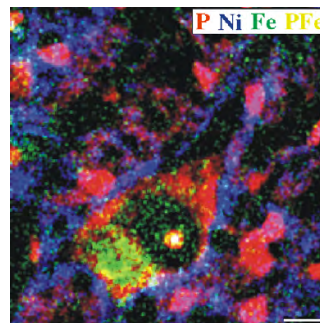
Fig. 5. Merged PIXE map of P, Ni and Fe of a PN ensheathed neuron in rat cerebellum. Obviously, there is a local accumulation of iron in the cytoplasm. Scale bar: 10 μm.

mic RNA species [25]. Our observations let assume that iron binds to RNA not only in the cytoplasm, but also in the nucleus. Another possibility could be that the nucleolus has an excess need for iron due to an increased iron-dependent enzyme and metabolic activity.

The intracellular punctiform iron spots possibly reflect ferritin bound iron (>90% of iron is bound to ferritin, [26]). Ferritin was normally considered as a cytoplasmic iron-storage protein, but is also found in cell nuclei [27].

Even it was shown that PNs are able to bind a large amount of iron [12] this could not be circumstantiated by PIXE studies under physiological conditions. An interpretation approach could be that free ferrous iron (Fe^{2+}) might be transformed into non-toxic ferric iron (Fe^{3+}) and immediately dissociates from the PN and is directly transported into the neuron or surrounding glia cells and
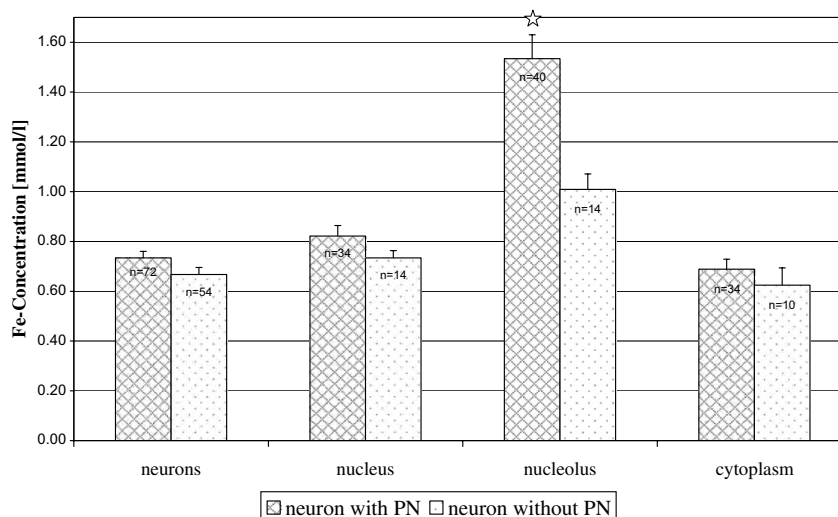

Fig. 4. Intracellular iron concentration of neurons with and without a PN observed in the different compartments. Star: significance $p < 0.01$ Student's t-test. Error bar: standard error.

stored in e.g. ferritin. The not always but consistent increase of total intracellular iron in PN-ensheathed neurons support the assumption that the PN-resorbed iron is probably stored intracellularly in a non-toxic form. Besides, PN-ensheathed neurons potentially have an increased energy metabolism and therefore a higher requirement for iron.

Not only PNs alone, but also iron specific proteins could be involved in the neuroprotection of PN-ensheathed neurons.

This study shows that a broad μPIXE study in combination with iron protein investigations might contribute to a deeper insight in the iron metabolism and homeostasis in iron related diseases.

Acknowledgements

References

[1] P.M. Doraiswamy, A.E. Finefrock, Metals in our minds: therapeutic implications for neurodegenerative disorders, Lancet Neurol. 3 (2004) 431.

[2] J.R. Burdo, J.R. Connor, Brain iron uptake and homeostatic mechanisms: an overview, Biometals 16 (2003) 63.

[3] K.J. Thompson, S. Shoham, J.R. Connor, Iron and neurodegenerative disorders, Brain Res. Bull. 55 (2001) 155.

[4] M. Gerlach, D. Ben-Shachar, P. Riederer, M.B.H. Youdim, Altered brain metabolism of iron as a cause of neurodegenerative diseases? J. Neurochem. 63 (1994) 793.

[5] M.E. Götz, G. Künig, P. Riederer, M.B.H. Youdim, Oxidative stress: free radical production in neuronal degeneration, Pharmacol. Therapeut. 63 (1994) 37.

[6] A.S. Polla, L.L. Polla, B.S. Polla, Iron as the malignant spirit in successful ageing, Ageing Res. Rev. 2 (2003) 25.

[7] G. Brückner, D. Hausen, W. Härtig, M. Drlicek, T. Arendt, K. Brauer, Cortical areas abundant in extracellular matrix chondroitin sulphate proteoglycans are less affected by cytoskeletal changes in Alzheimer's disease, Neuroscience 92 (1999) 791.

[8] K. Schüppel, K. Brauer, W. Härtig, J. Grosche, B. Earley, B.E. Leonard, G. Brückner, Perineuronal nets of extracellular matrix around hippocampal interneurons resist destruction by activated microglia in trimethyltin-treated rats, Brain Res. 958 (2002) 448.

[9] M. Morawski, M.K. Brückner, P. Riederer, G. Brückner, T. Arendt, Perineuronal nets potentially protect against oxidative stress, Exp. Neurol. 188 (2004) 309.

[10] M.R. Celio, I. Blümcke, Perineuronal nets – a specialized form of extracellular matrix in the adult nervous system, Brain Res. Rev. 19 (1994) 128.

[11] G. Brückner, K. Brauer, W. Härtig, J.R. Wolff, M.J. Rickmann, A. Derouiche, B. Delpech, N. Girard, W.H. Oertel, A. Reichenbach, Perineuronal nets provide a polyanionic, glia-associated form of microenvironment around certain neurons in many parts of the rat brain, Glia 8 (1993) 183.

[12] T. Reinert, M. Morawski, T. Arendt, T. Butz, Quantitative microanalysis of perineuronal nets in brain tissue, Nucl. Instr. and Meth. B 210 (2003) 395.

[13] M. Morawski, T. Reinert, C. Meinecke, T. Arendt, T. Butz, Antibody meets the microbeam – or how to find neurofibrillary tangles, Nucl. Instr. and Meth. B 231 (2005) 229.

[14] R. Rajendran, M. Ren, G. Casadesus, M.A. Smith, G. Perry, E. Huang, W.Y. Ong, B. Halliwell, F. Watt, Nuclear microscopy of diffuse plaques in the brains of transgenic mice, Nucl. Instr. and Meth. B 231 (2005) 326.

[15] J. Makjanic, F. Watt, Nuclear microscopy in Alzheimer's disease, Nucl. Instr. and Meth. B 150 (1999) 167.

[16] M. Ren, W. Ong, X. Wang, F. Watt, A nuclear microscopic and histochemical study of iron concentrations and distribution in the midbrain of two age groups of monkeys unilaterally injected with MPTP, Exp. Neurol. 184 (2003) 947.

[17] P.S.P. Thong, F. Watt, D. Ponraj, S.K. Leong, Y. He, T.K.Y. Lee, Iron and cell death in Parkinson's disease: a nuclear microscopic study into iron-rich granules in the parkinsonian substantia nigra of primate models, Nucl. Instr. and Meth. B 158 (1999) 349.

[18] C. Sergeant, M.H. Vesvres, G. Deve's, F. Guillou, Calcium, potassium, iron, copper and zinc concentrations in the white and gray matter of the cerebellum and corpus callosum in brain of four genetic mouse strains, Nucl. Instr. and Meth. B 231 (2005) 234.

[19] R. Ishihara, A. Ide-Ektessabi, K. Ikeda, Y. Mizuno, S. Fujisawa, T. Takeuchi, T. Ohta, Investigation of cellular metallic elements in single neurons of human brain tissues, Neuroreport 13 (2002) 1817.

[20] A. Ide-Ektessabi, S. Fujisawa, S. Yoshida, Chemical state imaging of iron in nerve cells from a patient with Parkinsonism-dementia complex, J. Appl. Phys. 91 (2002) 1613.

[21] I. Adams, K. Brauer, C. Arélin, W. Härtig, A. Fine, M. Mäder, T. Arendt, G. Brückner, Perineuronal nets in the rhesus monkey and human basal forebrain including basal ganglia, Neuroscience 108 (2001) 285.

[22] T. Butz, C. Meinecke, M. Morawski, T. Reinert, M. Schwertner, D. Spemann, J. Vogt, Morphological and elemental characterisation with the high-energy ion-nanoprobe LIPSION, Appl. Surf. Sci. 252 (2005) 43.

[23] C. Ryan, Developments in dynamic analysis for quantitative PIXE true elemental imaging, Nucl. Instr. and Meth. B 181 (2001) 170.

[24] O. Kakhlon, Z.I. Cabantchik, The labile iron pool: characterization, measurement, and participation in cellular processes, Free Radical Bio. Med. 33 (2002) 1037.

[25] K. Honda, M.A. Smith, X. Zhu, D. Baus, C. William, C. Merrick, A.M. Tartakoff, T. Hattier, P.L. Harris, S.L. Siedlak, H. Fujioka, Q. Liu, P.I. Moreira, F.P. Miller, A. Nunomura, S. Shimohama, G. Perry, Ribosomal RNA in Alzheimer disease is oxidized by bound redox-active iron, J. Biol. Chem. 280 (2005) 20978.

[26] K.L. Double, M. Maywald, M. Schmittel, P. Riederer, M. Gerlach, In vitro studies of ferritin iron release and neurotoxicity, J. Neurochem. 70 (1998) 2492.

[27] N. Surguladze, S. Patton, A. Cozzi, M.G. Fried, J.R. Connor, Characterization of nuclear ferritin and mechanism of translocation, Biochem. J. 388 (2005) 731.

High resolution quantitative element mapping of neuromelanin-containing neurons

Tilo Reinert [a,*], Anja Fiedler [a,b], Markus Morawski [b], Thomas Arendt [b]

[a] *Nukleare Festkörperphysik, Universität Leipzig, Linnéstrasse 5, 04103 Leipzig, Germany*
[b] *Paul-Flechsig-Institut für Hirnforschung, Universität Leipzig, Jahnallee 59, 04109 Leipzig, Germany*

Available online 16 February 2007

Abstract

Neuromelanin is a dark coloured intracellular pigment that appears in a specific population of neurons (dopaminergic and noradrenergic) predominantly in the *substantia nigra* and in the *locus coeruleus*. In recent years, there is increasing interest in the role of neuromelanin because of a hypothesised link between this pigment and the cell death of neuromelanin-containing neurons in Parkinson's disease (PD). Therefore, the role of neuromelanin in the pathology of PD is an actual focus in neuroscience.

We have investigated the elemental contents and distributions of sulphur, calcium, iron, nickel and copper of neuromelanin in dopaminergic neurons for a Parkinson case and a control case (*in situ*, 6 μm brain sections). There was no difference in the iron concentration between the two cases. However, the calcium concentration was 3-fold higher in the Parkinson case, whereas the copper and nickel concentrations decreased.

An ultrastructural investigation of the concentrations of calcium and iron within the neuromelanin suggests that these two elements are not necessarily co-localized.

© 2007 Elsevier B.V. All rights reserved.

PACS: 87.64.−t; 82.80.Yc; 41.75.Ak; 07.78.+s

Keywords: Neuromelanin; Iron; Quantitative analysis; Submicron resolution

1. Introduction

The relevance of trace elements in association with neurodegenerative diseases of the Alzheimer- and Parkinson-type is of growing interest since elevated concentrations of elements like iron in these diseases could be linked to increased oxidative processes (radical formation) [1] as well as other metals like i.e. cadmium, mercury, lead and calcium could provide direct neurotoxicity leading to cell death [2].

In the present investigation, we give an example in trace element analysis with sub-micron resolution on neuromelanin. Neuromelanin is a dark coloured intracellular pigment appearing in a specific population of neurons (dopaminergic

and noradrenergic) in senescent mammals predominantly in the *substantia nigra pars compacta* and in the *locus coeruleus*, being formed by oxidation of catecholamines. In recent years, there is increasing interest in the role of neuromelanin because of a hypothesised link between this pigment and the cell death of neuromelanin-containing neurons in Parkinson's disease (PD), due to metal ion binding of neuromelanin and a consequential generation of advanced free radicals. The biology, i.e. the structure, synthesis, physiology and its role in the neuron is still not entirely understood [3]. It is likely that, similar to other types of melanins, neuromelanin acts as a protector against free radicals by inactivating or chelating free toxic metal ions (e.g. iron, copper, calcium). However, in the case of redox-active metal ion excess – and this is controversially discussed – neuromelanin could potentiate the free radical production due to a reduced binding capacity. The role of

---

* Corresponding author. Tel.: +49 341 97 32706; fax: +49 341 97 32708.
  E-mail address: reinert@physik.uni-leipzig.de (T. Reinert).
  URL: http://www.uni-leipzig.de/~nfp (T. Reinert).

neuromelanin in the pathology of PD is therefore an actual focus in neuroscience [4].

2. Experimental

2.1. Biological sample preparation

Brains from a control (CO) (age 69 years, male) and a patient with idiopathic Parkinson's disease (PD) (age 72 years, male) were obtained at autopsy (Brain Bank of the University of Leipzig). The control brain was obtained at routine autopsy from patients who died without any history of neuropsychiatric disorders or mental impairment. The Ethical Committee of Leipzig University has approved the case recruitment.

Both brains (the PD and the control brain) were fixed by immersion in 4% paraformaldehyde in 0.1 M phosphate-buffered saline (PBS), pH 7.4. From the midbrain tissue blocks were dissected encompassing the *substantia nigra*, following conventional protocols for paraffin embedding and block mounting.

The sections were prepared without any staining to interfere as little as possible the native elemental state. The tissue was cut into 6 μm thick sections. These sections were deparaffinised with xylene and rinsed with ethanol to bring it into xylol. Then the slices were embedded in mounting medium (DePeX, Merck). After 24 h the embedded sections were peeled off and mounted on a sample holder for microbeam analysis.

2.2. Sample processing and elemental content

The human brain samples examined in this study were taken from the Brain Bank where the available material is prepared for storage according to standard protocols. Cryofixation of the natural state is usually not possible in the case of human material. These standard procedures reduce the influence on the tissue processing before microsectioning. The elemental distribution as well as the concentration of *unbound* ions and molecules is surely altered. However, the analysis of metal ions *bound* to macromolecular structures like storage, transport and similar proteins such as neuromelanin is likely to be unaffected due to the high affinity for metal ions. An effective release of metal ions from the (non-pathological) metalloproteins only occurs under acidic conditions or by adding metal chelators, which were both avoided.

Special care was taken to keep contaminations of the brain sections with metal ions as low as possible by using freshly prepared chemicals with high purity. A PIXE analysis of the paraffin and DePeX embedding material revealed metal ions impurities below 1 μg/g.

2.3. Microbeam analysis

The analysis of the brain sections was performed at the ion beam laboratory LIPSION (University of Leipzig) [5].

We used a 2.25 MeV proton beam with beam currents ranging from 50 pA for high spatial resolution below 500 nm and a beam current of 250 pA at a slightly diminished resolution of 500 nm [6]. Prior to the sub-500 nm PIXE analysis of neuromelanin we tested the spatial resolution on the Chessy test structure (1×1 μm^2 gold squares on silicon). Fig. 1 shows a rough estimation of the spatial resolution in vertical and horizontal directions. With the high resolution settings we are able to analyse elemental distributions with a spatial resolution below 500 nm.

The typical measurement time for the analysis of neuromelanin was about 1 h. The X-rays were detected with a high purity germanium, IGLET-X, detector (EG&G Ortec) that subtended a solid angle of 211 msr. Simultaneously, we performed backscattering spectrometry (BS) in order to obtain information on the matrix composition, on the sample thickness and on the accumulated beam charge by fitting the proton backscattering spectrum (yielded from the total scanned area). The information on the matrix composition, thickness and on the accumulated charge was used as input for quantitative analysis in the PIXE data analysis program GeoPIXE II [7]. The programme uses the input to correct for matrix effects and to calculate the elemental content normalised by the sample area mass density. We decided to convert the mass ratio (unit of μg/g) into a volume concentration in order to avoid variances of the results due to changes in the mass density of the sample during ion beam analysis. We have normalised the results by the section thickness which is given by the microtome settings.

For the spatially resolved elemental analysis we have chosen dopaminergic cells containing neuromelanin (CO $n = 8$ and PD $n = 6$) of the *substantia nigra pars compacta* which appeared morphological regularly shaped. Extracellular neuromelanin resulting from degenerated neurons was excluded from the analysis because extracellular neuromelanin is continuously degraded by microglia. The high intensity sulphur X-rays within the scan revealed the
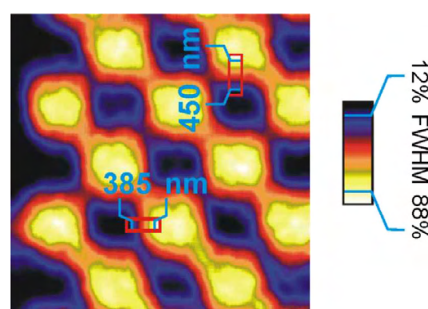

Fig. 1. PIXE elemental map (250×250 pixels) of 1 μm^2 gold squares on silicon (Chessy test structure). The spatial resolution is below 500 nm (full width at half maximum corresponds to the width between 12% and 88% of the gold signal from the edge). The map was obtained within 15 min at a beam current of 50 pA. Due to the statistical uncertainty we have applied a Gaussian filter (FWHM 10 pixels).

cellular region with neuromelanin on which the elemental content was analysed.

3. Results and discussion

Fig. 2 shows in the upper row the distribution of the elements P, S, Fe, Ca, Cu, Ni on neuromelanin in a dopaminergic neuron in the control case. The phosphorous map mainly represents the cytosolic phosphorous, thus giving an image of the cell body. Within the cell body the melanin appears due to its high sulphur content in the S-map. The elements Fe, Ca, Cu, Ni are at the first glance co-localized with the neuromelanin. The minimum detection limit of these elements was about 50 µmol/l (2 µg/g) in the total scan area. The lower row of Fig. 2 shows the elemental distributions for the Parkinson case.

Differences in the Ca-, Cu- and Ni-maps of the control case in comparison with the PD case are clearly visible.

Fig. 3 reveals in higher magnification the distributions of calcium and iron in the pigment itself. It reveals that

the distribution of iron and calcium are not necessarily co-localized. There seem to be domains of different binding capacity or behaviour for iron and calcium. However, this ultrastructural appearance is very challenging for ion beam analysis and up to now on the edge of assured results.

Table 1 shows the mean concentration values of sulphur, calcium, iron, copper and nickel in neuromelanin.

3.1. Iron concentration

The most surprising result was found in the iron concentration. There was no difference in the iron concentration of neuromelanin between the Parkinson case ($n = 6$) and the control ($n = 8$). In the literature there are more reports on altered iron concentrations. However, there are also a few references which report on unaffected iron concentrations under pathological conditions of Parkinson's disease [8]. Since we analysed morphological intact neurons, one could speculate that the remaining neurons in the Parkinson case were less or were not affected by pathological
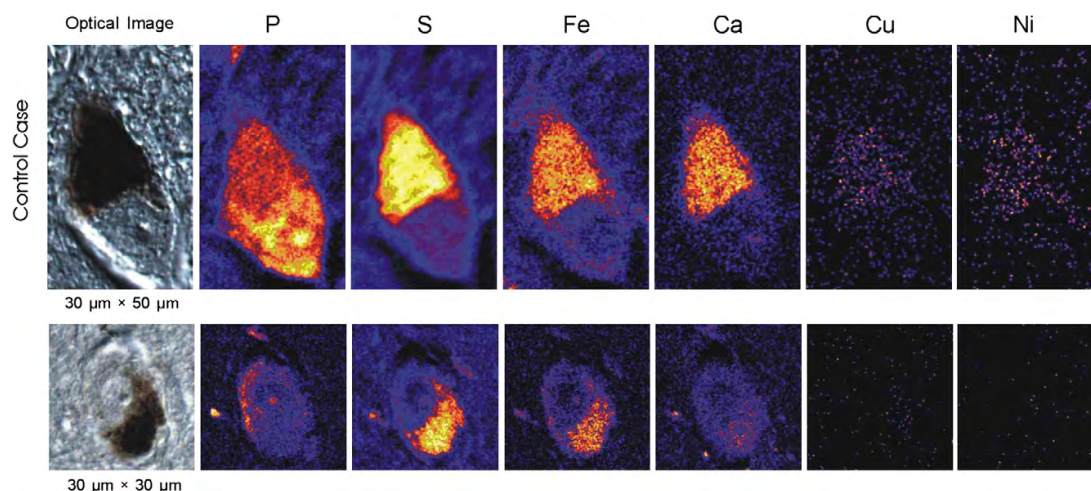

Fig. 2. Optical image (left) and PIXE elemental maps of two neuromelanin containing dopaminergic neurons, the upper one from the control, the lower one from a Parkinson case.
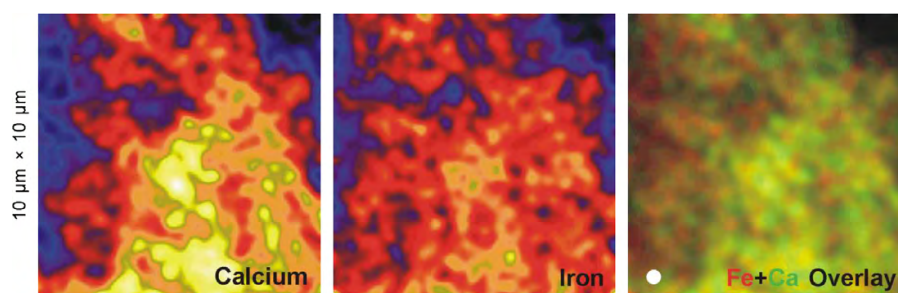

Fig. 3. PIXE elemental maps showing the ultrastructural distribution of calcium and iron within the neuromelanin of Fig. 2, Parkinson case. In the Fe + Ca overlay image the white circle corresponds to a 500 nm spot.

Table 1
Mean elemental concentrations of neuromelanin (in six cells) of a Parkinson case and a control case (neuromelanin of eight cells)

Element	S	Ca	Fe	Cu	Ni
Control case: concentration (mmol/l)					
Mean	65	21	79	2.1	1.1
SD	10	3	16	0.9	0.4
Parkinson case: concentration (mmol/l)					
Mean	60	66	78	0.73	0.1
SD	11	18	19	0.42	0.08
Trend	⇔	⬈	⇔	⬊	⬊

SD: standard deviation, trend: change in concentration in comparison to the control case.

changes relating to excess iron. Therefore, the inclusion of all types of neuromelanin into the analysis is necessary for a better understanding of the conflicting results.

3.2. Calcium, copper and nickel concentrations

The analysis of nickel revealed in comparison to the control a 10-fold lower concentration in neuromelanin of the Parkinson case. Because of lacking information on the relevance of nickel in the human brain an interpretation of this result is difficult at this point. The interpretation of the reduced copper concentration is based on the copper/zinc-superoxide dismutase. It is a metallo-enzyme which is a key player in the antioxidant defense system [9]. A reduced copper concentration in the neuromelanin could display a lower concentration of copper in the microenvironment of the neurons which is linked to a reduced activity of the copper/zinc-superoxide dismutase leading to a higher oxidative stress.

The 3-fold higher calcium concentration in the Parkinson case is remarkable because calcium is known to have direct toxic effects when it is released in excess from the intracellular calcium stores and can lead to programmed cell death in the affected neurons [10].

4. Conclusion

The aim of this study was to determine the content and distribution of trace elements in neuromelanin *in situ* of Parkinsonian and healthy brain tissue in order to reveal any possible differences. Since the ultrastructure of neuromelanin shows different binding capacities a sub-micron elemental analysis is needed. These are first results that demand for a differentiated analysis of intra- and extracellular neuromelanin. Especially, studies of individual pathological cases with different stages of Parkinson's disease are required for a assured interpretation of the results.

Acknowledgements

References

[1] P.M. Doraiswamy, A.E. Finefrock, Lancet. Neurol. 3 (7) (2004) 431.
[2] T.W. Clarkson, Environ. Health Perspect. 75 (1987) 59.
[3] L. Zecca, D. Tampellini, M. Gerlach, P. Riederer, R.G. Fariello, D. Sulzer, Mol. Pathol. 54 (6) (2001) 414.
[4] H. Fedorow, F. Tribl, G. Halliday, M. Gerlach, P. Riederer, K.L. Double, Prog. Neurobiol. 75 (2005) 109.
[5] T. Butz et al., Appl. Surf. Sci. 252 (2005) 43.
[6] T. Reinert, D. Spemann, M. Morawski, T. Arendt, Nucl. Instr. and Meth. B 249 (2006) 734.
[7] C.G. Ryan, E. van Achterbergh, D.N. Jamieson, Nucl. Instr. and Meth. B 231 (2004) 162.
[8] M.E. Götz, K. Double, M. Gerlach, M.B.H. Youdim, P. Riederer, Ann. NY Acad. Sci. 1012 (2004) 193.
[9] J.A. Tainer, E. Getzoff, J.S. Richardson, D.C. Richardson, Nature 306 (1983) 284.
[10] H.J. Choi, S.W. Kim, S.Y. Lee, Y.W. Moon, O. Hwang, Exp. Neurol. 181 (2) (2003) 281.

lithium as a new target of this drug. KA binds and stimulates a subtype of ionotropic receptor of the brain neurotransmitter glutamate and results in transmembrane ion imbalance, especially causing calcium influx. However, 3-NP by inhibition of the mitochondrial respiratory chain modifies the Ca^{2+} homeostasis. Here we describe the calpain activation by two different ways. First, we measured the calpain activity by a comercial kit, and then by Western blot analysis of the calpain substrate α-spectrin. Both assays revealed calpain activation in the two models of toxicity. As calpain activation is related to cdk5 activation we studied cdk5/p25 pathway. Our results showed that the p25/p35 ratios were higher in treated cells than in controls. Preliminary results show neuroprotection mediated by lithium, a GSK3 inespecific inhibitor. The effect of lithium has been seen in an increase of the cell viability, and decreases of the calpain activity as well as in the cascade that it triggers. It seems that not only GSK3 pathway is implicated to this neuroprotection as other factors could be modified after lithium treatment.

PS2-16
Chromatographic analysis of neurochemical changes in the rat striatum after chronic diclofenac treatment

BARANYI M., MILUSHEVA E. and SPERLÁGH B.
Institute of Experimental Medicine, Hungarian Academy of Sciences, H-1450 Budapest, PO Box 67, Hungary

Non-steroidal anti-inflammatory drug (NSAID) diclofenac is a non-selective inhibitor of inducible cyclooxygenase (COX-2) and the mitochondrial complex I, both *in vivo* and *in vitro*. The present study examined the content of biogenic amines and adenine nucleotides and the distribution of released [3H]dopamine (DA) and its metabolites from rat striatum after chronic diclofenac infusion (3.0 mg/kg/day). The release of DA was determined using microvolume perfusion method. For the separation of samples liquid–liquid two-dimensional reversed phase (RP) and ion pair-reversed phase (IPRP) chromatographic analysis was developed. On-line solid phase extraction was used for the enrichment of samples. The identification of analytes was assisted by electrochemical and liquid scintillation detection. After 28 days, diclofenac infusion induced a significant ($P < 0.05$) reduction in ATP concentration (from 3.55 ± 0.67 to 0.55 ± 0.05 nmol/mg protein) in rat striatum with moderate decrease of energy charge (from 0.75 ± 0.09 to 0.51 ± 0.004; $n = 4$). Conversely, dopamine concentrations remained largely unaffected (515.9 ± 135.8 vs. 498.8 ± 102.7 pmol/mg protein) comparing the sham-operated controls to treated animals. On the other hand there was a significant decline in concentrations of dihydroxyphenylacetic acid (DOPAC) (51.9 ± 13.2 vs. 20.7 ± 3.2 pmol/mg protein; $n = 8$). The DA-DOPAC ratio in the basal effluent was 1.78 ± 0.14 and 0.69 ± 0.19 in sham operated and chronically diclofenac treated animals, respectively. When H_2O_2 was used

to induce tritium release, the amount of [3H]DA decreased from 5700 ± 1960 to 4100 ± 1130 DPM and the ratio of DA-DOPAC increased from 2.43 ± 0.37 to 10.5 ± 4.7 after diclofenac treatment. Under these conditions octopamine, tyramine and phenyl-ethylamine, non-monoaminooxidized metabolites of DA were also appeared in the effluent.

PS2-17
Iron compartmentalisation in the rat brain: do perineuronal net-ensheathed neurons play a special role?

MORAWSKI M.,*,‡ FIEDLER A.,*,† REINERT T.,† BRÜCKNER G.* and ARENDT T.*
*Paul Flechsig Institute of Brain Research, University of Leipzig, Jahnallee 59, 04109 Leipzig, †Institute for Experimental Physics II, University of Leipzig, Linnéstr. 5, 04103 Leipzig, ‡Interdisciplinary Center of Clinical Research (IZKF), Faculty of Medicine, University of Leipzig, Germany

Perineuronal nets (PNs) of extracellular matrix consist of aggregating chondroitin sulfate proteoglycans complexed with hyaluronan and tenascin-R, forming polyanionic coats around many neurons. Vulnerable neurons, such as the dopaminergic neurons in the substantia nigra, are devoid of PNs. Aggrecan-based PNs may be capable to scavenge and bind redox-active iron ions, thus reducing oxidative stress that may initiate neurodegeneration in Alzheimer's and Parkinson's disease. However, mechanisms comprising iron transport and storage in PN-associated neurons have not been studied. We investigated the involvement of PN-associated neurons in iron processing by: (1) Particle Induced X-ray Emission (PIXE), a sensitive spectroscopic method, to produce quantitative elemental maps from which extra- and intraneuronal concentration levels of iron in PN-ensheathed vs. non-ensheathed neurons were derived. (2) Quantitative PCR with intron-overarching primers specific for divalent metal transporter (DMT 1), metal transport protein 1, ferric reductase (Dcytb), transferrin, transferrin receptor and ferritin (Fr), as well as β-actin, GFAP, and aggrecan. (3) Immunhistochemistry using polyclonal antibodies to corresponding components of iron processing in combination with *Wisteria floribunda* agglutinin-stained PNs. Here, we show that net-associated neurons in the cerebral cortex and different subcortical regions have higher intracellular iron concentrations compared with neurons devoid of PNs. Further, in immunhistochemical preparations, PN-ensheathed neurons show a strong expression of DMT 1, Fr and Dcytb in the red nucleus and substantia nigra pars reticulata. These results strongly indicate a prominent role of PN-ensheathed neurons in neuronal iron compartmentalisation.

for radiobiological studies at a 7 MV Van de Graaff accelerator. *Nucl. Instrum. Methods A* **256**, 576–580 (1987).

2. P. G. Bizzetti, T. Fazzini and N. Taccetti, A fast electrostatic chopper of low power consumption. *Nucl. Instrum. Methods* **159**, 575–579 (1979).

3. M. Conzato, R. Cherubini, G. Galeazzi and S. L. Gerardi, Light ion microcollimated beam facility for single ion—single mammalian cell irradiation studies. *LNL Annual Report*, in press.

Session III

Chair: P. Rossi

INFN, Padua, Italy

The Leipzig High-Energy Ion-Nanoprobe LIPSION: Design of Single-Ion Bombardment of Living Cells

J. Tanner,[a] D. Spemann,[b] T. Reinert,[b] J. Vogt[b] and T. Butz[b]

[a]*Universität Halle, Klinik und Poliklinik für Strahlentherapie, Dryanderstr.4–7, D-06110 Halle, Germany; and* [b]*Universität Leipzig, Fakultät für Physik und Geowissenschaften, Linnéstr. 5, D-04103 Leipzig, Germany*

The Leipzig High-Energy Ion-Nanoprobe became operational in October 1998. It consists of a single-ended electrostatic accelerator by HVEE, a 3.5 MV Singletron, and a nuclear microprobe by Marco, Melbourne, equipped with quadrupole pair lenses in the split Russian quadruplet arrangement. Relevant specifications for 2.25 MeV protons are: less than 30 V ripple, long-term voltage stability better than 100 V/8 h, reduced brightness of larger than 20 pA/mrad^2 m^2 MeV (*1–3*), demagnification up to 130 in x and y, minimum focused beam size at 0.1 fA of 40 nm (*4*). This beam has been tested by scanning over an atomically flat interface of GaAs/InGaP. Thus far this is the smallest proton beam worldwide.

Contrary to existing microprobes with collimated beams approximately 1 μm in diameter, we are now in a position to aim at cells and subcellular structures using the beam scanning and single ion facilities. A difficulty of our system is that the beam is horizontal, in contrast to the existing systems at the Gray Laboratory in the UK and at Columbia University in New York, which have vertical beams. To extract the beam into ambient air as required for the bombardment of living cells, we shall use an irradiation platform that can be inserted into one of the CF160 flanges of the target chamber and that is equipped with a 100-nm thin, 1 mm × 1-mm Si_3N_4 window. The energy loss and lateral straggling for protons and α particles should be quite small according to TRIM simulations. We plan to use the following scheme:

First, cells are sowed onto miniaturized petri dishes with a central bore covered with a 0.5- or 3-μm thin Mylar foil and with two or more fiducial markers. A cell observation system detects the cells and stores the coordinates of the cell nuclei and the fiducial markers. Then the petri dish is transferred to the irradiation platform, where it is positioned in front of the ion exit window with a precision of about 1 μm using an *x,y* translation stage. The fine *z* positioning will be accomplished by a piezoelectric transducer so as not to damage either the ion exit window or the Mylar foil and to minimize the air gap in between. Next we aim at the fiducial markers using secondary electron detection or scanning transmission ion microscopy. Thus we carefully avoid hitting the medium/cells. After we determine the coordinates of the fiducial markers, we hit our target, i.e. a cell nucleus, the cytoplasm, intracellular structures, or the medium, with a predetermined number of particles, starting from a single ion and moving upward, using the coordinates from the cell observations. The ions traversing the exit window, the Mylar foil, and the cell covered with a thin layer of medium will be detected in a particle

detector immediately behind the cell. Thus we obtain a signal to close the beam gate, and we also know the amount of energy deposited. Preliminary tests at the Gray Laboratory showed that AG 01522 fibroblasts adhere to the Mylar foil for 5 to 10 min when placed in a vertical position as required for our horizontal beam. This is more than we need for investigations of the bystander effect, where only a single hit or a small number of hits are required. After bombardment, we transfer the petri dish back to the cell observation system and verify that the original positions have been retained. The same experiments will be carried out with human arterial endothelial cells. The end point will be micronucleus formation and apoptosis, accompanied with TUNEL assays, including morphology, and flow cytometry.

References

1. D. J. W. Mous, R. G. Haitsma, T. Butz, R-H. Flagmeyer, D. Lehmann and J. Vogt, A novel ultrastable 3 MV Singletron™ accelerator for nanoprobe applications. *Nucl. Instrum. Methods B* **130**, 31 (1997).

2. T. Butz, R-H. Flagmeyer, J. Heitmann, D. N. Jamieson, G. J. F. Legge, D. Lehmann, U. Reibe-Tanz, T. Reinert, A. Saint and J. Zhu, The Leipzig high-energy ion nanoprobe: A report on first results. *Nucl. Instrum. Methods B* **161–163**, 323–327 (2000).

3. D. Spemann, T. Reinert, J. Vogt, T. Butz, K. Otte and K. Zimmer, Novel test sample for submicron ion-beam analysis. *Nucl. Instrum. Methods B* **181**, 186–192 (2001).

4. D. Spemann, T. Reinert, J. Vogt, D. Dobrev and T. Butz, Suitable test structures for submicron ion-beam analysis. *Nucl. Instrum. Methods B* **190**, 312–317 (2002).

Single-Particle Detection for the MIT Charged-Particle Microbeam

J. M. O'Meara,[a] R. P. Boisseau,[b] A. Dart,[b] R. J. Ledoux,[b] W. P. Nett[b] and J. C. Yanch[a]

[a]*Laboratory for Accelerator Beam Applications, Massachusetts Institute of Technology, Cambridge, Massachusetts; and,* [b]*Pyramid Technical Consultants, Waltham, Massachusetts*

Introduction

The development of a biological charged-particle microbeam is under way at the Laboratory for Accelerator Beam Applications at MIT. The facility is comprised of a vertical beam from a 1.5 MV single-ended electrostatic proton/α-particle accelerator for the irradiation of cells *in vitro*. The system is being designed such that it is fully automated; the cells are imaged with a coupled epifluorescence microscope, the cellular or subcellular targets are recognized, and their positions are recorded under computer control. The stage, which has a precision of 1 μm, is instructed to position each cell in turn at the beam aperture, and the controlling software opens an electrostatic shutter in the beam until a preset number of particles have irradiated the cell.

To know precisely the energy deposited in each target, particle detection with ∼100% efficiency is required. The detector configuration adopted at the MIT microbeam is that of positioning the detection system between the collimator and the cell substrate. One can envision placing the detector to intercept particles after they have traversed the cells, but this would significantly hamper the ability to support and irradiate cells in medium. Furthermore, such a post-cell detection system would not be appropriate for experiments in which the particles deposit all their energy in the cell. Therefore, a pre-cell detection system was implemented at MIT, as is the case at some other microbeam facilities (*1, 2*). Such a configuration imposes significant constraints on the ultimate design. For example, a thin, transmission-type detector is necessary to minimize energy loss of the particulate beam to a few hundred keV. A BC400 thin

Single ion bombardment of living cells at LIPSION

T. Reinert [a,*], A. Fiedler [a,b], J. Škopek [a,d], J. Tanner [c], J. Vogt [a], T. Butz [a]

[a] *Fakultät für Physik und Geowissenschaften, Universität Leipzig, Nukleare Festkörperphysik, Linnéstr. 5, Leipzig D-04103, Germany*
[b] *Fakultät für Biowissenschaften, Pharmazie und Psychologie, Universität Leipzig, Leipzig, Germany*
[c] *Klinik und Poliklinik für Strahlentherapie, Martin-Luther-Universität Halle-Wittenberg, Germany*
[d] *Ústav biofyziky a informatiky, 1. lékařská fakulta, Univerzita Karlova v Praze, Czech Republic*

Abstract

We report on the development of an irradiation platform for living cells at the Leipzig nanoprobe LIPSION and on first irradiation experiments. The platform enables cell irradiation with targeted and counted ions (H^+, He^+) (2–3 MeV) in specially constructed mini-Petri dishes in vertical position in air. The use of a 200 nm (Si_3N_4) thick Petri dish irradiation window, a 100 nm (Si_3N_4) thick beam exit window and the high precision beam positioning ensure a hit accuracy significantly better than 0.5 μm. Hit verification tests using CR-39 are shown. For the cell irradiation we seeded epithelial cells (HUVEC) in the special irradiation Petri dishes. Initially, we tested parameters such as attachment, survival and sedentariness of the cells on the irradiation window. After 14 h about 50% of the seeded cells attached to the window with sufficient survival and sedentariness. The cell handling for the irradiation procedure did not significantly affect the cells. The first patterned irradiation experiments were carried out with 2.25 MeV protons.
© 2004 Elsevier B.V. All rights reserved.

PACS: 87.50; 07.79; 41.75.A
Keywords: Single event; Microbeam; Cell; Irradiation

1. Introduction

It was often stated that the advantages of scanned focused ion beams for radiobiological applications are easily lost due to formidable difficulties arising from the horizontal configuration of the microprobes and the need of a beam exit window [1,2]. Despite these restrictions we try to overcome these difficulties in taking advantage of our system. Currently we are developing our existing horizontal nuclear microprobe for radiobiological application.

Our key objective is the investigation of the cellular response to targeted irradiation with light ions (H^+, He^+), especially the radiation induced bystander effect [3]. This effect is, in short, the radiation related response of non-irradiated cells neighbouring an irradiated cell. For these studies a precise targeting on the cells is mandatory. Furthermore, the measurement of the number and energy loss of the ionising particles within the cell determines precisely the applied dose. The next challenging step is to precisely determine and to target on selected positions for the irradiation

---

* Corresponding author. Tel.: +49-341-97-32706; fax: +49-341-97-32708.
E-mail address: reinert@physik.uni-leipzig.de (T. Reinert).
URL: http://www.uni-leipzig.de/~nfp.

within the cells, e.g. to distinguish between the cytoplasm and the cell nucleus or even between smaller structures within the cell. Therefore, we developed an irradiation platform for living cells at the high-energy ion nanoprobe laboratory LIPSION. The platform enables the irradiation of living cells in a mini-Petri dish with as little liquid as possible in a vertical position and the detection and energy loss measurement of the transmitted projectile ions.

Technically, our primary concern is to increase the hit accuracy to better than 1 μm. Therefore, we use thin Si_3N_4 films as beam exit window and as irradiation window in the Petri dish bottom. Scientifically, our studies started with adhesion, survival and sedentariness tests with endothelial cells and first patterned irradiation experiments.

2. Technical

2.1. LIPSION laboratory and irradiation platform

The nanoprobe LIPSION designed for ion microprobe applications consists of a 3.5 MV Singletron™ accelerator providing H^+ or He^+ ion beams and a MARC-type microprobe [4]. The beam can be focused by a magnetic quadrupole lens system down to below 50 nm in diameter in the low current mode [5]. In this mode, the beam intensity is easily controlled from about 10,000 ions per second down to a few ions per second using the object micro-slits and the accelerator

settings. A fast electrostatic beam switcher (Avtech, VVR-7B-PS-UMA1 high voltage pulser) with a rise time of nominally 500 ns can switch off the beam on demand. Experimentally, the total system (ion detection and counting, triggering and blanking) can select one single ion from count rates up to 5000 ions per second. A magnetic scanning system directs precisely the focused beam to the target position. However, a dedicated beam control system for irradiation purposes, i.e. the software for selecting the target position and the number of ions with interfaces to the beam control units, is still under development.

The irradiation platform is constructed to fit into the target chamber (Fig. 1). It consists of a tunnel with a beam exit window (1×1 mm, 100 nm thick Si_3N_4) in which a vertically fixed mini-Petri dish (Fig. 2) can be slid into the tunnel such that the Petri dish irradiation window (2×2 mm, 200 nm thick Si_3N_4) is in the beam focus plane close to the beam exit window. The irradiation window is slightly pressed against the beam exit window to ensure a minimum air gap (about 100 μm) maintained by the exit window bent due to the air/vacuum pressure difference. The slider is equipped with a windowless p–i–n-diode (Hamamatsu) working as a particle detector behind the irradiation window of the Petri dish (Fig. 2). A light guide fed through the p–i–n-diode provides illumination of the irradiation window for a retractable front view microscope. A digital camera (Nikon, 3.2M pixels) is connected to the retractable microscope in order to get "beam view images" of the cells within
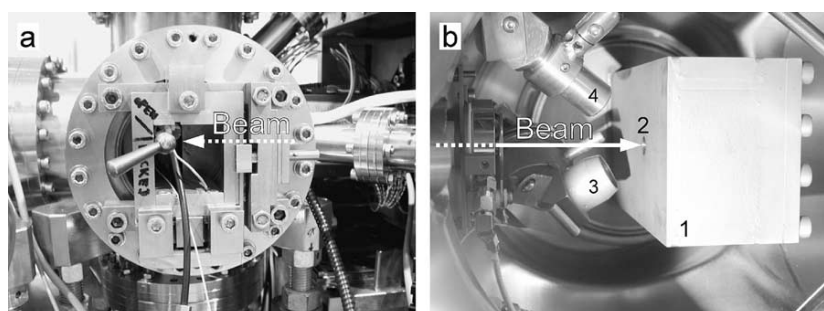

Fig. 1. (a) The tunnel of the irradiation platform with Petri dish holder inserted; beam from the right. (b) Inside view of the target chamber from the opposite to the tunnel flange with inserted tunnel (1), beam exit window (2), fixed long distance pseudo-front microscope (3), light-source (4); beam from the left.
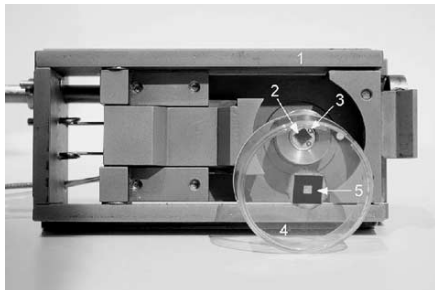
Fig. 2. (1) Mini-Petri dish holder, (2) windowless p–i–n-diode as particle detector, (3) light guide for illumination, (4) mini-Petri dish, (5) Petri dish irradiation window.

the beam exit window. These images provide the relative positions of the cells (in image co-ordinates) with respect to the corners of the exit window. The positions of the corners with respect to the beam (beam co-ordinates) are known from a beam scan over the hole exit window, i.e. a scanning transmission ion microscopic (STIM) image. The corners can be used as fiducial markers because they are fix points. Thus, the cell positions can be expressed in beam co-ordinates to target the ions on the cells. Since the beam co-ordinates are known from the STIM image with an accuracy significantly better than 1 μm the total targeting accuracy is dominated by the resolution of the "beam view" microscopic image only, which in our case is still a few microns.

2.2. Hit accuracy tests

In order to determine the hit accuracy, tests on CR-39 with different patterns were performed. The CR-39 foil was glued onto the bottom of the mini-Petri dish and irradiated through the exit window. Since the protons of 2.25 MeV cannot penetrate the thick CR-39 foil we could not detect single events. Therefore, we set up the beam intensity to about 3000 protons per second. At each target position the beam gate was opened for 1 ms enabling the passage of three protons on the average. We wrote a 10×10 dot pattern and the word "LIPSION" with dots separated by 2 μm (Fig. 3). The statistical analysis of the hit positions revealed a hit accuracy significantly better than 0.5 μm. Using the SRIM code [6] we calculated for
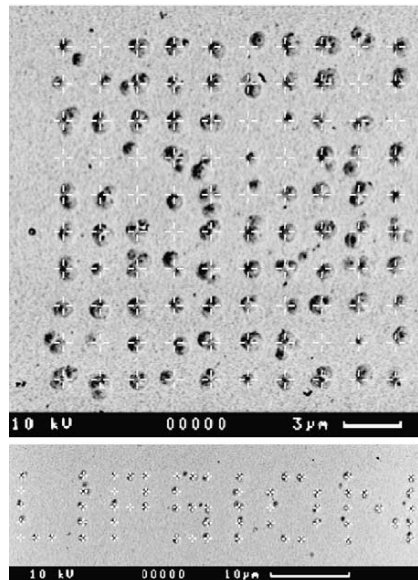
Fig. 3. Hit verification tests on CR-39 ($\sim$3000 protons per second, 1 ms beam gate per position): the pattern was drawn with dots separated by 2 μm. The target position markers (white crosses) have a size of 1 μm. The REM images reveal a hit accuracy significantly better than 0.5 μm.
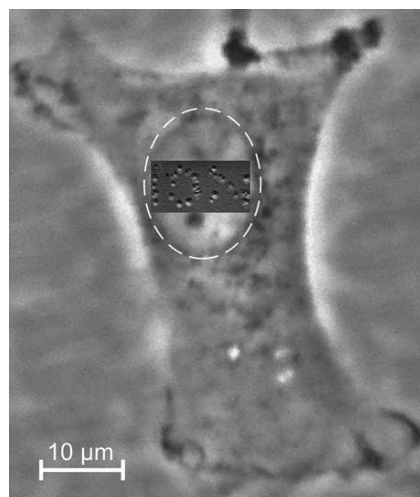

Fig. 4. The REM image of the word "ION" from a 1 μm spaced "LIPSION" on CR-39 was overlaid to the microscopic image of an epithelial cell right on top of the nucleus of the cell (dashed oval).

2.25 MeV protons through 100 nm Si_3N_4 and 100 μm air a lateral straggling of less than 0.2 μm. Our high hit accuracy would enable us to write the small word "ION" into a cell nucleus (Fig. 4) if the target recognition would be of similar precision.

However, in some cases large angle scattering occurred. Additional tests with four spots, each having about 1000 protons, showed in total eight hits between 2.5 and 5 μm away from the targeted position which is 0.2% of the total number of ions only.

3. Biological

Adjacent to the accelerator laboratory we have established a cell culture laboratory with standard cell culturing equipment. At present we cultivate EaHy 926, a hybrid cell line (fusion of HUVEC and epithelial cell line A459). The cells are seeded into small Petri dishes (35 mm in diameter) with a 2×2 mm, 200 nm thick Si_3N_4 irradiation window on the bottom. The reaction of the cells on the Si_3N_4 window was tested.

3.1. Adhesion, survival and sedentariness tests

We seeded about one million cells onto the bottom of the entire mini-Petri dish. Thus, 4000–5000 cells were distributed over the 4 mm^2 of the Si_3N_4 window. After 14 h, 50% of the cells adhered on the Petri dish bottom as well as on the Si_3N_4 window. Most of the cells which did not adhere were found to be dead. The growth rate of the cells adhered on the Si_3N_4 window was determined to 33 h doubling time.

The irradiation of the cells is intentionally carried out with as little liquid as possible around the cells to ensure the transmission and therefore the detection and energy loss measurement of the ions. Additionally, the lack of liquid will prevent the production of reactive oxygen species in the intercellular space which might affect the non-targeted neighbouring cells. However, the effect of medium removal and cell handling for irradiation had to be tested in a control study. Therefore, we sham irradiated the cells: i.e. the medium was taken out of the mini-Petri dish, the cells were washed with PBS-buffer and fixed in the vertical position for 15 min simulating the irradiation conditions. After the sham irradiation, the Petri dishes were horizontally repositioned and the usual medium level was restored. About 95% of the cells survived the procedure. The cell positions did not change significantly due to this procedure.

3.2. First irradiation

First irradiation experiment of living cells were carried out with 2.25 MeV protons homogeneously distributed in different patterns and number of protons over the cells [7]. We checked for survival at different times after irradiation. Surprisingly, the cells were not affected too much; the growth rate seemed to be slightly lower. Additionally, the area with dead cells exceeded the area of irradiation.

4. Conclusion and future prospects

It was shown that the hit accuracy of a high performance focusing system can be improved to better than 1 μm by using a thin exit window and minimizing the air gap between exit window and target. However, the merit of this high precision is not yet fully exploited as long as the cell (or cell compartment) recognition does not reach a similar accuracy. The development of a high resolution imaging and cell recognition system combined with beam control capabilities is mandatory. In order to facilitate the target finding fiducial markers on the 200 nm thick Si_3N_4 irradiation window on which the cells adhere are desired. The cells could be better addressed in the mini-Petri dish. In order to produce fiducial markers we checked out the possibility to write structures into the Si_3N_4 window using a focused gallium ion beam. The results are promising, the structures give good contrasts. The effect of the gallium on the stability and biocompatibility have still to be tested.

References

[1] B.E. Fischer, M. Cholewa, H. Noguchi, Nucl. Instr. and Meth. B 181 (2001) 60.

[2] M. Folkard, K.M. Prise, B. Vojnovic, S. Gilchrist, G. Schettino, O.V. Belyakov, A. Ozols, B.D. Michael, Nucl. Instr. and Meth. B 181 (2001) 426.

[3] J. Österreicher, K.M. Prise, B.D. Michael, J. Vogt, T. Butz, J. Tanner, Strahlenther. Onkol. (2) (2003) 69.

[4] T. Butz, R.-H. Flagmeyer, J. Heitmann, D.N. Jamieson, G.J.F. Legge, D. Lehmann, U. Reibetanz, T. Reinert, A. Saint, D. Spemann, R. Szymanski, W. Tröger, J. Vogt, J. Zhu, Nucl. Instr. and Meth. B 161–163 (2000) 323.

[5] D. Spemann, T. Reinert, J. Vogt, D. Dobrev, T. Butz, Nucl. Instr. and Meth. B 190 (2002) 312.

[6] J.F. Ziegler, SRIM-98, Version 98.01, www.srim.org.

[7] A. Fiedler, J. Škopek, T. Reinert, J. Tanner, J. Vogt, J. Österreicher, L. Navratil, T. Butz, Radiat. Res. 161 (1) (2004) 95.

diated neighbors of irradiated cells. *Radiat. Res.* **155**, 397–401 (2001).

4. D. Blöcher, DNA double strand break repair determines the RBE of alpha-particles. *Int. J. Radiat. Biol.* **54**, 761–771 (1988).

5. D. J. Brenner, J. B. Little and R. K. Sachs, The bystander effect in radiation oncogenesis: II. A quantitative model. *Radiat. Res.* **155**, 402–408 (2001).

6. M. Folkard, B. Vojnovic, K. M. Prise, A. G. Bowey, R. J. Locke, G. Schettino and B. D. Michael, A charged-particle microbeam I. Development of an experimental system for targeting cells individually with counted particles. *Int. J. Radiat. Biol.* **72**, 375–385 (1997).

7. M. Folkard, B. Vojnovic, K. J. Hollis, A. G. Bowey, S. J. Watts, G. Schettino, K. M. Prise and B. D. Michael, A charged particle microbeam: II A single-particle micro-collimation and detection system. *Int. J. Radiat. Biol.* **72**, 387–395 (1997).

8. G. Randers-Pehrson, C. R. Geard, G. Johnson and D. J. Brenner, The Columbia University single-ion microbeam. *Radiat. Res.* **156**, 210–214 (2001).

First Irradiation Experiments with Living Cells at LIPSION

A. Fiedler,[a,b] J. Škopek,[a,d] T. Reinert,[a] J. Tanner,[c] J. Vogt,[a]
J. Österreicher,[e] L. Navratil[d] and T. Butz[a]

[a]*Faculty of Physics and Earth Science, University of Leipzig, Germany;*
[b]*Faculty of Biology, Pharmacy and Psychology, University of Leipzig,
Germany;* [c]*Clinic and Polyclinic for Radiation Oncology, University of
Halle-Wittenberg, Germany;* [d]*Department of Biophysics, 1st Medical
Faculty, The Charles University in Prague, Czech Republic; and*
[e]*Department of Radiobiology and Immunology, Purkyne MMA,
Hradec Králové, Czech Republic*

We report here on the development of an irradiation platform for living cells at the high-energy ion nanoprobe at the LIPSION Laboratory, Leipzig, Germany, and on the first experiments with living cells that were carried out in the course of studies of radiation-induced bystander effects using a focused ion beam (*1*).

The LIPSION Nanoprobe Laboratory

The high-energy ion nanoprobe LIPSION at the University of Leipzig has been operational since 1998 (*2*). The ultrastable single-ended 3.5 MV Singletron™ accelerator supplies a H^+ or He^+ ion beam. The beam can be focused by a magnetic quadrupole lens system down to below 50 nm in diameter for the low-current mode. A magnetic scanning system moves the focused beam across the sample according to the desired number, width and velocity of the position steps. Thus we are able to apply a selected number of ions to each target position.

For the cell preparation and analysis procedures, we have established a cell culture laboratory adjacent to the accelerator laboratory.

Irradiation Platform and Mini-petri Dishes

The irradiation platform consists of a tunnel with a rectangular cross section which can be attached to a CF160 flange on our target chamber. Bellows allow for fine adjustment of the tunnel from the outside. The side facing the ion beam is equipped with an ion exit window made of Si_3N_4 that is 1 mm × 1 mm in area and 100 nm thick (called frames because the windows are framed by 200 μm silicon). This exit window bends toward the vacuum side of the beam line but withstands a pressure difference of one atmosphere. A mini-petri dish holder can be slid into the tunnel with a sufficient gap between the exit window and the bottom of the petri dish and is subsequently moved toward the exit window, ensuring a minimal air gap. The mini-petri dish is a conventional 35-mm-diameter plastic dish with a Si_3N_4 window at the center whose dimensions are 2 mm × 2 mm and a thickness of 200 nm. The particle detector is placed downstream immediately after the cells.

Adhesion Tests

We carried out adhesion tests with EaHy 926, a hybrid cell line (fusion of HUVEC and epithelial cell line A459) grown in enriched DMEM (*3*). We used about 0.25 million cells/ml and added 2 ml cell-containing medium to the entire bottom of the mini-petri dish. In this way we seeded an average of 2000–4000 semi-confluent cells on 4 mm². Cells that did not adhere were taken up together with the medium with a micropipette and were counted in a counting chamber. We found that up to 50% of the cells adhere after 14 h equally on the petri dish and on the Si_3N_4 frame. Using trypan blue staining, we determined that most of the cells that did not adhere were dead. Similar results were obtained with polyethylene terephthalate (PET) foils that were 0.9 μm thick; however, these were abandoned because they wrinkle easily. The ability to adhere was also studied with fluorescent Hoechst 33258 stain. The cells were incubated with 1 μ*M* Hoechst stain 33258 for 1 h and then put into Hepes medium.

Medium Removal, Vertical Positioning, Short-Term Survival, and Migration Tests

We are using a horizontal beam line and therefore must bring the mini-petri dishes to a vertical position for irradiation. Since we have the particle detector behind the cells, we must remove as much medium as possible, at least at the position where we plan to irradiate. Using a micropipette, we removed the medium and washed the cells twice with PBS buffer so that a thin film remained in the center of the window while a significant meniscus remained at the edges of the frames. About 95% of the cells survived the following procedure as checked by fluorescein diacetate (FDA) and propidium iodide (PI) staining: medium removal, vertical positioning and sham irradiation for 15 min, horizontal repositioning, and restoration of the usual medium level. Extensive studies of the accuracy of the cell positions before and after this procedure were carried out. Images of stained cells (Hoechst 33258) were recorded with a digital camera, and it was found that cell positions were unchanged within the resolution of the digital camera (2000 × 1400 pixels), apart from those cells that did not survive and floated away. Thus the immobility of the cells is sufficient. The normal situation encountered was that a single cell was totally missing after the procedure and might have floated away from the field of view. Occasionally, a new cell that might have floated into the field of view from outside appeared after the whole procedure.

Irradiation of Living Cells

An area of 540 μm × 540 μm close to the upper edge of the 2 × 2-mm Si_3N_4 frame that was roughly centered was irradiated with 2.25 MeV protons in the scanning transmission ion microscopy (STIM) mode with the following parameters: We used 250 × 250 pixels, and the beam scanner was advanced by one pixel after a single proton was detected. In this way a rectangular grid with 2.16 μm spacing with exactly one proton per point was produced. This allowed us to get a STIM image of the cells, albeit with less resolution than would normally be achievable (with smaller pixel size).

The energy loss from the ion exit window, the bottom of the mini-petri dish, the air gap between both (estimated to be less than 100 μm), and about 4 mm air in front of the particle detector was calculated to be roughly 140 keV using the SRIM code (SRIM-2003; http://www.srim.org). The cells received on average about 100 protons. The linear energy transfer (LET) for 2.25 MeV protons is of the order of 15 keV/μm. With an estimated cell thickness of 5 μm (averaged over cytoplasm and nucleus), each cell received an energy of about 5–10 MeV. Using the above numbers, we thus estimate that each cell received a dose of about 0.5 Gy.

We subsequently stained the cells with FDA and PI and checked for survival at 15 min and 17.5 h after irradiation; a very large number of cells survived.

However, further experiments are necessary to extract significant in-

formation on cell survival. In addition, further end points like interleukin 1α, $β_1$-integrin and ROS will be examined because ^{60}Co γ irradiations showed that these are sensitive indicators of the response of cells to ionizing radiation (4). We expect similar sensitivity for proton irradiation, although it is unclear whether we can reach the detectable threshold to visualize such changes.

References

1. J. Österreicher, K. M. Prise, B. D. Michael, J. Vogt, T. Butz and J. Tanner, The bystander effect of ionizing irradiation: its mechanisms, biological implications and current investigations at the Leipzig LIP-SION facility. *Strahlenther. Onkol.* **179**, 69–77 (2003).
2. T. Butz, R-H. Flagmeyer, J. Heitmann, D. N. Jamieson, G. J. F. Legge, D. Lehmann, U. Reibetanz, T. Reinert, A. Saint and J. Zhu, The Leipzig high-energy ion nanoprobe: A report on first results. *Nucl. Instrum. Methods Phys. Res. B* **161–163**, 323–327 (2000).
3. G. Hildebrant, L. Maggiorella, F. Rödel, V. Rodel, D. Willis and K. R. Trott, Mononuclear cell adhesion molecule liberation after X-radiation of activated endothelial cells *in vitro. Int. J. Radiat. Biol.* **78**, 315–325 (2002).
4. J. Österreicher, J. Jahns, G. Hildebrandt, J. Psutka, J.M. Tanner, J. Vogt and T. Butz, The $β_1$-integrin and IL-1α expressions on the bystander effect model via medium transport from irradiated cells: The pilot study. *Acta Histochem.,* in press.

Development of a Charged-Particle Microbeam for Single-Particle Subcellular Irradiations at the MIT Laboratory for Accelerator Beam Applications

J. C. Yanch,[a] M. F. Folkert,[a] R. J. Ledoux,[b] A. Dart,[b] J. R. Albritton,[a] R. P. Boisseau,[b] J. M. O'Meara,[a] W. P. Nett,[b] E. D. Johnson[a] and K. D. Held[c]

[a]Department of Nuclear Engineering and Whitaker College of Health Sciences and Technology, Massachusetts Institute of Technology, Cambridge, Massachusetts; [b]Pyramid Technical Consultants, Waltham, Massachusetts; and [c]Department of Radiation Oncology, Massachusetts General Hospital, Boston, Massachusetts*

Introduction

A charged-particle microbeam for single-particle, subcellular irradiations is nearing completion at the Massachusetts Institute of Technology Laboratory for Accelerator Beam Applications (MIT LABA). The microbeam apparatus includes an electrostatic accelerator, horizontal beam tube, a 90° bending magnet to render the charged-particle beam vertical, and a dedicated endstation for biological irradiations. The entire apparatus is less than 4 m long, so the microbeam can be completely housed in a single room. The He^{++} or H$^+$ charged-particle beam is delimited using either a slit or a single-hole collimator assembly. Particle counting is performed below the cell dish with a plastic scintillator in combination with two photomultiplier tubes counting in coincidence mode. Control software, developed in-house, manipulates all aspects of the hardware including the accelerator, beam-line components, vacuum systems, and all subsystems of the biological endstation.

Accelerator and Beam Line

The microbeam uses a 1.5 MV single-stage electrostatic accelerator that is capable of generating a variety of particle types and charge states. The accelerator, designed by Newton Scientific Inc. (Cambridge, MA), is very compact: only 1.8 m long and 0.77 m in diameter. The accelerator comprises an accelerating column that contains the accelerating tube, the high-voltage power supply, and the high-voltage terminal assembly including the ion source and associated electronics. The ion beam is continuously injected at low energy (15–30 keV) into the accelerating tube from the radiofrequency ion source located in the high-voltage terminal. The beam is accelerated and focused by the electrostatic field of the accelerating tube and will attain a final maximum energy of 1.5 MeV (single-charged ion) or 3.0 MeV (doubly charged ions).

The particle beam emerging from the accelerator travels down a 1.2-m-long beam tube. This beam tube houses X-Y steering plates for beam deflection and a magnetic quadrupole triplet. In the microbeam's original configuration (a horizontal beam), this magnet was designed to provide a highly focused (1 μm) beam spot in vacuum for proton-induced X-ray emission (PIXE) and other surface analysis methods. Since a vertical beam was considered optimum for biological experiments, however, the focusing capability of the triplet is not used in the present configuration of the microbeam. Instead, this magnet is used simply to defocus the ion beam somewhat prior to its entry into a 90° bending magnet. The bending magnet serves two purposes. First, the ion beam now becomes vertical, which allows cell dishes to be positioned in the horizontal orientation. This is desirable if irradiation times are long and require some amount of medium to remain on the cells. Second, since the bending of ions in a magnetic field is a function of the charge on the ions, the magnet allows us to selectively transport the ions of choice into the vertical orientation. For instance, for the generation of helium beams, the magnet ensures the transport of 3.0 MeV He^{++} ions to the cell irradiation endstation and the rejection of 1.5 MeV He$^+$ ions that would result in the detection of a particle (through interaction with the plastic scintillator located below the cell dish) but only partial or no cell irradiation due to the limited range of these particles.

Cell Irradiation Endstation

Subsystems of the cell irradiation endstation are housed in a 49 × 49 × 31-cm^3 light-tight box mounted immediately above the 90° bending magnet. The cell irradiation endstation comprises the following subsystems: a collimator or slit assembly to delimit the beam, a two-dimensional motorized stage, a plastic scintillator, light guide and two photomultiplier tubes for particle counting, a specially designed cell dish, UV objective with z-motion for focusing, dichroic mirror, and a CCD camera for cell visualization. A light source is mounted on the outside of the endstation box; light passes from the source through a 3.2-cm-diameter tube to interact with the dichroic mirror. The deflection plates, motorized stage, photomultiplier tubes, light source, and CCD camera are interfaced with a PC for computer control of all aspects of cell irradiation.

Slit and Collimator

Beam delimiting is performed using either a slit or a single-hole collimator. The slit is a laser-drilled aperture (Lenox Laser Inc, Glen Arm, MD) 1.8 μm wide and 1 mm long drilled in 45-μm-thick stainless steel and glued to a 9.5-mm-diameter mount. This mount can be removed and the collimator assembly installed in its place. The collimator is made from 285-μm-diameter fused silica tubing with a 1.5-μm-diameter bore. Collimators are cut from the tubing in lengths of approximately 1 mm and inserted into a mounting assembly that also holds the single-particle counting apparatus (light guide, plastic scintillator and two photomultiplier tubes). Efforts are under way to characterize the ''beam size'' generated by the collimator in its mount using track-etch detectors (CR-39

replaced and the microscope-stage driver software has been improved. The new focus-control unit consists of a stepping motor (1000 pulses = 1 rotation = 100 μm focus movement) and its controller, jog-dial control pad with full remote control function, and optical upper and lower limit sensor. The stage driver software was modified for the new unit. Before this improvement, we inserted a waiting code to make stage movement stable, because occasional instability (software hanging up, etc.) was observed with the previous hardware configurations. With the insertion of the waiting code, the instability of system, which was mainly caused by instability of the previous focus unit, was decreased. However, the movement of the microscope stage was slower because of the architecture of the combined control of both *X-Y* sample stage and focus control unit in stage driver software. To verify the effects of the improvement, the movement speed of the stage using both the previous driver and the improved driver was measured with an online microscope system. The overhead time of the driver software with a single stage action was reduced markedly from 1.37 s to 0.62 s due to the deletion of the waiting code.

Besides bystander effect studies using Chinese hamster ovary (CHO-K1) cells (*2*) and normal human foreskin fibroblast AG01522 cells (*4, 5*), radiobiological studies using tobacco BY-2 protoplasts (*6*) and germline cells of the nematode *Caenorhabditis elegans* (*7*) are in progress.

References

1. Y. Kobayashi, T. Funayama, S. Wada, M. Taguchi and H. Watanabe, System of cell irradiation with a precise number of heavy ions. *Radiat. Res.* **161**, 90–91 (2004). [extended abstract]
2. T. Funayama, S. Wada, Y. Kobayashi and H. Watanabe, Irradiation of mammalian cultured cells with a collimated heavy-ion microbeam. *Radiat. Res.* **163**, 241–246 (2005).
3. Y. Kobayashi, T. Funayama, S. Wada, Y. Furusawa, M. Aoki, C. Shao, Y. Yokota, T. Sakashita, Y. Matsumoto and N. Hamada, Microbeams of heavy charged particles. *Biol. Sci. Space* **18**, 235–240 (2004).
4. C. Shao, Y. Furusawa, Y. Kobayashi, T. Funayama and S. Wada, Bystander effect induced by counted high-LET particles in confluent human fibroblasts: A mechanistic study. *FASEB J.* **17**, 1422–1427 (2003).
5. Y. Furusawa, M. Aoki, C. Shao, Y. Kobayashi, T. Funayama, T. Sakashita and S. Wada, Development of irradiation procedure to detect distance the signal transfer of GJIC bystander effect. *JAERI Rev.* **2004-025**, 88–90 (2004).
6. Y. Yokota, T. Funayama, Y. Kobayashi, T. Sakashita, S. Wada, Y. Hase, N. Shikazono, A. Tanaka and M. Inoue, Development of an ion microbeam system for irradiation single plant cell[s]. *Biol. Sci. Space* **17**, 298–601 (2003).
7. T. Sugimoto, K. Dazai, T. Sakashita, T. Funayama, S. Wada, N. Hamada, T. Kakizaki, Y. Kobayashi and A. Higashitani, Cell cycle arrest and apoptosis in *Caenorhabditis elegans* germline cells following heavy-ion microbeam irradiation. *Int. J. Radiat. Biol.* **82**, 31–38 (2006).

Status of the New Single-Ion Hit Facility for Irradiation of Living Cells at LIPSION

C. Nilsson, S. Petriconi, T. Reinert and T. Butz

Faculty of Physics and Geosciences, University of Leipzig, Linnéstrasse 5, 04103 Leipzig, Germany

Introduction

At the LIPSION nanoprobe laboratory, single-ion irradiation experiments on single living cells have been carried out since 2003. Previous cell irradiation experiments include patterned irradiations of HeLa cells and primary fibroblasts with a low number of protons and α particles (*1, 2*). Biological end points include changes in the rate of apoptosis and radiation-induced DNA double-strand breaks. This is a report on the current status of the new single-ion hit facility (SIHF), an upgrade that will allow for truly targeted cell irradiation.

The LIPSION Nanoprobe Laboratory

The LIPSION laboratory consists of a 3.5 MV Singletron™ accelerator with a horizontal beam line where H^+ or He^+ ions are accelerated to energies up to 3 MeV (*3*). The cell irradiation experiments have been carried out at an energy of 2.25 MeV. Using this system, a focused beam spot size of less than 350 nm in air can be achieved. Due to the horizontal orientation of the beam line, a vertical petri dish arrangement is required, and such an arrangement has been successfully implemented and tested at the facility.

New Developments Regarding the Beam Line

Currently, a major rebuilding of the target chamber is being carried out to increase the versatility and accessibility of the nanoprobe. The old target chamber, a system of cylinders and flanges, which has been part of the setup since the facility became operational in 1998, will be replaced by a new target chamber that is the shape of a box with a removable top, with the dimensions 450 mm × 300 mm × 480 mm. The new chamber will be equipped with a new translation stage as well as with a separate irradiation platform for the irradiation of single, living cells with single ions. The implementation of the new chamber is planned for the second quarter of 2006.

The new seven-axis translation stage with goniometer has been custom-manufactured (Feinmess Dresden, Germany). It is movable in the *x, y* and *z* directions as well as in the θ, *x, y'* and φ directions (the goniometer will be needed, e.g., for STIM tomography and channeling experiments). The translation part consists of two piezo motors that control the horizontal motion and the motion in the axial (beam) direction and one stepper motor that controls the vertical motion. Initial tests indicate that a positioning accuracy and repeatability of about 1 μm can be achieved for this stepper motor-controlled axis. The rotation part consists of four piezo motors that control rotation in two axes as well as additional horizontal and vertical motion.

New Developments Regarding the Cell Irradiation

To enable irradiation of living cells, one key issue is to extract the beam into air through a vacuum window. In the case of the LIPSION SIHF, this extraction will be realized by attaching an exit nozzle to the beam entrance in the chamber wall.

This solution is space saving and allows not only for cell irradiation experiments but also for other kinds of in-air ion beam analysis, such as PIXE investigations of archeological samples. The end piece of the nozzle is exchangeable and can be made either of stainless steel, to be used for cell irradiation experiments, or of aluminum, for PIXE measurements.

The exit window on the nozzle is a 100-nm-thick Si_3N_4 vacuum window with an area of 1×1 mm², which has proven to withstand the pressure difference well. Other new vacuum windows that will be tested are ones that are 50 nm thick as well as circular windows.

The new irradiation platform will consist of several separate components to ensure maximum flexibility. The integral component is the petri dish holder, a holder for the particle detector, a p-i-n diode that is placed after the Petri dish microscope objectives, and a holder for the microscope eyepiece and the CCD camera.

This combination with a downstream microscope enables online cell recognition. Another possibility is to use fiducial markers on the petri dish itself, thereby allowing recognition of the cells offline. At the LIPSION facility, such fiducial markers could be fabricated using proton beam writing.

Software Development

In parallel with the upgrades of the beam line, software improvements are also under way. These include the development of completely new scan control software that runs in a hard real-time environment under Linux/RTAI. First measurements of response times have given encouraging results, suggesting that beam blanking may be triggered reliably directly from software. The limiting factor to the current system's accuracy appears to be the slow ADC conversion time of 20 μs during which the beam remains unblanked. Various strategies to improve the accuracy are currently being investigated. With an adaptive blanking algorithm, irradiation rates in excess of 200 s^{-1} have been reached without relying on external hardware blanking triggers, and a single-hit accuracy of better than 99% has been observed.

Future development efforts will focus on providing a user-friendly graphical user interface for the scan control as well as for the control of the new translation stage and goniometer. The stage control will run over a network and use the software under development at the division, using C++ and Qt, a C++ class library and application framework. Likewise, cell recognition software will also be developed at the division, using C++ together with the commercially available software package ImagePro Plus. The use of cell recognition software will make automated and/or semi-automated truly targeted cell irradiation possible, as opposed to the predetermined patterns (dots, lines, bands and crosses) that have been used so far.

References

1. A. Fiedler, J. Skopek, T. Reinert, J. Tanner, J. Vogt, J. Österreicher, L. Navratil and T. Butz, First irradiation experiments with living cells at LIPSION. *Radiat. Res.* **161**, 95–96 (2004). [extended abstract]
2. T. Reinert, A. Fiedler, J. Skopek, J. Tanner, J. Vogt and T. Butz, Single ion bombardment of living cells at LIPSION. *Nucl. Instrum. Methods Phys. Res. B* **219–220**, 77–81 (2004).
3. T. Butz, R-H. Flagmeyer, J. Heitmann, D. N. Jamieson, G. J. F. Legge, D. Lehmann, U. Reibetanz, T. Reinert, A. Saint and J. Zhu, The Leipzig high-energy ion nanoprobe: A report on first results. *Nucl. Instrum. Methods Phys. Res. B* **161–163**, 323–327 (2000).

Biological Validation of the Ion Microbeam Developed at CENBG to Generate Localized Ionizing Radiation-Induced Damage on Keratinocyte Cells Expressing GFP-Tagged Protein

H. Seznec, T. Pouthier, S. Incerti, M. Heiss, Ph. Barberet and Ph. Moretto

Centre d'Etudes Nucléaires de Bordeaux-Gradigan, IN2P3/CNRS, Université Bordeaux 1, Chemin du Solarium, 33175 Gradignan Cedex, France

The CENBG Microbeam Line and the Irradiation Procedure

The CENBG cellular irradiation facility is based on a focused microbeam line that has been described extensively elsewhere (*1, 2*). This setup allows single cell irradiation with precise control of the delivered dose; a predetermined number of α particles can be sent to a selected cell within a population. The layout and irradiation procedure using the microbeam at the CENBG have been presented elsewhere (*1, 2*). Approximately 1500 exponentially growing cells were plated into "home-made" microbeam dishes. The DNA content of attached cells was visualized without the use of chemical agents (like Hoechst 33342) but using the transgenic and chimeric fluorescently labeled protein histone GFP-H2B. The position of individual nuclei was determined by optical imaging of the fluorescent staining pattern at $\lambda = 490$ nm. The image analysis system then located the centroid of each nucleus, and the nuclei were irradiated one at a time with an exact number of α particles.

On average, it took less than 90 min to localize and irradiate up to 1500 cells. We used 3×1500 irradiated cells per group per experiment in the present study. The overall spatial precision of the setup is about ± 10 μm. Because the average cross-sectional area of the nucleus of live attached HaCaT/(GFP-H2B)tg cells was determined to be 100 μm^2, we estimated by Monte Carlo modeling that the particle beam would hit the target nucleus 97% of the time. The average energy of the α particles after the cell-polypropylene plating foil was 2.37 ± 0.01 MeV (*3*) delivered at a dose rate of about 1000 α particles per second. Due to the lag time of the shutter closure, cells were illuminated during 400 ms. After irradiation, the dish was removed from the stage, and the cells were maintained for 24 h in normal culture.

The HaCaT/(GFP-H2B)tg Transgenic Cell Line

We chose HaCaT cells because they would attach to a surface as a monolayer to ensure reasonably uniform radiation doses over the cell population (*1*). Exponentially growing HaCaT cells were transfected by lipofection with the GFP-H2B expression vector (*1*). After 2 weeks of drug selection (G418, 5 μg/ml), several GFP-positive colonies were isolated using fluorescence-activated cell sorting (FACS). Before irradiation, HaCaT/(GFP-H2B)]tg cells were grown in DMEM supplemented with 10% fetal calf serum with 100 μg/ml streptomycin/penicillin at 37°C in a 95% air, 5% CO$_2$ and water-saturated atmosphere. The exposure of the cells to α particles was accomplished as follows: 1500 HaCaT/(GFP-H2B)tg cells were plated onto 3.8-μm-thick polypropylene film-bottomed tissue culture dishes and incubated 24 h before exposure to α particles.

Results

We used transfected immortalized HaCaT cells expressing the chimeric recombinant histone GFP-H2B. This GFP-H2B protein is involved in the DNA architecture and precisely localizes the DNA in the cell nucleus. *In vivo*, these cell nuclei are visualized under a visible-light microscope and targeted in full control mode (down to the ultimate dose of one α particle per cell). The behavior of the GFP-H2B protein also allows us to determine the integrity of chromatin and chromosomes and the induction of cell death. Thus we are able to identify dividing cells, genetic instability, and living and apoptotic cell nuclei. This newly established cell line has been characterized to validate its proliferative capacity and the integrity of its cellular response; and no significant differences were found between transgenic and non-transgenic cells. High-resolution images of interphase nuclei were acquired by confocal microscopy with a Leica DMR/TCS/SP2 microscope. In combination with immunocytochemical techniques using antibody targeted against the specific phosphorylated form of the histone H2AX (called γ-H2AX) (*6*), DNA DSBs were analyzed 24 h after irradiation with α particles. Digital monochrome images were collected for each appropriate channel and were analyzed using the Metamorph software. The quantitative analyses were performed in all regions of the nucleus, and the fluorescence intensities in both channels were calculated in the presence of predetermined masks applied to the whole stack of images after filtering of serial acquisition images. Data were acquired from different cells for each double labeling condition (GFP-H2B and γ-H2AX). Discrete foci of γ-H2AX can be seen distributed homogeneously in the whole cell nucleus of nonirradiated control cells. In contrast, in irradiated cells, we have observed an inhomogeneous distribution of intense and bright γ-H2AX foci, indicating a clear increase of DNA DSBs and also suggesting the putative α-particle impacts. We have also observed a correlation between the number of DNA DSBs generated (γ-H2AX foci) and the number of initial incident α particles.

DNA double strand breaks and Hsp70 expression in proton irradiated living cells

Anja Fiedler [a,b,*], Tilo Reinert [a], Judith Tanner [c], Tilman Butz [a]

[a] *Institute for Experimental Physics II, University of Leipzig, Germany*
[b] *Faculty of Biology, Pharmacy and Psychology, University of Leipzig, Germany*
[c] *Clinic and Polyclinic for Radiation Oncology, University of Halle-Wittenberg, Germany*

Abstract

DNA double strand breaks (DSBs) in living cells can be *directly* provoked by ionising radiation. DSBs can be visualized by immunostaining the phosphorylated histone γH2AX. Our concern was to test the feasibility of γH2AX staining for a direct visualization of single proton hits. If single protons produce detectable foci, DNA DSBs could be used as "biological track detectors" for protons.

Ionising radiation can also damage proteins *indirectly* by inducing free radicals. Heat shock proteins (Hsp) help to refold or even degrade the damaged proteins. The level of the most famous heat shock protein Hsp70 is increased by ionising radiation.

We investigated the expression of γH2AX and Hsp70 after cross and line patterned irradiation with counted numbers of 2.25 MeV protons on primary human skin fibroblasts.

The proton induced DSBs appear more delocalised than it was expected by the ion hit accuracy. Cooling the cells before the irradiation reduces the delocalisation of DNA DSBs, which is probably caused by the reduced diffusion of DNA damaging agents.

Proton irradiation seems to provoke protein damages mainly in the cytoplasm indicated by cytoplasmic Hsp70 aggregates. On the contrary, in control heat shocked cells the Hsp70 was predominantly localized in the cell nucleus. However, the irradiated area could not be recognized, all cells on the Si_3N_4 window showed a homogenous Hsp70 expression pattern.

© 2007 Elsevier B.V. All rights reserved.

1. Introduction

Ionising radiation can initiate direct and indirect radiation effects in biological systems. One *direct effect* of ionising radiation is the break of the DNA double strand (DNA DSB). Consequently, in living cells a repair complex of special proteins gets activated at the damaged DNA site. One of these proteins, activated by phosphorylation at serin 139, is the histone H2AX (phosphorylated form: γH2AX) [1]. The immunostaining of γH2AX visualizes the DNA double strand breaks in the form of a focus.

γH2AX is used as a marker for DSBs induced by single heavy particles (e.g. carbon, bismuth [2]) or by several

hundred protons (20 Gy with 3.2 MeV protons [3]), but at this point it was not clear whether a single proton (∼2 MeV) can produce a detectable focus. Our concern was to test the feasibility of γH2AX staining for a direct visualization of single proton hits. If feasible, the system could be used as "biological track detector" for hit verification.

Ionising radiation also produces free radicals (e.g. reactive oxygen species), which again induce *indirect radiation effects* by damaging cell macromolecules like proteins. Damaged and denatured proteins can either get refolded into a functional structure or even get degraded by heat shock proteins (Hsp). The most famous heat shock protein is Hsp70. Under normal conditions Hsp70 occurs in the cell nucleus and the cytoplasm. However, stress can induce the recruiting of Hsp70 to special cell compartments as well as an overall increased expression. Ionising radiation is also an Hsp70 increasing stressor. However, this was shown mostly for heavy ions, γ- and X-rays, but hardly ever for

---

proton irradiation [4–9]. Therefore, we investigated the expression of the cellular stress response protein after focussed proton beam irradiation.

2. Material and methods

2.1. LIPSION nanoprobe laboratory and irradiation platform

The high-energy ion nanoprobe LIPSION at the University of Leipzig supplies H^+ or He^+ ion beams by a 3.5 MV Singletron™ accelerator. The horizontal beam can be focussed down to below 50 nm diameter in vacuum for the low current mode. In air the hit accuracy for protons is still better than 0.5 μm [10]. However, targeted irradiation at LIPSION is still under development. To easily recognize the irradiated area and the ion hits, specific irradiation patterns with a selected number of ions to each target position were utilized (Fig. 1). A cross irradiation pattern (one cross consists of 7×7 pixels with 1 μm distance and an intercross distance of 5 μm) and a line irradiation pattern (spacing 4 μm × 2 μm or 6 μm × 3 μm distance) were applied.

The cell preparation and analysis procedures were carried out in a cell culture laboratory adjacent to the accelerator laboratory. Standard Petri dishes of 35 mm diameter equipped with a Si_3N_4 window at the centre whose dimension are 2 mm × 2 mm (200 nm thick) were used. The dish can be clamped into a holder and slid in front of the irradiation window (Si_3N_4 of 1 mm × 1 mm, 100 nm thick) with a minimal air gap. The energy loss of the ions after transmission through the cells is measured with a PIN diode that acts as a particle detector.

2.2. Cell irradiation

Primary human skin fibroblasts were regularly maintained in enriched D'MEM at 37 °C and 5% CO_2. For irradiation experiments the cells were transferred into sterilized irradiation dishes. They attached well on the Si_3N_4 window [11]. Two days after seeding the cells were sufficiently confluent (70–90%) for irradiation. Since we have the particle detector behind the cells we have to remove as much medium as possible. To reduce pH-changes the cells were washed twice with PBS buffer after medium removal. Prior to the irradiation the fluid was removed with a micro-pipette whereby the cells were still covered with a remaining thin film. The irradiation dishes were immediately transported from the cell laboratory to the adjacent LIPSION laboratory and positioned for irradiation at ambient conditions (21 °C, 55% rel. humidity). The cells were irradiated with 2.25 MeV protons (LET ~15.7 keV/μm) or with 2 MeV α-particles (He^+, LET ~100 keV/μm) with a particle rate of about 1000 cps in a patterned mode. The applied dose, calculated for the cell nucleus, was approximately 10 mGy/proton and 100 mGy/α. The cells were irradiated with 5, 10, 20 and 40 protons/pixel or 1 and 2 α-particles/pixel so that a dose of approximately 0.7–12 Gy/nucleus was applied. A sham irradiation without any particle application was done for control. Immediately after irradiation the Petri dishes were refilled with culture medium and brought back into the incubator. The whole procedure where the cells were without medium took less than 2 min which preserves the viability of the cells [11]. A short incubation at 37 °C was chosen (longest 1.5 h) to prevent the decline of the irradiation effects. Due to the short incubation time changes in the cell cycle (most of the cells were in the G_1-phase) can be ignored. For the immunocytochemistry the culture medium was removed. The cells were washed twice in PBS buffer (Sigma), fixed with 2% paraformaldehyde (Sigma) for 15 min at RT, washed twice with PBS again, permeabilized with 0.5% Triton X-100 (Sigma) for 10 min at RT and blocked with 1% BSA (Sigma) for at least 15 min at RT.

2.3. Immunocytochemical staining of DNA DSBs and Hsp70

The irradiation experiments of the DSBs were carried out at room temperature; in later studies the cells and the sample holder were cooled down on ice before irradiation without knowing the exact temperature during the irradiation. The incubation time at 37 °C was stopped 1 h after the irradiation. The DNA DSBs were identified with primary anti-phospho-H2A.X (Ser139) rabbit polyclonal IgG antibody (upstate) over night at 4 °C, washed thrice with PBS and visualized by treatment with secondary Alexa Fluor 488 goat anti-rabbit IgG (H + L) antibody (Molecular Probes) for 30 min at RT. Antibody solutions
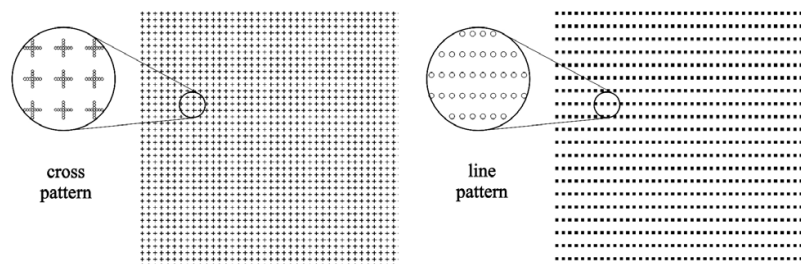

Fig. 1. Schematic representation of cross and line irradiation patterns.

were prepared with PBS and 0.5% BSA. The cells were washed thrice with PBS again and covered with mounting medium (Vectashield) and an object slide.

For the Hsp70 expression an additional comparable control was done by heat shocking the cells for 30 min at 42 °C by swimming on a water bath surface. The post treatment incubation at 37 °C was 1.5 h, similar to that of the irradiated cells. The fixed cells were treated with a polyclonal rabbit-anti-Hsp70-IgG antibody (upstate) and an secondary Alexa Fluor 488 goat anti-rabbit-IgG antibody (Molecular Probes) in the same way as mentioned above. The optical analysis of the endpoints was done by laser scanning microscopy (Zeiss 510 Meta, Leica DM IRE2).

3. Results

3.1. DNA double strand breaks

No foci could be recognized in the sham irradiated controls, meaning that the medium removal for less than 2 min
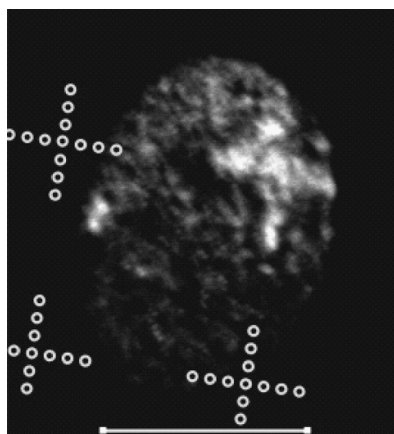
Fig. 2. Cross of DNA DSBs written in a fibroblasts nucleus with 1 α-particle (2 MeV He$^+$) per pixel. DSBs marked by γH2AX antibody. Scale bar: 12 μm.

does not cause stress induced DSB lesions in the DNA. In order to definitely induce and recognize DNA DSBs the cells were irradiated in a cross pattern with 1 and 2 α-particles (He$^+$) per pixel, respectively. The corresponding dose per cell nucleus was approximately 100/200 mGy. The cells showed a significant DNA DSB response signal (Fig. 2). The irradiation pattern was recognized in some cell nuclei showing a cross of DNA DSB-foci in the nucleus. However, several pixels of the cross were fusing together and therefore hardly visible as well-defined dots. The signal did not get brighter when using 2 α-particles per pixel.

For the proton irradiation at 21 °C a line pattern was used. Already with 5 protons/pixel (~1.5 Gy/cell nucleus) the quadratic irradiation area was reflected by DSB foci. With increasing number of protons per pixel the number of foci increased. However, for all proton numbers the irradiation pattern (lines) was not clearly recognizable. It seems that the DSB foci appear in the vicinity of the proton hits. Only in a few cells the patterned lines were barely visible.

In order to reduce delocalisation effects of the foci the cells and the dish holder were cooled on ice before the irradiation [3,12–14]. The irradiation at low temperatures was carried out with the cross pattern. The cooled cells showed much less diffuse proton hit response with more local DSB inductions (Fig. 3). Even in the case where single foci were hardly visible, the irradiation cross was clearly recognizable in many cells.

3.2. Heat shock protein 70

Control and sham irradiated cells showed a homogenous weak expression of Hsp70. The Hsp70 expression of heat-shocked cells was generally increased, whereby the expression in the cell nucleus was notable, contrary to the results obtained by proton irradiation. The proton irradiation leads to a stronger signal of Hsp70 in the cytoplasm than in the nucleus. After an irradiation of 10 protons/pixel (line pattern) bright Hsp70 aggregates were observed in the cytoplasm (Fig. 4). The intensity and the number of these point like protein aggregates tended to be increased with
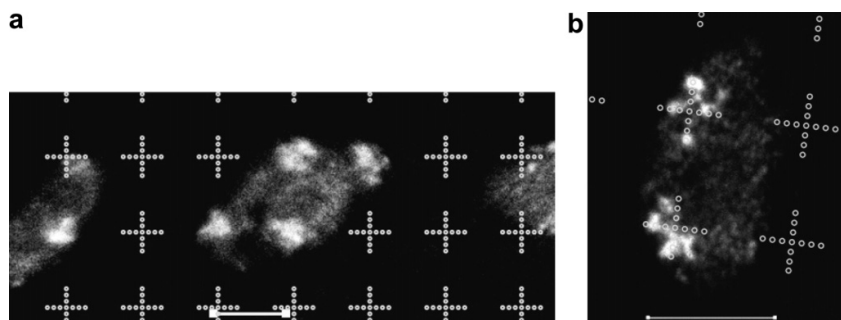

Fig. 3. Induction of DNA DSBs by proton irradiation in cross patterns at low temperatures. The crosses (7 × 7 pixel, 1 μm distance, 5 μm intercross distance) are blurred, but still recognizable. 10 protons/pixel. DSBs stained by γH2AX antibody. Scale bar: 12 μm.
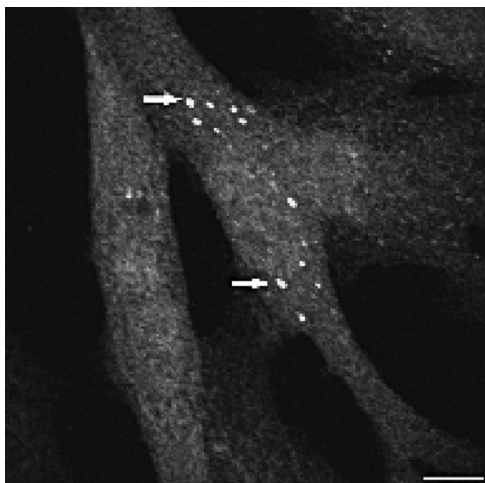
Fig. 4. Cytoplasmic Hsp70 aggregates 1.5 h after irradiation with 10 protons/pixel in a line pattern. The irradiated area is not reflected in the cells. Arrows show examples of Hsp70 aggregates. Scale bar: 10 μm.

increasing number of protons per pixel. However, the irradiated area could not be recognized, all cells on the Si_3N_4 window showed a homogenous expression pattern.

4. Discussion

4.1. DNA double strand breaks

The irradiation with 2 MeV α-particles induces relatively localized DNA DSBs in the cells. On the contrary, the proton induced DSBs appear more delocalised than it was expected by the ion hit accuracy. This is certainly a consequence of the higher LET than for protons. Possibly, due to the less dense ionising processes of the proton irradiation the DSBs are induced predominantly by indirect, secondary effects. This assumption is based on the observation that cooling reduces the delocalisation of DNA DSBs which is probably caused by the reduced diffusion of DNA damaging agents.

4.2. Heat shock protein 70

The localisation of Hsp70 after heat shock pre-dominantly in the cell nucleus assumes that Hsp70 mainly induces gene expressions to avert damages caused by heat and even participates in DNA repair. Proton irradiation, contrary to the heat shock, seems to provoke protein damages mainly in the cytoplasm indicated by the cytoplasmic Hsp70 aggregates. Perhaps these directly or indirectly induced protein damages are more pronounced than damages in the cell nucleus where no increased Hsp70 activity was observed. The different expression patterns after heat shock and proton irradiation lead to the assumption that

the Hsp70 pathways depend on the type of the stressor and its damages.

Additional note We also assayed the expression of the transmembrane receptor *integrin-β_1* and the pro-inflammatory cytokine *interleukin-1α* 26 h/6 h after proton irradiation. X-rays and γ-rays are reported to increase the expression of integrin and interleukin, though the effect of proton irradiation is largely unknown [15–21]. The detection has been carried out by immunocytochemical staining and was analysed by laser scanning microscopy afterwards. We could not observe a significant change in expression of integrin-β_1 and interleukin-1α. Thus, we do not discuss these endpoints here any further.

5. Conclusion

5.1. DNA double strand breaks

A single proton of 2.25 MeV is not sufficient to surely induce a detectable γH2AX focus in human primary fibroblasts. Anyhow, several protons (e.g. 5 protons/pixel) can induce foci. The number and intensity of the foci increases with increasing number of protons. However, for our proton irradiation measurements an induction of approximately 0.8 DSBs/proton [22] seems overestimated. By cooling the cells on ice directly before irradiation, the delocalisation of the γH2AX foci can be reduced. Therefore, cell cooling for DSB based proton hit verification is mandatory.

5.2. Heat shock protein 70

A proton irradiation with at least 10 protons/pixel increases the Hsp70 expression in the cytoplasm and is represented by point like Hsp70 aggregates. This is contrary to the expression pattern of Hsp70 after heat shock, where Hsp70 is upregulated mainly in the cell nucleus and no cytoplasmic aggregates are found. Because the expression pattern was homogenous on the whole Si_3N_4 window and not only in the cells located in the irradiated area, this might probably remind of a bystander effect and remains to be investigated in more detail.

References

[1] E.P. Rogakou, D.R. Pilch, A.H. Orr, V.S. Ivanova, W.M. Bonner, J. Biol. Chem. 273 (10) (1998) 5858.

[2] B. Jakob, M. Scholz, G. Taucher-Scholz, Radiat. Res. 159 (5) (2003) 676.

[3] L. Tartier, C. Spenlehauer, K.M. Prise, B.D. Michael, J.M. de Murcia, G. de Murcia, Mutagenesis 18 (5) (2003) 1.

[4] E. Sierra-Rivera, M.L. Voorhee, G.J. Freeman, Radiat. Res. 135 (1) (1993) 40.

[5] H.S. Melkonyan, T.E. Ushakova, S.R. Umansky, Int. J. Radiat. Biol. 68 (3) (1995) 277.

[6] S. Sadekova, S. Lehnert, T.Y. Chow, Int. J. Radiat. Biol. 72 (6) (1997) 653.

[7] C.M. Kang, K.P. Park, C.K. Cho, J.S. Seo, W.Y. Park, S.J. Le, Y.S. Lee, Radiat. Res. 157 (6) (2002) 650.

[8] S.H. Park, S.J. Lee, H.Y. Chung, T.H. Kim, C.K. Cho, S.Y. Yoo, Y.S. Lee, Radiat. Res. 153 (2000) 318.

[9] S.J. Lee, S.A. Choi, K.H. Lee, H.Y. Chung, T.H. Kim, C.K. Cho, Y.S. Lee, Cell Stress Chaperon. 6 (2001) 273.

[10] T. Reinert, A. Fiedler, J. Skopek, J. Tanner, J. Vogt, T. Butz, Nucl. Instr. and Meth. B 219–220 (2004) 77.

[11] A. Fiedler, J. Škopek, T. Reinert, J. Tanner, J. Vogt, J. Österreicher, L. Navratil, T. Butz, Radiat. Res. 161 (2004) 95.

[12] K. Elmrozh, J. Nygren, B. Stenerlow, R. Hultborn, Int. J. Radiat. Biol. 79 (10) (2003) 809.

[13] G. Taucher-Scholz, B. Jakob, G. Becker, M. Scholz, Nucl. Instr. and Meth. B 209 (2003) 270.

[14] K.H. Karlsson, B. Stenerlöw, Radiat. Res. 161 (2004) 517.

[15] J. Österreicher, J. Škopek, J. Jahns, G. Hildebrandt, Z. Vilasova, J.M. Tanner, J. Vogt, T. Butz, Acta Histochem. 105 (3) (2003) 223.

[16] S. Konemann, T. Bolling, J. Malath, A. Kolkmeyer, K. Janke, D. Riesenbeck, S. Hesselmann, R. Diallo, J. Vormoor, N. Willich, A. Schuck, Int. J. Radiat. Biol. 79 (11) (2003) 897.

[17] S. Boisnic, M.C. Branchet-Gumila, D. Nizri, L. Ben Slama, Int. J. Tissue React. 25 (1) (2003) 9.

[18] J.H. Hong, C.S. Chiang, C.Y. Tsao, P.Y. Lin, W.H. McBride, C.J. Wu, Int. J. Radiat. Biol. 75 (11) (1999) 1421.

[19] M. Chang, C.A. Limanni, W.H. Baker, M.E. Dobson, J.F. Kalinich, M.L. Patchen, J. Interf. Cytok. Res. 17 (9) (1997) 567.

[20] N. Cordes, V. Meineke, J. Mol. Histol. 35 (3) (2004) 327.

[21] V. Meineke, K.P. Gilbertz, K. Schilperoort, N. Cordes, T. Moede, D. van Beuningen, Strahlenther Onkol. 178 (12) (2002) 709.

[22] G. Dollinger, V. Hable, A. Hauptner, R. Krücken, P. Reichart, A.A. Friedl, G. Drexler, T. Cremer, S. Dietzel, Nucl. Instr. and Meth. B 231 (2005) 195.

The new target chamber at LIPSION: The new translation stage and goniometer and the new irradiation platform for single cell experiments

Charlotta Nilsson *, Silvio Petriconi, Tilo Reinert, Tilman Butz

Institute for Experimental Physics II, University of Leipzig, Linnéstrsse 5, 04103 Leipzig, Germany

Available online 14 February 2007

Abstract

A new target chamber as well as a new 7-axes translation stage with goniometer will shortly be implemented at the LIPSION nanoprobe in Leipzig. This new stage should enable linear motion as well as rotary motion with high precision, positioning accuracy and repeatability. These different features have been investigated online as well as offline, with encouraging results. Along with the new equipment, new software is also being developed, to provide stage control running over network. These software developments, including a graphical user interface, will also be described. As part of the new target chamber, a new external beam facility and irradiation platform for single ion experiments on single living cells is being assembled. A detailed description of the new cell irradiation platform, including beam extraction, new cell dishes, and cell recognition aspects will be given. It will be shown that the possibility of offline cell recognition, possibly using a differential interference contrast microscope, is an option.
© 2007 Elsevier B.V. All rights reserved.

PACS: 07.05.−Dz; 07.10.Cm; 07.30.Kf; 41.75.Ak; 87.50.−a; 87.64.−t

Keywords: Translation stage; Goniometer; Cell irradiation; Single cell; Single ion

1. Introduction

In order to increase the versatility and accessibility of the LIPSION nanoprobe, a major rebuild of the target chamber is currently being carried out. The old target chamber, a system of cylinders and flanges, will be replaced by a new target chamber (Fig. 1(a)). It has the shape of a box with a removable top with the dimensions 450 mm * 300 mm * 480 mm, and is equipped with a new translation stage. The implementation of the new chamber is planned for the second half of 2006.

One research field at LIPSION is irradiation of living cells using a micro- or nanoprobe which has been a topic of interest in radiation biology for some time since this enables targeting a selected cell with a predefined radiation dose, thereby excluding uncertainty factors due to Poisson statistics that are present in broad beam experiments. Further advantages with this method are e.g. that sub-cellular targets can be selected and that the reactions of non-hit cells neighbouring irradiated cells can be investigated. A number of facilities around the world – mostly in Europe, the US and Japan [1–4] – are working in this field, thus utilizing their existing microprobes for new purposes. At the LIPSION nanoprobe laboratory, single ion irradiation experiments on single, living cells have been carried out since 2003 [5,6]. Currently, a new platform for irradiation of single, living cells is being assembled.

2. The LIPSION laboratory

At LIPSION, the single-ended 3.5 MV Singletron™ accelerator (High Voltage Engineering Europe) together

---

* Corresponding author. Tel.: +49 341 9732702; fax: +49 341 9732708.
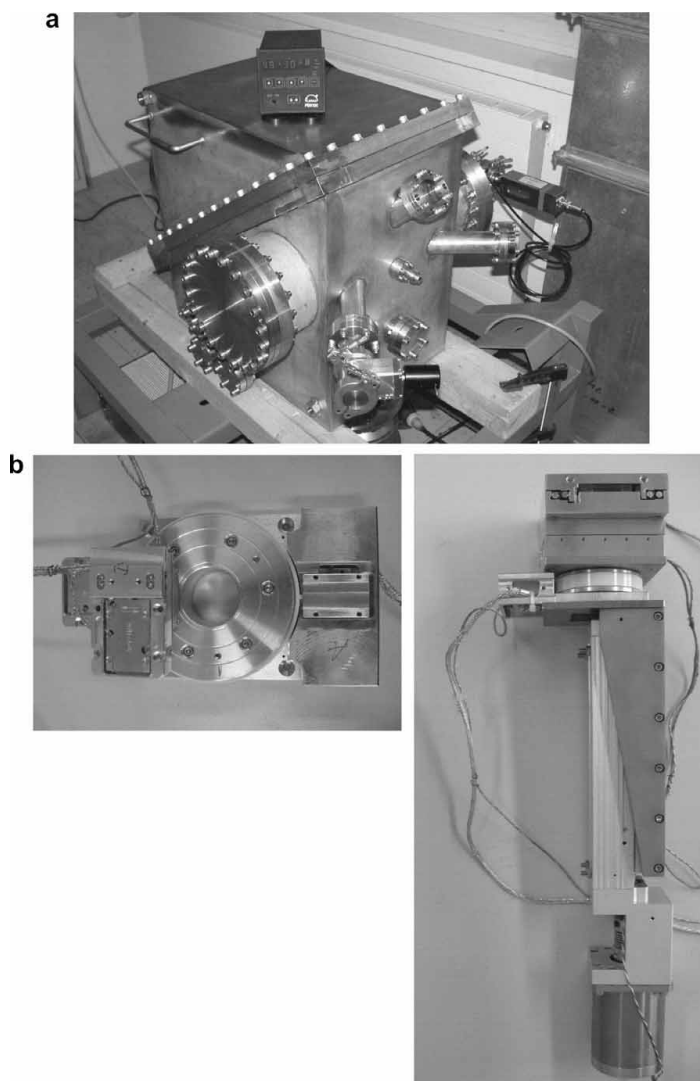 *E-mail addresses:* nilsson@physik.uni-leipzig.de, charlotta.nilsson@pixe.lth.se (C. Nilsson).

Fig. 1. (a) The new target chamber at LIPSION. (b) The 7-axis translation stage with goniometer.

with the horizontal nuclear microprobe (MARC, Melbourne) delivers protons or alpha particles with energies up to 3 MeV. The smallest beam spot size that has been attained so far was about 40 nm in the low current mode [7], and in STIM mode a beam spot size of about 100 nm can be achieved on a regular basis [8].

The ion beam at LIPSION is focused, as opposed to collimated, and this is favourable when irradiating living cells, as the beam can be scanned while keeping the cell dish fixed. Most of the work carried out so far in the area of cell irradiation has been experiments where 2.25 MeV protons have been used, but on a few occasions 2 MeV alpha par-

ticles have been utilized. The beam spot size in the low current mode is around 350 nm for the beam extracted to the ambient air.

3. New translation stage and goniometer

Thus far, a 3-axes (x, y and z-directions) linear translation stage from Physik Instrumente has been used for sample manipulation. This translation stage was not suited for vacuum applications, and as a consequence, it had to be kept at air pressure outside the target chamber. The motion

was transmitted into vacuum to the sample holder through a system of bellows.

The new 7-axes translation stage with goniometer (Fig. 1(b)) from Feinmess Dresden is movable in x, y and z-directions as well as in θ, x', y' and φ-directions. The translation part consists of 2 piezo motors, controlling the horizontal motion and the motion in the axial (beam) direction, and 1 stepping motor, controlling the vertical motion. The rotation part consists of 4 piezo motors that control rotation in two axes, as well as additional horizontal and vertical motion.

4. Experimental tests

Several experiments, using the proton beam at the LIPSION nanoprobe, have been carried out to investigate the accuracy and repeatability of the linear part of the translation stage. As targets for these measurements, a 200 mesh (i.e. 125 μm/mesh) TEM copper grid with printed letters and numbers was mounted on a sample holder on the stage, along with a 2000 mesh (i.e. 12.5 μm/mesh) copper grid without any numbers or letters.

4.1. Resolution

The two piezos controlling the x- and z-motion both have a stated resolution of 10 000 counts/mm, i.e. 10 counts/μm, meaning that shifting the position of either of these axes by a single step should correspond to a displacement of a mere 100 nm. The stated positioning accuracy, i.e. the difference between the desired position and the actually reached position, is 1 μm for both piezos. The x-axis piezo has a travel of 50 mm (i.e. ±25 mm) and the z-axis piezo has a travel of 25 mm (i.e. ±12.5 mm).

The resolution, as well as the positioning accuracy, has been investigated at the LIPSION nanoprobe and the

results are shown in Fig. 2. What is shown is consecutive, stepwise motion, where the axis has been moved one single step upwards, after which an image of the 2000 mesh copper grid was made and a vertical traverse was selected. In Fig. 2, the dotted line shows the start position, the dashed line the position after one step and the solid line the position after two steps. It is evident that a single step corresponds to more than the stated 0.1 μm – the relationship is close to 0.5 μm. For motions consisting of a greater number of counts, however, the relationship 1 count = 0.1 μm is true – that is, moving an axis 5000 counts does correspond to a displacement of 0.5 mm. Apparently, there is a threshold, at around 5 counts, below which the axis still moves 0.5 μm, regardless of the number of counts entered into the software. This means that the minimum step size in practice is 0.5 μm. During all experiments, the positioning accuracy was determined to be less than ±1 count.
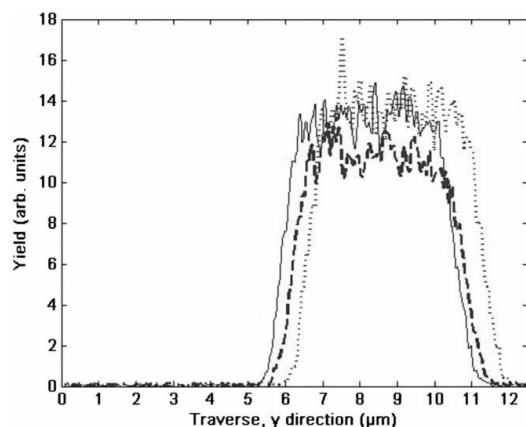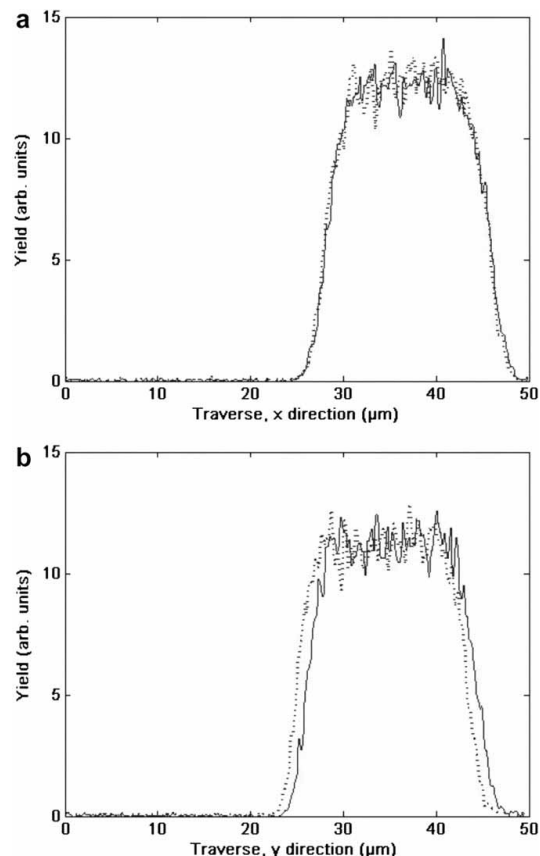

Fig. 3. Sample position steadiness test in horizontal (a) and vertical (b) directions. Dotted line shows $t = t_0$ and dashed line shows $t = t_0 + 60$ min.

Fig. 2. Resolution test with start position (dotted line) and two consecutive steps (dashed and solid lines).

4.2. Stability over time

The actual lateral resolution in an experiment will deteriorate if the stage is not stable enough, but instead makes the sample drift during longer lasting irradiations. The long term position stability of the sample has been proven to be less than 1 μm for the Physik Instrumente stage. The images in Fig. 3 show the steadiness of the sample position during an experiment lasting one hour. The position of the sample on the stage was fixed over a time span of one hour, and every 15 min a new image of the 2000 mesh copper grid was made, in order to see whether the sample position had changed or not.

Fig. 3(a) shows a horizontal traverse and Fig. 3(b) a vertical traverse. In both figures, the dotted line indicates the position of the copper grid at the beginning of the measurement and the solid line the position after 1 h. As can be seen in the figure, only a slight shift in the vertical position of the grid can be seen over this period of time. According to the Galil Motion Control software [9], the difference in position between the beginning and the end of the measurement was one count.

4.3. Repeatability

The stated repeatability of the *x*- and *z*-motion piezos is 0.3 μm, and this feature has been investigated at the nanoprobe, too. A particular position on the copper grid sample was repeatedly revisited, after travelling shorter (0.5 mm) as well as longer (>20 mm) distances, and every time a new image of the grid was made. These revisits of the sample position can be seen in Fig. 4.

The left image of Fig. 4 shows a 50 μm × 50 μm image of the numbered 200 mesh copper grid. The image in the middle was taken after the grid had been moved a vertical distance of 5000 counts and back to the start position. The image to the right was taken after the grid had been moved again, a vertical distance of 220 000 counts back and forth. Here, it is evident that, when revisiting a position on a sample, the error in the vertical axis is insignificant. A small error, on the order of 1 μm, in the horizontal axis can be seen after the stage had travelled practically to its end stop

and back. According to the Galil Motion Control software, there was no difference in the vertical position before and after the movement, however the horizontal position had drifted by 2 counts. If this drifting remains after the new target chamber and the stage have been implemented, it will be corrected for as part of the software developments.

The stepping motor controlled axis, controlling the *y*-motion, has a screw pitch of 4 mm/turn and a stated repeatability of 1 μm. Initial tests, carried out outside of the nanoprobe, indicated that for the stepping motor controlled axis a positioning accuracy and repeatability of about 1 μm can be achieved.

5. Software developments

During these initial experiments, the stage has been computer controlled via handshake using software from Galil Motion Control, that was delivered together with the stage. In the future, however, the control of the new translation stage will, like the beam control, run over network, using software that has been developed at our division. This new software incorporates the Galil commands into a code that has been written using C++ and Qt, a C++ class library and application framework. TCP type sockets have been programmed to administer the communication between the user interface and the stage controller unit. Qt was chosen as it is a relatively user-friendly way of managing this socket communication as well as providing a user-friendly graphical user interface for the stage control.

6. Cell irradiation setup

Due to the horizontal orientation of the LIPSION beam line, a vertical cell dish arrangement is required, and such an arrangement has been successfully implemented and tested at the facility [5,6]. The new cell irradiation platform will be built up around the new translation stage, and to ensure maximum flexibility it will consist of several separate components. Integral components are 1) the cell dish holder, 2) the holder for the particle detector, a retractable Hamamatsu p-i-n diode which is placed after the cell dish, and a holder for the microscope objectives and 3) the
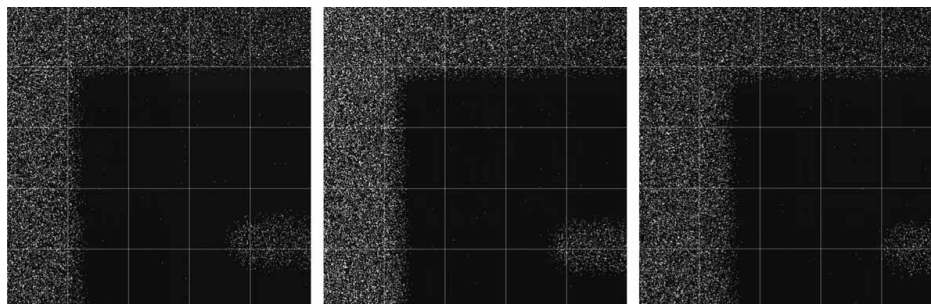

Fig. 4. Repeatability test – images showing (from left to right) start position, revisit after 0.5 mm travel and revisit after 22 mm travel.
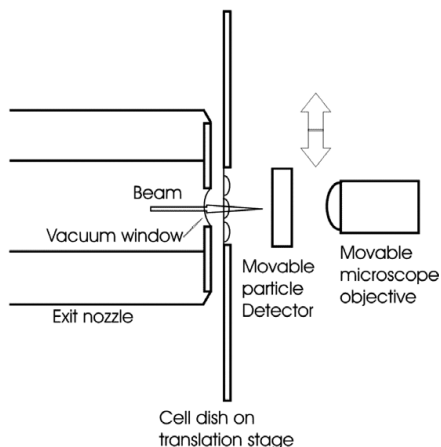
Fig. 5. Schematic of the cell irradiation platform.

holder for the microscope eyepiece and/or the CCD camera. In Fig. 5 a sketch of the set up is shown.

7. External beam

At the LIPSION facility, the extraction of the beam into air is realized by attaching an exit nozzle to the beam entrance in the target chamber wall (Fig. 6). The nozzle is attached to a flange, onto which the RBS detector is mounted otherwise. The end piece of the nozzle is exchangeable and can be adapted for special needs. For cell experiments, an end piece made of stainless steel will be used. Where the beam exits the nozzle a 100 nm thick Si_3N_4 vacuum window, with an area of $1 \times 1 \text{ mm}^2$, is glued, a solution that has proven to withstand the pressure difference well.

8. Cell dish holder and cell dishes

The prototype for the new cell dish holder is made of stainless steel and has a slot where the cell dish is inserted. The holder is attached to the sample stage, after which some fine-tuning of the stage's z-position (i.e. in the direction of the beam) will ensure that the cell dish is in the right

Fig. 6. The exit nozzle mounted at the beam entrance in the chamber.

place for irradiation, with the irradiation window as close to the vacuum window as possible.

A prototype for a new variant of cell dishes is currently being tried out. These are custom-made, consisting of a rectangular outer frame, $2 \times 2.5 \text{ cm}^2$, made of 1 mm thick acrylic glass, with a circular hole (5.5 mm in diameter) where the irradiation window is glued. So far, $2 \times 2 \text{ mm}^2$ Si_3N_4 frames, 200 nm thick, have served as the entrance window of the cell dish as this material best fulfils the requirements of being both thin and flat. An alternative would be Mylar, with a thickness of 0.9 μm. SRIM simulations [10] of the two alternatives show that, with respect to beam spreading as well as energy loss, although Si_3N_4 is superior to Mylar, the difference is negligible. The irradiation windows have so far been glued to the bottom of the cell dishes using common stearin, a substance which has proven not to influence the cell growth negatively. What could be an alternative is medical glue – something which is being used by some other groups [11].

9. Cell recognition

Cell recognition software will also be developed at our division using C++ together with the commercially available software package ImagePro Plus. The use of cell recognition
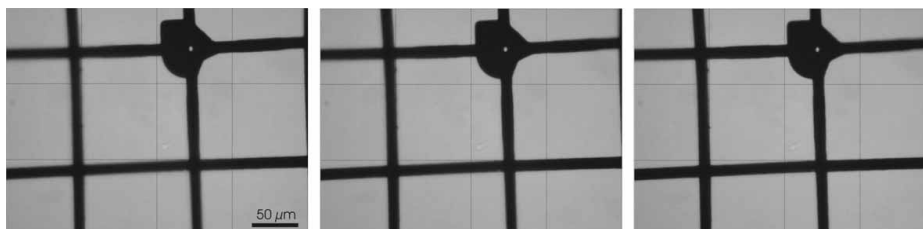

Fig. 7. Repositioning accuracy test – images showing (from left to right) start position and the acrylic glass frame after being repositioned into the cell dish holder twice.

software will render automated and/or semi-automated truly targeted cell irradiation possible, as opposed to the pre-determined patterns that have been used so far. The combination with a downstream microscope enables online cell recognition – another possibility is to utilize fiducial markers on the cell dish itself, thereby recognizing the cells offline. At the LIPSION facility, such fiducial markers could be fabricated using proton beam writing. An advantage of offline cell recognition at LIPSION is that there is a possibility of recognizing unstained cells, using an offline differential interference contrast microscope.

However, for offline recognition to function properly, accurate positioning of the cell dish in the holder is required if the coordinates delivered from the software are to agree with the situation during the irradiation. Fig. 7 shows images where the reproducibility of positioning when inserting the cell dish in the holder has been investigated. The cell dish with a numbered 200 mesh copper grid was placed in the holder three times and after each installation a photo was taken. From these images it can be seen that the cell dish can be repositioned with an accuracy of about ± 1 μm with the present holder.

10. Conclusion

A new target chamber, with a new 7-axis translation stage and goniometer, will shortly be operational at the LIPSION nanoprobe. The preparatory experiments presented here show that, using this new stage, the accuracy and repeatability of sample positioning meets the requirements at LIPSION very well, which ensures improved future experimental conditions.

Acknowledgement

References

[1] M. Heiss, B.E. Fischer, B. Jakob, C. Fournier, G. Becker, G. Taucher-Scholz, Targeted irradiation of Mammalian cells using a heavy-ion microprobe, Radiat. Res. 165 (2006) 231.

[2] M. Folkard, K. Prise, G. Schettino, C. Shao, S. Gilchrist, B. Vojnovic, New insights into the cellular response to radiation using microbeams, Nucl. Instr. and Meth. B 231 (2005) 189.

[3] A. Bigelow, G. Ross, G. Randers-Pehrson, D.J. Brenner, The Columbia University Microbeam II endstation for cell imaging and irradiation, Nucl. Instr. and Meth. B 231 (2005) 202.

[4] Y. Kobayashi, T. Funayama, S. Wada, M. Taguchi, H. Watanabe, Irradiation of single mammalian cells with a precise number of energetic heavy ions – Applications of microbeams for studying cellular radiation response, Nucl. Instr. and Meth. B 210 (2003) 308.

[5] T. Reinert, A. Fiedler, J. Škopek, J. Tanner, J. Vogt, T. Butz, Single ion bombardment of living cells at LIPSION, Nucl. Instr. and Meth. B 219–220 (2004) 77.

[6] A. Fiedler, J. Škopek, T. Reinert, J. Tanner, J. Vogt, J. Österreicher, L. Navratil, T. Butz, First irradiation experiments of living cells at LIPSION, Radiat. Res. 161 (2004) 95.

[7] D. Spemann, T. Reinert, J. Vogt, D. Dobrev, T. Butz, Suitable test structures for submicron ion beam analysis, Nucl. Instr. and Meth. B 190 (2002) 312.

[8] D. Spemann, T. Reinert, J. Vogt, J. Wasserman, T. Butz, Active compensation of stray magnetic fields at LIPSION, Nucl. Instr. and Meth. B 210 (2003) 79.

[9] Galil Motion Control, URL: <http://www.galilmc.com/>.

[10] J.F. Ziegler, SRIM 2003, Version-2003-20, URL: <http://www.srim.org>.

[11] W. Polak, O. Veselov, J. Lekki, Z. Stachura, M. Zazula, R. Ugenskiene, M. Polak, J. Styczen, Irradiating single cells using Cracow microprobe facility, Nucl. Instr. and Meth. B 249 (2006) 743.

Scanning transmission ion microscopy tomography at the Leipzig nanoprobe LIPSION

T. Reinert [a,*], A. Sakellariou [b], M. Schwertner [a], J. Vogt [a], T. Butz [a]

[a] *Fakultät für Physik und Geowissenschaften, Nukleare Festkörperphysik, Universität Leipzig, Linnéstr. 5, D-04103 Leipzig, Germany*
[b] *Former at the Microanalytical Research Center, School of Physics, The University of Melbourne, Melbourne 3010, Victoria, Australia*

Abstract

Scanning transmission ion microscopy (STIM) of joint cartilage could visualise single collagen fibrils. Thus, answers to the controversial questions of their alignment could be given. However, the fibrils form three-dimensional structures that are not yet fully disclosed. STIM tomography is needed to give more detailed information. The size of the structures requires a challenging resolution of about 100 nm. The first STIM tomographic experiment has been performed at the Leipzig nanoprobe LIPSION. 360 projections of a cartilage sample (30 μm $\times$ 32 μm $\times$ 10 μm) were taken. The pixel resolution was 250 $\times$ 250 pixels for each projection. The data set was reconstructed at MARC Melbourne using the backprojection of filtered projections technique. The data show the feasibility of STIM tomography in cartilage research. However, experimental inaccuracies (rotational displacement and magnetic stray fields) have limited the resolution thus far. Improvements in the experimental set-up will lead to higher resolution. © 2002 Elsevier Science B.V. All rights reserved.

PACS: 07.78.+s; 41.75.Ak; 42.30.Wb; 87.16.Ka
Keywords: Ion microbeam; Scanning transmission ion microscopy; Tomography; Subcellular; Cartilage; Collagen

1. Introduction

High resolution scanning transmission ion microscopy (STIM) is a powerful tool to visualize internal structures of biological tissue with a resolution down to 100 nm [1]. The main advantage of ion microscopy is the capability of the high energy ions to penetrate the relatively thick samples ($\sim$10 μm) without significant beam spreading. Thus, we could investigate with STIM the collagen network in articular cartilage [2]. Articular cartilage consists of a collagen fibrous network filled with highly hydrated macromolecules (proteoglycans) and embedded cells (chondrocytes). The collagen fibres and the proteoglycans have different densities due to their different structures. The tightly packed collagen fibres have a higher density than the bottlebrush-like proteoglycans [3]. Thus, they can be distinguished by STIM due to the different energy loss of the ions. This is the reason why complicated preparation methods (chemical fixation, substitution and embedding) can be avoided, contrary to electron microscopy.

* Corresponding author. Tel.: +49-341-97-32706; fax: +49-341-97-32497.
E-mail address: reinert@physik.uni-leipzig.de (T. Reinert).
URL: http://www.uni-leipzig.de/~nfp.

It is known, that ultrastructural electron microscopy studies often suffer from artefacts caused by the preparation techniques [4]. This is one of the main reasons, why certain network structures are not yet fully discovered, especially the topic of fibre orientation in the midzone of the cartilage is controversial. We found radially aligned fibres in the proliferating zone (the middle zone) of the tibial cartilage [2], whereas a leaf-like network with randomly oriented fibrils was reported by Goodwin et al. [5]. In the proliferating zone of the femoral cartilage we found the suspected tangentially oriented collagen structures. However, the fibrils seemed to form tubular structures. This is a relatively new idea about the network architecture and reported only once [6]. Tubular structures are difficult to resolve in 2D images. Thus, the investigation of the three-dimensional arrangement with STIM-tomography (STIM-T) [7] becomes necessary for a further proof of the tubular structure.

2. Materials and methods

2.1. Sample preparation

The cylindrically shaped samples were taken from the medial tibial articular cartilage plateau of pig's knee. The samples were shock frozen in liquid nitrogen for cryosectioning. The cartilage cylinders were cut into radial cross-sections at a temperature of $-25°$. Cross-sections with thicknesses of 10–30 μm were prepared. Afterwards, the cryosections were freeze dried for 24 h. In order to find a region with clearly visible collagen fibres the cartilage slices were investigated using two-dimensional STIM.

For the first STIM-T experiment we have chosen to prepare a sample out of the proliferative zone, where separated radially aligned collagen fibres predominate. The procedure was to cut the freeze dried cryosection in radial direction with a scalpel into small strips. One of the small strips (10 μm × 30 μm × 500 μm) was glued with carbon glue onto a needle tip, which was fixed on a goniometer for the axial alignment of the cartilage sample in the rotating axis of the chamber.

2.2. Experimental procedure

A 3D-STIM-tomography experiment consists of recording a number of 2D-STIM images of the sample, called projections, under different incident angles from 0–180° degree (the third dimension). The number N of projections which is needed to completely probe the sample in a circular, cross-sectional area with diameter $2r$ (equal to the scan width) is given by the formula $N = (\pi/2)A$, where A is the scan width in pixels of size s (Fig. 1). From these projections the 3D density distribution can be reconstructed.

The STIM-T experiment of the cartilage sample was performed at the Leipzig Nanoprobe LIPSION [8,9]. For the analysis the sample was scanned over an area of 32 μm × 32 μm with a resolution of 250 × 250 pixels. This gives a step width (pixel size) of 128 nm. The scan width of 250 pixels requires 393 projections. For practical reasons we used 360 projections from 0° to 180° with a step width of 0.5°. The resulting probed area is 29 μm in diameter, where the sample essentially fits in.

We used a 2 MeV proton beam focused to a spot size of less than 100 nm (10 μm circular object and aperture diaphragms) [10]. The beam current was kept below 10,000 protons s^{-1} using the microslits behind the object diaphragm. The energies of the transmitted protons were analyzed using a
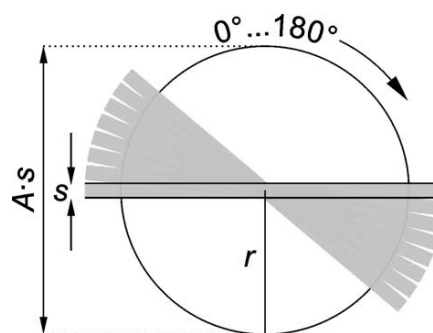

Fig. 1. Schematic presentation of the probed area (grey) during N numbers of projections (rotation from 0° to 180°). The scan width is given by the number A of steps with width s. One needs $N = (\pi/2)A$ projections to completely probe a circular area of radius r.

PIPS detector (Canberra, PD-50-11-300-RM) positioned 40 mm behind the sample at 0°, i.e. on axis geometry. The energy resolution was 9 keV for the 2 MeV protons. The projections were recorded by horizontally scanning the beam over the sample from top to bottom. The beam dwelled at each sample point (pixel) until five protons were collected before moving onto the next point. The detector was slightly displaced every three to four projections to prevent changes in energy-channel-calibration due to detector damage. The recording time of one projection was less than 1 min. The rotation was performed by a computer controlled high precision step motor. The total recording time of the 360 projections was 8 h.

2.3. Three-dimensional reconstruction

The data set was reconstructed at the Micro-analytical Research Centre (MARC) Melbourne using the backprojection of filtered projections (BFP) technique. The reconstruction is of the energy loss data. No composition information has been used, it has not been corrected for stopping power and there has been no pixel averaging. The only information that can be extracted from the reconstruction are qualitative values showing the contrast of morphology within the sample.

3. Results and discussion

3.1. 2D analysis

The first step for STIM-T was to record a stereoscopic image of radially aligned collagen fibrils of the tibial proliferative zone (Fig. 2). The two images were recorded with an angular offset of 6.5°. The scan width was 40 μm × 40 μm with a sample thickness of 30 μm. Thus an overview of the cartilage structure in a relatively large cubic volume was obtained.

The 3D arrangement of the chondrocytes within the cartilage matrix is clearly visible. However, to see the arrangement of the collagen fibres is more challenging. The reason is a beam position instability during the STIM measurements due to magnetic stray fields in the laboratory ($\Delta B \approx 1$ μT). The fluctuation in the position of the beam was determined to be ± 150 nm using the test sample for submicron ion-beam analysis [11].

3.2. 3D analysis

Despite these experimental troubles we performed the 360 projections for the STIM-T experiment. Fig. 3 shows a set of projections giving an overview of the sample (30 μm × 32 μm × 10 μm). The main feature is an isogonic pair of chondro-
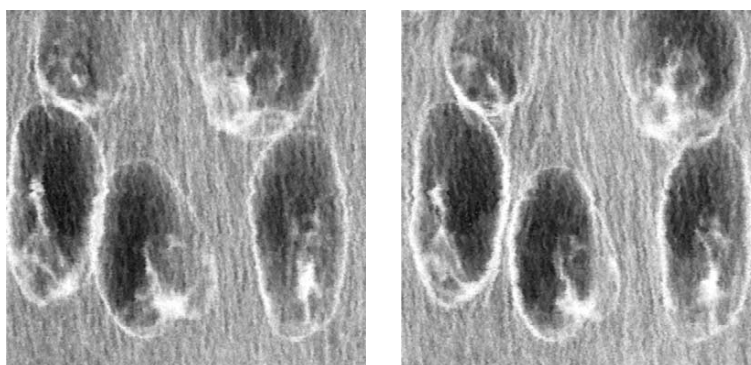
Fig. 2. Stereoscopic representation (grey scale energy loss STIM-images, median transmitted energy, range: 1826 keV (black)–1949 keV (white)) of radially aligned collagen fibres (bright strings) surrounding five cartilage cells (chondrocytes). The proteoglycans are represented by the grey shadow between the fibres. The stereoscopic image gives an overview of the internal cartilage structure in a volume of 40 μm × 40 μm × 30 μm in size. Look at the stereoscopic image in parallel view, the left eye looks at the left image, the right eye at the right image.

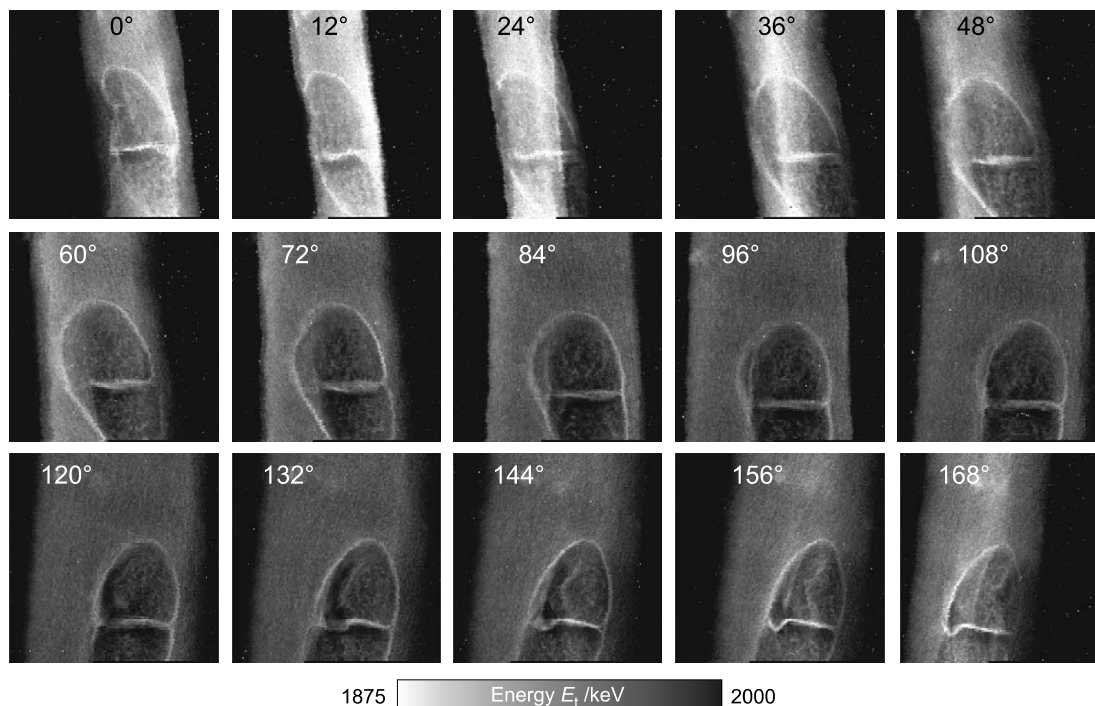Fig. 3. Set of projections (32 μm × 32 μm) showing the cartilage sample from different angles. Brighter parts within one projection refer to higher energy loss, i.e. higher density. The intracellular structures are clearly visible. In the projection at 84° to 120° the radially aligned fibres become just visible. There is a sample shift from 0° to 180° of 4 μm downwards.

cytes. Inside the chondrocytes intracellular structures are visible (probably mitochondria). The projection at 12° shows the sample from the smaller (10 μm) side. In the projection at 84–120° the radially aligned fibres are just visible. During the rotation, the sample shifted downwards by 4 μm. This caused problems during the reconstruction but was corrected to some extent.

Fig. 4 presents the reconstructed 3D qualitative density distribution and four tomograms of different planes through the sample [12]. The large image in the middle represents a superposition of two rendered densities: the overall grey represents a medium density and the denser parts (on the left edge of the sample) appear in dark grey. The low density is not presented for the sake of clarity. In this image the planes are indicated from which the four tomograms were extracted. The planes 1, 3 and 4 show the cells with the internal structures.

These structures, already known from the higher resolution images of the projections (Fig. 3), represent probably mitochondria. Mitochondria are cell organelles with a high phosphorus content, and may be a worthy goal for a PIXE-tomographic attempt [13,14].

Plane 2 was extracted from the cell free region, where the collagen fibres were cut transversally. In this matrix region above the cells, density variations appear. Due to the experimental inaccuracy it is not likely, that these variations show single collagen fibres. However, they reveal that density variations due to internal cartilage matrix structure can be visualized with high resolution. Due to the relatively low energy loss the beam spatial broadening is less than 100 nm. This shows that the limitations in resolution were mainly based on experimental inaccuracies (rotational displacement and magnetic stray fields).
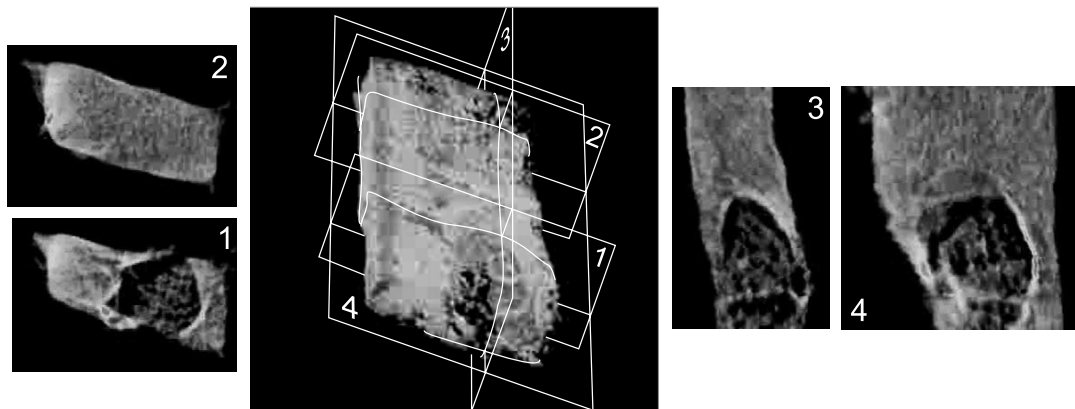
Fig. 4. Middle: Rendering of the reconstructed 3D density distribution of the cartilage sample (30 μm × 32 μm × 10 μm), see text for details. Left: horizontal planes, as indicated in the middle figure, above and through a chondrocyte. Right: vertical planes, as indicated in the middle figure. The images are black and white copies of colour originals from Ref. [12] showing the contrast of morphology.

4. Conclusions

The 3D qualitative density distribution of a cartilage sample, i.e. a complicated biological system, was obtained using STIM-tomography. The results show that the 3D visualization of the collagenous network is possible. Thus, the full structural information on tubular structures in cartilage can be obtained, but requires microprobes with excellent performance in terms of lateral resolution and stability. Therefore, we plan to install an active compensation of magnetic stray fields in order to get image resolutions comparable to the beam spot size of less than 50 nm [10]. Furthermore, we are engaged in the development of software for image reconstruction and 3D visualization.

Acknowledgements

References

[1] G.S. Bench, G.J.F. Legge, Nucl. Instr. and Meth. Phys. Res. B 68 (1989) 655.

[2] T. Reinert, U. Reibetanz, J. Vogt, T. Butz, A. Werner, W. Gründer, Nucl. Instr. and Meth. Phys. Res. B 181 (2001) 511.

[3] B. Alberts, D. Bray, J. Lewis, M. Raff, K. Roberts, J.D. Watson, Molekularbiologie der Zelle, Übersetzung von L. Jaenicke, VCH, Weinheim, 1995.

[4] P. Echlin, Low-Temperature Microscopy and Analysis, Plenum, New York, 1999.

[5] D.W. Goodwin, H. Zhu, J.F. Dunn, Am. J. Radiol. 174 (2000) 405.

[6] A.P. Gwynn, S. Wade, M.J. Kääb, G.R.H. Owen, R.G. Richards, J. Microsc. 197 (2) (2000) 159.

[7] G. Bench, A. Saint, M. Cholewa, G.J.F. Legge, D.L. Weirup, A.E. Pontau, Nucl. Instr. and Meth. Phys. Res. B 68 (1992) 481.

[8] J. Vogt, R.-H. Flagmeyer, J. Heitmann, D. Lehmann, T. Reinert, St. Jankuhn, D. Spemann, W. Tröger, T. Butz, Mikrochim. Acta 133 (2000) 105.

[9] T. Butz, R.-H. Flagmeyer, J. Heitmann, D.N. Jamieson, G.J.F. Legge, D. Lehmann, U. Reibetanz, T. Reinert, A. Saint, D. Spemann, R. Szymanski, W. Tröger, J. Vogt, J. Zhu, Nucl. Instr. and Meth. B 161–163 (2000) 323.

[10] D. Spemann, T. Reinert, J. Vogt, D. Dobrev, T. Butz, these proceedings.

[11] D. Spemann, T. Reinert, J. Vogt, T. Butz, K. Otte, K. Zimmer, Nucl. Instr. and Meth. Phys. Res. B 181 (2001) 186.

[12] http://www.uni-leipzig.de/~nfp/cart_reco.html, 2001.

[13] C. Michelet, Ph. Moretto, Nucl. Instr. and Meth. Phys. Res. B 150 (1999) 173.

[14] A. Sakellariou, D.N. Jamieson, G.J.F. Legge, Nucl. Instr. and Meth. Phys. Res. B 181 (2001) 211.

Scanning transmission ion micro-tomography (STIM-T) of biological specimens

Michael Schwertner[a,*], Arthur Sakellariou[b], Tilo Reinert[a], Tilman Butz[a]

[a]*Fakultät für Physik und Geowissenschaften, Nukleare Festkörperphysik, Universität Leipzig, Linnéstrasse 5, D-04103 Leipzig, Germany*
[b]*Research School of Physical Sciences and Engineering, The Australian National University, Canberra, ACT 0200, Australia*

Abstract

Computed tomography (CT) was applied to sets of Scanning Transmission Ion Microscopy (STIM) projections recorded at the LIPSION ion beam laboratory (Leipzig) in order to visualize the 3D-mass distribution in several specimens. Examples for a test structure (copper grid) and for biological specimens (cartilage cells, cygospore) are shown. Scanning Transmission Micro-Tomography (STIM-T) at a resolution of 260 nm was demonstrated for the first time. Sub-micron features of the Cu-grid specimen were verified by scanning electron microscopy.

The ion energy loss measured during a STIM-T experiment is related to the mass density of the specimen. Typically, biological specimens can be analysed without staining. Only shock freezing and freeze-drying is required to preserve the ultra-structure of the specimen. The radiation damage to the specimen during the experiment can be neglected. This is an advantage compared to other techniques like X-ray micro-tomography. At present, the spatial resolution is limited by beam position fluctuations and specimen vibrations.
© 2006 Elsevier B.V. All rights reserved.

PACS: 41.75.Ak; 87.59.F

Keywords: STIM-T; Focussed ion beam; Tomography; Energy loss projection; Biological specimen; Sub-micron resolution

1. Introduction

The technique of Computed Tomography (CT) is used to determine the 3D distribution of a physical property in a specimen from a set of projections taken at different orientations [1]. The development of CT was mainly driven by medical applications. The first medical scanner used X-rays and was presented by Godfrey Hounsfield in 1973 (later he was awarded the Nobel Prize together with Allan Cormack). However, the theory of reconstruction from projections is universal and can be modified for other forms of radiation, such as focussed ion beams.

The physical quantity measured in scanning transmission ion micro-tomography (STIM) is the energy loss of the ions. This primary data can then be fed into a STIM-T 3D reconstruction process. Focussed ion beams were first used for tomographic analysis by Cormack and Koehler [2]. Their first test used a 128 MeV proton beam with a diameter of 2 mm. Pontau et al. [3] and Fischer [4] showed that ion-beam tomography is possible with a resolution of several microns. With further development, beams with smaller diameters became available, and sub-micron resolution was achieved [5]. This development led the way for practical biological applications [6].

This paper gives examples for high-resolution tomography, addresses the effects specific to ions like lateral beam broadening, energy straggling, detector damage and the energy dependence of the stopping power of the ions. The standard reconstruction method of backprojection of

---

*Corresponding author. Current address: Department of Engineering Science, University of Oxford, Parks Road, OX13PJ Oxford, UK. Tel.: +44 1865 273097; fax: +44 1865 273905.
E-mail address: michael.schwertner@eng.ox.ac.uk (M. Schwertner).

filtered projections (BFP) [1,7] was used and problems of beam position fluctuations and inaccuracies of the rotational movement at the sub-micron scale are discussed.

The advantages and drawbacks of STIM-T can be summarized as follows:

(1) Non-transparent objects can be studied in contrast to confocal laser scanning microscopy; however, samples have to be in vacuum, i.e. living specimens cannot be studied. The focal range of STIM-T is large and of the order of 100 μm. STIM of living cells, however, is feasible without noticeable increase in apoptosis or other endpoints.
(2) The sample preparation is easy: freeze-dried samples without fixation and dyes are adequate; this reduces the risk to study preparation artefacts. Electron tomography is an emerging new technique, however sample dimensions have to be far below 1 μm due to excessive lateral straggling.
(3) The radiation dose is about two orders of magnitude lower compared to X-ray micro-tomography; thus no cryo-fixation is required and radiation damage plays little role.

2. Experimental setup

A schematic view of a STIM-T experiment is shown in Fig. 1. The ion beam is scanned across the specimen using magnetic coils. The angular displacement of the beam can be neglected since the distance between the coils and the specimen is ∼30 cm. A windowless PIN photodiode (Hamamatsu 1223-01) with a resolution of 27 keV at full-width at half-maximum (FWHM) measures the residual energy of the protons after traversing the specimen. The FWHM value of roughly 35 keV for the energy straggling
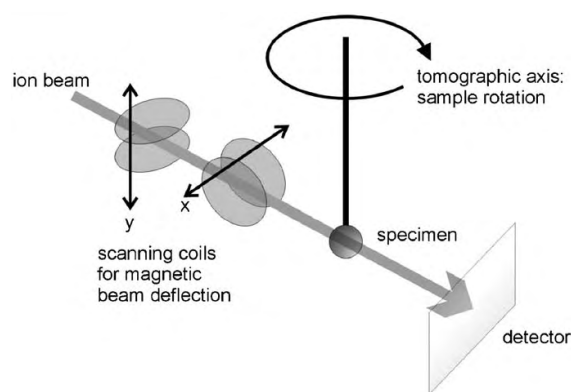
Fig. 1. Schematic drawing of a STIM-T experiment. For the experiments described in this paper, the spot size of the incident beam at the specimen surface was adjusted to 80 nm. Energies of single protons are measured with a p–i–n photo diode. The co-ordinates of the scanning system are combined with the measured energy values to map the specimen since the detector has no spatial resolution.

is slightly larger than the FWHM of the detector, which means the effects of energy straggling can be ignored. Because of the statistical nature of the interaction between individual protons and a specimen, multiple energy loss measurements are made and are later median filtered to remove non-representative values. The detector suffers from damage during the experiment since the protons are implanted into the crystal. Thus, as soon as the deviation of the measured energy for protons in vacuum, i.e. outside the sample, decreases by 1%, the detector is shifted to expose a fresh region. This occurs every 10 to 20 projections.

2.1. Sample preparation

The cartilage specimens were prepared as follows: a small cylinder was punched from a knee joint (tibia) of a juvenile pig within 48 h after slaughter and plunged into liquid nitrogen. The frozen specimen was cut into slices of 20 μm thickness with a cryo-microtome and subsequently freeze dried. Under a microscope, rods of ∼15–20 μm in diameter were cut from the micro-sections using a scalpel. Another biological specimen, a cygospore, was simply dried in air. The test specimen was a portion of a 2000-mesh Cu-grid with known dimensions.

All specimens were mounted on a steel needle using carbon glue (Leit-C, Plano GmbH). The needle is attached to a goniometer head and, with the help of the integrated microscope in the specimen chamber, is shifted and tilted to align the rotational axis with respect to the long axis of the specimen. The projection angle of the specimen axis is controlled via a step motor during the experiments. A motorized x/y stage corrects the specimen position in case it moves out of the field of view during specimen rotation.

2.2. Data acquisition and pre-processing

The diameter of the incident proton beam was 80 nm. For all experiments a set of 361 projections, 250×250 pixels each, were recorded in steps of $0.5°$. Depending on the proton count rate the acquisition of a single projection took about 30 to 60 s. Ideally, for a projection width of $N_x = 250$ pixels, a set of $N_x \pi/2 = 392$ projections should be acquired [8]. However, only 360 projections are collected and we tolerate that the full resolution is only achieved within a central area of 229 pixels in diameter because the object is confined within this area. At each position of the scan, the proton beam dwells until five protons are collected before the scan proceeds to the next position. These five energy values are median filtered. Median filtering is the method of choice for STIM because it excludes spurious and random events from contributing to the measured energy loss [9].

The damage of the detector causes artefacts because the sensitivity is locally reduced and phantom energy losses next to the specimen's image may occur. This can be corrected for by thresholding the energy values. Since
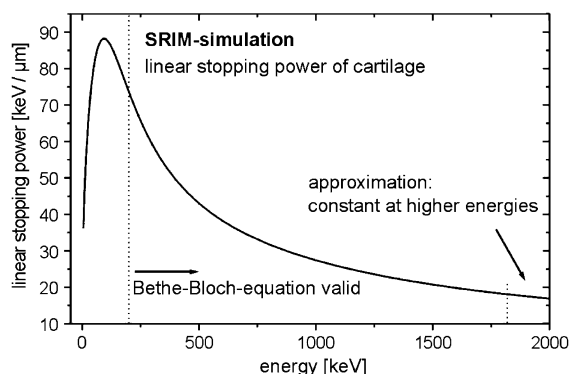
Fig. 2. Monte Carlo simulation for the energy loss of protons in cartilage. The SRIM software package [15] was used for the simulation and the assumed composition of cartilage was $C_{10}H_{13}NO_{2.2}$. For the qualitative reconstructions of the specimen density no dependence of the stopping power on the energy was used. This amounts to the approximation that the linear stopping power is constant in the range between 1800 and 2000 keV.

thresholding can lead to an erosion of contours in regions of the specimen with very low energy losses a second method was applied in the case of the Cu-grid: the object contour was detected with a special algorithm and every energy loss value outside the object was set to zero. Furthermore, the projection data was aligned by fitting the centre of mass of the individual energy loss projections to a sine curve, using a curve fitting algorithm developed in Refs. [10,11] and described in Ref. [12]. This is an essential step since the bearings of the goniometer are not accurate at the µm-scale as required for the reconstruction.

In our experiments we used proton beam energies of 2 and 2.25 MeV. The maximum energy loss of the cartilage-specimen was 200 keV and the stopping power was approximated to be constant in that range between 1800 and 2000 keV (see Fig. 2). If the energy loss of the ion is independent of its instantaneous energy and the composition of the specimen is homogenous, the energy loss is proportional to the areal mass density. Because of these assumptions for our cartilage specimen, the qualitative reconstruction of the specimen morphology could be obtained directly from the energy loss values without a conversion to the areal mass densities. No a priori knowledge was used for the reconstruction of the biological specimen. For the copper grid we used the knowledge of the composition for the conversion of the energy losses to the areal mass densities.

2.3. Tomographic reconstruction and ion beam specific effects

The experimental procedure of measuring a set of projections within one slice of a specimen is mathematically equivalent to sampling the Radon transform of the object slice [1,7]. There are two ways to invert the Radon transform. The first one is an iterative approach. It involves a forward simulation of the Radon transform which is then compared to the projections measured in the experiment so that iterative corrections are applied to the tomogram. These iterations continue until the simulated and measured projection data are sufficiently similar. Examples are the Algebraic Reconstruction Technique (ART-algorithms) [7,13] and the Discretized Image Space Reconstruction Algorithm (DISRA) [14]. The second approach is a direct approximation of the inverse Radon transform, and such methods are sometimes called transform-based techniques. The most common transform-based algorithm is the Backprojection of Filtered Projections (BFP) [1]. In this paper, BFP was used to reconstruct all sets of experimental data apart from the copper grid specimen, where DISRA was used. Both algorithms were implemented in the software package [11].

In STIM-T experiments, many deviations from the ideal projection process occur which need to be corrected. Alternatively, the experimental conditions can be adjusted to get an approximation closer to the ideal projection process. The specific ion beam characteristics of concern are the energy dependence of the stopping power, the beam broadening within the specimen (lateral straggling) and the energy straggling. These phenomena are discussed next.

The energy loss of an ion passing through a specimen can be described by the linear stopping power dE/dx which consists of a nuclear fraction, which is insignificant at the typical ion energies used for STIM, and a dominating electronic fraction. The electronic part of the linear stopping power is due to the elastic Coulomb interactions between the penetrating ion and the electrons in the specimen and is described by the Bethe–Bloch-equation [15], for ion energies above 200 keV. It is proportional to the electron density of the material. Usually the stopping power is defined as

$$S(E) = \frac{1}{\rho}\frac{dE}{dx} = \frac{dE}{d(\rho z)} = \frac{dE}{d\mu}, \tag{1}$$

where ρ indicates the volume mass density and μ the areal mass density. For a compound, the stopping power is calculated using the Bragg rule:

$$S_C(E) = \sum_Z c_Z S_Z(E). \tag{2}$$

Here, c_Z denotes the mass fraction for the element in the compound with atomic number Z and has a corresponding stopping power S_Z. The values for the stopping powers S_Z are tabulated [16,17]. An illustrative graph for the linear stopping power (dE/dx) of protons in cartilage is shown in Fig. 2.

If a quantitative reconstruction of the mass density in a specimen is required, the energy loss has to be converted to the projected areal mass density μ along this trajectory prior to the reconstruction [3]. The conversion at every

scan position t within the projection line is accomplished via

$$\mu(t) = \int_{E_0}^{E_R(t)} \frac{1}{S_{C(t)}(E)} \, dE, \tag{3}$$

where E_0 is the incident beam energy and $E_R(t)$ is the measured residual energy of the transmitted ion. Typically, quantitative reconstructions can only be performed when the specimen's composition $C(t)$ is known and Eq. (3) is applied. To obtain this information, other techniques like particle-induced X-ray emission (PIXE) or a priori knowledge may be used. Nevertheless, for biological specimens, the accuracy of the areal mass density can be as good as several percent with only an approximate knowledge of the composition [13,18]. Therefore, to obtain a specimen's 3D morphology, a qualitative reconstruction using only the energy loss projections is usually adequate.

Another point to be considered is the lateral beam straggling [19]. The resulting beam profile that defines the interaction volume within the specimen is a convolution of the incident beam profile and the broadening function due to the multiple scattering with the electrons in the specimen. A simulation of beam broadening using SRIM [17] revealed a quadratic dependence between broadening and depth of penetration. For a 2 MeV proton beam and a cartilage specimen of 15 μm thickness, a beam broadening of only 120 nm is calculated [17]. An investigation of lateral beam broadening [20] shows that the widely used SRIM-code may underestimate the experimental values of beam broadening by about 40%. It is important that the interaction volumes for each ion trajectory do not overlap otherwise the spatial resolution of the reconstructed specimen is degraded. In such a case, the effects of beam broadening must be accounted for in the reconstruction process. For a given specimen, the two parameters that control the broadening of the proton beam are the incident energy and the specimen thickness.

A further effect caused by the statistical nature of the multiple interactions between ions and the electrons of the material is energy straggling: a beam of defined energy will have a Gaussian energy distribution after interacting with matter [21]. A SRIM simulation of the energy distribution assuming 2 MeV protons and 20 μm of (freeze dried) joint cartilage yields a FWHM of 34.8 keV [12]. This is in good agreement with the theoretical predictions in Ref. [20].

All data sets but one were reconstructed qualitatively by reconstructing the sinogram data directly with a BFP program. Only the copper grid was reconstructed using the DISRA program in addition. A Ram-Lak apodizing function [22] with a bandwidth of 0.6 was used because it turned out to be a good compromise between the sensitivity to noise in the data and the attainable resolution. To reconstruct these $250 \times 250 \times 250$ voxel data sets on a 1 GHz Athlon PC running under Linux, the non-iterative qualitative BFP reconstruction takes 4 min, whereas the iterative quantitative DISRA reconstruction takes 2.5 h.

3. Results and discussion

Figs. 3–6 show transparent volume renderings of the tomograms, generated by the program drawer3D [11]. All reconstructed data sets have a size of $250 \times 250 \times 250$ voxels. In Figs. 3 and 4 (stereo-image pair), the internal structures of the cartilage cells embedded in a dense matrix are clearly visible. Since the time between slaughtering of the pig and the freezing of the specimens was 48 h, the cells seem to be necrotic and cell structures like the nucleus were therefore already disintegrated. In future experiments, the specimen preparation has to be improved, e.g. faster freezing with liquid nitrogen cooled isopentane. Some structures of the cell organelles are clearly visible at a sub-micron level as can be inferred from the scales shown in the figures.

Fig. 7 shows slice #150 of the Cu-grid tomogram. Note the well-resolved sharp structure at the bottom. This was the result of cutting the Cu-grid with the scalpel and is well resolved.

It should be pointed out that all the reconstructions of biological specimen shown here were performed without the use of any prior knowledge of the specimen. For the copper grid an additional quantitative reconstruction was done using the DISRA technique. The composition of the material was known (copper) and the accuracy of the reconstructed density agreed with the tabulated value of 8.96 g/cm^3 within 4%. The accuracy of the density values depends on the knowledge of the specimen's composition and physical dimensions of the scan area. Compared to the qualitative reconstruction, there was no noticeable difference in morphology. However, a slightly increased level of noise was observed.
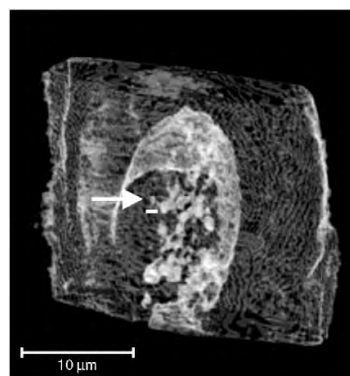

Fig. 3. The tomogram of a cartilage cell from the knee joint (tibia) of a juvenile pig, shown as a semitransparent rendering, generated with drawer3D [11]. Cell structures like the nucleus were not preserved and the cell seems to be necrotic because of the delay between slaughter of the animal and freezing of the specimen. The data set of the reconstruction has a size of $250 \times 250 \times 250$ voxels and the spacing between scanned points in the projections was 140 nm. The arrow indicates a sub-micron structure, the small bar below indicates the size of 1 μm.
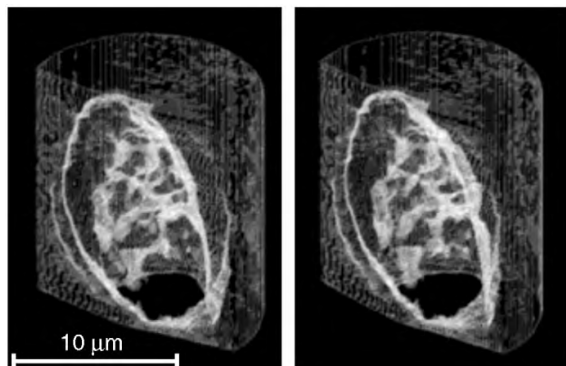
Fig. 4. The tomogram of a cartilage cell from the knee joint of a juvenile pig, showing some selected regions. The distance between sampled points in the projections was 117 nm. This stereopair may be viewed with the optical axis of your eyes almost parallel but still focussing to the paper.
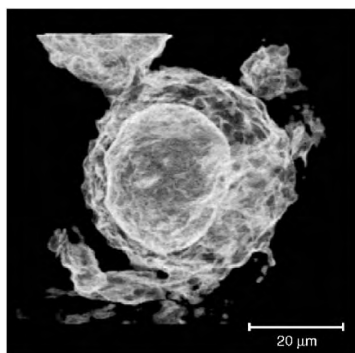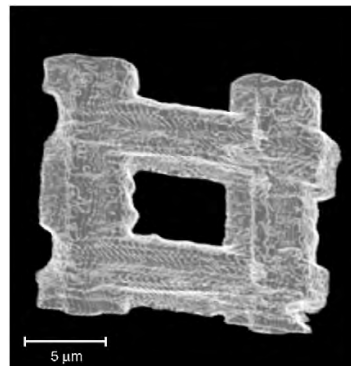

Fig. 6. The tomogram of a section of Cu-grid (2000 mesh per inch), shown as a semitransparent rendering. The spacing between the sampled points of the projections was 96 nm.
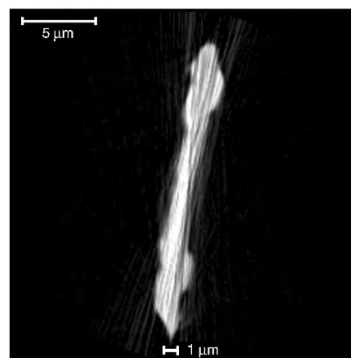

Fig. 5. The tomogram of a cygospore, shown as a semitransparent rendering. An internal, clearly segmented structure of lower density can be seen.

Fig. 7. A cross-section at slice 150 from the Cu-grid tomogram depicted in Fig. 6. One pixel corresponds to 96 nm. The bar next to the lower edge corresponds to 1 µm.

In order to verify the accuracy of STIM-T, additional scanning electron microscopy (SEM) was performed on the Cu-grid. In Fig. 8, the surface rendering of the Cu-grid tomogram is compared to the electron micrograph of the specimen surface. The morphology and several sub-micron features present in the STIM-T tomogram were confirmed by the SEM images.

To determine the resolution of the reconstruction, one edge of the Cu-grid tomogram was analysed via a line scan. An error function was fitted to the intensity profile and yielded a resolution of 260 nm, as shown in Fig. 9. The edge definition of the copper grid is not exactly known. However, it is certainly better than 200 nm, judging from the SEM-images. Therefore, this figure seems a conservative estimate. Since biological specimens usually do not provide sharp edges or other test structures similar to the copper grid, it is difficult to extract a similar figure from line scans over fragments of the cartilage cell nucleus or the cygospore core structure. However, we expect a comparable resolution for biological specimens as for the copper

grid because of the absence of shrinkage at currents in the order of 0.1 fA (10^{-16} A). Repeated STIM-microscopy images yield identical results for the same projection. Furthermore, the doses in STIM-T experiments are too low to affect the morphology, as will be discussed below. Fluctuations of the beam position due to external stray magnetic fields in the order of 1 µT and specimen vibrations limited the attainable resolution thus far. The Leipzig Nanoprobe can produce beam cross sections below 50 nm [23], but the statistical fluctuations of the specimen and beam positions were measured to have a FWHM of 350 nm (vertical) and 290 nm (horizontal), respectively [12]. Therefore, the position uncertainty rather than the beam broadening or the diameter of the beam limited the spatial resolution of the tomograms. This problem has subsequently been alleviated by the installation of an active compensation system against stray magnetic fields [24]. However, the specimen vibration remains to be eliminated. A new target chamber with UHV-translation stages with shorter dimensions and a UHV-goniometer are under
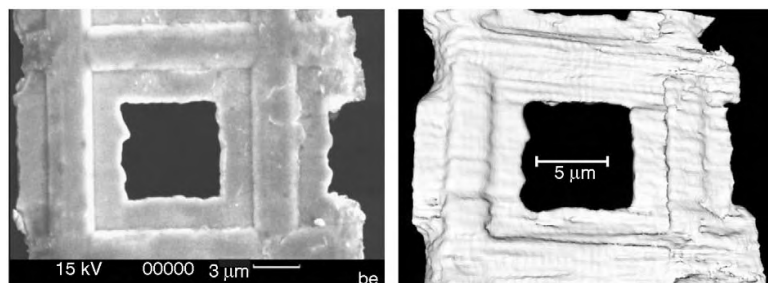
Fig. 8. Left: Scanning Electron Microscope image of the Cu-grid specimen. Some distinct features are in the sub-micron range and are clearly reproduced in the STIM-T tomogram. Right: Iso-surface rendering of the Cu-grid tomogram shown in Fig. 6. One period of the 2000 mesh grid corresponds to 12.7 μm.
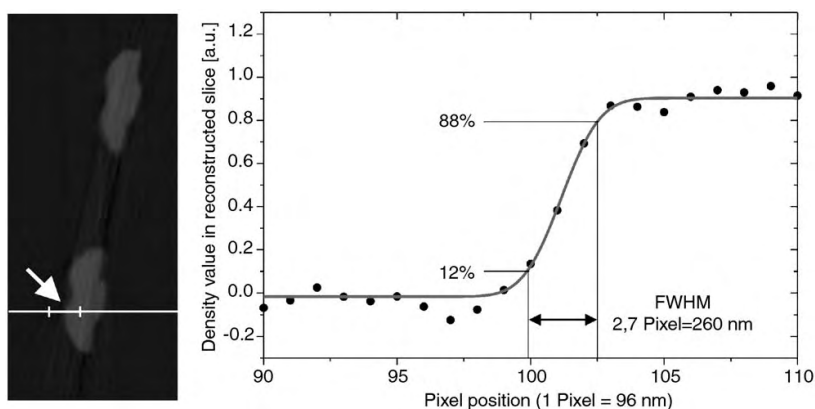

Fig. 9. Slice of the 3D dataset of the reconstructed density of the copper-grid. The arrow indicates the location where the profile data shown on the right was extracted. The solid line is an error function fitted to the edge. This yields a lateral resolution of 260 nm assuming an infinitely sharp edge definition of the copper-grid.

construction and should greatly reduce specimen vibrations.

We did not correct for beam broadening during the reconstruction since fluctuations of the beam position were found to be larger than the simulated beam broadening expected for these biological specimens. Hence, only a small improvement of the resolution would be expected for these data sets. Bench et al. [25] demonstrated an improvement in resolution by incorporating beam broadening into the reconstruction process of STIM-T, but the model was restricted to a similar geometry and composition over neighbouring slices. An implementation of a full 3D model for lateral beam broadening should be feasible for an iterative technique such as DISRA [14], but at the cost of increased computation time and the development of a more sophisticated model for beam broadening.

3.1. Comparison to other methods

There are other methods, for example X-ray micro-tomography, that can reconstruct the 3D volume of biological specimens at a resolution down to 60 nm [26], but synchrotron radiation is required and the radiation dose of 10^8–10^9 Gy may damage the specimen. For STIM-T the dose is more than two orders of magnitude lower. This number can be estimated as follows: An upper limit for the linear energy transfer in a biological specimen for 2.25 MeV protons is about 15 keV/μm. A cartilage specimen of 20 μm × 20 μm × 20 μm (volume: 8000 μm^3) receives in the order of 200 (pixels) × 200 (pixels) × 5 (protons/pixel) = 2×10^5 protons per projection each of which deposits 15 keV/μm × 20 μm = 300 keV, i.e. a total deposited energy of 300 keV × 2×10^5 (protons) = 6×10^{10} eV per 1 g/cm^3 (density of water) × 8000 μm^3 = 8×10^{-12} kg. This results in a dose of 0.75×10^{22} eV/kg = 1.2×10^3 J/kg (or Gy). With a total of 360 projections we finally obtain a figure about 4×10^5 Gy. Thus, cryo-fixation is not required to preserve the morphology.

Another technique with 3D capability, high resolution and low radiation dose is Electron Tomography [27]. Unfortunately, because of the very small penetration depth of the electrons, the specimen size is below 1 μm, which

Table 1
Characteristics of common 3D micro-analysis techniques

	Resolution X/Y	Resolution Z	Specimen size	Spec. damage
STIM tomography	< 300 nm	<300 nm	<100 μm	Low dose
Electron tomography	Up to 5 nm	Up to 5 nm	<1 μm	Low dose
X-ray tomography	Up to 60 nm	Up to 60 nm	~10 μm, more at lower res.	High dose
Serial block face EM	Approx. 10 nm	50–70 nm	>200 μm	Destructive

makes the specimen preparation difficult and restricts the applications.

One further 3D analysis technique is the Serial Block-Face Scanning Electron Microscopy reported recently [28] where a resolution of 50–70 nm in axial direction and about 10 nm in lateral direction was accomplished. This method is destructive since the respective top layers of the specimen are physically removed. If the loss of the specimen and the technical effort is not a problem, relatively large specimen areas can be analysed at high resolution. For a quick overview, the features of the mentioned 3D methods are compared in Table 1.

4. Conclusion

STIM-T can be used to image the 3D structure of biological specimens at a resolution better than 300 nm and does not require any staining techniques to enhance the contrast of the material density in the specimen nor does it require cryo-fixation.

Without prior knowledge of the specimen composition, accurate 3D morphological images are obtained. If the specimen composition is known, a quantitative reconstruction of the 3D density distribution may be calculated with a potential accuracy of 10% [9].

To our knowledge, the resolution of 260 nm is the best value obtained with the STIM-T method so far; it can still be improved. A resolution of 100 nm may be obtained if the stray magnetic fields in the lab are sufficiently compensated and specimens smaller than 15 μm in diameter can be prepared. In this case, simulations of the lateral beam broadening show that interaction volumes smaller than 100 nm in diameter can be accomplished and modelling of beam broadening in the reconstruction process is not necessary. STIM-T can be applied to analyse the 3D structure of a wide range of biological and technical specimens. A precondition is that the ion-beam has sufficient energy to traverse the specimen. The technique offers a combination of high resolution, simple specimen preparation and very low radiation damage.

References

[1] A.C. Kak, Principles of Computerized Tomographic Imaging, IEEE Press, New York, 1987.
[2] A.M. Cormack, A.M. Koehler, Quantitative proton tomography: preliminary results, Phys. Med. Biol. 21/4 (1976) 560–569.
[3] A. Pontau, A.J. Antolak, D.H. Morse, A.A. Ver Berkmoes, J.M. Brase, D.W. Heikkinen, H.E. Martz, I.D. Procter, Ion Microbeam tomography, Nucl. Instrum. Methods B 40/41 (1989) 646–650.
[4] B.E. Fischer, C. Mühlbauer, Microtomography by heavy ions, Nucl. Instrum. Methods B 47 (1990) 271–282.
[5] G.S. Bench, K.A. Nugent, Submicron STIM tomography reconstruction techniques, Nucl. Instrum. Methods B 54 (1991) 390–396.
[6] C. Michelet, Development d'une technique de micro-tomographie par faisceau d'ions a l'échelle cellulaire, Ph.D-thesis, Université Bordeaux I, 1998.
[7] S.R. Deans, The Radon Transform and Some of its Applications, Krieger Publishing Company, Malabar, Florida, 1993.
[8] A. Pontau, A.J. Antolak, D.H. Morse, Minimum data set requirements for ion microtomography, Nucl. Instrum. Methods B 54 (1991) 383–389.
[9] J.C. Overley, R.M.S. Schofield, J.D. MacDonald, H.W. Lefevre, Energy loss image formation in scanning transmission ion microscopy, Nucl. Instrum. Methods B 30 (1988) 337–341.
[10] A. Sakellariou, STIM and PIXE tomography, Ph.D Thesis, The University of Melbourne, School of Physics, 2002.
[11] A. Sakellariou, Software for STIM- and PIXE tomography: spt_disra 0.93, Department of Applied Mathematics, Australian National University, Canberra.
[12] M. Schwertner, Hochauflösende Ionenstrahl-Mikrotomographie am Lipsion, Diplomarbeit, Universiät Leipzig, Fakultät für Physik und Geowiss, 2002.
[13] R. Gordon, A tutorial on ART, IEEE Trans. Nucl. Sci. NS 21 (1974) 78–93.
[14] A. Sakellariou, M. Cholewa, A. Saint, G.J.F. Legge, An accurate reconstruction algorithm for tomography experiments that involve complex probe sample interactions, Meas. Sci. Technol. 8 (1997) 746–758.
[15] J.F. Knoll, Radiation Detection and Measurement, Wiley, New York, 1989.
[16] J.F. Ziegler, SRIM: the Stopping Power and Ranges of Ions in Solids, Pergamon Press, New York, 1985.
[17] J.F. Ziegler, SRIM: The stopping power and ranges of ions in solids, Program for IBM PC, Version 96.01, www.srim.org
[18] H.W. Lefevre, R.M.S. Schofield, J.C. Overley, J.D. MacDonald, Scanning transmission ion microscopy as it complements particle induced X-ray emission microanalysis, Scan. Microsc. 1 (1987) 879–889.
[19] A.J. Antolak, An empirical treatment of nonrelativistic proton beam spreading, Nucl. Instrum. Methods B 30 (1988) 182–184.
[20] C. Michelet, Ph. Moretto, G. Laurent, W.J. Przybylowicz, V.M. Prozesky, C.A. Pineda, Ph. Barbaret, F. Lohste, J. Kennedy, Measurement of lateral straggling using a microbeam, Nucl. Instrum Methods B 181 (2001) 157–163.
[21] M. Breese, D.N. Jamieson, P. King, Materials Analysis using Nuclear Microprobes, Wiley, New York, 1996.
[22] A.K. Jain, Fundamentals of Digital Image Processing, Prentice-Hall, Englewood cliffs, NJ, 1989.

[23] D. Spemann, T. Reinert, J. Vogt, D. Dobrev, T. Butz, Suitable test structures for submicron ion beam analysis, Nucl. Instrum. Methods B 190 (2002) 312–317.

[24] D. Spemann, T. Reinert, J. Vogt, J. Wassermann, T. Butz, Active compensation of stray magnetic fields at LIPSION, Nucl. Instrum and Methods B 210 (2003) 79–84.

[25] G.S. Bench, A.J. Antolak, D.H. Morse, A.E. Pontau, A. Saint, G.J.F. Legge, On the effect of spatial beam broadening in ion microtomography (IMT) image quality, Nucl. Instrum. and Methods B 82 (1993) 447–458.

[26] D. Weiß, Computed tomography of cryogenic biological specimens based on X-ray microscopic images, Ultramicroscopy 84 (2000) 185–197.

[27] W. Baumeister, Electron tomography: towards visualizing the molecular organization of the cytoplasm, Curr. Opin. Struct. Biol. 12 (5) (2002) 679–684.

[28] W. Denk, H. Horstmann, Serial block-face scanning electron microscopy to reconstruct three-dimensional tissue nanostructure, PLoS Biol. 2 (11) (2004) e329.

List of supervised/co-supervised theses

Supervised Diploma/MSc-theses

1. Uta Reibetanz, Diplom, Dezember 1998
"Untersuchung mechanisch belasteter und unbelasteter Knorpelproben mit dem Ionenstrahl"

2. Michael Schwertner, Diplom, March 2002
"Hochauflösende Protonenstrahl-Mikrotomographie am LIPSION"

3. Frank Menzel, Diplom, November 2002
"Ionenstrahlanalytische Untersuchung der perkutanen Aufnahme von ultrafeinen Partikeln"

4. Christoph Meinecke, Diplom, Oktober 2003
"Bestimmung der intra- und extraneuronalen Eisenkonzentration im Gehirn mittels Ionenstrahlanalytik"

5. Anja Fiedler, Diplom, March 2005
"Bestrahlung lebender Humanzellen mit hochenergetischen Protonen"

6. Christian Ostwald, Diplom, August 2005
"Mikrodosimetrie an lebenden Zellen"

7. Nirav Barapatre, MSc, February 2007
"In-situ trace element analysis of neuromelanin"

8. Marcus Hohlweg, Diplom, January 2008
"Entwicklung strukturierter Petrischalen und Ionenbeschuss lebender Zellen zur Untersuchung des Bystander-Effektes unter Ausschluss von Zell-Zell-Kommunikation über Gap-Junctions"

9. Daniela Kolbe, Diplom, March 2008
"STIM-Untersuchungen an lebenden und fixierten Zellen"

10. Tobias Andrea, Diplom, January 2009
"STIM-Tomographie an biologischen Proben"

Co-supervised PhD-theses

1. Markus Morawski PhD, February 2006
"Perineuronal nets - A potentially neuroprotective structure against iron mediated oxidative processes in Alzheimer's and Parkinson's disease"

2. Anja Fiedler, January 2009
"Eisen und Eisenproteine in Neuronen mit perineuronalem Netz"

3. Martin Rothermel, ongoing
"Proton-Microtomographie"

4. Nirav Barapatre, ongoing
   "Trace element analysis in biological materials"

5. Torsten Koal, ongoing
   "Aufbau einer Platform zur gezielten Bestrahlung lebender Zellen für radiobiologische Experimente"

List of Publications

44. A. Fiedler, **T. Reinert**, G. Brückner, T. Arendt, and M. Morawski.
Neurons bearing a perineuronal net possess a high concentration of iron and iron
specific proteins
(in preparation).

43. Martin Rothermel, Tilman Butz, and **Tilo Reinert**.
Rearranging a Nanoprobe: Line Foci, Grid Shadow Patterns and Performance
Tests
*Instruments and Methods in Physics Research Section B: Beam Interactions with
Materials and Atoms*, (accepted for publication).

42. T. Andrea, M. Rothermel, T. Butz, and **T. Reinert**.
The improved STIM tomography set-up at LIPSION: Three-dimensional recon-
struction of biological samples
*Instruments and Methods in Physics Research Section B: Beam Interactions with
Materials and Atoms*, (accepted for publication).

41. E. Gontier, M.-D. Ynsa, T. Bíró, J. Hunyadi, B. Kiss, K. Gáspár, T. Pinheiro, J.-
N. Silva, P. Filipe, J. Stachura, W. Dabros, **T. Reinert**, T. Butz, Ph. Moretto,
J.-E. Surlève-Bazeille.
Is there penetration of titania nanoparticles in sunscreens through skin? A com-
parative electron and ion microscopy study
Nanotoxicology, 2(4) 218–231, (2008).

40. M. Morawski, A. Fiedler, **T. Reinert**, G. Brückner, and T. Arendt.
Iron compartmentalisation in the rat brain: do perineuronal net-ensheathed neu-
rons play a special role?
Journal of Neurochemistry, 101:35, 2007.

39. T. Reinert, A. Fiedler, M. Morawski, and T. Arendt.
High resolution quantitative element mapping of neuromelanin-containing neu-
rons.
*Nuclear Instruments and Methods in Physics Research Section B: Beam Interac-
tions with Materials and Atoms*, 260(1):227–230, 2007.

38. A. Fiedler, **T. Reinert**, J. Tanner, and T. Butz.
DNA double strand breaks and Hsp70 expression in proton irradiated living cells.
*Nuclear Instruments and Methods in Physics Research Section B: Beam Interac-
tions with Materials and Atoms*, 260(1):169–173, 2007.

37. A. Fiedler, **T. Reinert**, M. Morawski, G. Brückner, T. Arendt, and T. Butz.
Intracellular iron concentration of neurons with and without perineuronal nets.
*Nuclear Instruments and Methods in Physics Research Section B: Beam Interac-
tions with Materials and Atoms*, 260(1):153–158, 2007.

36. C. Nilsson, S. Petriconi, **T. Reinert**, and T. Butz.
The new target chamber at LIPSION: The new translation stage and goniometer

and the new irradiation platform for single..
Nuclear Instruments and Methods in Physics Research Section B: Beam Interactions with Materials and Atoms, 260(1):71–76, 2007.

35. A. Fiedler, **T. Reinert**, J. Tanner, and T. Butz.
DNA DSBs and HSP70 expression in proton-irradiated living cells at LIPSION.
Radiation Research, 166(4):674–675, 2006.

34. C. Nilsson, S. Petriconi, **T. Reinert**, and T. Butz.
Status of the new single-ion hit facility for irradiation of living cells at LIPSION.
Radiation Research, 166(4):672–673, 2006.

33. **T. Reinert**, D. Spemann, M. Morawski, and T. Arendt.
Quantitative trace element analysis with sub-micron lateral resolution.
Nuclear Instruments and Methods in Physics Research Section B: Beam Interactions with Materials and Atoms, 249(1):734–737, 2006.

32. Ch. Meinecke, M. Morawski, **T. Reinert**, T. Arendt, and T. Butz.
Cellular distribution and localisation of iron in adult rat brain (substantia nigra).
Nuclear Instruments and Methods in Physics Research Section B: Beam Interactions with Materials and Atoms, 249(1):688–691, 2006.

31. M. Schwertner, A. Sakellariou, **T. Reinert**, and T. Butz.
Scanning transmission ion micro-tomography (STIM-T) of biological specimens.
Ultramicroscopy, 106(7):574–581, 2006.

30. T. Butz, Ch. Meinecke, M. Morawski, **T. Reinert**, M. Schwertner, D. Spemann, and J. Vogt.
Morphological and elemental characterisation with the high-energy ion-nanoprobe LIPSION.
Applied Surface Science, 252(1):43–48, 2005.

29. M. Morawski, **T. Reinert**, Ch. Meinecke, Th. Arendt, and T. Butz.
Antibody meets the microbeam - or how to find neurofibrillary tangles.
Nuclear Instruments and Methods in Physics Research Section B: Beam Interactions with Materials and Atoms, 231:229–233, 2005.

28. M. Morawski, **T. Reinert**, C. Meinecke, T. Arendt, and T. Butz.
Antibody meets the microbeam - or how to find neurofibrillary tangles.
Nuclear Instruments and Methods in Physics Research Section B: Beam Interactions with Materials and Atoms, 231(1):229–233, 2005.

27. M. Morawski, Ch. Meinecke, **T. Reinert**, A. C. Dorffel, P. Riederer, T. Arendt, and T. Butz.
Determination of trace elements in the human substantia nigra.
Nuclear Instruments and Methods in Physics Research Section B: Beam Interactions with Materials and Atoms, 231(1):224–228, 2005.

26. F. Menzel, **T. Reinert**, J. Vogt, and T. Butz.
Investigations of percutaneous uptake of ultrafine TiO"2 particles at the high energy ion nanoprobe LIPSION.
Nuclear Instruments and Methods in Physics Research Section B: Beam Interactions with Materials and Atoms, 219:82–86, 2004.

25. **T. Reinert**, A. Fiedler, J. Skopek, J. Tanner, J. Vogt, and T. Butz.
Single ion bombardment of living cells at LIPSION.
Nuclear Instruments and Methods in Physics Research Section B: Beam Interactions with Materials and Atoms, 219:77–81, 2004.

24. **T. Reinert**, M. Morawski, T. Arendt, and T. Butz.
Quantitative microanalysis of perineuronal nets in brain tissue.
Nuclear Instruments and Methods in Physics Research Section B: Beam Interactions with Materials and Atoms, 210:395–400, 2003.

23. D. Spemann, **T. Reinert**, J. Vogt, J. Wassermann, and T. Butz.
Active compensation of stray magnetic fields at LIPSION.
Nuclear Instruments and Methods in Physics Research Section B: Beam Interactions with Materials and Atoms, 210:79–84, 2003.

22. D. Spemann, **T. Reinert**, J. Vogt, D. Dobrev, and T. Butz.
Suitable test structures for submicron ion beam analysis.
Nuclear Instruments and Methods in Physics Research Section B: Beam Interactions with Materials and Atoms, 190(1):312–317, 2002.

21. **T. Reinert**, A. Sakellariou, M. Schwertner, J. Vogt, and T. Butz.
STIM Tomography at the Leipzig Nanoprobe LIPSION.
Nuclear Instruments and Methods in Physics Research Section B: Beam Interactions with Materials and Atoms, 190:266–270, 2002.

20. **T. Reinert**, U. Reibetanz, A. Sakellariou, M. Schwertner, J. Vogt, and T. Butz.
The Architecture of Cartilage: Elemental Maps and Scanning Transmission Ion Microscopy/Tomography.
Nuclear Instruments and Methods in Physics Research Section B: Beam Interactions with Materials and Atoms, 188:1–8, 2002.

19. J. Tanner, D. Spemann, **T. Reinert**, J. Vogt, and T. Butz.
The Leipzig High-Energy Ion-Nanoprobe LIPSION: Design of single-ion bombardment of living cells.
Radiation Research, 158(3):372, 2002.

18. **T. Reinert**, U. Reibetanz, J. Vogt, T. Butz, A. Werner, and W. Grunder.
Spatially resolved elemental distributions in articular cartilage.
Nuclear Instruments and Methods in Physics Research Section B: Beam Interactions with Materials and Atoms, 181(1):516–521, 2001.

17. **T. Reinert**, U. Reibetanz, J. Vogt, T. Butz, A. Werner, and W. Grunder.
Visualisation of collagen fibrils in joint cartilage using STIM.

Nuclear Instruments and Methods in Physics Research Section B: Beam Interactions with Materials and Atoms, 181:511–515, 2001.

16. D. Spemann, **T. Reinert**, J. Vogt, T. Butz, K. Otte, and K. Zimmer.
Novel test sample for submicron ion-beam analysis.
Nuclear Instruments and Methods in Physics Research Section B: Beam Interactions with Materials and Atoms, 181:186–192, 2001.

15. S. Lebed, J. Butz, T. Vogt, D. **Reinert**, **T.** Spemann, J. Heitmann, Z. Stachura, J. Lekki, A. Potempa, J. Styczen, and B. Sulkio-Cleff.
A novel ultra-short scanning nuclear microprobe: Design and preliminary results.
Nuclear Instruments and Methods in Physics Research Section B: Beam Interactions with Materials and Atoms, 181:32–38, 2001.

14. T. Butz, D. Lehmann, **T. Reinert**, D. Spemann, and J. Vogt.
Ion Microscopy and Tomography.
Acta Physica Polonica A, 100:603, 2001.

13. J. Vogt, R.-H. Flagmeyer, J. Heitmann, D. Lehmann, **T. Reinert**, St. Jankuhn, D. Spemann, W. Tröger, and T. Butz.
Solid State Analysis with the New Leipzig High-Energy Ion Nanoprobe.
Mikrochim. Acta, 133:105, 2000.

12. J. Wang, P. Guo, X. Li, J. Zhu, **T. Reinert**, J. Heitmann, D. Spemann, J. Vogt, R.-H. Flagmeyer, and T. Butz.
Source Identification of Lead Pollution in the Atmosphere of Shanghai City by Analyzing Single Aerosol Particles (SAP).
Environ. Sci. Technol., 34:1900, 2000.

11. J. Wang, P. Guo, X. Li, J. Zhu, **T. Reinert**, J. Heitmann, D. Spemann, J. Vogt, R.-H. Flagmeyer, and T. Butz.
Identification of air pollution sources by single aerosol particle fingerprints - micro-PIXE spectra.
Nuclear Instruments and Methods in Physics Research Section B: Beam Interactions with Materials and Atoms, 161:830–835, 2000.

10. P. Guo, J. Wang, X. Li, J. Zhu, **T. Reinert**, J. Heitmann, D. Spemann, J. Vogt, R.-H. Flagmeyer, and T. Butz.
Study of metal bioaccumulation by nuclear microprobe analysis of algae fossils and living algae cells.
Nuclear Instruments and Methods in Physics Research Section B: Beam Interactions with Materials and Atoms, 161:801–807, 2000.

9. T. Butz, R.-H. Flagmeyer, J. Heitmann, D. N. Jamieson, G. J. F. Legge, D. Lehmann, U. Reibetanz, **T. Reinert**, A. Saint, and D. Spemann.
The Leipzig high-energy ion nanoprobe: A report on first results.
Nuclear Instruments and Methods in Physics Research Section B: Beam Interactions with Materials and Atoms, 161:323–327, 2000.

8. St. Jankuhn, T. Butz, R.-H. Flagmeyer, **T. Reinert**, J. Vogt, J. Hammerl, R. Protsch v. Zieten, M. Wolf, and K. Bethge.
   Elementbestimmung an historischen menschlichen Knochen mittels Röntgenspektroskopie. In C. Vogt, R. Wennrich, and G. Werner, editors,
   CANAS97: Colloquium Analytische Atomspektroskopie. 1998.

7. **T. Reinert**, T. Butz, R.-H. Flagmeyer, St. Jankuhn, J. Vogt, W. Gründer, M. Kanowski, M. Wagner, A. Werner, D. Grambole, and F. Herrmann.
   Investigation of the calcium content in joint cartilage: Is it connected with (early arthrotic) changes in cartilage structure?
   Nuclear Instruments and Methods in Physics Research Section B: Beam Interactions with Materials and Atoms, pages 936–940, 1998.

6. St. Jankuhn, T. Butz, R.-H. Flagmeyer, **T. Reinert**, B. Barckhausen, J. Hammerl, R. Protsch v. Zieten, D. Grambole, F. Herrmann, and K. Bethge.
   Ion microprobe analyses of ancient human bone.
   Nuclear Instruments and Methods in Physics Research Section B: Beam Interactions with Materials and Atoms, 136:329–333, 1998.

5. T. Butz, R.-H. Flagmeyer, S. Jankuhn, **T. Reinert**, W. Tröger, M.F. Da Silva, and J.C. Soares.
   RBS studies of the intercalation compound Hg_xTiS_2: Morphology and staging.
   Nuclear Instruments and Methods in Physics Research Section B: Beam Interactions with Materials and Atoms, 136:253–257, 1998.

4. J. Hammerl, R. Protsch von Zieten, M. Wolf, H. Baumann, K. Bethge, I. Symietz, St. Jankuhn, T. Butz, R.-H. Flagmeyer, **T. Reinert**, and J. Vogt.
   Ermittlung der Knochenmineraldichte sowie der Haupt- und Spurenelemente an historischen Knochen. In M. Kokabi, editor,
   Beiträge zur Archäozoologie und Prähistorischen Anthropologie, volume 1. 1997.

3. St. Jankuhn, H. Baumann, K. Bethge, T. Butz, R.-H. Flagmeyer, J. Hammerl, R. Protsch v. Zieten, **T. Reinert**, I. Symietz, J. Vogt, and M. Wolf.
   Osteodensitometrical Studies and Elemental Analysis of Ancient Human Bones. In D. Dirksen and G. v.Bally, editors,
   Optical Technologies in the Humanities, volume 4, page 137. 1997.

2. St. Jankuhn, R.-H. Flagmeyer, **T. Reinert**, J. Vogt, T. Butz, J. Hammerl, R. Protsch v. Zieten, M. Wolf, H. Baumann, K. Bethge, and I. Symietz.
   Bestimmung der Knochenmineraldichte und der Elementgehalte von historischen Knochen. In H.-J. Krebs, editor,
   Einsatz neuer Technologien in den Geisteswissenschaften, volume 4, page 35. 1997.

1. St. Jankuhn, T. Butz, R.-H. Flagmeyer, **T. Reinert**, J. Vogt, J. Hammerl, R. Protsch v. Zieten, M. Wolf, H. Baumann, K. Bethge, and I. Symietz.
   Ion Beam Analysis of Ancient Human Bone.
   Proc. 14th Int. Conf. on Appl. of Accelerators in Res. and Ind., page 575, 1997.

Danksagung

Assistenten Herrn Raimund Wipper für die sorgfältige Pflege der technischen Anlagen und seine humorvolle Herzlichkeit in der Abteilung persönlich zu danken. Ich hoffe, ich konnte es in den vergangenen Jahren im täglichen Umgang bereits zum Ausdruck bringen.

Ich möchte mich auch bei den Kollegen aus der Werkstatt bedanken; ohne sie wäre so manche Idee nicht Realität geworden. Frau Lepping gilt auch mein herzlicher Dank für ihre pragmatische Unterstützung und Hilfe in allen verwaltungstechnischen Angelegenheiten.

Schon viel eher und vor allem mehrfach hätte auch meine Freundin Dipl.-Biol. Anja Fiedler in besonderer Weise genannt werden müssen. Die Ergebnisse ihrer Arbeiten in unseren Laboren, als Diplomandin auf radiobiologischem Gebiet und als Doktorandin in der Neurowissenschaft, haben mein Forschungsfeld enorm bereichert. Aber mein innigster Dank gilt ihr für die große Unterstützung, die sie mir in persönlich sehr schwerer Zeit gewesen ist.

Selbständigkeitserklärung

Hiermit erkläre ich, die vorliegende Habilitationsschrift selbständig und ohne unerlaubte fremde Hilfe angefertigt zu haben. Ich habe keine anderen als die angeführten Quellen benutzt und sämtliche Textstellen, die wörtlich und sinngemäß aus veröffentlichten oder unveröffentlichten Schriften entnommen wurden, und alle Angaben, die auf mündlichen Auskünften beruhen, als solche kenntlich gemacht. Ferner versichere ich, dass die vorgelegte Arbeit weder im Inland noch im Ausland in gleicher oder ähnlicher Form einer anderen Prüfungsbehörde zum Zwecke einer Habilitation oder eines anderen Prüfungsverfahren vorgelegt und in ihrer Gesamtheit noch nicht veröffentlicht wurde und keine früheren erfolglosen Habilitationsversuche stattgefunden haben.

Leipzig, den 16.03.2008

Curriculum Vitae – Tilo Reinert

Education/Qualification

1989 – 1996	Study in Physics, University of Leipzig, Germany, and Université de Lyon, France
1996 – 1997	Medical Physics, University of Heidelberg, Germany
1996	Degree in Physics (Dipl.-Phys.), University Leipzig
1996 – 2001	PhD student, ion beam laboratory, University of Leipzig
2001	Doctorate in Physics (Dr. rer. nat) with great honour (magna cum laude), University of Leipzig
2004	Qualification for Radiation Protection personnel
2008	postdoctoral lecture qualification (Dr. rer. nat. habil.)
Languages:	German (mother tongue), English, French, Russian (refreshable)

Employment

1996 – 2001	Scientific employee, Faculty of Physics, University of Leipzig
2001 – 2008	Research Assistant at the Faculty of Physics, University of Leipzig

Teaching Experience

Laboratory	Ion Beam Analysis Biophysics Undergraduate Physics
Tutorials	Experimental Physics (basic course) Nuclear Physics Particle Physics
Lectures	Nuclear Physics Ion Beam Analytical Methods
Co-/Supervision	10 diploma/MSc and 5 PhD students

Research Experience

- Implementation of an advanced nuclear microprobe laboratory

- Ion beam analysis of trace elements with sub-micron lateral resolution

- Application of PIXE / PIGE / RBS / STIM / STIM-tomography

- Proton Beam Writing

- Development of an irradiation platform for radiobiological applications

- Development of specialized Petri dishes for radiobiological applications

- Irradiation of living cells with counted single ions

- Work in close interdisciplinary collaboration (biophysics, biology, neuroscience, environmental science, forensic sciences, material science)

Publications and Presentations_____

44 publications (more than 30 in refereed journals)

15 national and international talks and more than

30 poster contributions on national and international conferences

Membership of Professional Societies_____

German Physical Society (DPG)

Conference organization / Meetings_____

International Conference on Hyperfine Interactions, Leipzig 1998

International Meetings of the NANODERM project

Application to host the next ICNMTA 2010 in Leipzig, secretary of the local organizing committee

Grant Applications_____

Contributions to:

NANODEM – Quality of skin as a barrier to ultra-fine particles (4th European Union Framework Programme)

CELLION – Studies on cellular response to targeted irradiation using nanotechnology (6th European Union Framework Programme)

NOTE – Non-targeted effects of ionising radiation (7th European Union Framework Programme)

INTERNEURO – Interdisziplinäre Ansätze in den zellulären Neurowissenschaften (Interdisciplinary Approaches in Cellular Neurosciences) (Research Training Group of the German Research Foundation DFG)